Silver-Based Nanocomposite Materials for Marine Antifouling Applications

Yee Swee Li Maxine
BEng., MTech.

Thesis submitted to the University of Nottingham for the degree of
Doctor of Philosophy

APRIL 2017

Abstract

Biofouling of marine surfaces is an age-old problem that affects natural and man-made surfaces exposed to the aquatic environment. The tenacious attachment of seaweed and invertebrates to man-made surfaces, notably on ship hulls, has incurred undesirable economic losses. The initial stage of the biofouling process has been attributed to the attachment of marine bacteria and their subsequent formation of biofilm which attract the settlement of larger sessile organisms including barnacles and seaweed.

Silver nanostructured materials have a well-documented history as antimicrobial agents against pathogenic bacteria due to their ability to penetrate cell walls and interfere with crucial cellular processes. However, there is a surprising lack of information on their activity against marine biofilm bacteria that have critical roles in the initiation of marine fouling processes. This PhD project explores the antifouling properties of novel silver nanocomposite materials as potent antifouling agents against targeted organisms present in marine environments.

The study consists of the syntheses of novel silver nanocomposite materials using various templates/matrices such as ion-exchange polymeric microspheres, zeolites, TiO_2 nanotubes and graphene nanosheets. These materials were characterized through various instrumentation techniques including scanning electron microscopy (SEM), energy dispersive X-ray spectrometry (EDX), X-ray powder diffraction (XRD), UV-visible (UV-vis) spectrophotometry, transmission electron microscopy (TEM), accelerated surface area porosimetry (ASAP), thermal gravimetric analysis (TGA), and Raman spectroscopy to elucidate their physical properties. Their antifouling effects were evaluated on *Halomonas pacifica*, a model marine microfouling bacterium, through an established static biofilm assay. In addition, the biological effects of these silver nanocomposites were also studied on marine microalgae *Dunaliella tertiolecta* and *Isochrysis* sp.

Silver-polymer nanocomposite (Ag-PNC) microspheres were formed through a rapid chemical synthesis procedure at room temperature via the reduction of silver nitrate by sodium borohydride. The introduction of Ag nanoparticles (AgNPs) enhanced the thermal stability of the Dowex microspheres by shifting the glass transition temperature to above 300 °C and the material decomposition occurred above 460 °C. XRD analysis confirmed the presence of metallic Ag, while UV-vis absorption studies showed the characteristic surface plasmon resonance (SPR) for AgNPs ranging from 406 – 422 nm maximum absorption wavelengths. SEM imaging revealed the uniform distribution of AgNPs with diameters between 20 – 60 nm on the surface of the microbeads. The Ag-PNC materials, diluted to a concentration of 1 mg/mL in marine broth, showed a potent inhibitory effect on *H. pacifica* biofilm formation, with up to 76% decrease of biofilm when contrasted with the polymeric microspheres without Ag. Ag-PNCs also caused significant growth inhibition of *D. tertiolecta* and *Isochrysis* sp.

Silver-zeolite nanocomposite clusters (AgZ) were formed through a low temperature chemical reduction method using the environmentally friendly trisodium citrate. The stable and porous inner structure of ZSM-5 zeolites performed a dual role as a stable size-control template and a reservoir of antimicrobial nanosilver. SEM revealed the globular and cluster-like morphology of the AgZ composites, with a homogenous distribution of silver particles on the surface of the clusters. EDX results displayed an increasing Ag loading with higher concentrations of Ag precursor, up to 10 wt% Ag. The UV-visible absorption displayed the characteristic SPR absorption

maximum ranging from 408 – 500 nm. The AgZ clusters with metallic silver loading of up to 10 wt% Ag, diluted to a concentration of 1 mg/mL, reduced *H. pacifica* biofilm attachment of up to 81% compared to pure zeolite alone. XRD analysis clearly indicated the presence of metallic Ag while the ZSM-5 zeolite crystalline framework remained largely intact after the Ag crystal growth process. Brunauer-Emmett-Teller (BET) analysis showed a reduction in surface area of up to 44% with the incorporation of AgNPs into the zeolite, indicating the formation and growth of Ag within the internal pores and channels of the zeolite. Although the introduction and crystal growth of silver nanoparticles within the porous structure of the zeolite caused a change from a mesoporous to a largely macroporous structure, the integrity of the zeolite template was preserved.

Silver-titania nanotube (Ag/TNT) composite material was prepared through a novel 2-step hydrothermal synthesis method. Titania nanotubes were chosen as a support material for the AgNPs as its greater specific surface area on the inner and outer surfaces of its tubular structure lead to enhanced properties. The morphology, particle size, chemical content, crystal structure, optical properties and surface area were systematically characterized. Determination of biofilm inhibitory properties revealed that Ag/TNT (concentration of 0.1 mg/mL) with the lowest silver content (0.95 wt% Ag) decorated with AgNPs of approximately 3 nm reduced biofilm formation of *H. pacifica* by 98% compared to pure titania nanotubes and bulk silver alone. Growth inhibition of *D. tertiolecta* and *Isochrysis* sp. were also observed. Interestingly, the antifouling properties were improved with a size decrease of AgNPs. The work shows that titania nanotubes are a stable and effective support for the anchoring and growth of AgNPs. The addition of very low amounts of Ag enhanced the antifouling property of pure TiO_2 to produce an extremely potent antifouling effect on the targeted organisms.

Graphene-Ag (GAg) nanocomposites were prepared from a novel and mild hydrothermal synthesis method which bypasses the formation of graphene oxide. The GAg nanocomposite combines the antimicrobial property of silver nanoparticles and the unique structure of graphene as a support material, with potent marine antifouling properties. The results show that GAg nanocomposites displayed significant biofilm inhibition property on *H. pacifica* and antiproliferative effects on *D. tertiolecta* and *Isochrysis* sp. As low as 1.3 wt% of Ag loading on a GAg sample, diluted to a concentration of 0.1 mg/mL, inhibited biofilm formation from *H. pacifica*. The GAg sample with 4.9 wt% Ag loading was associated with a biofilm inhibition of 99.6%. The marine antifouling properties of GAg nanocomposites were a synergy of the biocidal AgNPs anchored on the flexible graphene sheets, thereby providing maximum active contact surface areas to the target organisms. The GAg material was characterized with SEM, EDX, TEM, XRD and Raman spectroscopy. In addition, the GAg material exhibited the surface-enhanced Raman scattering (SERS) effect. The AgNPs were estimated to be between 72-86 nm, observed supported on micron-scaled graphene flakes.

These results strongly suggest that the 4 types of silver-based nanocomposite materials are promising marine antifouling agents. The addition of very low amounts of Ag enhanced the antifouling property of the support structure, and the nanocomposites were shown to be more effective on the targeted organisms compared to the matrix material or bulk silver alone. In addition, the precursor materials used in the syntheses are affordable and easily available, whilst the synthetic methods and conditions are facile, environmentally friendly, and capable of producing high yields.

Published Work

Yee, M. S-L., Khiew, P.S., S.S. Lim, Chiu, W.S., Tan, Y.F., Kok, Y-Y., Leong, C-O. 2017. "Enhanced Marine Antifouling Performance of Silver-Titania Nanotube Composites from Hydrothermal Processing". *Colloids and Surfaces A: Physicochemical and Engineering Aspects*, 457, 382 – 391. http://doi.org/10.1016/j.colsurfa.2017.02.034

Yee, M. S-L., Khiew, P.S., Tan, Y.F., Chiu, W.S., Kok, Y-Y., Leong, C-O. 2016. "Green Synthesis of Graphene-Silver Nanocomposite and its Application as a Potent Marine Antifouling Agent". *Colloids and Surfaces B: Biointerfaces,* 148, 392 – 401. http://doi.org/10.1016/j.colsurfb.2016.09.011

Yee, M. S-L., Khiew, P.S., Tan, Y.F., Chiu, W.S., Kok, Y-Y., Leong, C-O. 2015. "Low Temperature, Rapid Solution Growth of Antifouling Silver-Zeolite Nanocomposite Clusters". *Microporous and Mesoporous Materials*, 218, 69 – 78. http://doi.org/10.1016/j.micromeso.2015.07.004

Yee, M. S-L., Khiew, P.S., Tan, Y.F., Kok, Y-Y., Cheong, K.W., Chiu, W.S., Leong, C-O. 2014. "Potent antifouling silver-polymer nanocomposite microspheres using ion-exchange resin as templating matrix". *Colloids and Surfaces A: Physicochemical and Engineering Aspects*, 457, 382 – 391. http://doi.org/10.1016/j.colsurfa.2014.06.010

Awards

Best Oral Presenter Award, *International Conference on Advanced Materials and Nanotechnology*; 23-24 November, 2016; Kuala Lumpur, Malaysia.

Oral presentation

Yee, M. S-L., Khiew, P.S., Tan, Y.F., Chiu, W.S., Kok, Y-Y., Leong, C-O. Investigation of Graphene-Silver Nanocomposite as a Potent Marine Antifouling Agent. *International Conference on Advanced Materials and Nanotechnology*; 23-24 November, 2016; Kuala Lumpur, Malaysia.

Poster presentation

Yee, M. S-L., Chiu, W.S., Loh, H-S., Khiew, P.S. 2013. Silver-zeolite nanocomposites for marine antifouling. Poster session presented at: *University of Nottingham Malaysia Campus Postgraduate Research Week 2013*; 30 Sep – 4 Oct, 2013; Semenyih, Selangor, Malaysia.

To my beloved children, Ethan and Maia,

may this inspire you on a lifelong journey of learning.

Acknowledgements

When I decided to embark on this journey, little did I realize how much it would change me. This journey has introduced me to some of the most incredible people in the world, while at the same time, I also discovered new dimensions to the people that were already in my life. Without their kindness and blessings, I would not be where I am today.

I would like to extend my deepest appreciation to my supervisor, Prof. Dr. Khiew Poi Sim, for the amazing opportunity to pursue this project. I am grateful to Prof. Khiew for his constant drive and encouragement, unwavering positivity, helpful discussions and valuable insights. Without his support and guidance, I would not be able to complete my studies. Many thanks also to my co-supervisor, Prof. Sivakumar Manickam, for the always enthusiastic support, useful suggestions and wise words of encouragement. I am grateful to Dr. Feroz Kabir, Dr. Lim Siew Shee, and various anonymous reviewers for providing helpful feedback on my work. I gratefully acknowledge Dr. Lim, Dr. Michelle Tan, Mr. Tan Thian Khoon and Prof. Dino Isa for providing the materials to facilitate my research. Pursuing a PhD by taking a career break can be a lonely journey, and I am thankful for the solid friendship of Ms. Nicole Ho Mui Yen.

To the staff of the Faculty of Engineering's Analytical Unit at University of Nottingham Malaysia Campus (UNMC), especially Mr. Andrew Yakin Sinit, Ms. Khairani Hasuna Jaapar, Mr. Ahmad Fareez Mohd. Rawi, Mr. Mohd. Faizal Abdul Hamid, Ms. Filzah Mohd. Fauzi, Ms. Noor Fatihah Suhaimi and Ms. Farawahida Mokhtar, I am forever indebted to all of you for your skillful technical support, helpful discussions and your kindness and enthusiasm in supporting my work. Thank you also to Mr. Mohd Riduan Mt Said from the Centre for Research and

Bandar Kinrara, Selangor.

December 2016

Table of Contents

List of Figures

List of Figures (continued)

List of Tables

List of Symbols

Ag	silver
g	gram
h	hour
M	molar
mg	milligram
min	minute
mL	millilitre
mW	milliwatt
nm	nanometre
O	oxygen
V	vanadium
wt%	weight percent
λ_{max}	wavelength of maximum absorbance

List of Abbreviations

AAS	atomic absorption spectroscopy
abs	absorbance
AFM	atomic-force microscopy
AgNM	silver nanomaterial
AgNO$_3$	silver nitrate
AgNP	silver nanoparticle
Ag-PNC	silver-polymer nanocomposite
Ag/TNT	silver-titania nanotube, silver-TiO$_2$ nanotube
AgZ	silver-zeolite
ASAP	accelerated surface area porosimetry
ASTM	American Society for Testing and Materials
a.u.	arbitrary unit
avg	average
BET	Brunauer-Emmett-Teller
BJH	Barrett, Joyner, and Halenda
BSA	bovine serum albumin
CAS	Chemical Abstracts Service
CCD	charge-coupled device
CRT	cathode ray tube
D. tertiolecta	*Dunaliella tertiolecta*
DA	deacetylation degree
DFT	density functional theory
DLS	dynamic light scattering
DSC	differential scanning calorimetry
DTG	differential thermal gravimetry
EDX	energy dispersive X-ray spectrometry
EELS	electron energy loss spectroscopy
ELISA	enzyme-linked immunosorbent assay
Em	emission
EPS	extracellular polymeric substances
Ex	excitation

FCC	face-centred cubic
FESEM	field emission scanning electron microscopy
FLG	few-layer graphene
FTIR	Fourier-transform infrared spectroscopy
FT NMR	Fourier-transform nuclear magnetic resonance spectroscopy
FWHM	full-width at half maximum
GAg	graphene-silver
GO	graphene oxide
H. pacifica	*Halomonas pacifica*
HRTEM	high-resolution transmission electron microscopy
ICDD	International Centre for Diffraction Data
ICP-AES	inductively coupled plasma atomic emission spectroscopy
ICP-MS	inductively coupled plasma mass spectroscopy
ICP-OES	inductively coupled plasma optical emission spectroscopy
IMO	International Maritime Organization
Isochrysis sp.	*Isochrysis* species
LaB_6	lanthanum hexaboride
LDH	lactate dehydrogenase
MTT	dimethyl thiazolyl diphenyl tetrazolium
Mw	molecular weight
$NaBH_4$	sodium borohydride
NP	nanoparticle
OD	optical density
PDF	powder diffraction file
PEI	polyethylenimine
PVA	polyvinyl alcohol
PVP	polyvinylpyrrolidone
RFU	relative fluorescence units
rGO	reduced graphene oxide
rpm	revolutions per minute
SAED	selected area electron diffraction

List of Abbreviations (continued)

s.d.	standard deviation
SEM	scanning electron microscopy
SERS	surface-enhanced Raman spectroscopy
SPC	self-polishing copolymer
SPR	surface plasmon resonance
SWAXS	small- and wide-angle X-ray scattering
TBT	tributyltin
TEM	transmission electron microscopy
TGA	thermal gravimetric analysis
TiO_2	titanium dioxide
TNT	titania nanotubes, or TiO_2 nanotubes
UV-vis	ultra violet – visible spectrophotometry
WAXD	wide-angle X-ray diffraction
WAXS	wide-angle X-ray scattering
XPS	X-ray photoelectron spectroscopy
XRD	X-ray powder diffraction
ZSM-5	Zeolite Socony Mobil – 5

Chapter 1: Introduction

1.1   Introduction to Marine Fouling

Marine fouling is the accumulation of organisms including bacteria, seaweed and barnacles on man-made surfaces which are continuously submerged in seawater [1]. Figure 1.1 shows examples of soft and hard fouling on ocean vessels. It is a natural phenomenon which has plagued sailors for as long as mankind have been sailing the oceans. One of the earliest mentions of marine fouling was by Plutarch (45 A.D. – 120 A.D.): "it was usual to scrape the weeds, ooze, and filth from the ships' sides to make them go more easily through the water" [2]. A 19th century British publication described fouling as a "most expensive and objectionable" phenomenon afflicting the hulls of the iron-clad ships of the time, costing "enormous amounts of time, ingenuity, and money" to remove [3].
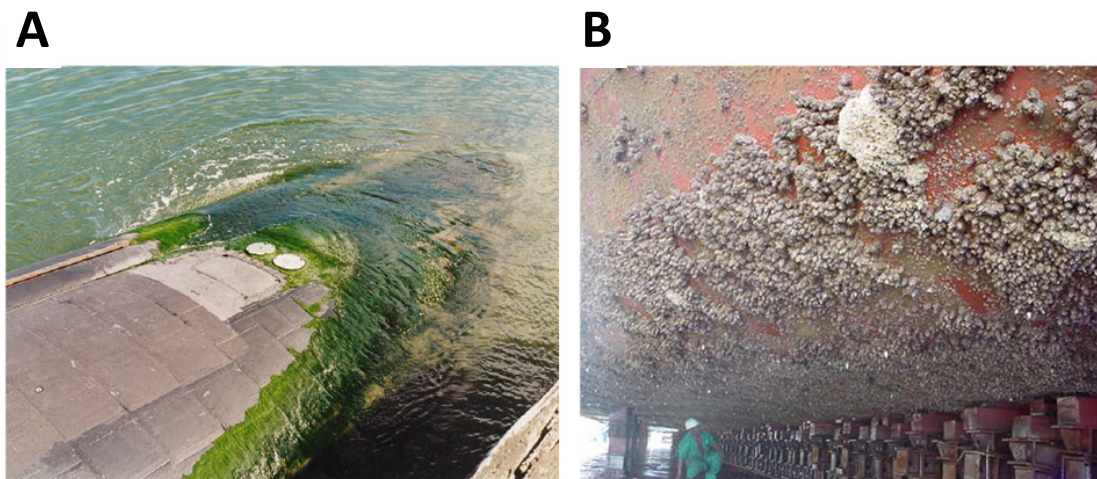
Figure 1.1: Evidence of advanced biofouling accumulation on marine surfaces.
(A) Soft fouling macroalgae *Enteromorpha* covers the hull of a submarine (Image credit: Dr. J. Lewis). (b) Hard macrofouling such as barnacles attached onto a ship hull. (Image credit: Dr C.D. Anderson) [4].

The biofouling process generally proceeds in incremental stages, with bacteria being recognized as playing an important role in the early formation of a fouling community [5]. The biofouling process is generally divided into 2 stages:

1) Microfouling: starts with biofilm formation by bacteria and diatoms, followed by attachment of algae spores. Biofilms are also known as "slime" [6].

2) Macrofouling: consisting of attachment by soft fouling such as seaweed, and hard fouling organisms including crustaceans and molluscs.

Bacteria which manage to attach onto a suitable surface will produce an adhesive filmy matrix made of extracellular polymeric substances (EPS), otherwise known as a microbial biofilm. In the marine environment, the larvae of invertebrates and spores of algae are prompted to search for, and bind to solid surfaces in order to further their chances of survival [6]. These larvae and spores identify settlement cues from the microbial biofilm surfaces as potential habitats which provide the necessary nutrients and shelter [7].

1.2   The Costs of Marine Fouling

Marine fouling is a ubiquitous and undesirable issue which affects shipping lines, naval fleets, oil rigs, underwater pipelines, aquaculture nets, marine environmental sensor equipment, and marine energy infrastructure. Although such

structures are exposed to challenging environmental conditions during their service lifetime (including exposure to seawater, temperature fluctuations and ultra-violet irradiation), biofouling presents substantial economic and environmental costs to the affected industries.

The hydrodynamics of a ship's hull or turbine blade is negatively affected, due to additional weight of the fouling attachments. This causes a substantial reduction of speed [8], an increase in fuel usage and higher overall voyage costs [1]. The international marine transport industry uses an estimated 50% of their operating costs on fuels, with USD18 billion spent in 1999 [9]. The total fuel consumption is estimated to grow at an annual rate of 3.1% [10].

Without effective antifouling protection, it has been estimated worldwide that an extra 72 million tonnes of fuel is burned each year. The carbon footprint of ships is estimated to contribute to an increase of 210 million tonnes of greenhouse gas emissions and 5.6 million tonnes of sulphur dioxide, causing unacceptable impacts on the environment [11]. Additional costs are involved in the maintenance of ship hulls, including manual removal of hard fouling substances and reapplication of antifouling coatings. These dry-docking activities limit the operations of the ship and cause a loss of economic opportunity.

The fouled hull of a ship is a major vector in the spread of invasive aquatic species. These invasive species are termed Introduced Marine Pests (Australia, New Zealand), Aquatic Nuisance Species (United States), and Harmful Aquatic Organisms (International Maritime Organization, Ballast Water Convention). As these terms

imply, invasive aquatic species are a threat to the survival and wellbeing of native species, reducing native biodiversity and can even cause extinction of fragile species. They also alter the habitat, degrade sensitive environments and spread disease [12].

1.3 History of Marine Fouling Prevention

The early sailors from Phoenicia and the Carthaginian Empire (1500 – 300 B.C.) were credited with the first antifouling coatings, consisting of pitch and copper sheathing for their wooden ships [2, 6]. Lead sheathing was used by Archimedes (287 – 212 B.C.), and later on by the Romans and the 15th century Spanish, English and French seamen as protection for their oak ships against "ship-eating sea worms"[2]. Eighteenth century British Admiralty experiments which used copper sheathing on their frigates noted the success of copper's antifouling properties. However, in the 19th century, with the introduction of iron-hulled ships, the implementation of copper sheathing was eventually abandoned due to its devastating corrosive effects on iron [2]. This spurred renewed interest in the development of novel antifouling technologies, primarily from various naval authorities with defensive and strategic motives.

Apart from using protective metallic sheets, protective paint coatings consisting of polymeric matrices laced with toxic substances were introduced to combat fouling [13]. In the mid-20th century, intensive research into antifouling paints culminated with a breakthrough in the form of self-polishing copolymer (SPC) antifouling paints laced with the highly toxic compound called tributyltin (TBT).

Patented by Milne and Hails in 1974 [14], these paint coatings have a controlled rate of wear (polishing rate ~ 5-20 microns/year) while at the same time releasing toxic TBT which kills fouling organisms. SPC-TBT paints are compatible with steel and aluminium, allowing the ship hulls to remain smooth and free from fouling for up to 5 years [13].

1.4   Issues with Tributyl Tin (TBT) and Its Substitutes

The toxic effects of TBT was discovered on non-target organisms, including causing sterility (imposex condition) and eventual death of female sea snails such as *Nucella lapillus* [15]. It devastated fisheries and aquaculture industries, and showed long-term persistence in the environment [16]. Due to such dire threats, a global ban on TBT was initiated by the International Maritime Organization (IMO), an agency of the United Nations which is responsible for improving maritime safety and the prevention of marine pollution from ships. Since 2008, TBT-containing antifouling paints have been outlawed according to the IMO's International Convention on the Control of Harmful Anti-fouling Systems on Ships [17].

The current generation of biocidal antifouling paints rely on toxic metal oxides such as copper oxide and zinc compounds. Although effective against certain common fouling organisms, these compounds are less toxic than the older generation TBT but have not achieved the same level of success as TBT in the prevention of marine fouling [18].

1.5   Rationale of Study

This thesis proposes to investigate silver nanocomposite materials as potential marine antimicrofouling agents. Composite materials are defined as the "combination of two or more materials that results in better properties than those of the individual components used alone" [19]. Nanocomposite materials contain domains or inclusions on the nanometre scale.

Metallic silver and silver ions have a long history as antimicrobial agents [20] and is well-tolerated by mammals. Over 2,400 years ago, Hippocrates, the Father of Medicine, described the use of silver to facilitate better wound healing and to preserve food and water from bacterial infections [21]. Due to their versatile antibacterial property, silver-based nanomaterials are becoming an increasingly viable class of materials for a wide range of biomedical applications [22-25].

Although most people are familiar with bulk silver, which is lustrous white in colour [Figure 1.2(A)], silver nanoparticles (AgNPs) can take on a variety of colours, due to a phenomenon known as surface plasmon resonance (SPR) effect [26]. Figure 1.2 (B) shows AgNPs in stable colloidal dispersions appearing as yellow, whilst unstable AgNPs which have undergone aggregation to form micron-sized clusters, appear brownish to greyish in colour [27]. In fact, suspensions of AgNPs with sizes ranging from 40-100 nm exhibit different colours [28].
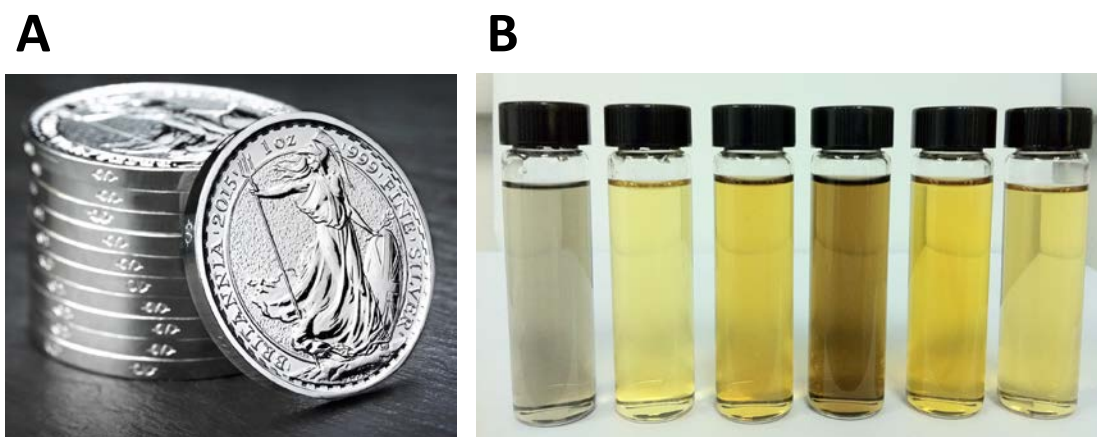
Figure 1.2: Various appearances of elemental silver. (A) Bulk silver coins appear shiny and lustrous [29], and (B) silver nanoparticles as yellow, brown and grey colloidal suspensions [30].

A nanoparticle is made up of atomic clusters with at least one dimension within the 100 nm size range. As a consequence of their quantum size effects, nanoparticles exhibit properties that are distinctly different from the bulk material [31]. Although a metallic nanoparticle is much smaller than the bulk metal, it possesses a higher surface-to-volume ratio. The extremely large surface area of nanomaterials improved the properties of the bulk material, while at the same time, reducing the material cost, as less material is needed to obtain similar, or enhanced results.

On the other hand, the extremely high surface-to-volume ratio of nanoparticles is associated with a higher state of surface energy. Without suitable stabilizers, nanoparticles are highly unstable and will coalesce with other nanoparticles to form large micron-sized particles, negatively impacting their properties. Thus, AgNPs are engineered with suitable stabilizers or supported on suitable substrates to form stable silver nanocomposite materials.

As the biofouling process usually proceeds from established bacterial colonies, silver-based nanomaterials are suitable candidates to investigate for their role in deterring the formation of biofilms and the prevention of microfouling. The antimicrobial property of silver becomes more potent with a decrease in its particle size, as atomic silver is more easily diffused through a suitable medium into bacterial cell walls.

One of the most promising routes to resolve fouling is the inhibition of bacterial settlement. Bacterial formation of a biofilm has been found to be an important link to the development of soft and hard fouling matter [5], which becomes increasingly difficult to remove after their settlement.

In terms of research into the antifouling property of silver-based materials, there has been a surprising lack of literature. Rana et al. (2011) [32] and Sawada et al. (2012) [33] have reported on the use of silver as antifouling agents in water treatment and filtration membranes. In paint coating applications incorporating the antimicrobial property of silver materials, Kumar (2008) [34] reported on general formulations of AgNPs-embedded antimicrobial paints using common household paints, whilst Holtz et al. (2012) [35] have reported on the use of silver vanadate nanowires as an antimicrobial agent in water-based paints for household and hospital use. However, to date, antifouling applications incorporating silver-based nanomaterials for marine environments remain scarce.

1.6   Aims of Study

The principal aim of this study is to synthesize novel silver nanocomposite materials and investigate their potential as antimicrofouling agents against marine fouling organisms. The aim is to produce silver nanocomposite materials with highly effective anti-microfouling properties, using relatively low amounts of silver precursor materials. In addition, the synthesis methods described in this thesis are novel, facile and affordable to produce silver nanocomposite materials for marine anti-microfouling applications. The methods are cost-effective, produce high Ag loading, employ low amounts of energy, and use easily available and conventional precursor materials. The major objectives in this project are:

1) Synthesize novel silver-polymer and silver-zeolite nanocomposite materials from low-temperature chemical processes.

2) Synthesize novel silver-titania and graphene-silver nanocomposite materials from hydrothermal processes.

3) Elucidate the key characteristics of the novel silver nanocomposite materials including their morphology, crystallinity, elemental composition, optical properties and other properties related to the specific material through scanning electron microscopy, X-ray powder diffraction, energy dispersive X-ray spectrometry, UV-visible spectrophotometry, transmission electron microscopy, thermal gravimetric analysis, accelerated surface area porosimetry, and Raman spectroscopy.

4) Evaluate the antifouling properties of the novel silver nanocomposite materials through their biological effects on marine bacteria and marine microalgae.

1.7   Scope and Limits

This thesis is organized into 8 chapters. Chapter 1 gives a background and motivation to the study, and outlines the major objectives of this project. Chapter 2 is a detailed review and discussion on the major areas covered by this project. It includes a survey on silver nanocomposite materials, their synthesis methods and their applications, as well as a review of the marine fouling process, marine organisms involved in fouling, and current antifouling technologies.

Chapter 3 is related to the materials and methodologies used in the studies, along with the instrumentation methods to characterize the silver nanomaterials. The characterization methods used are selected based on their suitability with the class of material being studied. Biological evaluation methods used to assess antimicrofouling activity is also described in this chapter. The antimicrofouling evaluation is limited to studies using 1 marine bacterium and 2 types of marine microalgae.

Chapters 4-7 are each devoted to a specific study of each silver nanocomposite system; i.e. silver-polymer nanocomposites, silver-zeolite nanocomposites, silver-titania nanocomposites, and graphene-silver nanocomposites. Each of these chapters is based on published scientific papers as a result of the work done in this PhD thesis.

Finally, Chapter 8 summarizes the major findings and key contributions of this thesis. A list of possible future work is proposed to follow up on the results from this project.

Chapter 2: Literature Review

2.1   Silver Nanoparticles

Nanostructured materials has been intensively investigated since Feynman contemplated on the possibility of the enormous range of properties that substances can possess "when we have some control of the arrangements of things on a small scale" [36]. Nanoparticles are atomic clusters with at least one dimension within the 100 nm size range. The use of the term "nanostructured materials" is preferred, however, "nanophase materials" and "nanocrystalline materials" are also used, depending on the context [36]. By the attribute of their nanoscale size, nanoparticles display properties that are distinctly different from the bulk material [31].

Elemental silver (Ag) is a transition metal located in Group 1b Period 5 of the periodic table. It is a noble metal, highly valued for consumer, industrial and medical applications. It has the highest known electrical and thermal conductivity of all metals and is an important material in the fabrication of electrical circuits. Silver nanowires with an electrical resistivity of 1.6×10^{-6} Ω cm are excellent candidates to replace indium tin oxide (ITO) electrodes due to better malleability and mechanical robustness [37].

Although bulk silver is lustrous white in colour, AgNPs can take on a variety of colours, due to a phenomenon known as surface plasmon resonance (SPR) [26]. Small particles absorb most light from the visible wavelengths while larger particles

scatter light. Silver nanoparticles in dispersed form appear yellow in solution, while aggregated silver in solution appear greyish in colour [38].

Silver has historically been used in medicine for at least 2000 years. Hippocrates used it in the treatment of ulcers and to facilitate better wound healing. The medical use of silver predates the discovery of bacteria as infectious agents and before the use of antibiotics [20]. Table 2.1 shows a summary of the applications of silver-containing nanomaterials. Silver materials have been systematically evaluated for their effectiveness against at least 650 species of unicellular organisms [20].

Due to their versatile antibacterial property, silver-based nanomaterials are becoming an increasingly viable class of materials for a wide range of biomedical applications. In Table 2.1, more than half of the surveyed research focused on the antimicrobial activity of nanosilver-containing materials, for example in hydrogels [39], as polymer composite films [40], dental resins [41] and for biocompatible artificial bone growth [42].

Smaller AgNPs of up to 2 nm are photoluminescent. Clusters of these AgNPs exposed to excitation wavelengths of 350 – 450 nm result in blue-green photoluminescent emissions. Cells which are conjugated to these AgNPs can be viewed more clearly using bio-imaging methods compared to traditional methods [43]. AgNPs are also important catalyst materials, for example in the synthesis of enaminones, the precursor to many pharmaceutical compounds [44].

13

Table 2.1: Applications of silver nanomaterials.

Application	Material	Reference
3D laser writing by multiphoton absorption lithography	Ag nanostructures in polymer matrix	[45]
Adsorption of volatile organic compounds (VOCs), e.g. Butyl acetate	Ag-zeolite	[46]
Adsorption of ammonia (20 - 37% from aqueous solutions).	Ag-zeolite	[47]
Ag ink or Ag paste for printable electronics	AgNP	[48]
Ag-based solid carbon paste electrode for detector in ion chromatography for sensitive detection of iodide	AgNP	[49]
Antibacterial	AgNP	[22], [23], [24], [25], [50]
	AgNP and Ag nanochains	[51]
	Ag-hydrogel nanocomposite	[39]
	Ag-PEI multilayer assembly	[52]
	Ag-polymer composite	[53]
	Ag-reduced graphene oxide	[54]
	Ag-zeolite	[47], [55]
	Ag nanocomposite film	[40]
	Ag(I) complex with L-tryptophan (TRP)	[56]
	AgNP-polysaccharide nanocomposites, hydrogels	[57], [58], [59]
Antibacterial - dental resins	Ag-Zn nanocomposite	[41]
Antibacterial - food preservation and food safety	Ag-zeolite in polyethylene composite films	[60]
Antibacterial food packaging material	AgNP-loaded cellulose-based filter paper	[61]
Antibacterial membrane	Ag-phospholipid membrane	[62]
Antibacterial membrane - Water treatment	AgNP in polysulfone ultrafiltration membranes	[63]
Antibacterial paint coating	AgNP	[34]
	Ag vanadate nanowires	[35]
Antibacterial coating for concrete sewer systems against sulphur oxidizing bacteria	Ag-zeolite	[64]
Antibacterial coatings with amide groups adhere effectively to glass surfaces	AgNP	[65]
Antibacterial textile	AgNP-filled nylon 6 nanofibers	[66]
Antibacterial, antifungal	AgNP	[67]

Table 2.1 (continued): Applications of silver nanomaterials.

Application	Material	Reference
Antibacterial, cytocompatible, free-radical scavenging	AgNP	[68]
Antifouling agent – preservation of underwater archaeological surfaces (marble/stone)	Ag doped-TiO$_2$	[69]
Antifouling membrane - seawater desalination	Ag salts incorporated in thin film composite (TFC) membranes	[32]
Antifouling membrane - water treatment	Ag-polymer membrane	[33]
	Ag-TiO$_2$/HAP/Al$_2$O$_3$ composite membrane	[70]
Antifungal	AgNP	[71]
Antiproliferative	Ag(I) complex with L-tryptophan (TRP)	[56]
	AgNP	[25]
Bioactivity. Promote apatite formation. Biocompatibility for bone regeneration	Ag-zeolite	[42]
Biocompatibility. No decrease in proliferation of 3T3 fibroblasts and rat aortic vascular smooth muscle cells (VSMCs)	AgNP	[72]
Biocompatible implant and prosthetic materials	Ag-Pt alloy NP	[73]
Bio-label for electroanalytical immunoassay to measure human chorionic gonadotropin (hCG)	AgNP as bio conjugate sensor	[74]
Biomedical	Ag nanocomposite film	[40]
Biomedical textiles for wound healing and wound dressing	AgNP in hyaluronan fibres	[75]
Catalytic oxidation of butyl acetate	Ag-zeolite	[76]
Catalytic oxidation of ethyl acetate	Ag-zeolite	[77]
Catalytic reduction of 4-nitrophenol	Ag-mesoporous carbon	[78]
Catalytic reduction of 4-nitrophenol by NaBH$_4$	Ag-polymer nanocomposite	[79]
Conductive polymeric metal NP	Ag-functionalized with bithiophene	[80]
Current cutting-off fuse component for microelectronics/micromechanical systems	Ag dendrites in thermosetting polymer resin	[81]
Electrocatalyst for ethanol oxidation - direct ethanol fuel cell applications	AgNP on self-organized TiO$_2$ nanotubes	[82]

Table 2.1 (continued): Applications of silver nanomaterials.

Application	Material	Reference
Electroluminescence (nano laser)	AgNP	[83]
Food safety – detection of melamine	Ag-graphene nanocomposite	[84]
Gratzel photoelectrochemical cells	Ag/TiO$_2$ nanocomposite	[85]
Hydrophilic and antimicrobial coating for condensers used within manned spacecraft. Microbiocidal to bacteria, fungus, marine yeast	Ag-zeolite coating	[86]
Luminescent in solid state and fluid solutions	Au-Ag mixed metal alkynyl complex	[87]
Luminescent, Raman enhancement effect for bioimaging and sensing	AgNP	[88]
Photocatalytic degradation of azo dye (Acid Red 88) enhanced by suppressing detrimental recombination of photogenated charge carriers	Ag-ZnO NP	[89]
Photodegradation of azo dyes (methylene blue) and methyl orange	AgNP	[90]
Photodetector	Ag-graphene nanocomposite	[91]
Photoluminescence	Ag-zeolite	[92]
Photoluminescence for bio-imaging	AgNP	[43]
Photothermal therapy of cancer cell	Ag-aptamer conjugated nanorods	[93]
Precursor for Ag-containing semiconductor NP eg. Ag$_2$S, AgI, AgO	Ag-chitosan nanocomposite	[94]
Real-time naked-eye detection of amine	AgNP	[95]
Recyclable catalyst for synthesis of different enaminones	AgNP	[44]
Reservoir of bactericidal metal ions	Ag-based metal-organic framework, Ag$_3$(3-phosphonobenzoate)	[96]
Sensor for nitrite	Graphene/AgNP/polypyronin paper electrode	[97]
Superhydrophobic, antifouling, antibacterial	Ag-perfluorodecanethiolate complex films	[98]
Surface-enhanced Raman scattering (SERS) active substrate for single-walled carbon nanotubes (SWCNTs)	Ag electrode with Au/Ag NP	[99]
Surface-enhanced Raman spectroscopy (SERS) substrates with excellent enhancement ability	Ag- or Au-chitosan films	[100]

Table 2.1 (continued): Applications of silver nanomaterials.

Application	Material	Reference
Transformation of spherical to triangular shape. Nanoprisms coupled with quantum dots for high performance single-photon source	Ag nanoprisms	[101]
Water treatment membrane	Ag on crumpled-reduced graphene oxide – TiO_2 nanocomposite	[102]

2.1.1   Synthesis Routes of Silver Nanoparticles

There are various techniques for the synthesis of AgNPs. Silver nanoparticle synthetic routes may be classified into chemical methods and physical / mechanical methods. Depending on the specific applications required of the silver nanomaterial, the methods, precursor materials and reagents used will determine the final structure of the material.

The challenge found in many synthetic routes for formation of silver nanostructures, is the ability to control the size and to maintain the stability of the product. Such small particles have a natural tendency to undergo agglomeration. Agglomeration is the propensity of small sized particles having a large surface area to reduce their high surface energy by coalescing with other particles to form larger, more stable aggregates. The process by which the particle growth occurs is known as Ostwald ripening [103]. In aqueous solutions, silver colloidal suspensions may agglomerate very quickly and require a stabilizer or capping agent such as a surface-active compound [104].

A review of recent published syntheses work of AgNPs is presented in Table 2.2. A majority of the synthetic methods involves chemical reduction of silver precursors, often, aqueous silver nitrate. The data presented in Table 2.2 also includes the size of the obtained AgNPs. AgNPs stabilization can be achieved through electrostatic or steric approaches. Electrostatic stabilization involves coordinating metal particles to anionic species such as halides, carboxylates or polyoxoanions, to prevent nanoparticles from agglomeration. To prevent agglomeration or particle growth, electrostatic stabilization uses the Coulombic repulsion of similarly charged molecules to keep them apart. On the other hand, steric stabilization employs polymers with bulky pendant groups or side groups to prevent the metallic nanoparticles from clustering [105].

The most popular chemical synthesis route to produce AgNPs is through the reduction of silver nitrate solution by sodium borohydride (a strong reducing agent) [106-108] or sodium citrate (a weak reducing agent) [107, 109].

The reduction of silver nitrate solution by sodium borohydride, with the reaction occurring in an ice bath [107, 108] will yield a clear yellow solution. The chemical reaction is shown in Equation 2.1, where silver nitrate is reduced to metallic silver by sodium borohydride.

$$AgNO_3 + NaBH_4 \rightarrow Ag + \frac{1}{2}H_2 + \frac{1}{2}B_2H_6 + NaNO_3$$

…. Equation 2.1

18
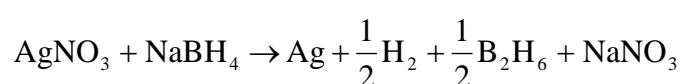
However, the conditions of reaction, such as precursor addition rate, stirring speed, and ratio of reactants, need to be controlled carefully in order to produce a stable colloidal solution. According to Mulfinger [108], an excess of borohydride anions are required to reduce the silver ions and stabilize the resultant AgNPs. Otherwise, the AgNPs will form agglomerates, and cause the colloidal solution to turn into a grey colour over a period of hours or days [108]. According to Zhu & Chen [37], the rate of addition of silver nitrate into the reactor influences the morphology of the final product. A slowly-controlled rate of silver nitrate addition will preferably form silver nanowires instead of AgNPs.

Table 2.2: Synthesis methods of silver nanoparticles, precursor material, reducing agent, capping agent and the reported particle size range.

Material	Method	Precursor	Reducing Agent	Capping Agent	Other	Size (nm)	Reference
Ag nanoprisms	Chemical reduction	Silver nitrate	Sodium borohydride, trisodium citrate ($Na_3C_6H_5O_7$)	PVP (Mw = 40,000)	$NaBH_4$ 0.1M volume 800 - 1300uL. NaOH, HNO_3 to adjust pH	~6 (NP), ~100 (triangular nanoplates)	[101]
Ag nanowires	Polyol process and solvothermal method	Silver nitrate	PVP (Mw 40K)	PVP (Mw = 40,000)	Ethylene glycol as solvent. CuCl to assist formation of twinned Ag seeds	~80 nm width	[37]
AgNP	Autoclave at 2MPa, 150 °C	Silver nitrate	Hydrogen	Polyvinyl alcohol (PVA)		Avg 40±10	[44]
	Biosynthesis using plant extracts	Silver nitrate	Extracts from xerophyte *Bryophyllum* sp., mesophyte *Cyprus* sp., hydrophyte *Hydrilla* sp.		Equal parts of extracts mixed with sterile distilled water. 40°C steam bath.	2-5	[110]
			Allium sativum (garlic) extract	*Allium sativum* (garlic) extract		4-6	[72]
			Extract from *Solanum torvum (S. torvum)* fruit.			4-10	[111]

Table 2.2 (continued): Synthesis methods of silver nanoparticles, precursor material, reducing agent, capping agent and the reported particle size range.

Material	Method	Precursor	Reducing Agent	Capping Agent	Other	Size (nm)	Reference
AgNP	Biosynthesis using plant extracts	Silver nitrate	*Abelmoschus esculentus* (L.) pulp extract			3-11 nm (TEM), 21.29 nm (DLS)	[112]
			Cinnamon zeylanicum bark extract and powder (water soluble organic compounds)			31-40, >100	[23]
			Extract of *Citrus sinensis* peel	Soluble starch	2M KOH to adjust pH	3-12	[68]
			Jatropha curcas seed extract			15-50	[113]
	Biosynthesis using bacteria	Silver nitrate	*Pseudomonas stutzeri* AG259			A few – 200 nm, or more	[114]
			Streptomyces sp. BDUKAS10			21-48	[115]
			Streptomyces hygroscopicus			20-30	[116]
	Biosynthesis using fungus	Silver nitrate	*Aspergillus niger*	-	-	3-30	[117]
			Aspergillus fumigatus	-	-	5-25	[118]
			Cladosporium cladosporioides	-	-	10-100	[119]
			Fusarium oxysporum	-	-	5-15	[120]

Table 2.2 (continued): Synthesis methods of silver nanoparticles, precursor material, reducing agent, capping agent and the reported particle size range.

Material	Method	Precursor	Reducing Agent	Capping Agent	Other	Size (nm)	Reference
AgNP	Biosynthesis using fungus	Silver nitrate	*Neurospora crassa*	-	-	Avg. 11	[121]
			Penicillium fellutanum	-	-	5-25	[122]
	Chemical reduction	Silver nitrate	*Chitosan (Mw = 400,000. DA=70%)*		1% acetic acid as solvent	10-15	[25]
			Dextran T40	Dextran T40	Sodium hydroxide (0.001M)	10-60	[50]
			Ethanol	Linoleic acid	Sodium linoleate	Avg. 16	[83]
			Hydrazine hydrate, sodium citrate	Sodium dodecyl sulphate, sodium citrate		8-50	[58]
			Hydroxypropyl cellulose	Hydroxypropyl cellulose		10-15	[123]
			Li(HBEt3)	Amidated polyethyleneimine	Toluene as solvent, amidating agent is palmitic acid or its methyl ester	1-2	[65]
			Preyssler acid H14(NaP5W30O110)	Poly(N-vinyl-2-pyrolidone) (PVP)		2-16	[90]
			Sodium borohydride (NaBH$_4$)	Branched polyethyleneimine (PEI) (Mw = 25000)		3-40	[59]
			Sodium citrate	Citrate 0.7mM, 100ml, NaBH$_4$ 5mg/ml, 4 °C	Avg. 9.2 ± 2.8	[22]

Table 2.2 (continued): Synthesis methods of silver nanoparticles, precursor material, reducing agent, capping agent and the reported particle size range.

Material	Method	Precursor	Reducing Agent	Capping Agent	Other	Size (nm)	Reference
AgNP	Chemical reduction	Silver nitrate	Sodium borohydride (NaBH$_4$)	Polyvinylpyrrolidone (PVP)		Avg. 12 ± 2	[108]
			Trisodium citrate			~100	[109]
	Decomposition of Ag(I) carboxylates	Ag(I) carboxylate synthesized from silver nitrate and carboxylic acid dissolved in NaOH	Ethanol amine derivatives (monoethanolamine, diethanolamine, triethanolamine, myristic acid, palmitic acid, stearic acid)			10-40	[48]
	Free-radical mediated autoxidation during curing process of drying oils	Silver benzoate	Free radicals naturally generated from drying of stearic acid, oleic acid, linoleic acid, linolenic acid	Fatty acids, in situ generated aldehydes, other intermediates.		12-16	[34]
	Gamma irradiation	Silver nitrate	Chitosan (Mw 400,000. DA=70%)			50-2000	[104]
			Hydrated electrons (e$^-_{aq}$), hydrogen atoms (H•)	Chitosan (low molecular wt)	Acetic acid	5-30	[24]
				Chitosan	1% acetic acid as solvent	28-1106	[124]

Table 2.2 (continued): Synthesis methods of silver nanoparticles, precursor material, reducing agent, capping agent and the reported particle size range.

Material	Method	Precursor	Reducing Agent	Capping Agent	Other	Size (nm)	Reference
AgNP	Chemical reduction via high-gravitational rotating packed bed reactor	Silver nitrate	Sodium hydroxide	Soluble starch		30-72	[125]
	In situ chemical reduction	Silver nitrate	Hyperbranched poly(amidoamine) (HPAMAM-NH$_2$)	Hyperbranched poly(amidoamine) (HPAMAM-NH$_2$)		4-15	[126]
			Hyperbranched poly(amidoamine) with terminal dimethylamine groups (HPAMAM-N(CH$_3$)$_2$)	Hyperbranched poly(amidoamine) with terminal dimethylamine groups (HPAMAM-N(CH$_3$)$_2$)		1.0-7.1	[67]
			Tyrosine residues in silk fibroin	Tyrosine residues in silk fibroin		N.a.	[127]
	Microwave assisted	Silver nitrate	Glucose	Sucralose	Triethylamine (TEA) as promoter and directing agent	4-10	[95]
	Thermal reduction	Silver nitrate	Glycine	Glycine		2-30	[88]

Table 2.2 (continued): Synthesis methods of silver nanoparticles, precursor material, reducing agent, capping agent and the reported particle size range.

Material	Method	Precursor	Reducing Agent	Capping Agent	Other	Size (nm)	Reference
AgNP	Thermal reduction at 445K in oil bath	Silver nitrate	Glycine	Glycine		0.5 - 17	[43]
AgNP, Ag nanochains	Chemical reduction	Silver nitrate	Ellagic acid (polyphenol) 5-15 μM	Ellagic acid		<10->500, time dependent	[51]
AgNP microbeads	Chemical reduction	Silver nitrate	Sodium citrate	4-mercaptomethylstyrene		30-70	[128]

Silver nitrate is also reduced to metallic silver by weak reducing agents such as sodium citrate. The chemical reaction is shown in Equation 2.2.

$$3AgNO_3 + C_6H_5O_7Na_3 + 2H_2O \rightarrow 3Ag + C_6H_5O_7H_3 + 3NaNO_3 + \frac{1}{2}H_2 + O_2$$
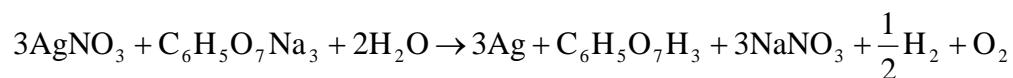
…. Equation 2.2

Other popular chemical routes include polyol synthesis, which involves heating polyols such as ethylene glycol with a silver salt precursor. Synthesis of the silver nanomaterials is conducted in the presence of polymeric capping agents such as poly(vinylpyrrolidone) (PVP) to produce metallic atoms [129]. According to Jiang et al. [129], the introduction of certain capping agents provides a powerful means of controlling the relative growth rates of different crystallographic facets. As these capping agents can interact strongly with specific facets, the relative free energies for different facets will change upon the incorporation of various capping ligands. As an example, the oxygen atoms from PVP bind most strongly to the {100} facets of Ag to facilitate the formation of Ag nanowires or nanocubes.

Lee et al. [59] studied the influence of polyethyleneimine (PEI) concentrations on the size of AgNPs. The synthesis was performed at room temperature in the presence of sodium borohydride as a reducing agent. PEI performed a dual role as a stabilizer and also as reducing agent. A schematic showing the stabilizing role of PEI is shown in Figure 2.1.
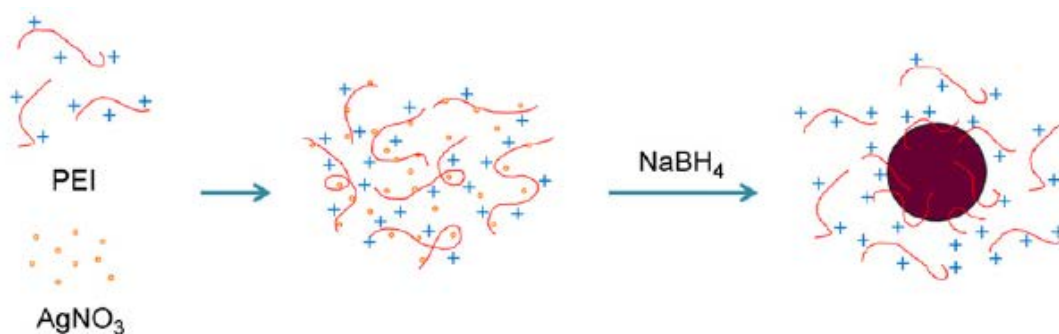
Figure 2.1: Formation of silver nanoparticles through reduction of silver nitrate.
Polyethyleneimine (PEI) is mixed with $AgNO_3$ and reduced by $NaBH_4$ to produce a
positively charged PEI-capped AgNPs. The AgNPs are kept stable by electrostatic
repulsion and steric stabilization due to pendant groups on the PEI polymer chain.
(Image taken from [59]).

According to Lee et al. [59], AgNPs would form only with the presence of

PEI, as its absence would favour the formation of bulk silver instead. At low

concentrations (0.001 wt% PEI) and high concentrations (0.04 wt% PEI), larger

particles (20-40nm) were found to outnumber smaller particles that were less than

10nm. The authors explained that at low concentration, the PEI was too weak to act as

stabilizers, whilst at high concentrations, the effect of PEI encouraged faster reduction

of Ag, and hence induce nucleation and particle growth. An optimum concentration of

0.01wt% was found to produce a majority of AgNPs in the 10 nm size range. The

observations here seemed to reinforce the findings by Aroca et al. (2005) who

reported on the synthesis of AgNPs using only silver salt reduced by sodium

borohydride, but in ice-cold conditions [107].

Clearly, apart from the rate of silver nitrate addition, there are many reaction

parameters which need to be considered and controlled in order to obtain the final

product with desired properties. These parameters include the temperature and pH of

the synthesis medium, the ratio of silver salt to reducing agent and to stabilizer, the

choice of stabilizer with specific steric influences, all of which contribute to the thermodynamics of the synthesis reaction and the kinetics of particle formation and growth.

To achieve highly dispersed nanoparticles with a narrow size distribution, Chi et al. [78] used a mesoporous carbon structure, functionalized with carboxylate groups. The mesoporous structure of CMK-3, prepared from a silica material, SBA-15, with sucrose as the carbon source, provided a solid template for the confined formation of metallic AgNPs whilst the carboxylate groups reduced the precursor $Ag(NH_3)_2NO_3$ *in situ*. The schematic of the functionalization and reduction process is shown in Figure 2.2. Metallic silver presence was confirmed through wide-angle XRD studies, with 4 diffraction peaks corresponding to the FCC structure of Ag (JCPDS card no. 4-783).
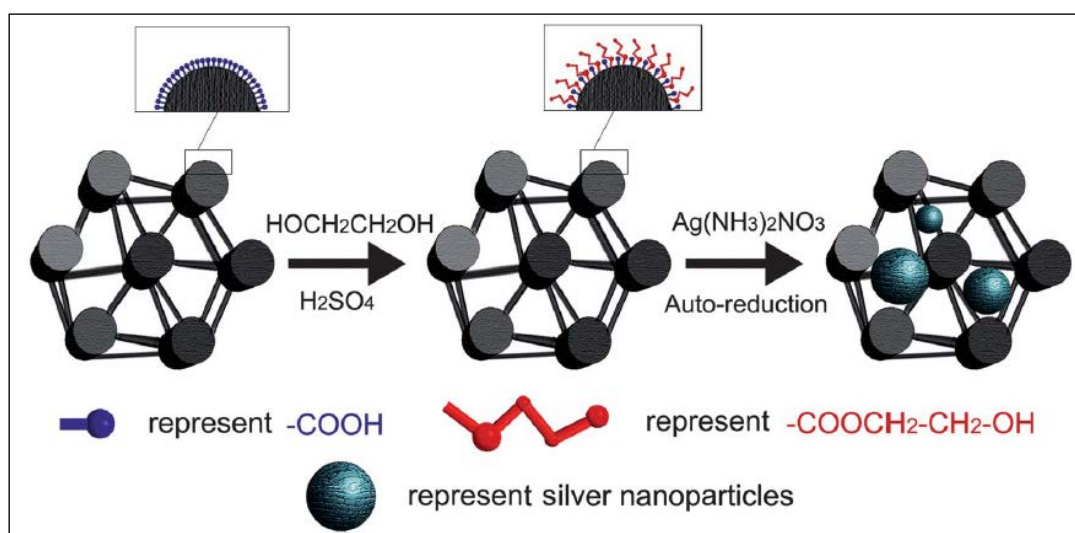
Figure 2.2: Preparation of silver nanoparticles using a mesoporous template.
This schematic representation illustrates the formation of AgNPs in a mesoporous carbon material, CMK-3. (Source: Chi et al. (2012) [78].

Apart from chemical reduction, physical methods such as microwave assisted method [130], photoreduction [131] and photochemistry [132] methods have been reported for the controlled synthesis of silver nanomaterials. The use of seed particles to form metallic nanocrystals has been touted as the ultimate approach in obtaining high precision and control over sizes, shapes and compositions of the product, with a view towards large-scale applications [133].

Due to limitations of traditional chemical methods, such as the use of toxic compounds in the synthesis process, researchers are turning to natural processes and green chemical methods such as biomineralization which exploits biomolecular templates that interact with inorganic material throughout its formation, resulting in the synthesis of particles with defined shapes and sizes [134]. Interestingly, bacteria are increasingly being used as biological reactors to synthesize silver nanomaterials. The biogenesis of AgNPs occur at very low concentrations of silver ions, as the organism undergoes cell death within minutes after the concentration is higher than the threshold level [135]. Bacteria such as *Pseudomonas stutzeri* AG259 [114], *Streptomyces* sp. BDUKAS10 [115], *Streptomyces hygroscopicus* [116], and diatoms such as *Coscinodiscus* sp. and *Cylindrotheca fusiformis* have been used for the mediated synthesis of various silver-based inorganic materials [136]. *Pseudomonas stutzeri* AG259 have been shown to form AgNPs up to 200 nm in size.

AgNPs have also been reported synthesized through extracellular methods by using the fungi *Fusarium oxysporum* [120], *Cladosporium cladosporioides* [119], *Aspergillus fumigatus* [118], *Neurospora crassa* [121], and *Penicillium fellutanum* [122], which reduces the use of extra reducing agents.

29

2.2   Silver Nanocomposite Materials

Nanocomposite materials contain domains or inclusions of nanometer size scale. Silver nanocomposite materials are usually fabricated of an organic or inorganic matrix or framework into which silver nanostructures are embedded. There are a wide variety of hybrid materials which have resulted in an interesting combination of properties, which enhances the individual traits of each material.

Among the polymer matrix or inorganic frameworks which have been used in assembly with AgNPs include nylon-6 [66, 137], polyurethane [138], polysulfone [63], polysaccharides [139, 140], phospholipids [62], zeolites [141-143], mesoporous carbon [78], graphene [54, 144], graphene oxide [102] and titanium dioxide [69, 85].

Table 2.3 shows the instrumentation methods commonly used to investigate the physical characteristics of Ag nanomaterials. Atomic/elemental composition is usually determined using energy dispersive X-ray spectroscopy (EDX) and X-ray photoelectron spectroscopy, while phase composition is studied using X-ray powder diffraction (XRD). Morphological observations through scanning electron microscopy (SEM) and transmission electron microscopy (TEM) are common, while optical properties are frequently investigated using UV-visible spectrophotometry (UV-vis). The antimicrobial properties of Ag nanomaterial are also frequently evaluated using various antibacterial assays including the disk diffusion method and growth inhibition assays.

Table 2.3: Ag nanomaterials and their characterization methods.

Characterization Functions / Objectives	Instrumentation/ Method	Ag Nanomaterial	Reference
Antibacterial	Agar disk diffusion method / Halo zone test / Kirby-Bauer test / Inhibition zone test	Ag(I) complex with L-tryptophan	[56]
		Ag-functionalized graphene composite	[84]
		Ag-graphene oxide composite	[145]
		Ag-hydrogel nanocomposite	[39]
		Ag nanocomposite film	[40]
		AgNP-loaded cellulose-based filter paper	[61]
		Ag-PEI multilayer assembly	[52]
		Ag-polymer composite	[53]
		Ag-thin film composite membranes	[32]
		Ag-TiO$_2$ nanocomposite	[69]
		Ag vanadate nanowires	[35]
		Ag-zeolite	[55]
	Antibacterial assessment assay / Bacteria growth inhibition / Liquid broth microdilution assay	Ag-based metal-organic framework, Ag$_3$(3-phosphonobenzoate)	[96]
		AgNP-filled nylon 6 nanofibers	[66]
		AgNP-polysaccharide hydrogel nanocomposite	[57]
		Ag-Zn nanocomposite	[41]
	BacLight Live/Dead bacteria viability kit	Ag-PEI multilayer assembly	[52]
		Ag-perfluorodecanethiolate complex films	[98]
	Optical density measurement in liquid culture medium	Ag-zeolite in polyethylene composite film	[60]
Atomic/elemental composition	AAS	Ag-zeolite	[86], [92]
	EDX	Ag-polymer composite	[53]
		Ag-zeolite	[55], [86]
		Ag-zeolite in polyethylene composite film	[60]
	EELS	Ag vanadate nanowires	[35]
	ICP-AES	Ag-zeolite	[77]
	ICP-OES	AgNPs in hyaluronan fibers	[75]

Table 2.3 (continued): Ag nanomaterials and their characterization methods.

Characterization Functions / Objectives	Instrumentation/ Method	Ag Nanomaterial	Reference
Atomic/elemental composition	ICP-OES	Ag-zeolite	[76]
		Ag-zeolite in polyethylene composite film	[60]
	XPS	Ag-graphene composite	[146], [147]
		Ag-mesoporous carbon	[78]
		Ag-perfluorodecanethiolate complex films	[98]
		Ag-Pt alloy NPs capped with bovine serum albumin protein	[73]
		Ag-TiO$_2$ nanocomposite	[69]
		Ag-zeolite	[77]
		Ag on self-assembled TiO$_2$ nanotube arrays	[82]
Crystallinity / Phase composition	2D SWAXS	AgNPs in hyaluronan fibers	[75]
	SAED	AgNP-loaded cellulose-based filter paper	[61]
	WAXD / WAXS	Ag-polymer nanocomposite	[79]
	XRD	Ag-carbon nanotube-reduced graphene oxide composite	[148]
		Ag-chemically converted graphene nanocomposite	[149]
		Ag-graphene composite	[145-147], [150]
		Ag-hydrogel nanocomposite	[39]
		Ag-mesoporous carbon	[78]
		Ag nanocomposite film	[40]
		AgNPs in hyaluronan fibers	[75]
		Ag on self-assembled TiO$_2$ nanotube arrays	[82]
		Ag-perfluorodecanethiolate complex films	[98]
		Ag-Pt alloy NPs capped with bovine serum albumin protein	[73]
		Ag-TiO$_2$ nanocomposite	[69]
		Ag vanadate nanowires	[35]
		Ag-zeolite	[55], [76], [77], [92]
		Ag-zeolite in polyethylene composite film	[60]
		Ag-Zn nanocomposite	[41]

Table 2.3 (continued): Ag nanomaterials and their characterization methods.

Characterization Functions / Objectives	Instrumentation/ Method	Ag Nanomaterial	Reference
Electrical properties	Electrocatalytic properties using cyclic voltametry	Ag-carbon nanotube-reduced graphene oxide composite	[148]
		Ag on self-assembled TiO_2 nanotube arrays	[82]
Morphology and particle size distribution	AFM	Ag-chemically converted graphene nanocomposite	[149]
		Ag-graphene composite	[151]
		Ag-graphene oxide composite	[102]
		Ag-PEI multilayer assembly	[52]
	FESEM	Ag-carbon nanotube-reduced graphene oxide composite	[148]
		Ag-functionalized graphene composite	[84]
		Ag-graphene oxide composite	[102]
		Ag-perfluorodecanethiolate complex films	[98]
	SEM	Ag-graphene composite	[145], [150]
		Ag-hydrogel nanocomposite	[39]
		Ag nanocomposite film	[40]
		AgNPs in hyaluronan fibers	[75]
		AgNP-filled nylon 6 nanofibers	[66]
		Ag on self-assembled TiO_2 nanotube arrays	[82]
		Ag-Pt alloy NPs capped with bovine serum albumin protein	[73]
		Ag-TiO_2 nanocomposite	[69]
		Ag vanadate nanowires	[35]
		Ag-zeolite	[76], [77], [86]
		Ag-zeolite in polyethylene composite film	[60]
	HRTEM	Ag-graphene composite	[150]
		Ag-mesoporous carbon	[78]
		Ag-Zn nanocomposite	[41]
	TEM	Ag-carbon nanotube-reduced graphene oxide composite	[148]
		Ag-chemically converted graphene nanocomposite	[149]
		Ag-chitosan nanocomposite	[94]

Table 2.3 (continued): Ag nanomaterials and their characterization methods.

Characterization Functions / Objectives	Instrumentation/ Method	Ag Nanomaterial	Reference
Morphology and particle size distribution	TEM	Ag-graphene composite	[145-147]
		Ag-hydrogel nanocomposite	[39]
		Ag-mesoporous carbon	[78]
		Ag nanocomposite film	[40]
		AgNP-filled nylon 6 nanofibers	[66]
		AgNP-loaded cellulose-based filter paper	[61]
		AgNP-polysaccharide hydrogel nanocomposite	[57]
		Ag on self-assembled TiO_2 nanotube arrays	[82]
		Ag- or Au-chitosan film	[100]
		Ag-polymer nanocomposite	[79]
		Ag-Pt alloy NPs capped with bovine serum albumin protein	[73]
		Ag vanadate nanowires	[35]
		Ag-zeolite	[55], [76], [77]
	cryo-TEM	Ag-polymer nanocomposite	[79]
Optical properties	FTIR	Ag-carbon nanotube-reduced graphene oxide composite	[148]
		Ag-chitosan nanocomposite	[94]
		Ag-graphene composite	[150]
		Ag-graphene oxide composite	[102]
		Ag-mesoporous carbon	[78]
		Ag nanocomposite film	[40]
		Ag on self-assembled TiO_2 nanotube arrays	[82]
		Ag-perfluorodecanethiolate complex films	[98]
		Ag-zeolite	[55]
	FT NMR for chemical bonding analyses	Ag nanocomposite film	[40]
	Photoluminescence spectroscopy	Ag-chitosan nanocomposite	[94]
		Ag nanocomposite film	[40]

Table 2.3 (continued): Ag nanomaterials and their characterization methods.

Characterization Functions / Objectives	Instrumentation/ Method	Ag Nanomaterial	Reference
Optical properties	Raman spectroscopy for determination of number of graphene layers	Ag-chemically converted graphene nanocomposite	[149]
		Ag-functionalized graphene composite	[84]
		Ag-graphene composite	[145], [151]
		Ag-graphene oxide composite	[102]
	Raman spectroscopy for SERS effect	Ag-mesoporous carbon	[78]
	Raman spectroscopy for determination of V-O bond length	Ag vanadate nanowires	[35]
	Reflectance spectroscopy	Ag-TiO$_2$ nanocomposite	[69]
		Ag-zeolite	[55]
	Spectrofluorimeter	Ag-zeolite	[92]
	UV-vis	Ag(I) complex with L-tryptophan	[56]
		Ag-chitosan nanocomposite	[94]
		Ag-graphene composite	[145], [150], [151]
		Ag-hydrogel nanocomposite	[39]
		Ag nanocomposite film	[40]
		AgNPs in hyaluronan fibers	[75]
		AgNP-polysaccharide hydrogel nanocomposite	[57]
		Ag- or Au-chitosan film	[100]
		Ag-PEI multilayer assembly	[52]
		Ag-polymer composite	[53]
		Ag-Pt alloy NPs capped with bovine serum albumin protein	[73]
Porosity / textural properties	BET	Ag-mesoporous carbon	[78]
		Ag vanadate nanowires	[35]
		Ag-zeolite in polyethylene composite film	[60]
	BJH	Ag-mesoporous carbon	[78]

Table 2.3 (continued): Ag nanomaterials and their characterization methods.

Characterization Functions / Objectives	Instrumentation/ Method	Ag Nanomaterial	Reference
Size distribution profile	DLS	Ag-polymer nanocomposite	[79]
		Ag vanadate nanowires	[35]
Thermal properties	DSC	AgNP-filled nylon 6 nanofibers	[66]
		Ag-zeolite in polyethylene composite film	[60]
	TGA	Ag-hydrogel nanocomposite	[39]
		Ag nanocomposite film	[40]
		Ag-perfluorodecanethiolate complex films	[98]
		Ag-polymer composite	[53]
		Ag-zeolite in polyethylene composite film	[60]
	TGA for Ag content analysis by combusting carbon matrix in air flow to 700°C	Ag-mesoporous carbon	[78]
Wetting properties	Surface hydrophilicity (water contact angle)	Ag-graphene oxide composite	[102]
		Ag-PEI multilayer assembly	[52]
		Ag-perfluorodecanethiolate complex films	[98]
		Ag-polymer composite	[53]
		Ag-zeolite coating	[86]
Miscellaneous			
Ag ion release	Cathodic stripping voltammetry	Ag-based metal-organic framework, Ag_3(3-phosphonobenzoate)	[96]
	AAS	AgNP-filled nylon 6 nanofibers	[66]
		Ag-zeolite in polyethylene composite film	[60]
	ICP-MS	AgNP-polysaccharide hydrogel nanocomposite	[57]
Cytoxicity	MTT reduction assay	Ag(I) complex with L-tryptophan	[56]
		AgNP-polysaccharide hydrogel nanocomposite	[57]
	Lactate dehydrogenase (LDH) assay	AgNP-polysaccharide hydrogel nanocomposite	[57]

Table 2.3 (continued): Ag nanomaterials and their characterization methods.

Characterization Functions / Objectives	Instrumentation/ Method	Ag Nanomaterial	Reference
Cytocompatibility	Enzyme-linked immunosorbent assay (ELISA)	Ag-Pt alloy NPs capped with bovine serum albumin protein	[73]
	Proliferation assay	Ag-Pt alloy NPs capped with bovine serum albumin protein	[73]
Membrane permeabilization of bacterial cells	Flow cytometric assays	AgNP-polysaccharide hydrogel nanocomposite	[57]
Rheological properties	Viscometer	AgNP-filled nylon 6 nanofibers	[66]
Swelling studies	Water uptake measurements	Ag nanocomposite film	[40]
		AgNP-loaded cellulose-based filter paper	[61]

2.2.1 Silver-Polymer Nanocomposites

Several methods to prepare polymer/silver nanocomposite microspheres were reported previously. These include the suspension polymerization of poly(vinyl acetate) in the presence of AgNPs [152], AgNPs crosslinkers coated with 4-mercaptomethylstyrene [128] and polystyrene-core/polyacrylic acid brush/Ag [79]. However, the complex polymerization synthetic procedures of these methods, variation in Ag nanoparticle size range, high cost and low yield remained a challenge to their production at the industrial scale. Although other supporting matrix material such as silica, zeolites and carbon have also been used to formulate AgNPs, the purification step which requires high-speed centrifugation or ultrafiltration remained the major limitation in industrial production.

Ion exchange resins have been shown to allow the immobilization of charged metal complexes on ion exchange sites through non-covalent electrostatic interactions [153]. In addition, the micron-sized and specific shapes of ion exchange resins can be recovered easily by simple filtration or decantation, suitable for industrial scale production. Furthermore, the use of ion exchange resins as an insoluble support material also possess several advantages over other matrix materials, including their ease of handling, ease of recycling, negligible levels of metal leaching, and their compatibility with water and other reaction solvents [153].

Several synthetic routes of ion exchange resins have been described previously including reaction of styrene and divinylbenzene monomers via a surfactant reverse micelles swelling method [154] or by conventional radical suspension polymerization method [155]. Dowex is the commercial name for a group of ion exchange resins produced by The Dow Chemical Company (Dow). These fine meshed resins can be broadly categorized as cation resins and anion resins. They consist of a styrene-divinylbenzene copolymer backbone formed into whole, spherical resin beads.

The Dowex spherical ion exchange resins are mainly used for fine chemical and pharmaceutical column separations, ion exchange applications and bioprocessing [156]. The H^+ ionic form of Dowex ion exchange resin (Dowex 50WX8) has a mesh size of 200-400, water retention capacity of 50-58% and a total exchange capacity of 1.7 meq/mL. The physical characteristics and antifouling properties of AgNPs supported on Dowex resins are discussed in Chapter 4.

2.2.2 Silver-Zeolite Nanocomposites

Zeolites are a family of aluminosilicate mesoporous ion exchange materials, with a stable network of hollow channels and pores within the size range of most monoatomic ions [157]. Due to their thermal stability and unique interconnected porous microstructure, natural and synthetic zeolites have been used as templating support materials to host a variety of metallic species including Ag [158], Mg [159], Ni [160], Zn [161], Fe [162], and Ga [163]. All these studies have shown that zeolites are efficient reaction templates to produce composite materials for various technological applications. The porous internal network structure of zeolites provides an ideal and stable template for the formation and growth of nanoparticles with nanometre dimensions. Furthermore, nanoparticles are physically prevented from agglomeration to form larger nanoparticles or micron-sized particles, as they are individually separated within the discrete pores and channels of the zeolite interior.

Previous studies on Ag-zeolite nanocomposite materials proposed an ion exchange process followed by high temperature calcination methods [76, 92, 158] to produce metallic Ag-zeolite materials. On the other hand, Shameli et al. [164] used sodium borohydride as a room temperature chemical reducing agent to form silver-doped Y-zeolites.

Silver-zeolite nanocomposites possess great potential for marine antifouling applications due to the remarkable antimicrobial property of silver against at least 650 unicellular organisms [20]. Furthermore, zeolites have no known environmental

hazards and are regularly used for environmental remediation [165], such as the removal of heavy metals from soils [166] and in the treatment of wastewater [167].

In fact, to the best of our knowledge, there have been very limited studies on adopting silver-zeolite nanocomposites for the evaluation of marine antifouling property. Previous related works include that of De Muynck et al. [168], which studied strategies for the prevention of algal fouling of outdoor terrestrial concrete surfaces using a Cu-Ag zeolite and also AgNPs. Krishnani et al. [47] reported on the bactericidal activity of silver ion-exchanged zeolite against shrimp pathogenic bacteria and its efficiency in the removal of ammonia. However, reports on Ag-zeolite composite materials against microfouling marine bacteria are still very scarce and difficult to come by. The physical characteristics and antifouling properties of silver-ZSM-5 zeolite nanocomposites are discussed in Chapter 5.

2.2.3   Silver-Titania Nanocomposites

Ever since the discovery of carbon nanotubes (CNTs) by Iijima in 1991 [169], interest has remained strong in nanotubular materials for their exceptional electronic and mechanical properties [170]. Titanium dioxide nanotubes, first reported by Kasuga [171, 172] are composed of single sheets of TiO_2 scrolled into a tubular structure with an exposed edge. The photocatalytic ability of TiO_2 under ultraviolet light and the self-cleaning property of TiO_2-coated glass when exposed to sunlight has been extensively investigated since their initial discovery by the Fujishima group [173]. The nanotubular structure of titania nanotubes (TNT) enhances the

photocatalytic activity of TiO_2 through its higher specific surface area on the inner and outer surfaces of the structure. TNT has been found in many diverse applications as a functional component in nanocomposite systems including as a photocatalytic hydrogen generator [174], as an electrode for sodium storage [175], in wastewater treatment [176], as a light-activated anti-bacterial platform [177] and for antifouling property against HeLa cells [178].

While the majority of studies have looked at Ag-TiO_2 nanotube composites in the areas of catalysis and energy [82], there have been limited studies on their marine antifouling property. Ruffolo et al. [69] compared the performance of pure TiO_2 nanoparticles and Ag-doped TiO_2 nanoparticles on the marine fouling of marble slabs for protection of underwater archaeological sites. Carl et al. [179] found that the use of TiO_2 as photocatalytic nanofillers in foul-release polydimethylsiloxane (PDMS) coatings improved their antifouling performance against the macrofouling mussel species *Mytilus galloprovincialis*, while TiO_2/fluorinated acrylic nanocomposite was used as a marine antifouling paint [180].

Apart from these scattered antifouling reports, more literature emerged from the field of water treatment depicting TiO_2 as a photocatalytic component of water filtration and microfiltration membrane systems to remove organic fouling matter including humic acid [70]. However, Ag-TiO_2 nanotubular composite materials have not yet been subjected to intensive study in the field of marine antifouling. Therefore, more studies remain to uncover the potential of Ag-TiO_2 nanotubular composites for marine antifouling applications. The physical characteristics and antifouling properties of silver-TiO_2 nanotube composites are discussed in Chapter 6.

41

2.2.4 Graphene-Silver Nanocomposites

Graphene is a 2D crystalline structure with large specific area, good electrical conductivity, and are thermally and chemically stable materials [181]. Since its initial discovery by Novoselov & Geim in 2004, various applications have been reported to take advantage of its unique properties [182]. Graphene has wide applications especially as electrochemical and bio-electrochemical sensors [183, 184], whilst graphene-based metallic nanocomposites have expanding applications [147, 148, 185].

The literature on graphene-silver nanocomposite materials are filled with reports of silver growth on graphene oxide precursors [84, 145, 149-151, 186-188]. AgNPs on graphene sheets have been produced with excellent electronic conductivity, optical and SERS properties [189, 190]. The inclusion of silver nanoparticles (AgNPs) on rGO sheets has yielded composites with antimicrobial properties [54, 191]. Nanoparticles of silver and other noble metals supported on graphene/GO/rGO have promising applications in food safety by detecting prohibited food additives [84, 151] and the presence of toxins [192]. AgNPs on GO sheets have been reported as promising fuel cell applications [146, 193], whereas the addition of noble bimetallic nanoparticles on GO/rGO hold promise as electrochemical sensors [194, 195]. However, comprehensive studies on antifouling properties of graphene-silver nanomaterials remain scarce.

Reduced graphene oxide (rGO) has been used as the substrate for the templated growth of metallic nanoparticles [191, 196-198]. Most of these studies

utilised graphene nanomaterials synthesized via the modified Hummers method, followed by chemical reduction to produce the rGO. These production methods employ harsh chemicals such as sulphuric acid and results in graphene surfaces decorated with defects, the presence of oxygen and other functional groups compared to pristine graphene [199].

In recent years, more environmentally friendly methods of graphene oxide synthesis with minimal toxic by-products have been reported [200]. Large scale graphene sheets have been produced through chemical vapour deposition (CVD) on various metal substrates, with copper substrate being the most promising for industrial applications due to their low affinity to carbon [201]. Lately, the CVD synthesis of graphene has been further simplified to single-step growth of both copper substrate and graphene sheet through a plasma enhanced process [202]. On the other hand, sonochemistry has been employed as an effective one-pot synthesis method for graphene oxide [203] and graphene [183].

The physical characteristics and antifouling properties of graphene-silver nanocomposites synthesized from a novel 2-step hydrothermal method are discussed in Chapter 7.

2.2.5   Antimicrobial Properties of Silver Nanomaterials

Silver has been used as a therapeutic and antimicrobial agent in medicine for centuries. The germicidal action is thought to be due to the degree of ionization of the

silver colloid, with particle size and charge playing important roles in disrupting the basic cellular function of the bacteria [204]. However, their use as antimicrobials has declined since the introduction of antibiotics in the early 20th century. With the proliferation of several strains of pathogenic bacteria which have developed resistance against various antibiotics, silver, especially in the form of nanoparticles, have again emerged as an interesting and valuable antimicrobial agent in many biomedical applications. These applications range from wound dressings to silver-coated medical implants and devices, and emerging in various forms including nanogels and nanolotions [205].

The antimicrobial property of AgNPs is of particular interest in the biomedical field, owing to their obvious benefits in decreasing the proliferation of disease-causing bacteria. AgNPs in an aqueous solution release silver ions. The silver ions are biologically active with bactericidal effects by combining the interaction effects of the three main components of the bacterial cell:

1) the peptidoglycan cell wall and plasma membrane,

2) the bacterial DNA

3) and the bacterial proteins, particularly enzymes [59].

The AgNPs can also interact extensively with bacteria cell walls and cause lysis. After penetrating the bacteria, further damage is done as a result of the interaction between the AgNPs and the bacterial DNA [59].

In a study on antimicrobial property of stabilized AgNPs with phospholipid membrane on *Escherichia coli* and *Staphylococcus aureus* bacterial strains, the authors found that the antibacterial properties of AgNPs depend on the particle size, stabilizer and lecithin concentrations. Only stabilized AgNPs showed a bacterial inhibition zone. Unstabilized AgNPs agglomerated quickly, settled on the wells and did not diffuse in agar. In addition, high lecithin concentrations reduced the release of AgNPs, leading to higher bacterial survival rates [62].

According to Modrzejewska et al. [104], the antimicrobial property of AgNPs depends on the particle dimensions. The mechanism of action for AgNPs antimicrobial activity is highly dependent on the type of microorganism. In fungi for instance, AgNPs disturb the natural water balance by blocking the ability of the fungi to bind water molecules. In viruses, AgNPs eliminates the catalytic decomposition of a lipid-protein substance. In bacteria, the high electrical conductivity of AgNPs disrupts the natural gradient of electric potential across the bacterial cell membrane to which it adheres. AgNPs also penetrate the protoplasm through capillaries in the cell membrane, causing disturbances in the mitochondrial and nucleus activities. In addition, silver ions which are released from AgNPs also bind with thiol groups (-SH) inside the bacteria, causing protein deactivation. Finally, bacterial growth is inhibited by atomic oxygen adsorbed on the surface of AgNPs.

Khan et al. (2011) studied the interaction of colloidal AgNPs with five different bacterial species (*Pseudomonas aeruginosa, Micrococcus luteus, Bacillus subtilis, Bacillus barbaricus* and *Klebsiella pneumonia*). The influence of surface charge on the adsorption of AgNPs on bacteria surfaces was investigated under acidic,

neutral and alkaline pH under varying sodium chloride salt concentrations. In general, an increase of adsorbed AgNPs increased the bacterial deaths, with a maximum adsorption and toxicity reported at pH 5 and < 0.5 M NaCl concentration [206]. Table 2.4 summarises the silver nanomaterials which were synthesized and tested for positive activity against bacterium.

Table 2.4: Antimicrobial silver-containing materials and their target organisms.

Ag-containing antimicrobial material	Model Organisms	Reference
Ag NP	*Aeromonas hydrophila*	[24]
	Bacillus cereus (MTCC 306)	[50]
	Bacillus subtilis	[25], [67], [126]
	Bacillus subtilis (MTCC 736)	[50], [68]
	Candida albicans	[25]
	Escherichia coli	[25], [51], [58], [65],[67], [126]
	Escherichia coli (MTCC 68)	[50]
	Escherichia coli strain BL-21 $EC_{50} = 11\pm$ 1.72 mg/L	[23]
	Escherichia coli strain K12, silver resistant strains J53 (pMG101) and (116AgNO3R)	[22]
	Klebsiella mobilis	[67]
	Klebsiella pneumoniae inhibited at 70ppm	[59]
	Lactobacillus fermentum	[25]
	Pseudomonas aeruginosa	[25], [58]
	Pseudomonas aeruginosa (MTCC 8158)	[50]
	Staphylococcus aureus	[25], [58], [67], [126]
	Staphylococcus aureus (MTCC 96)	[50]
	Staphylococcus aureus inhibited at 105ppm	[59]
	Staphylococcus aureus strain MRSA	[24]
	16 marine biofilm isolates: Myroides odoratimimus (MB1); Micrococcus luteus (MB2); Halomonas aquamarina (MB3) Proteus mirabilis (MB4); Micrococcus luteus (MB5); Exiguobacterium aurantiacum (MB6);	[207]

Table 2.4 (continued): Antimicrobial silver-containing materials and their target organisms.

Ag-containing antimicrobial material	Model Organisms	Reference
Ag NP	*Exiguobacterium arabatum (MB7, MB8); Jeotgalibacillus alimentarius (MB9); Bacillus megaterium (MB10); Bacillus pumilus (MB11); Bacillus pumilus (MB12); Bacillus pumilus (MB13); Bacillus megaterium (MB14); Halotalea alkalilenta (MB15); Arthrobacter mysorens (MB16)*	[207]
Ag NP and Ag nanochains	*Staphylococcus aureus*	[51]
Ag vanadate nanowires	*Enterococcus faecalis (ATCC21814 and 29212)*	[35]
	Escherichia coli (ATCC 25922)	
	Salmonella enterica Typhimurium strain LT2	
	Staphylococcus aureus strain BEC9393 *(MRSA)*, strain Rib1 (MRSA) (ATCC29213)	
Ag(I) complex with L-tryptophan (TRP)	*Enterococcus faecalis*	[56]
	Escherichia coli	
	Pseudomonas aeruginosa	
	Staphylococcus aureus	
Ag-based metal-organic framework, Ag$_3$(3-phosphonobenzoate)	*Escherichia coli (MG1655)*	[96]
	Pseudomonas aeruginosa (PA130709, PA240709)	
	Staphylococcus aureus (strains RN4220, Newman and MRSA N315)	
Ag-graphene	*Escherichia coli*	[196]
Ag-graphene oxide	*Candida albicans,*	[145]
	Candida tropical	
	Bacillus subtilis	[191]
	Staphylococcus aureus	[149], [191]
	Escherichia coli	[188]
Ag-hydrogel nanocomposite	*Escherichia coli*	[39]
Ag NP in polysulfone ultrafiltration membranes	*Escherichia coli K12*	[63]
	MS2 bacteriophage	
	Pseudomonas mendocina KR1	
Ag NP-filled nylon 6 nanofibers	*Bacillus cereus (B002)*	[66]
	Escherichia coli O157:H7 (B179)	

47

Ag-containing antimicrobial material	Model Organisms	Reference
Ag NP-loaded cellulose-based filter paper	*Escherichia coli*	[61]
Ag NP-polysaccharide nanocomposites, hydrogels	*Escherichia coli (ATCC 25922)*	[57]
Ag NP-polysaccharide nanocomposites, hydrogels	*Pseudomonas aeruginosa (ATCC 27853)*	[57]
	Staphylococcus aureus (ATCC 25923)	
	Staphylococcus epidermidis (clinical isolate)	
Ag-PEI multilayer assembly	*Escherichia coli DH5 (ATCC 53868)*	[52]
	Staphylococcus aureus (ATCC 25923)	
Ag-perfluorodecanethiolate complex films	*Pseudomonas aeruginosa PAO1*	[98]
Ag-phospholipid membrane	*Escherichia coli*	[62]
	Staphylococcus aureus	
Ag-polymer composite	*Escherichia coli*	[53]
	Klebsiella pneumoniae	
	Pseudomonas aeruginosa	
	Staphylococcus aureus	
	Escherichia coli	[33]
	Escherichia coli (MTCC 1303)	[40]
	Pseudomonas aeruginosa (MTCC 1688)	
	Staphyloccus aureus (MTCC 3160)	
Ag-TiO$_2$	*Escherichia coli*	[208]
	Micrococcus sp. BC 654	[69]
	Stenotrophomonas maltophilia BC 652	
Ag-zeolite	*Escherichia coli (ATCC 25922)*	[55]
	Escherichia coli (MIC = 40ug/ml)	[47]
	Pseudomonas aeruginosa (ATCC 27853)	[55]
	Salmonella typhimurium (ATCC 14028)	
	Shigella flexneri (ATCC 12022)	
	Staphylococcus aureus (ATCC 25923)	
	Staphylococcus epidermidis (ATCC 12228)	

Table 2.4 (continued): Antimicrobial silver-containing materials and their target organisms.

Ag-containing antimicrobial material	Model Organisms	Reference
Ag-zeolite	*Vibrio cholerae* (MIC=50 - 60ug/ml)	[47]
	Vibrio harveyi (MIC=40ug/ml)	
	Vibrio parahaemolyticus (MIC=50 - 60ug/ml)	
	Acidothiobacillus thiooxidans (ATCC 19703)	[64]
Ag-zeolite coating	*Escherichia coli*	[86]
	Listeria innocua	
	Pseudomonas putida	
	Staphylococcus epidermidis	
Ag-zeolite in polyethylene composite films	*Escherichia coli* MIC = 0.5 mg zeolite/mL or 25 ug Ag/mL	[60]
Ag-Zn nanocomposite	*Escherichia coli*	[41]
	Streptococcus faecalis	

2.3   Fouling

Scientific research on fouling and antifouling technology is a unique example of multidisciplinary work which requires the collaboration of materials scientists, synthetic chemists, marine biologists, microbiologists and environmental scientists in order to produce effective and environmentally-safe products. Intensive research efforts at commercial enterprises and academia in the last decade has been conducted, to develop systems and solutions which are environmentally benign, yet effective on the industrial scale, to ward off and control the fouling phenomenon.

Figure 2.3 shows an upward trend, particularly in the last decade, in the publication of papers related to antifouling research. Although the data was obtained

from one database (Elsevier's ScienceDirect), it is not a stretch of the imagination to state the emerging importance of enhanced antifouling materials and applications. The research areas encompass the discovery and formulation of novel coatings and surfaces, as well as simpler and more efficient processing methods, to the exploration of natural alternatives to synthetic active molecules. The spike in research in this area could be attributed to recent legislations imposed on ship owners to remove TBT-containing antifouling coatings on ships effective from 2008 [209].
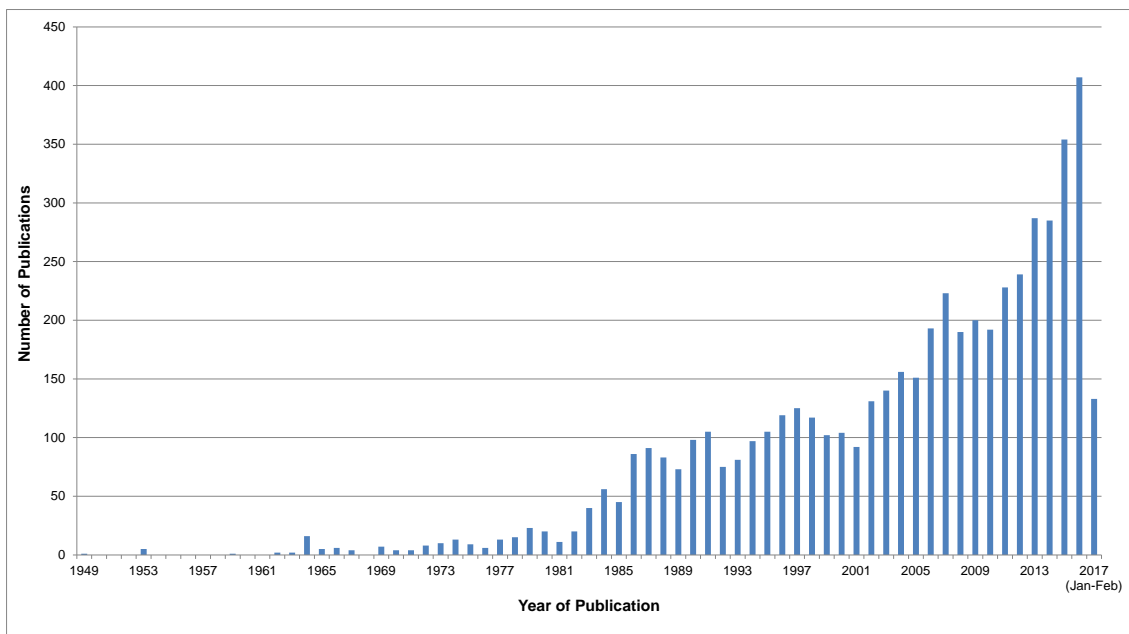
Figure 2.3: Scientific publications related to marine antifouling research. The chart shows an upward trend in the number of scientific papers related to marine antifouling published by Elsevier from the 1950s to 2017.

2.3.1 Definition of Fouling

Fouling is a general term used to describe the attachment of unwanted organisms on wetted surfaces [1], such as in food processing and in biomedical implants [210], desalination and water treatment plants [211], pipelines for oil/water

[212, 213], in shipping [13], as well as in closed systems such as submarines and space craft [214]. Biological fouling in the marine environment is a significant subset of the general fouling problem. As the biofouling process involves the settlement of epibiont organisms on surfaces providing protection and nutrients [215], this process is sometimes known as colonization, or simply, fouling. The colonizing organisms use an array of biological glues as a means of adhesion [6]. This undesirable phenomenon commonly afflicts ship hulls [13], aquaculture cages [216], and other immersed marine surfaces. In wastewater treatment, biofouling of separation membranes is a serious problem as well [217]. Real-time monitoring of biofilm growth has been advocated, especially in water supply engineering systems to identify the site and extent of biofilm development [218].

Although biofouling occurs in nature and on natural surfaces, it presents a significant problem to manmade surfaces immersed in seawater. This is because natural surfaces, for instance, mollusk shells, have developed a natural defense system against fouling, whereas manmade surfaces have not.

2.3.2   Stages of Fouling Development

According to Abarzua and Jakubowski [5], the development of the biofouling process can generally be divided into 3 progressive stages:

1) biofilm formation

2) microfouling

3) macrofouling

Table 2.5 shows the temporal stages in the biofouling process. The process begins with the conditioning of a submerged surface, where a conditioning film develops within the first minute of wetting. Physical forces initiate the adhesion of organic molecules such as proteins, polysaccharides and proteoglycans, as well as some inorganic molecules onto the immersed surface. Other molecules which adhere to the surface include humic acid, fulvic acid, as well as ions in the marine environment. Representative molecules in the conditioning film are shown in Figure 2.4. These organic molecules cause the surface to become wettable, as well as provide biological cues for microorganisms such as bacteria and simple diatoms to attach [219].

This is immediately followed by the formation of a microbial biofilm by single-celled organisms, such as marine bacteria and diatoms. As shown in Figure 2.4, the microfouling stage or the primary colonization is dominated by the attachment of bacteria and diatoms. Initially, a reversible adsorption of bacteria takes place. The interaction between these primary colonizers and the wetted surface has been attributed to physical forces including Brownian motion, electrostatic interaction, and Van der Waals forces [13, 220]. The bacteria will then form a nonreversible adhesion onto the surface by producing organic anchoring fibrils comprising mostly of glucose and fructose [7, 221]. This bacterial adhesion is known as a microbial 'biofilm'.

Approximately one week after the formation of the biofilm, microfouling continues with microalgae spores and protozoans settling over the microbial biofilm. This is attributed to the biofilm's capacity to provide a conducive and nutrient-rich environment. Greater protection from predators, toxicants and environmental

uncertainties is also provided by the biofilm for the larvae of macro-organisms to settle. Callow and Callow (2006) [222] stated that although a biofilmed surface is not a pre-requisite for settlement of fouling organisms, in practice, colonization by spores and larvae of those organisms almost usually occurs via a biofilmed surface. The biofilms exert a host of surface-associated and diffusible signals with the possibility of moderating the settling behaviour of cells, spores and larvae.

Macrofouling is the final stage in the fouling process whereby spores of macroalgae, protozoa and sessile marine organisms such as barnacles attach to the microfouling film. Figure 2.4 shows a representative hard macrofouler, the cyprid larvae of the barnacle, searching for settlement sites in the macrofouling stage. Railkin [223] described the first stage of the macrofouling process being dominated by fast-growing organisms such as hydroids, serpulids, and bryozoans. This is followed by slow-growing organisms such as mollusks. The entire fouling settlement process has been observed to take place within the span of one month.

Timeframe	First minute	First 24 hours	First week	First month
Event	**Conditioning film / Adhesion of organic molecules;**	**Microbial biofilm**	**Microfouling**	**Macrofouling**
Attached Organisms	Proteins, proteoglycans, polysaccharides	**Primary Colonizers:** • **Bacteria** (e.g. *Pseudomonas putrefaciens*, *Vibrio alginolyticus*) • **Diatoms** (e.g. *Achnantes brevipes*, *Amphiprora paludosa*, *Amphora coffeaeformis*, *Licmophora abbreviata*, *Nitzchia pusilla*)	**Secondary Colonizers:** • **Spores of macroalgae** (e.g. *Enteromorpha intestinalis*, *Ulothrix zonata* [Chlorophyta]) • **Protozoa** (e.g. *Vaginicola* sp., *Vorticella* sp., *Zoothamnium* sp. [Ciliata])	**Tertiary Colonizers:** **Larvae of macrofoulers such as** • **Crustacea** (e.g. *Balanus amphitrite*) • **Bryozoa** (e.g. *Electra crustulenta*) • **Coelenterata** (e.g. *Laomedia flexuosa*) • **Mollusca** (e.g. *Mytilus edulis*) • **Polychaeta** (e.g. *Spirorbis borealis*) • **Tunicata** (e.g. *Styela coriacea*)

Table 2.5: A schematic of the timeframe for biofouling processes and the typical organisms which are involved. Adapted from Abarzua & Jakubowski [5].
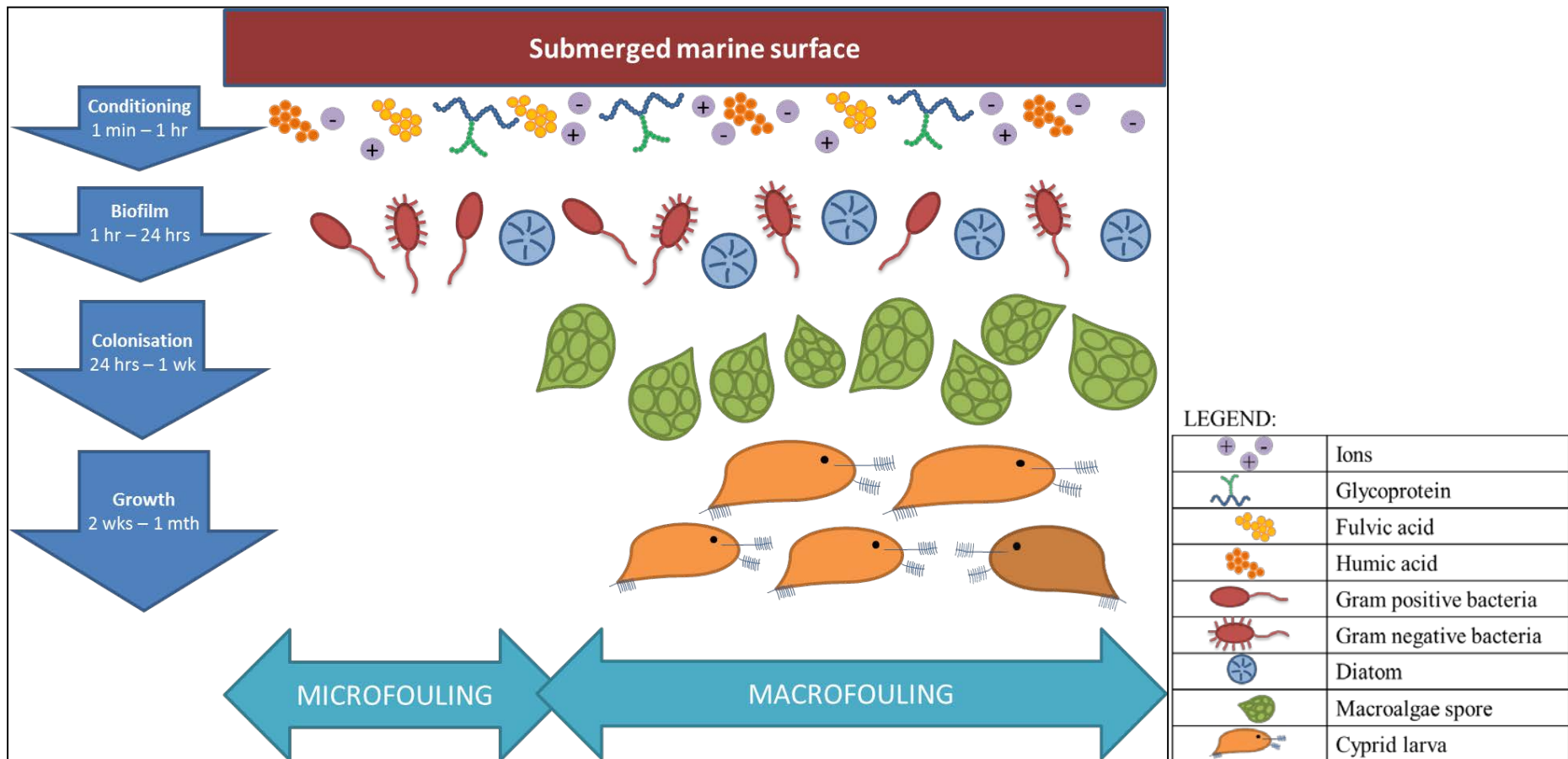
Figure 2.4: A schematic of the temporal stages of biofouling. It proceeds from the moment a surface is wetted (conditioned), which facilitates the biofilm formation by bacteria and diatoms, to the colonization and growth of the soft and hard fouling organisms. Organisms shown are representatives of the common classes of fouling organisms.

2.3.3   Main Marine Fouling Species

Distinct to each habitat are the abundance and variety of fouling organisms, as well as the rate of fouling development by those organisms. In the tropics, *Hydroides* and tube-like polychaetes form the majority of the initial colonizers, while barnacles, mollusks and bivalves dominate the fouling community in temperate waters. In the polar region, diatoms comprise the main fouling organisms [215].

Figure 2.5 shows the diversity and size scales of a range of fouling organisms. They range in size from micrometre (bacteria, spores of macroalgae and diatoms) to millimetre (larvae of invertebrates such as barnacles and mussels). These organisms have spores and larva with highly specialized attachments with the capability to seek out suitable settlement sites by sensing chemical and biological cues secreted by their surrounding environment.

Fouling organisms are classified by the type of fouling observed, and are divided into the following three major fouling groups:

1) microfoulers or "slime",

2) soft macrofoulers, and

3) hard macrofoulers.

Microfoulers or biofilm-causing organisms are identified as bacteria, diatoms and microscopic unicellular algae spores. Macrofouling organisms may be divided into soft macrofoulers, e.g. macroalgae, anemones, and hydroids, while hard macrofoulers are typically composed of barnacles, mussels and tubeworms. The most

common marine foulers consist of algae and invertebrates such as the hard-shelled

genera *Balanus* and *Molluscs*, grass-like or bush-like *Hydroids* and *Bryozoans*, and

spineless organisms such as *Ascidians* and sponges.
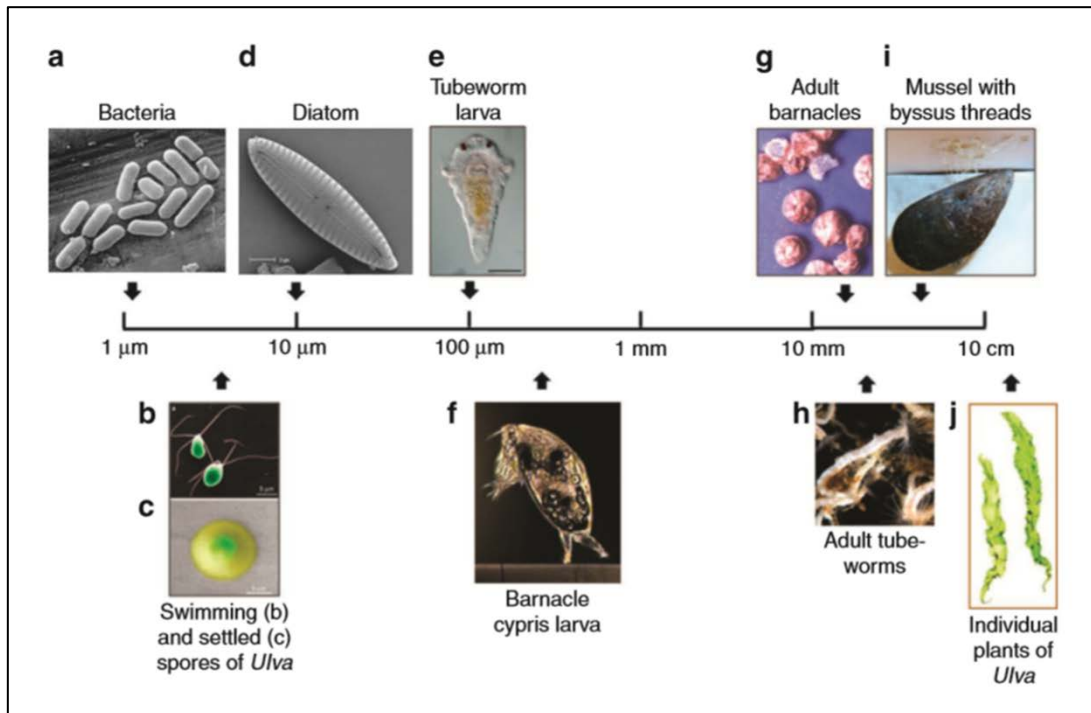
Figure 2.5: A schematic of the diversity and size scale of representative fouling organisms. (**a**) Bacteria (scanning electron micrograph (SEM)), (**b**) false-colour SEM of motile, quadriflagellate spores of the green alga (seaweed) *Ulva*, (**c**) false-colour environmental SEM image of settled spore of *Ulva* showing secreted annulus of swollen adhesive, (**d**) SEM of diatom (*Navicula*), (**e**) larva of tube worm, *Hydroides elegans* (image courtesy of B. Nedved), (**f**) barnacle cypris larva (*Amphibalanus amphitrite*) exploring a surface by its paired antennules (image courtesy of N. Aldred), (**g**) adult barnacles (image courtesy of AS Clare), (**h**) adult tubeworms (*H. elegans*; image courtesy of M. Hadfield), (**i**) adult mussels showing byssus threads attached to a surface (image courtesy of J. Wilker), (**j**) individual plants of the green alga (seaweed) *Ulva*. (Reproduced from Callow and Callow, 2011) [4].

As these colonizing organisms possess such variety in size as well as

complexity in searching for settlement sites, to date, there is no one single solution to

successfully stop the process of fouling from all classes of organisms.

Table 2.6 contains a list of some of the fouling organisms identified in various antifouling studies. The most common model organisms used to challenge the effectiveness of prospective antifouling agents or coatings include marine bacteria *Halomonas pacifica* and diatoms, green algae *Ulva linza*, and the barnacle *Amphibalanus amphitrite*.

Table 2.6: List of marine fouling organisms identified in literature.

Fouling Organism Classes	Organism by Species		Reference
Microfouling	Bacteria	*Alcaligenes* sp.	[18]
		Bacillus macroides (strain KORDI-13724)	[224]
		Cobetia marina (Halomonas marina)	[225]
		Escherichia coli	[226]
		Halomonas marina	[227]
		Halomonas pacifica	[228], [229]
		Loktanella hongkongensis	[230]
		Marinobacter	[229]
		Micrococcus luteus (UST950701-006)	[230]
		Micrococcus sp.	[18]
		Proteus sp.	[18]
		Pseudoaltermonas piscida	[230]
		Pseudoalteromonas sp.	[231]
		Pseudomonas aeruginosa (strain KORDI 13716)	[224]
		Pseudomonas aeruginosa PA01	[98]
		Pseudomonas sp.	[18]
		Psychrobacter sp.	[229]
		Rhodobacter sp.	[231]
		Rhodovulum sp. *(UST950701-012)*	[230]
		Ruegeria sp. *(UST010723-008)*	[230]
		Staphylococcus sp.	[18]
		Streptococcus sp.	[18]

Table 2.6 (continued): List of marine fouling organisms identified in literature.

Fouling Organism Classes	Organism by Species		Reference
Microfouling	Bacteria	*Vibrio fisheri*	[232]
		Vibrio harvayi (UST020129-010)	[230]
		Vibrio sp.	[18]
	Diatoms	*Achnanthes* sp.	[18]
		Amphora sp.	[18], [233]
		Amphora coffeaeformis (KMCC B027)	[224]
		Fragiliria sp.	[18]
		Haslea sp.	[233]
		Navicula sp.	[18]
		Navicula incerta (KMCC B001)	[224]
		Nitzschia sp.	[18]
		Synedra sp.	[18]
Soft macrofoulers	Macroalgae	*Dunaliella tertiolecta*	[232], [234]
		Ulva linza	[225], [235], [236]
	Hydroids	*Dynamena pumila*	[237]
		Gonothyraea loveni	[237]
Hard macrofoulers	Ascidians	*Ciona intestinalis*	[238]
		Pyura praeputialis	[238]
	Bryozoans	*Bugula dentata*	[233]
		Bugula flabellata	[233]
		Bugula neritina	[230], [233]
	Cirripedia	*Amphibalanus amphitrite*	[230], [232], [239], [240], [241], [242], [243]
		Amphibalanus improvisus	[244]
		Amphibalanus reticulates	[233]
		Amphibalanus variegatus	[245]
	Molluscs	*Mytilus edulis*	[237]
		Brachidontes pharaonic	[240]

2.3.4 Effects of Marine Fouling

The effects of fouling on maritime vessels and infrastructure are a common problem which lead to serious negative efficiency, economic and environmental issues. The hydrodynamics of a ship's hull will be affected due to increased roughness and wall shear stress, adding to skin friction drag [246]. Although macrofouling of maritime surfaces with attachment of barnacles and trailing seaweed will substantially reduce the speed and performance of ships, it is surprising that microfouling has also been found to contribute considerable negative effects, as described by Cassé and Swain [18]. Compared with a clean hull, a hull covered by as little as a 1-mm thick layer of slime has been shown to cause an 80% increase in skin friction coefficient, along with a 15% loss in ship speed [8]. According to Bohlander [247], biofouling, mostly in the form of microfilms, caused an increase of 8-18% in drag in full-scale power trials of a frigate.

It has been found that unprotected hull bottoms have accumulated up to 200 tons of foulant upon docking [248]. To overcome the extra drag force, up to 40% increase in fuel consumption, and as much as 77% increase in voyage overall costs of oceangoing vessels, have been noted [1].

The international marine transport industry uses an estimated 50% of their operating costs on fuels. In 1999, the annual consumption of bunker fuel (fuel oil used for ships) by the world's fleet was estimated at 180 million tonnes. In 1999, the cost of bunker fuel was approximately USD100/tonne, therefore, the total consumption cost amounted to USD18 billion [9]. The worldwide use of bunker fuels jumped to an

estimated 278 million tonnes in 2001, while between 2001 and 2020, the total consumption averaged at 3.1% growth annually [10]. With such high fuel costs, the addition of biofouling to ships would certainly increase operating costs over time, if no measures are put in place to control the settlement and growth of fouling matter.

As a direct result of the increased fuel usage, higher carbon footprint will accelerate greenhouse emissions and global warming. In addition, ship owners are faced with decreased vessel availability due to more frequent dry-docking intervals for removal of foulant and maintenance works [13].

As ships travel throughout major shipping routes globally, they have unwittingly become the vectors in transmitting invasive species of fouling organisms into new marine environments. These alien aquatic species have the potential to threaten the survival of native marine populations and their ecosystems [249-251].

Without adequate protection of the maritime surfaces, most commonly attained through the use of antifouling paint systems, the maritime industry will continue to spend considerable resources on the removal of biofouling organisms and expend precious economic resources to overcome their negative impacts. However, as described in the next section, the antifouling paint systems which have been in use for the past century and earlier, relied on biocidal effects of toxic compounds. These toxic paint compounds kill fouling organisms but also reveal long-lasting effects to non-target organisms, with high potential for such contaminants to enter the marine food chain [252]. They have been found to persist with disastrous effects on the marine environment, especially in areas around dry docks and busy ports [13].

2.4   Marine Antifouling Paint Systems

Ship hulls and its parts that are usually immersed underwater, are exposed to a complicated and challenging environment. They require protection from seawater corrosion, UV degradation as well as biofouling. Almeida et al. [13] described the protective painting systems for ships, which includes an anticorrosive primer and an antifouling topcoat, with the addition of a suitable tie coat which is sometimes applied between the primer and the topcoat. The antifouling coating usually contains one or more biocidal agents to kill off fouling species. Several studies [221, 228, 253, 254] have focused on the prevention of biofilm formation through the use of biocides as a strategy to halt the progress of fouling.

According to the International Maritime Organization [209], a good biocide for use in an anti-fouling system should possess these characteristics: broad spectrum activity against targeted fouling organisms, low toxicity to mammals, low solubility in water, does not accumulate in the food chain, is not persistent in the environment, is compatible with paint raw materials, and finally, has a favourable price-to-performance ratio.

2.4.1   Primitive Antifouling Systems

Interest in overcoming the blight of fouling has existed for as long as human civilization used ships to traverse the globe. The early Phoenicians and Carthaginians were reported to protect their wooden hulled ships with wax, tar and asphalt as early

as 700 B.C. [13]. In 1625, the first patent on antifouling paints was filed by William Beale [246].

A 19th century manuscript on this topic described fouling as the "most expensive and objectionable" phenomenon on the hulls of the iron-clad ships of the time, with up to 300 patents having been filed - attesting to the vigorous attempts by the British Royal Navy and commercial shipping fleet owners to battle this significant issue [3]. Many of the early antifouling remedies relied on coatings based on heavy metals and copper sheathing on wooden boats. However, most of these early coatings, which included a mixture of toxic and sometimes bizarre ingredients, were not successful in combating fouling, with some vessels reported to have accumulated at least 10 tons of foulant in only 10 months of ocean voyage.

One of the most successful methods employed was the use of zinc sheathing with the iron-clad ships, introduced by one Mr. Daft C.E., employing the principle of galvanic action. Organisms which attached to the zinc layer would be removed together with the oxidized zinc layer through 'exfoliation', and hence preventing further fouling from occurring [3].

2.4.2   Tributyltin (TBT) – Based Paints

Since the 1960s, remarkably successful antifouling coatings with biocidal properties have been employed, most notably in the use of tributyltin (TBT) self-polishing copolymer (SPC) paints. These TBT-based or organotin-based paints have

the advantage of keeping the immersed hull surfaces clear of foulants for up to 5 years [13]. Thus ships are able to extend their dry-docking intervals for maintenance and cleaning purposes.

Antifouling paints based on the biocidal tributyltin (TBT) organic compound can be classified under the following three categories [5, 13, 255]:

1) Free association paints

2) Ablative paints

3) Self-polishing copolymer paints

The biocidal properties of these antifouling paint systems kill bacteria and prevent other microorganisms from beginning the first stage of colonization, therefore, inhibiting the fouling process. However, these organotin-based paints have been found to cause severe reproductive damage to a variety of marine life forms, most famously the imposex condition of the gastropod *Nucella lapillus*, causing a decline in their population [15].

These toxic compounds also accumulate in mammals and may pose health risks to larger organisms further up the food chain. Due to the serious side effects of TBT-based paints, the usage of such active antifouling compound have been globally banned by the International Maritime Organization (IMO), the United Nations Agency concerned with the safety of shipping and the prevention of marine pollution. In October 2001, the IMO adopted the International Convention on the Control of Harmful Anti-fouling Systems on Ships, which calls for a global prohibition on the application of organotin compounds which act as biocides in anti-fouling systems on

ships by January 1st 2003, and a complete prohibition by January 1st 2008. Under the terms of this Convention, Parties to the Convention are required to prohibit and restrict the use of harmful anti-fouling systems on ships which fly their flag, operate under their authority, and all ships that enter their port, shipyard or offshore terminals [209].

2.4.2.1 Free Association Paints

This type of antifouling paint consists of biocidal molecules dispersed in an insoluble resinous matrix. They are also known as contact paint. The biocides are leached out in an uncontrolled rate, causing a high initial concentration of biocide in the marine environment. The antifouling performance diminishes over time as the reserve of biocides is depleted. The surface becomes porous due to the leaching of the biocides, leaving behind a honeycomb microstructure in the coating, contributing to surface roughness. The structure can also trap pollutants from seawater and is liable to block the release of biocides. Their service life is between 12-24 months. Figure 2.6 illustrates the working mechanism of free association paints.

2.4.2.2 Ablative Paints

The biocide is bonded in a less permeable matrix, with binders based on rosins and their derivatives. The paint slowly flakes off due to chemical reaction with the water and the scouring action of water on the ship hull. Due to the constant erosion of

paint from the painted surface, the protective lifetime is between 12-15 months. The

biocide molecules are dispersed in a resinous matrix, and are able to freely leach from

the matrix. The initial release rate is high due to large concentrations of biocide

present. As time passes, the supply of biocides is depleted and the release rate slows

down.
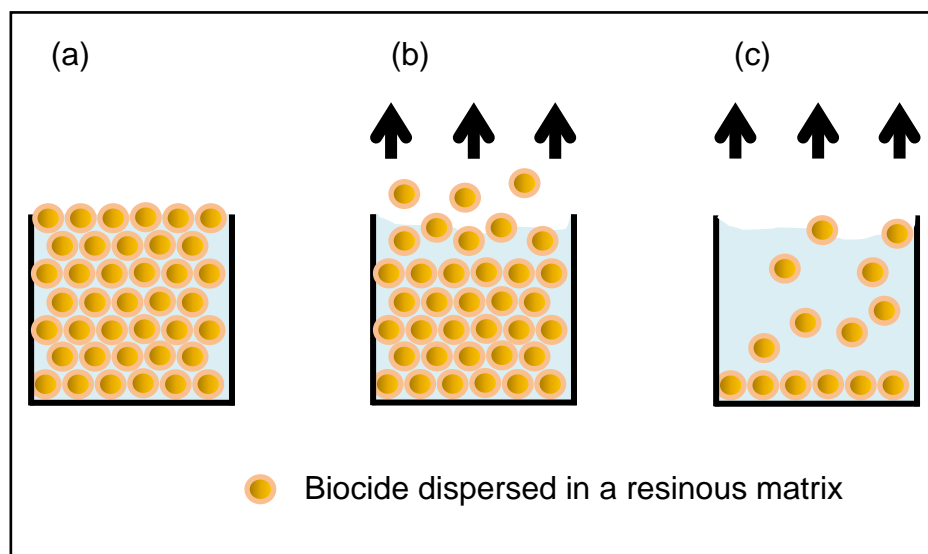
Figure 2.6: Schematic diagram of biocidal action of free association paints. (a)
Biocide molecules are dispersed in a resinous matrix. (b) The biocide leaches freely
from the matrix. Initial release is rapid. (c) Subsequent release declines so antifouling
performance of paint diminishes over time. Adapted from International Maritime
Organization [209].

2.4.2.3 Self-Polishing Copolymer (SPC) Paints

The TBT biocide is chemically bound by ester bonds to a copolymer resin

(usually acrylic or methyl methacrylate), and is released through a hydrolysis process,

as shown in Figure 2.7. Due to the weak mechanical strength of the resin, the paint

wears off to reveal a smooth, new layer. This is referred to as the "polishing action",

as a fresh layer of TBT biocidal action is exposed. The release rate can be controlled

to a polishing rate of about 5-20 μm a year, ensuring a protection from fouling for up

to 5 years. These paints are protective at all times, regardless of sailing speed.

Therefore, it is not a surprise that with its many advantages over free association

paints and ablative paints, almost 70% of commercial shipping was protected by SPC-

TBT paints in 1999 [13].
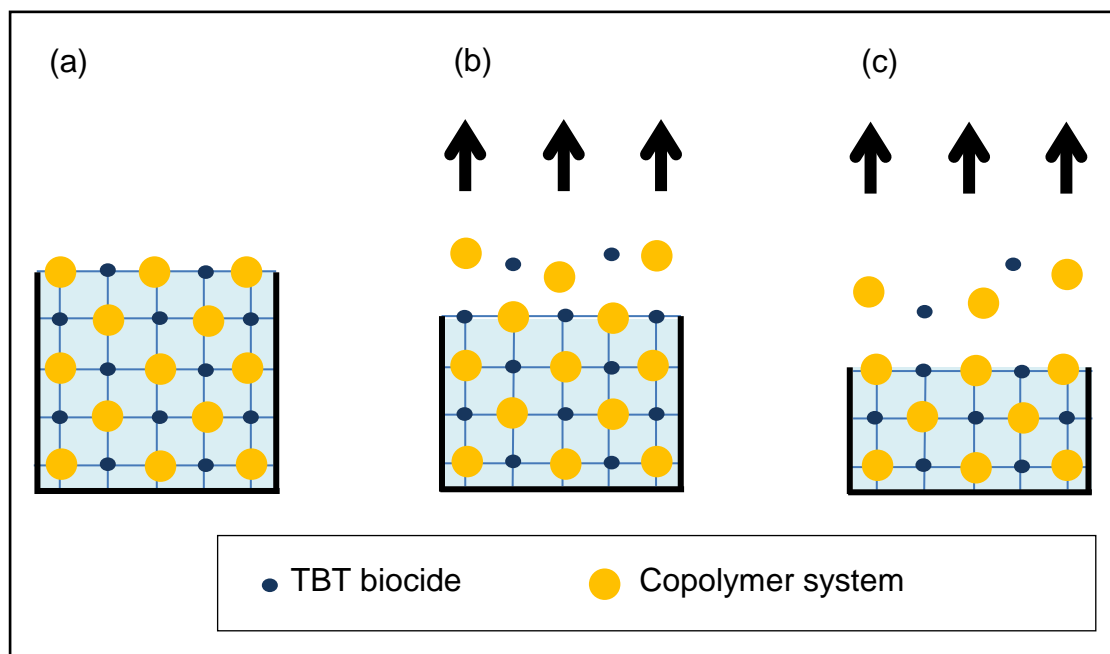
Figure 2.7: Self-polishing copolymer paints with tributyltin (TBT) biocidal compounds. (a) The TBT and copolymer molecules are covalently bound in a polymer matrix. (b) Sea water hydrolyses the TBT copolymer bond and the TBT biocide and copolymer resin is released. (c) The release rate is controlled through use of specific copolymer systems. Uniform anti-fouling performance is achieved throughout the lifetime of the paint. (Adapted from International Maritime Organization [209]).

From 2003, major antifouling paint manufacturers have stopped producing

products with TBT [1]. In the US, the Office of Naval Research sponsors research

into novel fouling-resistant solutions [256], whilst in Europe, regional initiatives such as the AMBIO Integrated Project funded by the European Union bring academic and industrial partners to develop novel solutions to control marine biofouling [257].

2.4.3   TBT Substitutes

As a result of legislation banning TBT, alternative antifouling coatings based on copper metal oxides and organic biocides were introduced, such as Irgarol 1051 (2-methylthio-4-tert-butylamine-6-cyclopropylamine-s-triazine), Diuron (3-(3,4-dichlorophenyl)-1,1-dimethylurea), Sea-nine™ 211 (member of 3(2H)-isothiazolone), zinc pyrithione, copper pyrithione, Zineb and dichlofluanid.

Voulvoulis et al. [258] rated zinc pyrithione and Zineb as least harmful to the environment while Irgarol and Diuron are considered to be more harmful. A review study by Konstantinou and co-workers [259] reports on the global occurrence and toxic effects of these TBT-replacement antifouling paint booster biocides on aquatic species. Their work revealed that several classes of aquatic vegetation, crustacean and fish contained lethal concentrations of the biocides. In addition, the acute toxicities of copper, TBT, as well as the booster biocides Irgarol, diuron, zinc pyrithione, copper pyrithione and chlorothalonil have also been found to have toxic effects on subtropical fish larvae [260]. Thus, it is imperative to seek greener alternatives to these current generations of antifouling formulations.

The current generation of antifouling paints are grouped under 3 categories:

1) Controlled depletion paints

2) Tin-free self-polishing copolymer paints

3) Biocide-free paints

2.4.3.1 Controlled Depletion Paints (CDPs)

Also known as tin-free ablative/erodible paints, this is similar to ablative paints (Section 2.4.2.2). However, they contain a large proportion of binder which has the following characteristics: physically drying, non-toxic, and sea water-soluble. When it comes into contact with sea water, the binder will dissolve together with the biocide and are 'washed' from the surface. However, they still contain high amounts of copper and a co-biocide.

2.4.3.2 Tin-Free Self-Polishing Copolymer Paints (TF-SPCs)

Pendent groups, without the presence of tin, are integrated in an acrylic matrix, which are then released upon contact with sea water. Almeida et al. [13] have asserted that in spite of the large numbers of patents registered in this domain, the effectiveness of these TF-SPCs are less impressive than those of TBT-SPCs. They cited the impact of the chemical nature of the pendent groups affecting the balance of hydrophilicity/hydrophobicity of the matrix, the alteration of the vitreous transition

temperature during hydrolysis, the absorption of water, and the possible intumescence of the polymer, amongst other reasons [13]. Commercial antifouling paint manufacturers such as Hempel Portugal and Chugoku of Japan have interesting examples of various technologies in this area. The paints do not contain rosins or their derivatives, and they are based on copper acrylates and zinc acrylates which are combined with co-biocides [13].

2.4.3.3 Biocide-Free Paints

These paints are designed to repel the adhesion of marine organisms due to their ultra-smooth, very low friction and hydrophobic surfaces. Known as 'fouling release' (FR) coatings, transient fouling is removed by movement of sea water or easily cleaned using pressurized water jets. They are based on fluorinated polymers and silicones, with many current commercial FR coatings based on non-polar, hydrophobic poly(dimethylsiloxane) (PDMS) elastomers. However, they are only suitable for high speed vessels with short idle periods. Furthermore, they are relatively expensive, have silicon contamination issues and require special applicators and cleaning technologies [13].

Genzer and Efimenko [261] reviewed the topic of superhydrophobic surfaces and their implications on biofouling phenomena. While the authors considered the importance of surface chemistry, topology and surface dynamics for efficient antifouling marine coatings, they stated that it may be impossible to design an environmentally benign coating which is universally non-fouling, due to the range of

70

marine organisms, their ability to adapt and the broad range of bioadhesives available. However, there has been a measure of success in fouling release coatings employing hierarchically wrinkled topographies or the use of multiple roughness length scales which are smaller-sized than the settling organisms. This is similar to the "Lotus leaf effect" to improve 'self-cleaning' surfaces.

2.4.4 Natural Bioactive Compounds-Based Antifouling Systems

Innovations in antifouling control technology have gained much inspiration from Mother Nature. Many marine mammals such as sharks and dolphins, as well as calcareous organisms such as mussels, have a multipronged approach at resisting fouling. This includes the existence of a physical defence in the form of micro topography on the exposed surfaces of the organism, combined with certain natural chemical compounds in their arsenal [262].

Fascinating reviews have been written on this subject [5, 263, 264]. For instance, Abarzua & Jakubowski [5] have summarized a comprehensive list of biogenic agents isolated from the microalgae Cyanophyceae, Chrysophyceae, Dinophyceae and Chlorophyceae, and the macroalgae Phaeophyceae, Rhodophyceae, Conjugatophyceae and Charophyceae, as well as several species of marine invertebrates including Porifera, Cnidaria, Tunicata and Mollusca. In many cases, extracts of these biogenic agents have been found to have a combination of antibacterial, anti-algal, anti-fungal and anti-macrofouling effects. The structures of these plant-based bioactive compounds include fatty acids, glycolipids/lipoproteins,

71

terpenes/carbohydrates, goniodomin, chlorophyll c and α-linolenic acid. The biogenic compounds from marine invertebrates include chemicals such as lactons, fatty acids, bromopyrroles, homarine, herbacin, pukalides, peptides, steroids and saponins.

The cytotoxicity, ichthyotoxicity, inhibition of bacterial growth, and enzyme inhibition of 3-alkylpyridinium compounds of the Haplosclerida marine sponges were studied, with promising antifouling activities demonstrated by Sepcic and Turk [265]. The linear structure 3-octylpyridinium polymers which were isolated from *Reniera sarai* inhibited the settlement of *B. amphitrite* cypris larvae with an EC_{50} of 0.27mg/mL, while having negligible toxicity on *B. amphitrite* nauplii larvae, *Tetraselmis suecica* microalga and *Mytilus galloprovicialis* larvae. The natural alkylpyridines were also found to prevent the formation of bacterial biofilm, while synthetic analogs of these structures also exerted antifouling activity.

Grandison et al. [233] studied the extracts of the periostracum of the marine mussel *Mytilus sp.* with considerable activity against marine diatoms and bryozoans. In order to study the structure of the antifouling compound, attempts were made to isolate and purify the periostracum compound – however, this was proved to be rather challenging. In addition, the authors acknowledged that the compound most likely work in tandem with other antifouling defenses, both physical and chemical, at the mussel's disposal.

An extensive review on the natural defenses of marine animals and plants against epibionts have been explored in detail by Railkin [223]. The defense system may be divided into the physical or mechanical, and the allelochemical action. The

defense mechanisms of many marine animals and plants, including algae, sponges, coral, and ascidians are based on an allelochemical action. These marine organisms release chemical compounds which naturally deter predators and prevent biofouling through inhibiting the settlement of epibionts. These compounds have been classified as phenolic derivatives, such as tannin, halogenorganics, terpenoids, acrylic acid and acrylates, and heterocyclic compounds. These compounds, known as secondary metabolites, have been documented to suppress the development of bacterial cultures and stop the movement of macrofouling larvae. These natural defenses were further classified by Railkin [223] as biocidal, repellent, antiadhesive, antilocomotory and suppressant of metamorphosis and growth.

Table 2.7 summarizes antifouling compounds derived from heavy metals, polymeric compounds and natural marine biocidal sources. The list includes the effect of these compounds on model organisms. Some researchers have studied commercial antifouling agents [18, 232], but most are focused on novel antifouling compounds, for example dihydrooroidin, a compound isolated from sponges of the Agelasidae family [228], the extracts of the periostracum from *Mytilus sp*. [233] and various extracts from other marine lifeforms [237]. There exists a rich diversity in the composition of potent antifouling compounds obtained from biological sources. The reality is that there is still much room for advancement in the discovery of new compounds and effective formulations which can resolve fouling issues.

Table 2.7: Antifouling compounds and their activity against model organisms.

Active Compound / Coating	Manufacturer	Commercial Name	Model Organisms	Notes , Qualitative assessment on antifouling tests	Reference
5-chloro-2-methyl-4-isothiazolin-3-one and 2-methyl-4-isothizolin-3-one	NALCO	73532 - NALCO®	*Balanus pharaonis*	Lowest efficacy on *B. pharaonis* among 3 NALCO biocides surveyed with 30% mortality at 1000 mg/l.	[240]
Benzoic acid	-	-	*Dynamena pumila*	Repellant agent: Planulae of hydroids turned away from capillary containing antifouling agent at concentration of 116mM	[237]
			Macrofouling	Percentage of macrofouling progressively increase to 29 ± 12 in 10-19 days, 45 ± 7 in 22-25 days, 48 ± 18 in 45 days, 78 ± 19 in 70 days	
			Mytilus edulis	Repellant agent: Foot of mussel turned away from capillary containing antifouling agent at concentration of 744mM	
Bromotysine-derived sponge metabolites and synthetic analogues including hemibastadin-1, debromo-hemibastadin-1, and 5,5'-dibromohemibastadin-1	-	-	*Balanus improvisus*	Compounds containing oxime substituents inhibit larval settlement at 1-10 μM.	[244]
Commercial serine endopeptidase Alcalase	-	-	Barnacle cyprid larvae	Alcalase reduce effectiveness of cyprid adhesives	[242]

Table 2.7 (continued): Antifouling compounds and their activity against model organisms.

Active Compound / Coating	Manufacturer	Commercial Name	Model Organisms	Notes , Qualitative assessment on antifouling tests	Reference
Cu^{2+} ions and/or phosphonium cations incorporated in styrene sulfonate, and/or acrylate or maleate with vinyl acetate or styrene copolymers	-	-	-	Immersion in seawater, visual observation after 1.5 months and 6 months.	[266]
Cuprous oxide	International Marine Coatings	Interspeed 642	*Achnanthes Amphora Fragiliria Nitzschia Synedra*	Abundant after static immersion (60d), dispersed after dynamic immersion (15d). All have some resistance to Cu oxide	[18]
			Alcaligenes Proteus Staphylococcus Streptococcus Vibrio	None after static immersion (60d) and remained clear after dynamic immersion (15d). All killed by Cu oxide.	
			Micrococcus Navicula Pseudomonas	Appeared after static immersion (60d), increased after dynamic immersion (15d). *Micrococcus* has high resistance to Cu oxide. Although both *Navicula* and *Pseudomonas* both showed resistance to Cu oxide, *Pseudomonas* was dispersed by shear force.	

Table 2.7 (continued): Antifouling compounds and their activity against model organisms.

Active Compound / Coating	Manufacturer	Commercial Name	Model Organisms	Notes , Qualitative assessment on antifouling tests	Reference
Cuprous oxide	Jotun	Sea Quantum Classic	*Achnanthes Fragiliria Nitzschia Proteus Vibrio*	None after static immersion (60d) and remained clear after dynamic immersion (15d). All killed by Cu oxide.	[18]
			Alcaligenes Staphylococcus Micrococcus Pseudomonas Streptococcus	Appeared after static immersion (60d), dispersed after dynamic immersion (15d). All have resistance to Cu oxide, but *Alcaligenes*, *Staphylococcus* and *Pseudomonas* are dispersed by shear force.	
			Amphora Navicula Synedra	Abundant after static immersion (60d), still abundant after dynamic immersion (15d). All are highly resistant to Cu oxide.	
Didecyl dimethyl ammonium chloride and isopropyl alcohol	NALCO	77531 - NALCO®	*Brachidontes pharaonis*	No efficacy even at 6 mg/l. Of the 3 NALCO biocides surveyed, this is the most toxic on *Artemia salina* (brine shrimp).	[240]
Dihydrooroidin (DHO)	-	-	*Halomonas pacifica*	Antibiofilm activity shown through biofilm inhibition assay (*H. pacifica*). Followed by negative cytotoxicity assay results (GH4C1 rat pituitary cells, N2A mouse neuroblastoma cells)	[228]
Enzyme Subtilisin A immobilized on maleic anhydride copolymer thin films	-	-	*Amphibalanus amphitrite*	The active immobilized enzyme inhibited settlement, and caused a fraction of settled cyprids to detach.	[239]

Table 2.7 (continued): Antifouling compounds and their activity against model organisms.

Active Compound / Coating	Manufacturer	Commercial Name	Model Organisms	Notes , Qualitative assessment on antifouling tests	Reference
Extract from book gills and carapace of horseshoe crabs (*T. gigas* and *C. rotundicauda*)	-	-	*Salmonella typhimurium, E. coli, S. aureus, Bacillus cereus*	Attachment test using glass slides and stained with crystal violet to view fouling mass. Ethyl acetate extract of *T. gigas* carapace inhibited all strains.	[226]
Extracts of the periostracum of mussel *Mytilus* sp.	-	-	*Amphibalanus reticulates* (cyprid larvae), *Amphora sp., Bugula dentate, Bugula flabellate, Bugula neritina, Haslea sp.*	Dichloromethane and ethyl acetate extracts exhibited considerable activity against marine diatoms and bryozoans.	[233]
Ferric benzoate-based paints	-	-	*Balanus amphitrite* nauplii	Ferric benzoate hydrolyzes in seawater producing a pH decrease. Benzoate anion showed intense narcotic effect on *B. amphitrite* nauplii. Ferric benzoate also as anticorrosive paint compound.	[243]
Intertidal biofilm bacterial isolates related to *Bacillus mojavensis* and *Bacillus firmus*	-	-	*Artemia salina Halomonas marina* (CCUG16095)	Ethyl acetate extracts antifouling effect on *H. marina* (88%) and toxic to *A. salina* (67%) Production of bioactive lipopeptides surfactin A, mycosubtilin and bacillomycin D.	[227]

Table 2.7 (continued): Antifouling compounds and their activity against model organisms.

Active Compound / Coating	Manufacturer	Commercial Name	Model Organisms	Notes , Qualitative assessment on antifouling tests	Reference
Isolates from wild bacteria *Alteromonas* sp. incorporated in an inert matrix (Phytagel™)	-	-	*Ciona intestinalis, Pyura praeputialis*	Larval settlements of these 2 ascidians are inhibited.	[238]
Methyl methacrylate (MMA) and acrylate terminated poly(ethylene oxide-coethylene carbonate) (PEOC) copolymer	-	-	-	PEOC side chains exhibits protein resistance. Marine field tests show marine biofouling inhibited for > 12 wks.	[267]
Mixture of commercial hydrolytic enzymes alpha-chymotrypsin, alpha-amylase and lipase	-	-	*Pseudoalteromonas, Rhodobacter*	Reduce adhesion of > 90% marine microorganisms when used in combination, for over 10 days incubation in lab assay which mimics marine conditions. When used singly, no reduction of biofilm.	[231]
N,N,N',N'-tetramethylethylenediamine	-	-	*Dynamena pumila*	Repellant agent: Planulae of hydroids turned away from capillary containing antifouling agent at concentration of 172mM.	[237]
			Gonothyraea loveni	Repellant agent: Planulae of hydroids turned away from capillary containing antifouling agent at concentration of 43mM.	

Table 2.7 (continued): Antifouling compounds and their activity against model organisms.

Active Compound / Coating	Manufact urer	Commerc ial Name	Model Organisms	Notes , Qualitative assessment on antifouling tests	Reference
N,N,N',N'-tetramethylethylenediamine	-	-	Macrofouling	Percentage of macrofouling progressively increase to 17 ± 1 in 22-25 days, 32 ± 4 in 45 days	[237]
			Mytilus edulis	Repellant agent: Foot of mussel turned away from capillary containing antifouling agent at concentration of 86mM	
p-acryloyloxybenzaldehyde (AcBA) polymer coating	-	-	*Bacillus macroides* (strain KORDI-13724), *Pseudomonas aeruginosa*, microalgae (*Amphora coffeaeformis, Navicula incerta, D. tertiolecta*)	High inhibition against *B. macrolides*, less inhibition of *P. aeruginosa*, inhibited growth of *D. tertiolecta*. Poly(AcBA) coating $3mg/cm^2$ effective in preventing attachment and biofilm formation of diatoms.	[224]
Polyhedraloligomeric silsesquioxane (POSS) as nano-reinforcement on diglycidyl ether of bisphenol-A type epoxy resin and tris (p-isocyanatophenyl) thio phosphate (DESMODUR) polymer coating	-	-	*Balanus variegatus*	Seawater immersion (1 year), Bay of Bengal, Tamil Nadu, India showed very slight fouling. Polyhedraloligomeric silsesquioxane (POSS)-NH_2 with polyamidoimidazoline curing agent	[245]

Table 2.7 (continued): Antifouling compounds and their activity against model organisms.

Active Compound / Coating	Manufacturer	Commercial Name	Model Organisms	Notes , Qualitative assessment on antifouling tests	Reference
Potassium sorbate	-	-	*Balanus amphitrite* nauplii and cyprid larvae	Reversible effect on *B. amphitrite* larvae	[241]
Secondary metabolites from a marine-derived fungi *Cladosporium* sp. F14, including 3-phenyl-2-propenoic acid and bis(2-ethylhexyl)phthalate	-	-	*Balanus amphitrite* larvae *Bugula neritina* larvae	3-phenyl-2-propenoic acid and bis(2-ethylhexyl)phthalate effectively inhibited larval settlement of *B. neritina* and *B. amphitrite* larvae, respectively.	[230]
Tetrakis (hydroxymethyl) phosphonium sulphate	NALCO	73503 - NALCO®	*Balanus pharaonis*	73503 is effective at 1000 mg/l killing 90% of *B. pharaonis*, but is least toxic on *Artemia salina* (brine shrimp).	[240]
Tributyltin oxide + cuprous oxide + tributyltin methacrylate	Hempel Paint	Hempels 79051	*Achnanthes Amphora Micrococcus Synedra*	Extremely abundant after static immersion (60d), still abundant or increased after dynamic immersion (15d). All have high resistance to Sn oxide and Cu oxide.	[18]
			Alcaligenes Navicula Pseudomonas Proteus	Appeared after static immersion (60d), dispersed after dynamic immersion (15d). All have resistance to Sn oxide and Cu oxide, but *Alcaligenes*, *Pseudomonas* and *Proteus* are dispersed by shear force.	[18]

Table 2.7 (continued): Antifouling compounds and their activity against model organisms.

Active Compound / Coating	Manufacturer	Commercial Name	Model Organisms	Notes , Qualitative assessment on antifouling tests	Reference
Tributyltin oxide + cuprous oxide + tributyltin methacrylate	Hempel Paint	Hempels 79051	*Fragiliria Nitzschia Staphylococcus Streptococcus Vibrio*	None after static immersion (60d) and remained clear after dynamic immersion (15d). All killed by Sn oxide and Cu oxide.	[18]
Silver-perfluorodecanethiolate complexes	-	-	*Pseudomonas aeruginosa PA01*	The wire shaped silver-thiolate complex possess superhydrophobic and antifouling properties due to highly fluorinated hierarchical structure	[98]
ω-substituted alkanethiolates with methyl and hydroxyl-terminated and methyl and carboxylic acid-terminated self-assembled monolayers	-	-	*Cobetia marina (Halomonas marina)*	Preferential attachment to hydrophobic surfaces. Monolayers are attached on gold-coated glass slides	[225]
Zinc	-	-	*Artemia salina nauplius* larvae	Prolonged extraction time of paint in seawater resulted in significant increase in mortality. $LC_{50}, 24h = 4000mg/L$, $LC_{50}, 1w = 2000mg/L$, $LC_{50}, 3w = 1000mg/L$	[232]
			Balanus amphitrite cypris larvae	Ten larvae all died within 24h of exposure to paint-coated petri dishes containing 5ml seawater.	

Table 2.7 (continued): Antifouling compounds and their activity against model organisms.

Active Compound / Coating	Manufacturer	Commercial Name	Model Organisms	Notes , Qualitative assessment on antifouling tests	Reference
Zinc	-	-	*Balanus amphitrite nauplius* larvae	LC_{50} = 1600 mg/L	[232]
			Danio rerio embryos	Embryos more susceptible to organic solvent-based paint (os) than water-solvent paint (ws). 100% mortality after 48h (os), 0 mortality (ws)	
			Dunaliella tertiolecta	ws severely inhibited extinction results (similar to blank). Os significantly reduced extinction results in 5d with turbidity half of control.	
			Vibrio fisheri	$EC_{50,ws}$=900 mg/L, $EC_{50,os}$=1400 mg/L	

2.4.5 Antifouling Coatings Containing Silver-Based Nanomaterials

Presently, antifouling coatings containing silver-based nanomaterials are not commercially available. There have been a few studies on silver-based antifouling agents for maritime environments or applications [207, 234]. However, more extensive literature in this area is still relatively scarce.

Ren et al. [234] studied the effects of silver nanoparticle modified surfaces against the adhesion of a marine microalgae *Dunaliella tertiolecta*. The polydopamine-mediated silver nanoparticle layer was coated on various substrates including glass, polystyrene, stainless steel, paint surfaces and cobblestone, with at least 85% inhibition of adhesion by the microalgae.

On the other hand, Inbakandan et al. [207] reported a biosynthesis procedure via a marine sponge to obtain AgNPs which were found to inhibit biofilm formation in a consortium of marine biofilm forming bacteria harvested from the hull of a fishing vessel. The biofilm formation was assessed using the crystal violet staining method while antimicrobial tests were assessed through microbial inhibition zones and bacterial growth curves.

2.5 Evaluation of Antifouling Agents

There is extensive interest amongst stakeholders to pursue safer, yet more effective antifouling materials. Potential candidate coatings are typically tested by

immersion in seawater under a variety of conditions, under standard guidelines published by the American Society for Testing and Materials (ASTM). As field testing often involves immersion in seawater for periods of 1 year or more, this can be time-consuming.

Callow and Callow [4] stated that the specific organisms that develop in a fouling community depend on the substratum, geographical location, the season and factors such as competition and predation. As fouling is a highly dynamic process, testing in one localized region of a harbour may yield results which are remarkably different from testing performed at another spot in the same harbour. Therefore, prior to undertaking field-testing, compounds with potential antifouling activity are tested in the lab, or in vitro, using a variety of biological organisms under carefully controlled conditions. The bioassays involve known microorganisms which typically induce fouling. This allows for better understanding of the mechanism of antifouling activity. In addition, a shorter period is used to shortlist viable candidates with high antifouling activity and to fine-tune compounds with average antifouling activity. To overcome the inconvenience of sourcing for regular supplies of natural seawater, commercial sea salt mixtures such as Tropic-marin® are available to prepare artificial seawater.

2.5.1 Biological Laboratory Assays

Bioassays are protocols which involve the exposure of target and non-target organisms to the antifouling compound in a controlled and micro-environment such as

a petri dish or a microarray well plate. As the organisms are being observed and tested in artificial surroundings or removed from their natural environments, these studies are called *in vitro*. Organisms such as bacteria and larvae of macrofoulers are placed in a medium based on seawater, either natural or artificial. Toxicity tests are run to establish the EC_{50} and LC_{50} points of potential antifouling candidates.

As the majority of fouling organisms fall into three broad categories (bacteria, algae and barnacles), typical screening studies of antifouling compounds use bioassays to test the anti-bacterial, anti-algal and anti-barnacle activities. The information obtained from biological assays is considered "static". This includes the degree of settlement, adhesion, and percentage removal.

Static biofilm systems, or surface-attached aggregations of bacteria, can be studied using the microtiter plate biofilm assay [268]. Commonly, cells are grown in 96-well microplates for a pre-determined period of time, after which the wells are gently washed to remove planktonic bacteria. Cells which remain attached to the wells are stained with a crystal violet dye. The solubilized dye allows for a semi-quantitative assessment of the biofilm formation. Melander et al. [228] describes a similar static biofilm inhibition assay protocol using *Halomonas pacifica* (ATCC 27122), a species of microbe which has been established as an agent for biofilm-formation [225, 229].

Löschau and Krätke [232] carried out toxicity tests of commercial paints on the nauplius larvae of the crustaceans *Balanus amphitrite* and *Artemia salina*, the marine algae *Dunaliella tertiolecta*, the bioluminescent bacteria *Vibrio fisheri*, and

embryos of the freshwater zebra fish *Danio rerio* after reporting the death of *B. amphitrite* cyprid larvae within 24 hours exposure to the paints. It was interesting to note that the commercial paints were being marketed as biocide-free.

In laboratory studies, Railkin [223] describes specially constructed Plexiglas chemotactic chambers with dimensions of 36 x 40 x 80 mm used to demonstrate the repellant nature of antifouling test agents. The chambers were built with 3 compartments, each separated by membrane filters. Hydroid larvae placed in the middle chamber were observed to swim away from the repellant agent, and towards the control solution (sea water).

According to Armstrong et al. [269], although a compound may show promising antifouling property when it is tested directly against fouling organisms, it is extremely important to incorporate these compounds into a paint formulation as part of the antifouling evaluation. This is because a compound that has been tested in laboratory assays may not be active when added as an antifouling agent in a paint formulation.

2.5.2   Attachment Tests

Rittschof et al [270] developed an *in vitro* assay using the barnacle *Balanus amphitrite,* which was used by Löschau and Krätke [232] to study the efficacy and potential toxicity of commercial, biocide-free, self-polishing antifouling paints. *B. amphitrite* is a common macrofouler found throughout the world's temperate and

tropical waters, having a high reproduction rate, as frequent as once a week. In order to show the antifouling efficacy of the paints, attachment tests with cypris larvae of *B. amphitrite* were carried out. All the larvae died within 24 hours of contact with the paints and their extracts.

The antifouling activity of a hybrid dendritic boltorn/star PEG thiol-ene polymeric coating was evaluated using the zoospores of the marine algae *Ulva linza* [235]. The coatings were assessed through spore settlement (attachment test) and the attachment strength (release test from varying impact pressures of a water jet).

2.5.3 Mesocosm Challenge Tanks

A mesocosm is defined as laboratory models of stable, natural ecosystems used to simulate short-term and long-term effect studies [271]. For antifouling research, a mesocosm would typically involve a tank containing a constant supply of pumped-in seawater or artificial seawater, inhabited by one or several representative species of fouling and non-fouling organisms. Pumps and rotors are added to simulate tidal cycles and wave motions.

Melander et al. [228] designed a mesocosm challenge tank to test the antifouling effectiveness of dihydrooroidin (DHO), a small organic molecule with amide and bromide groups, which is mixed with commercial marine paint without additional antifouling agents. The tank contained seawater collected from Cherry Point boat landing on Wadmalaw Island, South Carolina, USA (32°35.876'N, 080°10.973'W). Intertidal sediment was collected from Leadenwah Creek

(32°38.848'N, 080°13.283'W). Organisms added to the tank included *Spartina alterniflora*, grass shrimp (*Palaemonetes pugio*), sheepshead minnows (*Cyprinodon variegatus*), and hard clams (*Mercenaria mercenaria*). To simulate a semidiurnal tidal cycle, a pump controlled by a multi-event timer was used.

2.5.4   Field Testing

Coatings or compounds which display promising antifouling properties in laboratory assessments progress on to field trials. Trials are commonly conducted in the protective waters of a harbour, or on specialized structures or rafts in the open sea. The American Society for Testing and Materials (ASTM) has published guidelines for performing standardized test procedures and evaluation of surfaces for fouling. The guidelines cover various parameters including shallow submergence, partial immersion, erosion through high velocity water, barnacle adhesion and physical performance of marine coating systems. The guidelines are listed in Table 2.8.

Table 2.8: ASTM Standards related to antifouling / biofouling.

Standard	Description
D3623	Test Method for Testing Antifouling Panels in Shallow Submergence
D4938	Test Method for Erosion Testing of Antifouling Paints Using High Velocity Water
D4939	Test Method for Subjecting Marine Antifouling Coating to Biofouling and Fluid Shear Forces in Natural Seawater
D5479	Practice for Testing Biofouling Resistance of Marine Coatings Partially Immersed
D5618	Test Method for Measurement of Barnacle Adhesion Strength in Shear
D6990	Standard Practice for Evaluating Biofouling Resistance and Physical Performance of Marine Coating Systems
G141	Guide for Addressing Variability in Exposure Testing of Nonmetallic Materials

2.6   Justification for Selection of Research Approach

Based on the literature review presented in this chapter, this thesis proposes to study Ag nanocomposites synthesized with polymeric ion exchange resins, zeolites, titanium dioxide nanotubes and graphene nanosheets. These support materials for AgNPs were chosen for the following reasons:

- Polymeric ion exchange resin – ease of handling, wide availability

- Zeolite ZSM-5 – nanostructured cavities which can serve as physical size barriers for nanoparticle growth, large effective surface area

- TiO_2 nanotubes – unique 1D structure, large effective surface area

- Graphene nanosheets – novel synthesis method, unique and flexible 2D structure, large effective surface area

To evaluate the marine antimicrofouling behaviour of the Ag nanocomposites, the target microorganisms were selected based on their natural marine environment habitat, identified as being microfouling organisms, with previous studies as model organisms in antifouling/biological studies and the availability of well-established and reproducible procedures for antifouling studies. The target organisms selected are:

- Marine bacteria – *Halomonas pacifica*
- Marine microalgae – *Dunaliella tertiolecta*, *Isochrysis* sp.

Based on the existing literature, wet chemical and solvothermal synthesis methods were selected to prepare the Ag nanocomposites due to the low cost and low energy associated with such methods. Additionally, the precursor materials are widely available.

The combination of preparation methods for Ag nanocomposites, choice of support materials, and the area of application in marine antifouling studies provide an interesting and novel study into the effects of Ag nanocomposites as marine antifouling agents.

Chapter 3: Materials and Methods

3.1 Materials for Synthesis

The chemical reagents used in the syntheses of the four different types of silver nanocomposite antifouling materials are listed in Table 3.1. All materials were used as received. All reagents were prepared with Millipore ultrapure water (18 MΩ/cm). The laboratory equipment and materials used in the syntheses are listed in Table 3.2.

Table 3.1: Chemical reagents used in the synthesis of silver nanocomposite antifouling materials.

Chemicals / Reagents	Manufacturer	Remarks
$AgNO_3$	Sigma-Aldrich, USA	Silver nitrate, analytical grade, 99.9999% metals basis granules. Product number: 204390. CAS No. 7761-88-8
$C_6H_5Na_3O_7 \cdot 2H_2O$	Sigma-Aldrich, USA	Sodium citrate tribasic dihydrate. Product number: S4641. CAS No. 6132-04-3
Dowex® 50WX8 hydrogen form styrene divinylbenzene polymer beads.	Sigma-Aldrich, USA	Diethenyl-benzene polymer with ethenylbenzene and ethenylethylbenzene, sulfonated. Product number: 217514. CAS No. 69011-20-7
Ethanol	Merck, Germany	Ethyl alcohol. EMSURE® grade. Catalogue number: 100974. CAS No. 64-17-5
Graphite flakes (purity ≥ 98% carbon)	Bay Carbon, USA	

Chemicals / Reagents	Manufacturer	Remarks
NaBH$_4$	Sigma-Aldrich, USA	Sodium borohydride 99.99% granules. Product number: 480886. CAS No. 16940-66-2
TiO$_2$ nanotubes	-	Kindly provided by Dr. S.S. Lim, University of Nottingham Malaysia Campus
Zeolite ammonium ZSM-5 powder	Zeolyst International, USA	Product name: CBV3024E. CAS No. 1318-02-1

Table 3.2: Accessories used in the synthesis of silver nanocomposite antifouling materials.

Accessories	Manufacturer
Analytical balance, model GR-200	A&D, USA
Centrifuge, model 2420	Kubota, Japan
Drying oven, model OV-11	Medline Scientific, UK
Filter papers	Sartorius Stedim, France
Furnace, model CWF 12/5	Carbolite, UK
Magnetic stirrer with hotplate, model Wise Stir MSH-A	Wisd/Witeg, Germany
Stainless steel autoclave (316 SS quarter shell. 80mm dia., 74mm height) with Teflon inner liner (54mm dia., 54mm height)	Grandtech Precision Engineering, Malaysia
Ultra sonicator, model S40-H	Elma, Germany

3.2 Synthesis Methods

3.2.1 Synthesis of Silver-Polymer Nanocomposites (Ag-PNCs)

The Dowex 50WX8 copolymer resin beads were incorporated with silver ions through an ion exchange process with silver nitrate solutions of various concentrations. The metallic Ag nanomaterials were obtained by chemical reduction with sodium borohydride (Table 3.3). In a typical synthesis, 2 g of Dowex 50WX8 was mixed with 10 ml of $AgNO_3$ aqueous solution (ranging from 1mM to 1M) and magnetically stirred at room temperature, in the dark, for 1 h to allow ion exchange to occur. 10 ml of 2mM – 2M sodium borohydride was added to the mixture at room temperature under continuous stirring. The Ag-PNCs were obtained by centrifugation at 4000 rpm and washed 3 times with deionized water followed by drying at 80 °C for 10 h.

Table 3.3: The concentrations of the $AgNO_3$ and $NaBH_4$ solutions for the synthesis of Ag-polymer nanocomposite (Ag-PNC).

Samples	Mass of polymer beads (g)	$AgNO_3$ concentration (M)	$NaBH_4$ concentration (M)
Ag-PNC-1	2.0	0.001	0.002
Ag-PNC-2	2.0	0.01	0.02
Ag-PNC-3	2.0	0.1	0.2
Ag-PNC-4	2.0	1.0	2.0

3.2.2 Synthesis of Silver-Zeolite (AgZ) Nanocomposites

Typically, 1 g of ammonium form-ZSM-5 zeolite was mixed with 20 ml of silver nitrate solution of varying concentrations from 0.1 M to 1.0 M, to produce silver-zeolite (AgZ) nanocomposite material (shown in Table 3.4). The mixture was magnetically stirred in the dark at room temperature for 2 h in order to induce ion exchange, after which the mixture was separated by centrifugation (4000 rpm, 20 min). The separated Ag ion-zeolite samples were subsequently redispersed in 20 ml of deionised water. 147 ml of 1% trisodium citrate dihydrate solution (concentrations ranging from 3.4×10^{-3} M to 0.034 M) were then added to Ag ion-zeolite samples, in order to reduce the encapsulated Ag ion into the metallic form.

The mixture was heated to 80°C under constant magnetic stirring for 30 min. The AgZ composites were obtained via centrifugation (7000 rpm) and repeatedly washed with excessive deionised water (three times), in order to remove impurities and unreacted precursor reagents. The metallic Ag-zeolite samples were then dried overnight in an oven at 80$^{\text{o}}$C.

Table 3.4: The concentrations of the silver nitrate and trisodium citrate solutions used for the synthesis of silver-zeolite (AgZ) nanocomposites.

Sample	Mass of zeolite ZSM-5 (g)	AgNO$_3$ concentration (M)	Concentration of trisodium citrate dihydrate (M)
AgZ-1	1.0	0.10	0.0034
AgZ-2	1.0	0.25	0.0085
AgZ-3	1.0	0.35	0.012
AgZ-4	1.0	0.50	0.017
AgZ-5	1.0	1.00	0.034

3.2.3 Synthesis of Silver-TiO$_2$ Nanotube (Ag/TNT) Composites

The synthesis of silver-titanium dioxide nanotube composites involves a 2-step process, in which titanium dioxide nanotubes (TNT) were synthesized from TiO$_2$ nanoparticles, before being used as a support template for the synthesis and growth of AgNPs. The TiO$_2$ nanotubes for this project were kindly provided by the lab of Dr. S.S. Lim (University of Nottingham, Malaysia Campus).

Typically, 0.2 g of TNT powder was dispersed in 40 ml of deionized water under magnetic stirring for 5 min. Silver nitrate granules were added to the TNT mixture and stirred for 30 min in the dark. 10 ml of 1% trisodium citrate dihydrate solution was then added to the TNT-silver nitrate mixture and stirred for 60 min in the dark. The mixture was transferred to a stainless steel autoclave with an inner Teflon liner and heated in a furnace from room temperature to 140°C (ramping rate of 10°C/min), and held at 140°C for 6 h. After cooling down to room temperature, the Ag/TNT precipitates were isolated from solution by centrifugation, washed 3 times

with excess water, and dried overnight at 80 °C in an oven. Table 3.5 shows detailed

information of the different ratios of TNT to silver nitrate which were used to prepare

the Ag/TNT nanocomposites.

Table 3.5: Different mass ratios of silver precursor and TiO$_2$ nanotubes used in the synthesis of silver-TiO$_2$ nanotube (Ag/TNT) composites.

Sample	Mass of AgNO$_3$ (g)	Mass of TiO$_2$ nanotube (g)	Mass ratio of AgNO$_3$ to TiO2 nanotubes
Ag/TNT-1	0.0121	0.1996	1:16
Ag/TNT-2	0.0203	0.1979	1:10
Ag/TNT-3	0.0485	0.2195	1:5
Ag/TNT-4	0.2070	0.2022	1:1
Ag/TNT-5	0.4011	0.2015	2:1
Ag/TNT-6	0.8074	0.2054	4:1
Ag/TNT-7	2.0030	0.2022	10:1

3.2.4   Synthesis of Graphene-Silver (GAg) Nanocomposites

The synthesis of graphene-silver nanocomposites involves a 2-step process, in

which graphene is first synthesized from graphite flakes, before it is used as a support

template for the synthesis of AgNPs.

3.2.4.1 Preparation of Graphene Flakes

Graphite was used as the precursor for synthesis of graphene via liquid phase exfoliation method, as reported in literature [183]. Typically, graphite (50 mg) material was dispersed in 100 ml of a mixed solution of ethanol and deionized water (2:3 ratio of ethanol to water). Sonication treatment was carried out in a conventional ultrasonic bath with working frequency of 50/60 Hz at room temperature for 3 h to form a darkish black suspension. The sonicated dispersions were then centrifuged at 1000 rpm for 30 min to remove unexfoliated graphite flakes. The supernatant is then filtered and dried at 80 °C overnight to evaporate any residual ethanol.

3.2.4.2 Preparation of Graphene-Silver (GAg) Nanocomposites

Graphene (0.2 g) nanomaterial was re-dispersed in 40 ml of a mixed solution of ethanol and deionized water (2:3 ratio of ethanol to water) under sonication for 30 min. Silver nitrate powder was added to the graphene solution and stirred for 30 min in the dark to produce a uniform dispersion (refer to Table 3.6 for sample details). 10 ml of 1% trisodium citrate dihydrate solution (0.5 M) were then added to the graphene-silver nitrate mixture and stirred for 15 min. The mixture was transferred to a stainless steel Teflon-lined autoclave chamber and heated in an oven from room temperature to 140°C with a ramping rate of 10°C/min. The temperature was then held at 140°C for 6 h before it was allowed to cool down to room temperature again. The solid precipitation was isolated from the solution by centrifugation, washed

alternatingly with excess water and ethanol for three times each, and dried overnight

at 80 °C in an oven.

Table 3.6: Different mass ratios of graphene to silver precursor used in the synthesis of graphene-Ag (GAg) nanocomposites.

Sample	Mass of graphene (g)	Mass of $AgNO_3$ (g)	Weight ratio of graphene:Ag precursor
GAg1	0.2	0.063	3:1
GAg2	0.2	0.200	1:1
GAg3	0.2	0.800	1:4
GAg4	0.2	2.000	1:10

3.3 Instrumentation for Silver Nanocomposite Materials Characterization

After the silver nanomaterials have been synthesized, as described in Sections

3.2.1, 3.2.2, 3.2.3 and 3.2.4 above, these samples are characterized using various

instrumentation techniques which are listed in Table 3.7.

The choice to perform a certain type of analysis is dependent on the type of

information required of the sample, as well as the material's suitability for a particular

analysis method. For instance, porosimetry measurements using gas adsorption-

desorption are conducted on the silver-zeolite materials due to the mesoporous nature

of zeolites, whereas thermal analysis was conducted on the silver-polymer materials

to determine the effect of silver inclusions on the thermal stability of the polymer

matrix. Raman analysis was performed on the graphene-silver nanomaterial to probe

the number of layers in the graphene composite, as well as to study the effect of

surface-enhanced Raman scattering after the inclusion of AgNPs.

The principles behind each instrumentation technique and the sample

preparation procedures are described in the following sections.

Table 3.7: List of instrumentation used in the physical characterization of the silver nanocomposite materials.

Instrumentation	Manufacturer
Accelerated surface area and porosimetry system, model Micromeritics ASAP 2020 system	Micromeritics, USA
Energy Dispersive Spectroscopy (EDS) Silicon Drift Detector, X-Max 20mm^2 detector with AZtecEnergy EDS Software for SEM	Oxford Instruments, UK
Raman spectrometer, model Renishaw inVia with CCD detector and holographic notch filter using a 514 nm diode laser excitation source	Renishaw, UK
Scanning electron microscope FEI Quanta-400 FESEM	FEI, USA
TGA/DSC thermal analysis system with alumina crucible	Mettler-Toledo, Switzerland
Transmission electron microscope (200 kV), model JEOL JEM-2100F	JEOL, USA
UV-visible spectrophotometer, model Varian Cary 50, with 10mm quartz cell	Agilent, USA
X-ray diffractometer, model Bruker D8 Advance equipped with a 1-D fast detector (Lynx-Eye) and Cu anode ($\lambda = 0.15406$ nm) with DIFFRAC.EVA phase analysis software	Bruker, Germany
X-ray diffractometer, model PANalytical X'Pert PRO, equipped with Cu K-alpha radiation	PANalytical, Netherlands

3.3.1   UV-Visible Spectrophotometry

3.3.1.1 Principle

UV-visible (UV-vis) spectrophotometry is used as a quick method to confirm the formation of silver nanomaterials (AgNM). Due to the nanostructure of the metallic Ag particles, energy from an incident light with an electrical field vector will polarize the samples. Figure 3.1 illustrates the polarization of the particle by the electric field. Free electrons present in the particles will form a dipole across the particle and begin to oscillate under the influence of the electric field. The layer of electrons on the nanoparticle surface will oscillate with reference to the interior of the particle, which remains constant. Upon reaching the condition of resonance, the UV-visible spectrum of the AgNM will display an intense absorption band. The absorption band for AgNM is at approximately 400 nm wavelength, and is called the "plasmon resonance band" [26].

A   **B**

Light

Electric Field

Absorbance (a.u.) $\lambda_{max} \approx 400$ nm

Wavelength (nm)
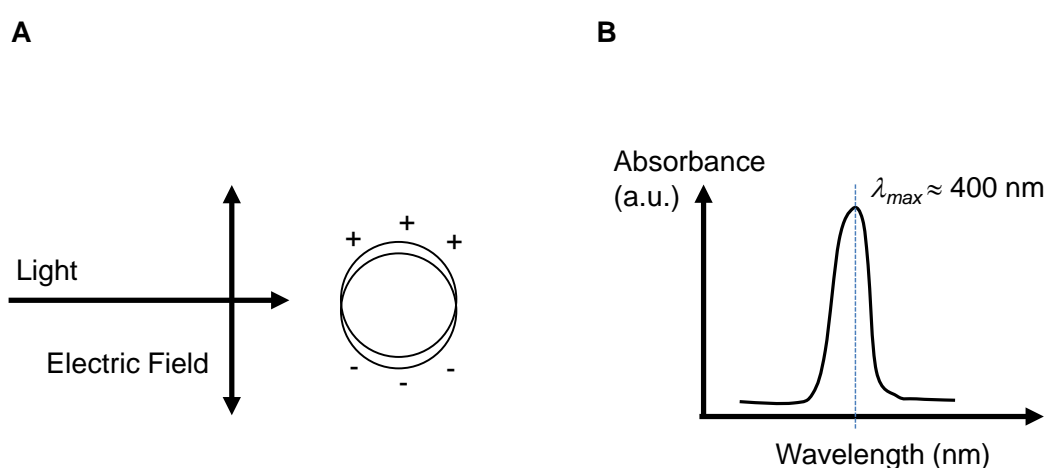
Figure 3.1: Polarization of a particle by an electric field. (A) Polarization of a spherical metal particle by the electrical field vector of the incoming light causes a plasmon resonance band in the UV-visible spectrum. (B) A typical UV-visible absorption spectrum for a silver nanomaterial with a maximum absorption wavelength at approximately 400 nm.

100

3.3.1.2 Sample Preparation

A Varian Cary 50 UV-visible spectrophotometer with a laser from a Xenon lamp was used in this analysis to measure the surface plasmon excitation of the nanoparticles. Samples were dispersed in a liquid medium and sonicated in an ultrasonic water bath for 2 minutes. This step was to ensure good dispersibility in the liquid medium and to remove air bubbles. Samples which were highly concentrated were diluted with deionized water until the maximum absorbance is approximately 1 unit (arbitrary). A typical test routine involved transferring 2ml of sample by pipette into a 10 mm quartz cell. The sample was illuminated with a laser from a Xe lamp from 800 – 200 nm wavelength. Prior to starting a measurement, a cell containing only deionized water was used as the blank sample.

3.3.2 Scanning Electron Microscopy (SEM)

3.3.2.1 Principle

Microscopy methods are an integral part of materials characterization studies, as it allows imaging of the material's structure by probing and mapping the surface and sub-surfaces. The principle behind scanning electron microscopy (SEM) lies in the various interactions which occur when an electron beam strikes a solid specimen (Figure 3.2). The SEM uses electrons instead of light waves to form an image. As electrons have smaller wavelengths, SEM images have higher resolution, up to approximately 1 nm [36]. An extremely focused electron beam rapidly moves over

(scans) a sample, causing the emission of secondary electrons. These electrons are

collected by a detector, converted to a voltage, and amplified. The amplified voltage

is applied to the grid of a cathode ray tube (CRT) and causes the intensity of the light

spot to change. Variations in the emission of secondary electrons are used to build up

an image. The image consists of thousands of spots with varying intensities on the

face of the CRT, which corresponds to the topography of the specimen.
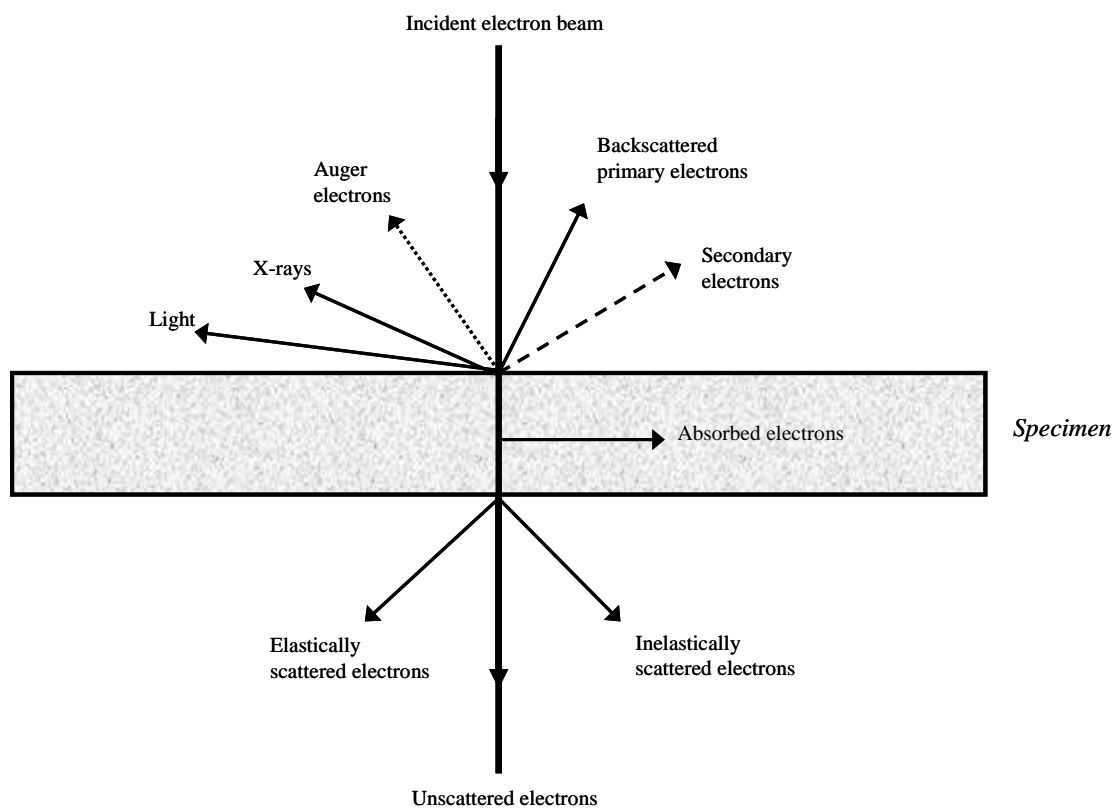
Figure 3.2: Effects of electron – specimen interaction. The SEM uses secondary
electrons while EDX uses characteristic X-rays emitted from the specimen.

3.3.2.2 Sample Preparation

The size and surface morphology of AgNM was observed through an FEI

Quanta 400F scanning electron microscope. For samples which are in powder form,

about 1 g of powder was evenly dusted onto a 1 cm length of a double-sided carbon tape, which was attached to the surface of an aluminium specimen stub. For samples dispersed in solvent, a drop of sample was carefully placed onto a silicon substrate and allowed to air-dry before being fixed onto the SEM sample stub. The prepared stub was then placed onto the SEM stage in the microscope chamber for analysis. Particle size analysis was conducted through analysis of a minimum of 30 points on the image to calculate the mean diameter and standard deviation.

3.3.3　Energy Dispersive X-ray Spectrometry (EDX)

3.3.3.1 Principle

Elemental analysis using energy dispersive X-ray spectrometry (EDX) is considered a form of X-ray microanalysis as it makes use of the characteristic X-rays that are emitted from the sample when it is struck by electrons from an external source. Consequently, these X-rays are used to identify and quantify the elements that are present in an unknown sample.

Figure 3.3 shows incoming electrons interacting with the electrons in the inner shell of an atom. This results in an electron being ejected from its shell, leaving the atom in an ionized condition. The instability of the condition is reduced if an electron from one of the higher energy outer shells falls to occupy the vacant position in the lower energy shell. The reduction in potential energy is released in the form of an X-ray. The energy of the X-ray produced is determined by the difference in energy

between the sharply defined quantum energy levels in the atom. Because each atom has unique energy levels, the X-ray produced is thus, characteristic of the atom from which it is emitted. The relationship between X-ray frequency ν and atomic number, Z, was first proposed by Henry Mosely (Equation 3.1):

$$\nu = 0.248(Z-1)^2 \times 10^{16}$$

…. Equation 3.1

The frequency of the X-ray radiation is related to its quantum energy, E, by the relationship E = hν, where h is Planck's constant.

3.3.3.2 Sample Preparation

The sample preparation for EDX was similar to the preparation for SEM imaging (Section 3.5.2). The elemental analysis was performed on the SEM samples after SEM micrographs have been taken. Three separate spots on each image were analysed and the average elemental composition was calculated from the obtained data.
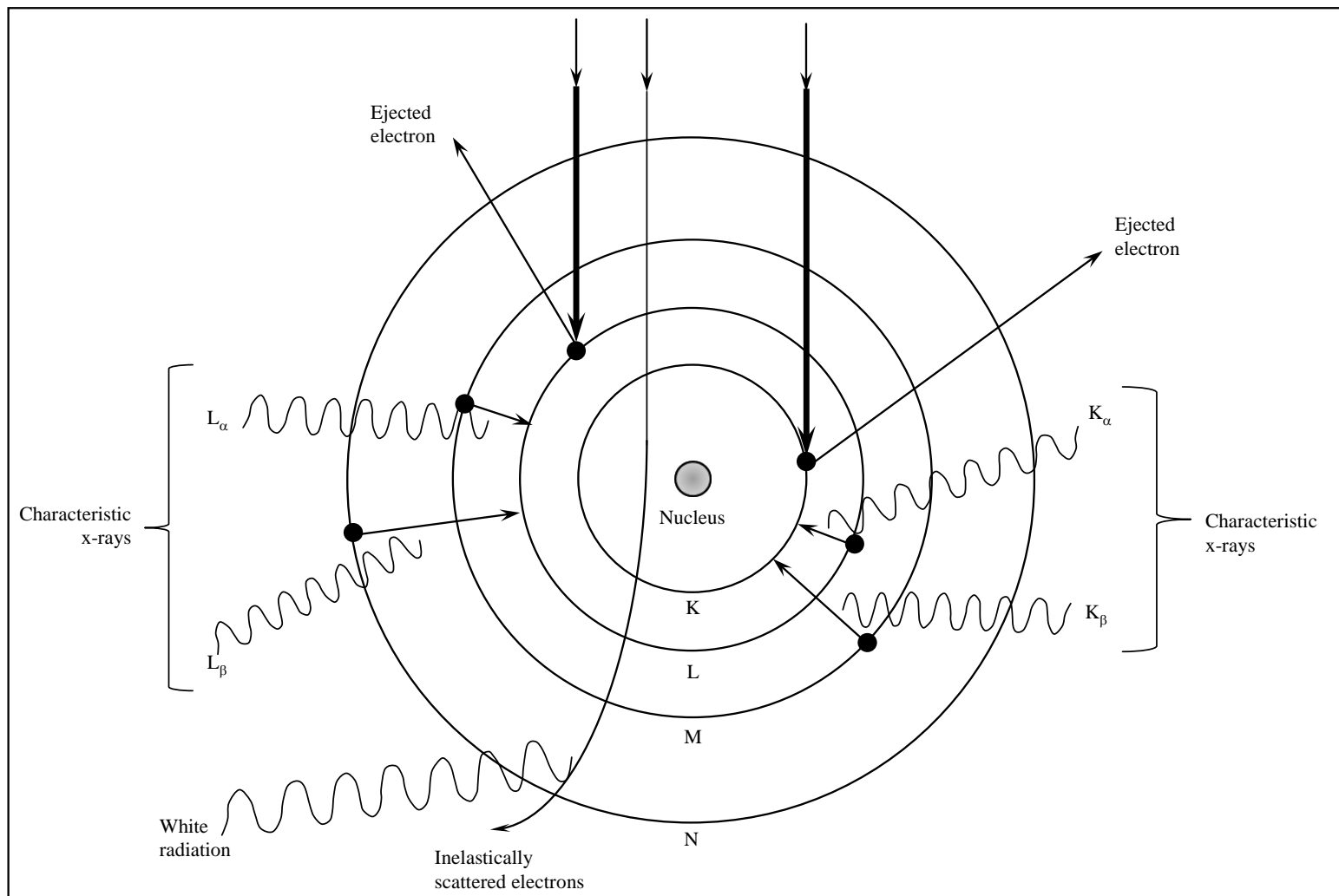
Figure 3.3: Production of characteristic X-rays for EDX.

3.3.4 Transmission Electron Microscopy (TEM)

3.3.4.1 Principle

Transmission electron microscopy is a valuable tool in materials characterization as it allows high resolution imaging, on the order of angstrom, down to near atomic levels. The image is formed from the interaction of a high energy electron beam (up to 300 kV) transmitted through thin specimens. In contrast to SEM, which provides a three-dimensional surface image of specimens, TEM provides a high-resolution sectional image of the samples. Thus, both SEM and TEM are complementary electron imaging techniques, allowing a more complete understanding of the material's morphology.

As shown in Figure 3.4, the TEM instrument has 3 major sections:

1) The illumination system: Electrons from an electron gun is transferred to the specimen. Electromagnetic condenser lenses focus the electron beam onto the specimen to illuminate only the area of study.

2) The objective lens and stage: The specimen stage is inserted into the objective lens for imaging purpose. The objective lens focus and magnify the image.

3) The TEM imaging system: This includes the intermediate lenses and projector lenses. The intermediate lenses magnify the image coming from the objective lens. Finally, projector lenses further magnify the image coming from the intermediate lens and projects it onto a phosphorescent screen. Images are digitally captured on a computer.

The TEM images are in grayscale, with the more dense areas appearing darker and less dense areas lighter. High resolution TEM (HRTEM) allows the imaging of atomic lattices of metallic nanoparticles and can be used to analyse the quality, shape and size of nanostructured materials.
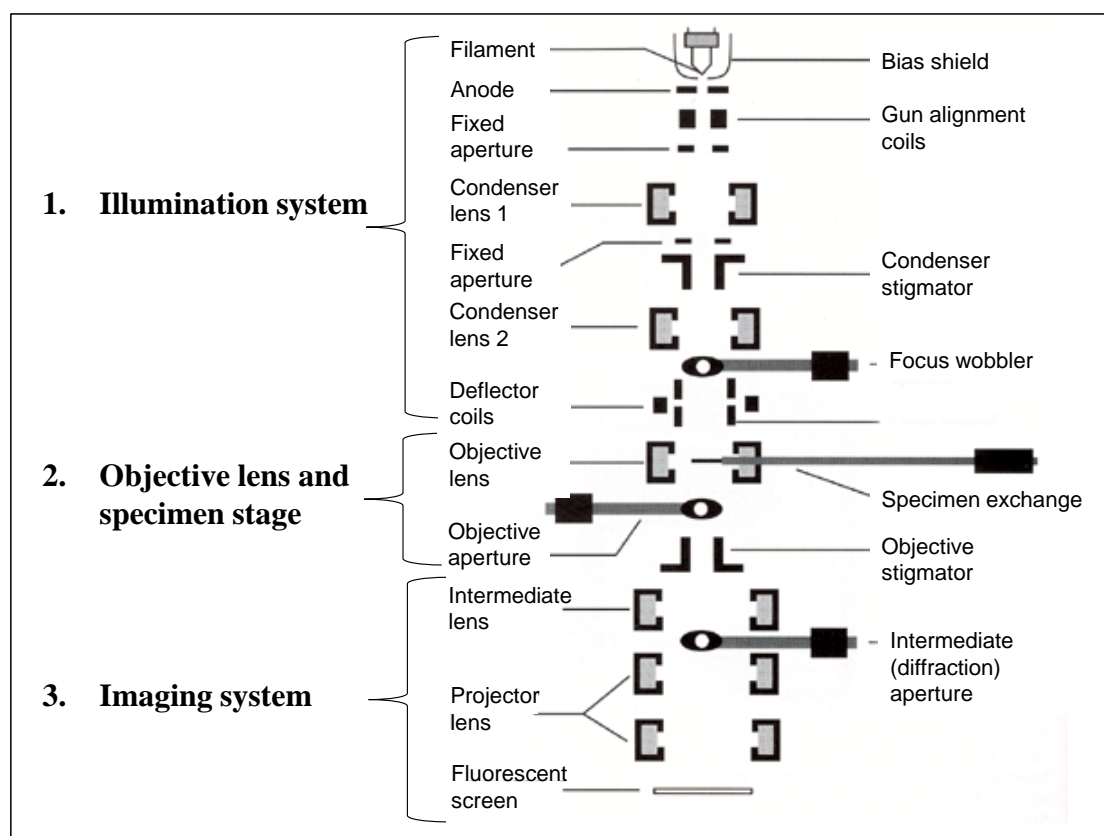
Figure 3.4: General layout of a transmission electron microscope.
(Figure modified from [272]).

3.3.4.2 Sample Preparation

About 20 ml of deionized water was added to 0.5 g of powder sample and dispersed by immersion in an ultrasonic bath until a fine suspension was formed. A drop of the dispersion was placed onto a carbon-coated copper grid and left to dry in a

drying cabinet. The grid was then inserted into the TEM sample holder and placed on the TEM stage for viewing. The samples were viewed under a JEOL JEM-2100F transmission electron microscope at an accelerating voltage of 200 kV.

3.3.5   X-ray Powder Diffraction (XRD)

3.3.5.1 Principle

X-ray diffraction works on the principle of X-ray beams being diffracted by the planes that exist within a crystalline powder sample (Figure 3.5). When a parallel, monochromatic and coherent X-ray beam with wavelength λ, is directed on two parallel planes of atoms at an angle of θ, the waves are scattered by atoms on adjacent planes. If the path length difference that both waves travel is equal to a whole number of wavelengths, n, both waves are in phase after being scattered. The condition for constructive interference of the scattered rays, or diffraction, is governed by Bragg's Law, given by:

$$n\lambda = 2d\sin\theta$$

… Equation 3.2

In Equation 3.2, d is the spacing between adjacent crystal planes, θ is the angle of scattering, and $n = 1$ is used as a standard procedure in the analysis of diffraction patterns for powder samples [273].
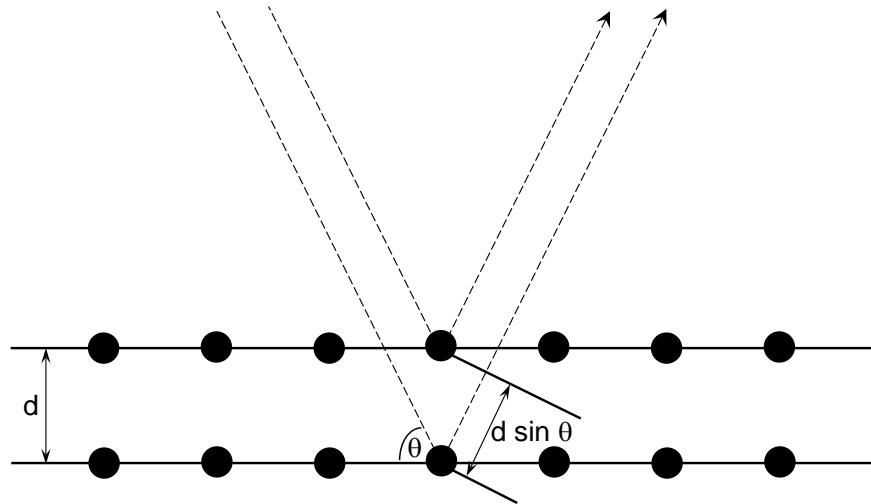
Figure 3.5: Diffraction of X-ray beams by planes of atoms, as governed by Bragg's Law.

Apart from identification of an unknown sample, the crystallite size of a sample can also be determined from the diffraction pattern if appreciable peak broadening is observed. Diffraction pattern of a nanostructured metal sample has broader peaks compared with the bulk metal. The extent of broadening is described by β, which is the full width at half maximum intensity of the peak. Smaller crystallite sizes contribute to larger peak broadening. Apart from this, peak broadening is also attributed to the instrumental profile and microstrain of the sample [274].

After the value of β (in radians) is corrected for the instrumental contribution, it can be substituted in Scherrer's equation, given as:

$$D = \frac{K\lambda}{\beta \cos \theta_\beta}$$

…. Equation 3.3

In Equation 3.3, D is the crystallite size, K is the crystallite shape factor, λ is the wavelength of the X-ray source, and θ_β is the Bragg angle. In the absence of detailed information about the shape of the particle, K is approximated as 0.9 in the crystallite size calculation [275].

For AgNPs, the samples are assumed to be spherical with cubic symmetry, therefore, $K = 0.94$ [276]. LaB$_6$ was used as a calibration standard to determine the instrumental profile of the Bruker D8 Advance XRD. The FWHM of LaB$_6$ over a range from 20-135° 2θ angle is shown in Figure 3.6. The instrumental broadening effect for each position can be directly calculated from an empirical formula obtained from the polynomial equation of the trend line (Equation 3.4).

$$y = 2 \times 10^{-5} x^2 - 0.0011x + 0.0669$$

…. Equation 3.4

Taking into consideration the instrumental broadening effect, β = FWHM (sample) – FWHM (instrument), hence, the Ag crystallite size, D_{Ag}, can be expressed as

$$D_{Ag} = \frac{0.94\lambda}{[\text{FWHM}(sample) - \text{FWHM}(instrument)]\cos\theta}$$

…. Equation 3.5

Equation 3.5 is used to estimate the crystallite sizes of AgNPs in later chapters. Crystallite size broadening, instrumental broadening and microstrain

broadening are larger and more pronounced at larger 2θ angles. If crystallite size approximations are performed using a single peak, better approximations are obtained from diffraction peaks between 2θ angles of 30-50° [277].
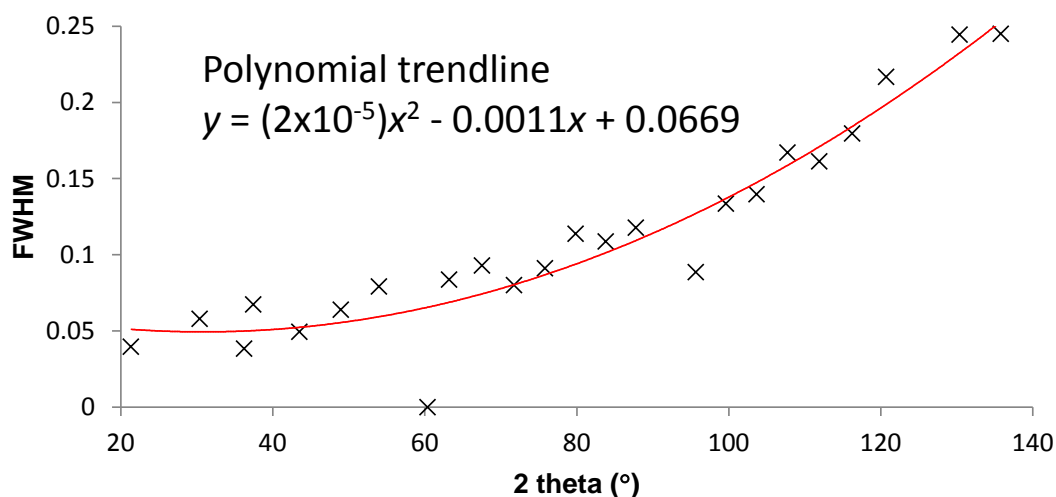
Figure 3.6: The FWHM of the instrumental profile. The instrumental broadening effect, FWHM (instrument) at each position can be calculated from the polynomial trend line.

3.3.5.2 Sample Preparation

Approximately 0.5 g of powder sample was placed onto silicon discs and flattened with a glass slide, before being loaded into the sampling chamber of the diffractometer.

The crystalline properties of the Ag-PNC and AgZ samples were studied using a PANalytical X'Pert PRO X-ray diffractometer with scan of 2θ angle from $5 - 80°$ at a step size of 0.02°/step and a count time of 1.5 s at each step, while the crystalline

properties of the Ag/TNT and GAg samples were studied using a Bruker D8 Advance X-ray diffractometer equipped with a 1-D fast detector (Lynx-Eye) and Cu anode ($\lambda =$ 0.15406 nm), in the 2θ range from 10° to 80°, with measurement parameters of 0.025°/step and exposure time of 0.1 s/step. A Cu-Kα tube ($\lambda = 0.15406$ nm) was used for the generation of X-rays in both equipment.

The raw XRD spectrum was analysed using the X'Pert analytical software package and the DIFFRAC.EVA phase analysis software package, respectively. Generally, the raw spectrum was subjected to a background removal, smoothening and peak identification routine. A search and match of the peaks with standard patterns from the International Centre for Diffraction Data (ICDD) database was performed to identify the phases present.

3.3.6 Accelerating Surface Area and Porosimetry (ASAP)

3.3.6.1 Principle

Surface area and porosity are important material properties, especially crucial for the study of nanoparticle textural characteristics. Textural attributes are capable of influencing the surface reactivity, rate of dissolution, bioavailability, and toxicity profile. The physical characteristics revealed by physical adsorption include surface area, total pore volume, and pore volume distribution by pore size. This method uses adsorbed inert gases, such as nitrogen or argon, whereby each particle of the powder

sample is enveloped in an adsorbed film (the adsorbate), to enable investigation of surface irregularities and pore interiors of the sample (the adsorbent).

Physical adsorption, compared to chemical adsorption (chemisorption) is suitable for surface area determination because of three reasons:

1) it is accompanied by low heats of adsorption, up to 50 kJ/mol, preserving the structural integrity of the adsorbent surface,
2) porous structures within the particle can be filled for volume measurements,
3) the process is fully reversible, enabling studies of both the adsorption and desorption processes [278].

The adsorption of inert gas molecules on samples are recorded in the form of an adsorption-desorption isotherm (Figure 3.7), which plots the change in quantity of adsorbates with changes in relative pressure. The desorption isotherm may be considered as a reverse of the adsorption isotherm as it records the removal of adsorbates from the sample.
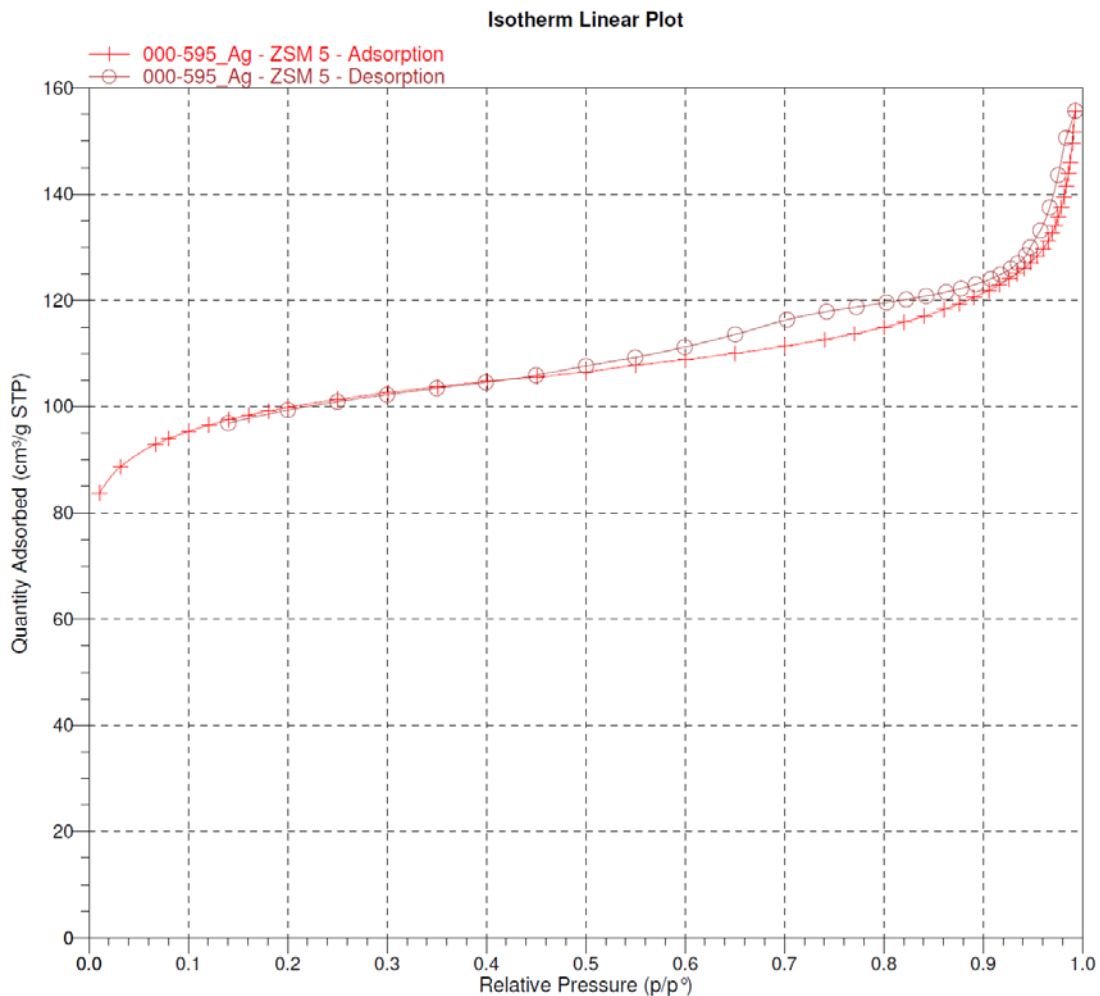
Figure 3.7: Example of an adsorption-desorption isotherm of a silver-zeolite nanocomposite material.

The Brunauer-Emmett-Teller (BET) method is used to calculate specific surface areas of the powdered samples. This method involves the determination of the amount of adsorbate required to cover the external and the accessible internal pore surfaces of a solid with a complete monolayer of adsorbate. The specific surface area can be calculated from the results of BET measurements through the linear form of the BET equation (Equation 3.6):

$$\frac{p}{q_a(p^0\text{-}p)}=\frac{1}{q_mC}+\frac{C\text{-}1}{q_mC}(\frac{p}{p^0})$$

…. Equation 3.6

where p is the absolute pressure, p^0 is the saturation pressure, q_a is the quantity of gas absorbed at a specific pressure, q_m is the quantity of gas to produce a monolayer, and C is the BET constant. The slope and y-intercept of the linear plot are $\frac{C\text{-}1}{q_mC}$ and $\frac{1}{q_mC}$, respectively.

Specific surface area, S_a, defined as the total surface area occupied by the molecules in the monolayer per mass of the sample, and can be calculated as:

$$S_a=\frac{q_m\sigma N_A}{m}$$

…. Equation 3.7

where $q_m=\frac{1}{\text{Slope+Intercept}}$ as determined from the BET plot, σ is the surface area occupied by one molecule at the analysis temperature (when nitrogen is used as the adsorbate molecule, $\sigma = 0.162$ nm^2/molecule) , N_A is Avogadro's number, and m is the mass of the sample used in the BET measurement [279].

For the determination of porosity and pore size volume, a full adsorption and desorption isotherm is measured. In mesoporous materials, capillary condensation may occur as mesopores are filled with liquid nitrogen before bulk condensation occurs. Pore size is estimated using the Kelvin equation (Equation 3.8):

$$\ln\left(\frac{p}{p^0}\right) = -\frac{2\gamma v_{liq}\cos\theta}{RTr_k}$$

<div align="right">…. Equation 3.8</div>

where γ is the surface tension of liquid nitrogen, θ is the contact angle of the liquid nitrogen ($\theta = 0$ for liquid nitrogen), v_{liq} is the molar volume of the liquid nitrogen, and R and T are the ideal gas constant and the analysis temperature, respectively. The pore radius, r, is determined through the relationship with the Kelvin radius, r_k, and the thickness of the multilayer adsorbed film, t, as shown in Figure 3.8.

The Barrett, Joyner, and Halenda (BJH) numerical integration method is used to calculate pore size distribution. The BJH method takes advantage of Wheeler's theory that condensation occurs in the pores when a critical relative pressure is reached which corresponds to r_k. The BJH method also assumes a multilayer of adsorbed film with a depth of t exists on the pore wall when evaporation or condensation occurs, which is of the same depth as the adsorbed film on a nonporous surface [278].
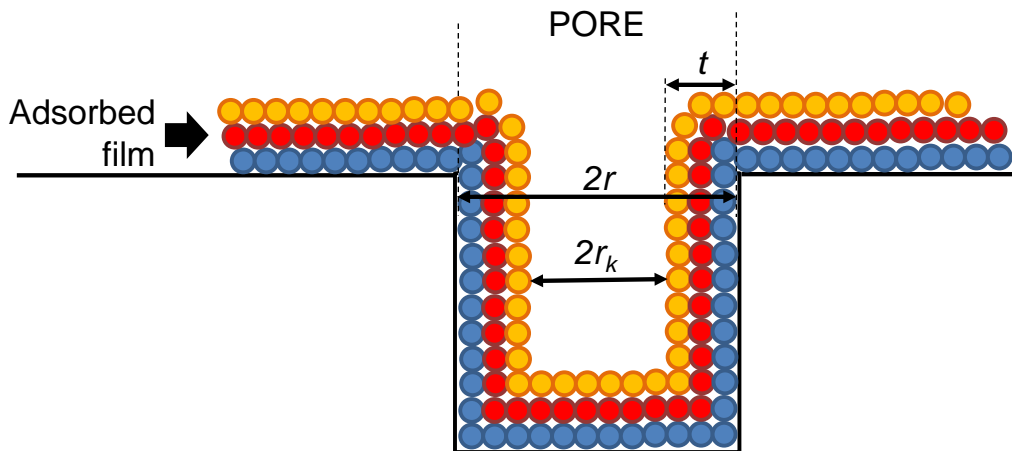
Figure 3.8: Determination of pore radius and pore volume.

3.3.6.2 Sample Preparation

The surface area and pore size was evaluated using a Micromeritics ASAP 2020 surface area and porosity analyser. Approximately 0.05 – 0.5 g of sample was weighed and inserted into a sample tube. After a degassing procedure at 200 °C for 2 hours to remove moisture, the sample was weighed again, after which it was inserted into the ASAP chamber. A steady flow of nitrogen gas flowed through the sample tube, with the maximum adsorption pressure set at 1000 mm Hg for the AgZ nanocomposite samples and selected Ag/TNT composite samples.

3.3.7   Thermal Analysis

3.3.7.1 Principle

Thermal analysis involves measuring the changes in the material with the application of heat. Using a thermal analyser, various analysis techniques are possible, including but not limited to thermogravimetric analysis (TGA), differential scanning calorimetry (DSC), differential thermal analysis (DTA) and evolved gas analysis (EGA). TGA and DSC analysis techniques were used to evaluate the Ag-PNC samples. TGA allows the study of the decomposition of the sample and its products, enabling conclusions to be drawn about their individual constituents.

In TGA, the changes in a sample's mass are measured as a function of temperature. The TGA curve and the first derivative of the TGA curve (known as the DTG curve) (refer to Figure 3.9) assists in the determination of the following:

1) Gains or losses in the mass of a sample.

2) Stepwise changes in mass (calculated as a percentage of the initial sample mass).

3) Temperatures at which the mass loss or mass gain occurs.

4) A typical TGA curve shows mass loss steps related to the loss of volatile components (e.g. moisture, solvents, and monomers), polymer decomposition, combustion of carbon black and final residues. When polymers undergo decomposition, chemical bonds are broken, resulting in the formation of gaseous products including water, carbon dioxide or hydrocarbons.

DSC measures the energy absorbed or released (heat flowing into or out of) by a sample when compared with a reference material. DSC curves are shown as energy of the sample in milliwatts as a function of temperature. The DSC signal can be recorded concurrently with the TGA measurement. Analysis of the DSC curves enables the determination of:

1) Endothermic or exothermic effects,

2) Transition and reaction enthalpies (measured from the area under a peak),

3) Temperatures that characterize endothermic or exothermic effects,

4) Specific heat capacity of the sample
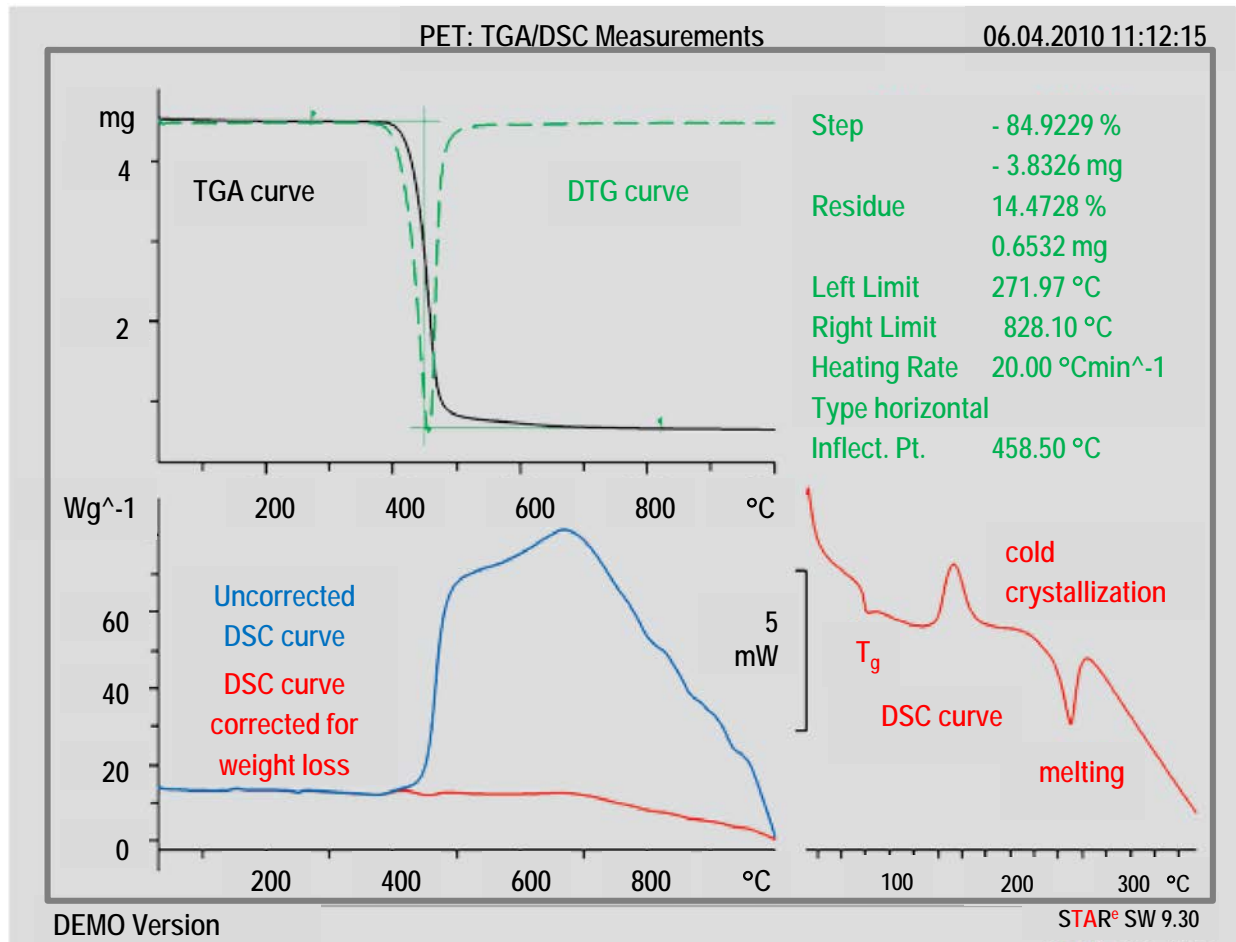
Figure 3.9: Typical thermal analysis results for a polymeric material. Thermal gravimetric analysis (TGA) and differential thermal gravimetry (DTG) curves of polyethylene terephthalate recorded from 30 - 1000°C at a heating rate of 20K/min using a TGA/DSC analyser. The TGA curve shows the change in mass of the sample while the DSC curve shows the endothermic and exothermic effects. (Figure taken from Thermal Analysis of Polymers Applications Handbook © Mettler-Toledo) [280].

For polymeric samples, the DSC curve may show the occurrence of the glass transition, cold crystallization and the melting process.

3.3.7.2 Sample Preparation

The thermal properties of Ag-PNC samples were investigated using a TGA/DSC thermal system (Mettler-Toledo, Switzerland). 10mg of samples were placed in an alumina crucible and heated in a nitrogen atmosphere from 25 – 1000 °C at a heating rate of 10 °C/min.

3.3.8   Raman Spectroscopy

3.3.8.1 Principle

Raman spectroscopy is a non-destructive, spectroscopic measurement method which allows the identification of substances through a characteristic "fingerprint" spectrum. The Raman spectra arise from the particular way molecular vibrations in a substance causes a shift in the wavelength of an incident light, known as the Raman effect [151]. When light from a laser diode is scattered by a substance, most of the scattering is elastic, or Rayleigh scattering, in which the energy of a photon absorbed by a molecule is the same as the energy of the photon emitted.

In Raman scattering, or inelastic scattering, the frequency of the emission is shifted lower (Stokes scattering) or shifted higher (anti-Stokes scattering) (Figure 3.10). The light source gives rise to an electric field which induces a dipole moment in the molecule. The photon causes molecular vibrations which are particular to a chemical structure, causing a shift in the emitted light. It should be noted that the energy of the photon is less than any particular electronic quantum energy; therefore, the molecule remains in the ground state.

When an incident electromagnetic wave interacts with a material, a dipole moment is induced within the molecular structure of the material. The strength of the induced dipole moment, P, is given by Equation 3.9:

$$P = \alpha \overline{E}$$

…. Equation 3.9

where α is the polarizability and $\overline{E}$ is the electric field strength of the incident electromagnetic wave. The polarizability of the material is dependent on the molecular structure and its chemical bonds.

The electric field can be expressed as

$$\overline{E} = E_0 \cos(2\pi \nu_0 t)$$

…. Equation 3.10

where ν_0 is the frequency of the incident light.
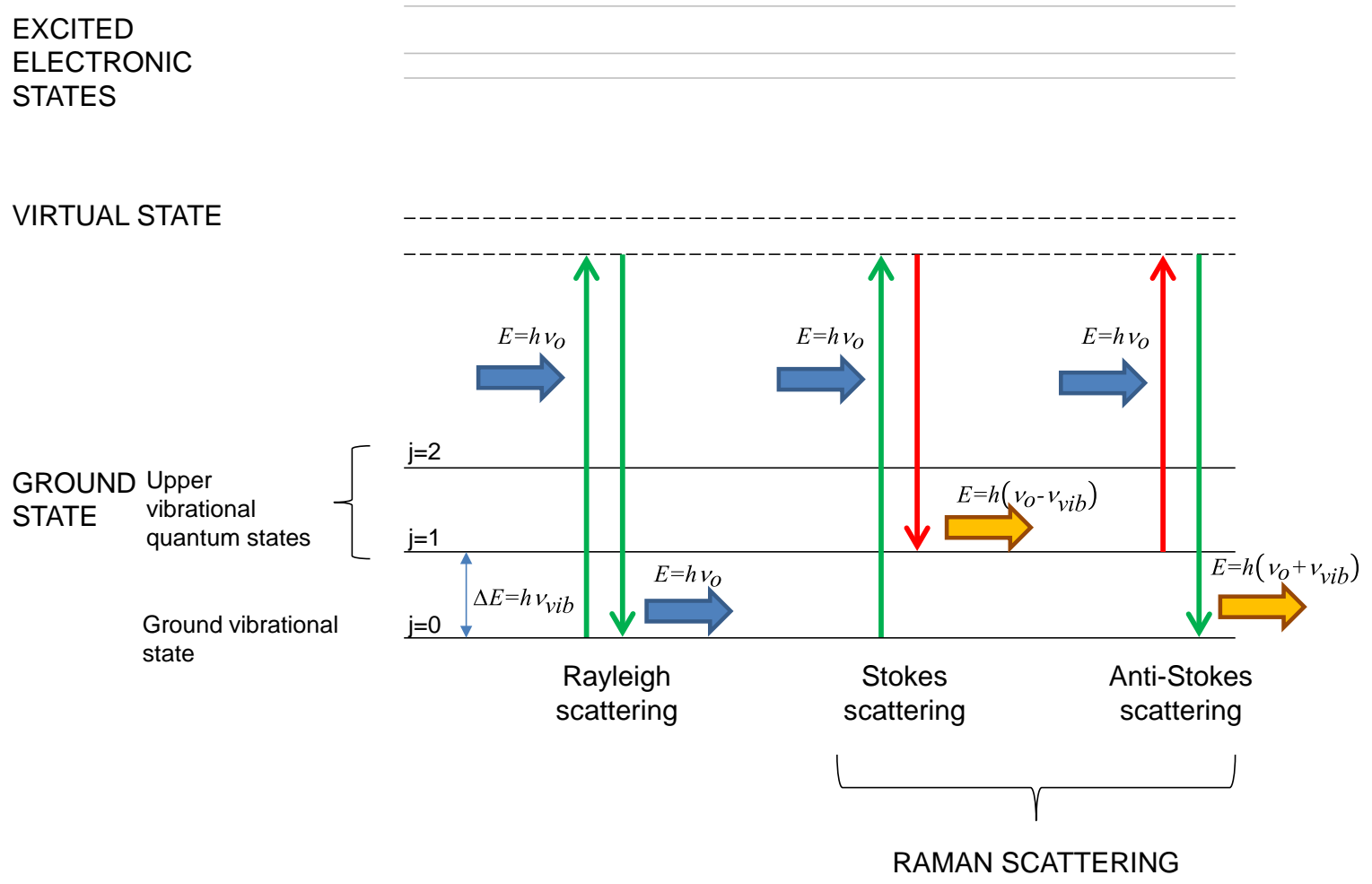
Figure 3.10: Representation of the vibrational energy states of a molecule. Raman scattering is the shift in vibrational energy state due to the interaction of an incident photon.

The vibrational energy of a particular mode is given by

$$E_{vib} = \left(j + \frac{1}{2}\right) h\nu_{vib}$$

.… Equation 3.11

where j is the vibrational quantum number ($j = 0, 1, 2, \ldots$), ν_{vib} is the frequency of the vibrational mode and h is Planck's constant.

Raman spectroscopy is an important tool in the characterization of graphene and graphene-based materials due to their ability to probe the number of layers present in the material [281]. An example of a Raman spectrum is shown in Figure 3.11. The x-axis (Raman shift) is usually shown in wave numbers in order for the frequency shift to be independent of the excitation light source. The Raman spectrum for graphene has three prominent characteristic peaks: the D peak at wavenumber ~ 1350 cm^{-1}, the G peak at ~ 1580 cm^{-1} and the G' peak (also known as the 2D peak) at ~ 2720 cm^{-1}. The D peak arises primarily from the existence of defects and disorder, particularly the edge defects in graphene [282]. The G' band provides information about the number of layers present in the graphene. Monolayer graphene has a sharp, single Lorentzian G' peak, in contrast to a broader G' band of few-layer graphene [281].
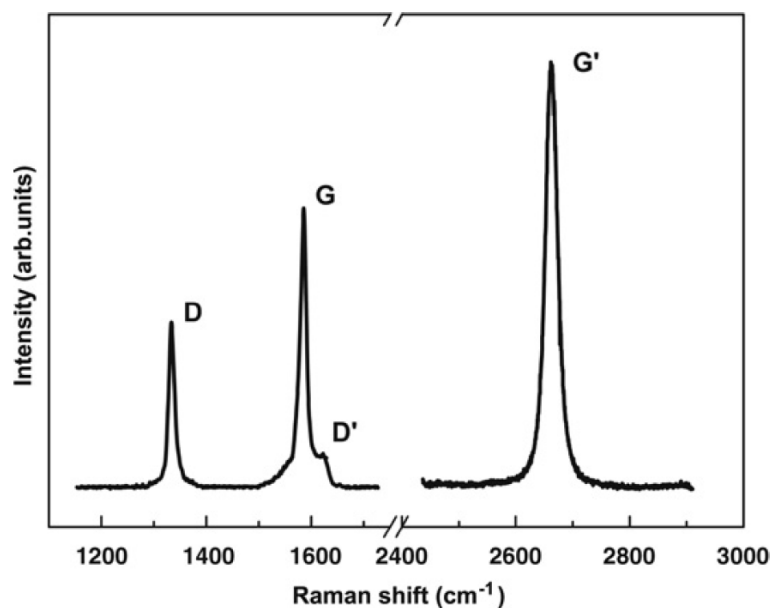
Figure 3.11: Raman spectrum of a graphene edge. The spectrum shows distinctive D, G and G' bands. (Figure taken from [281]).

3.3.8.2 Sample Preparation

About 0.5 – 1 g of GAg powder sample was placed on a glass microscope slide and carefully positioned on the viewing stage of a Raman microscope. The Raman spectra of the powdered samples were recorded on a Renishaw inVia Raman microscope at room temperature. The system was equipped with a CCD detector and a holographic notch filter. An excitation source using a 514 nm laser diode was used with power setting below 0.5 mW so that the samples were not damaged by the laser source.

3.4   Biological Evaluation of Marine Antifouling Properties of Silver Nanocomposite Materials

The silver nanocomposite materials were used in biological experiments to assess their effects on inhibition of biofilm production and effects on microalgae growth. There are two main biological experiments for evaluating the antifouling properties:

1) General static biofilm inhibition assay using the marine bacterium *Halomonas pacific.*

   - *H. pacifica* was used as a model biofilm-causing organism as described in previous studies [228, 229]. In brief, bacterial cells were grown in microtiter dishes for a desired period of time, and then the wells were washed to remove planktonic bacteria. Cells remaining adhered to the wells were subsequently stained with a dye that allowed visualization of the attachment pattern. This surface-associated dye was solubilized for a semi-quantitative assessment of the biofilm formed [268].

2) Evaluation of growth inhibition of marine microalgae using *Dunaliella tertiolecta* and *Isochrysis* sp.

   - *D. tertiolecta* is a green marine microalgae that is widely used for toxicity testing while *Isochrysis* sp. is a brown marine microalgae that is used as feeds for molluscs and rotifers in aquacultures. They have been identified as common marine biofoulers [232, 234].

- Briefly, the microalgae cells were grown in 24 well microplates for up to 72 hours. Cell viability and proliferation were assessed daily using a ready-to-use reagent (PrestoBlue™). The reagent contains resazurin, a blue dye, which was quickly reduced by metabolically active cells to a highly fluorescent red colour. It provided a fast, quantitative measure of viability and cytotoxicity [283].

3.4.1 Materials

The list of organisms, chemical reagents and the instrumentations used for the biological evaluations are presented in Table 3.8, Table 3.9 and Table 3.10 respectively.

Table 3.8: Biological organisms used for antifouling evaluation.

Organisms / Cells	Species	Source
Marine Bacterium	*Halomonas pacifica* (Baumann et al.) Dobson and Franzmann (ATCC® 27122)	American Type Culture Collection (ATCC), USA
Marine Microalgae	*Dunaliella tertiolecta* (LB999)	Algae Culture Collection of University of Texas, Austin, USA (UTEX)
	Isochrysis sp. (CS177)	Algae Culture Collection of Commonwealth Scientific and Industrial Research Organization (CSIRO), Australia

Table 3.9: Chemical reagents used for antifouling evaluation.

Chemical Reagents	Manufacturer	Remarks
Acetic acid	Sigma-Aldrich, USA	Glacial acetic acid. Product number: A6283. CAS No. 64-19-7
Crystal violet solution, 1% aqueous	Sigma-Aldrich, USA	Crystal violet solution, 1% aqueous. Product number: V5265
DMSO	Sigma-Aldrich, USA	Dimethyl sulfoxide
Ethanol	Merck, Germany	Ethyl alcohol. EMSURE® grade. Catalogue number: 100974. CAS No. 64-17-5
PrestoBlue® cell viability reagent	Life Technologies, USA	-
Provasoli medium	-	Kindly provided by Dr. Yih-Yih Kok, International Medical University
Zobell Marine Broth	HiMedia Laboratories, India	-

Table 3.10: Instrumentation used for antifouling evaluation.

Instruments/Accessories	Manufacturer
24-well flat bottom, cell culture plate	Corning, USA
96-well FluoroNunc™ black plate microplate	Thermo Scientific, USA
96-well microplate, flat bottom, sterile with cover	Fischer Scientific, USA
Microplate reader, model Tecan Infinite® 200	Tecan, Switzerland
Monochromater plate reader, model SpectraMax® M3 Multi-mode Microplate Reader	Molecular Devices,

3.4.2   General Static Biofilm Inhibition Assay

H. pacifica was cultured in Zobell Marine Broth. An overnight culture of *H. pacifica* in marine broth was seeded into a 96-well plate at an optical density of 600

127

nm (OD_{600}) at a value of 0.01 in the presence or absence of silver nanocomposites of predetermined concentrations (0.001 mg/mL – 1.0 mg/mL). The bacteria were incubated under stationary conditions at 26 °C for 24 h, after which the medium was discarded and the plates were washed with water.

The wells were then stained with a 0.1% aqueous solution of crystal violet and allowed to stand at room temperature for 30 min. The stained bacteria on the biofilm were washed twice with water and the stain was solubilized with 30% acetic acid. The solubilized stain was transferred into a fresh microtiter plate. Biofilm inhibition was quantified by using a Tecan Infinite 200 microplate reader to measure the optical density at 570 nm (OD_{570}). A higher optical density reading correlated to a greater amount of biofilm mass attachment. All data was normalized against the untreated culture. Three replicate wells were used for each sample, in order to determine the mean and standard deviation values.

3.4.3   Evaluation of Growth Inhibition in Marine Microalgae

D. tertiolecta and *Isochrysis* sp. were cultivated in Provasoli medium and kept on illuminated shelves (42 μmol/m^2/s, 12:12 h light – dark cycle). For the toxicity testing, the algal inoculum was taken from an exponentially growing pre-culture, standardized at an optical density of 620 nm at a value of 0.4. Next, 200 μL of inoculums was inoculated into 1.8 mL of sterilized Provasoli medium in a 24-well plate. The concentration of silver nanocomposites tested was between 0.1-1 mg/mL.

The treated cultures were carried out in triplicates and cell viability was determined using PrestoBlue® (Life Technologies) within 72 h. At 0, 24, 48 and 72 h time points, 90 µL of algal cells were withdrawn and mixed with 10 µL of PrestoBlue® in a 96 Well FluoroNunc^{TM} black plate (Nunc) in triplicates. After 30 minutes of incubation in the dark, the fluorescent intensity was then measured using an excitation wavelength of 560 nm and an emission wavelength of 590 nm. All the fluorescence data were collected using a monochromater plate reader (Spectramax M3, Molecular Devices). Higher fluorescence measurements correlated to greater total metabolic activity.

Chapter 4: Silver-Polymer Nanocomposite Microspheres Using Ion-Exchange Resin as Templating Matrix

4.1   Introduction

Ion-exchange is a physical process of interchanging ions between a solid and a solution passing through the solid. Ion-exchangers are usually made of polymer resins or zeolites. These materials are extremely useful in water treatment, and have also been successfully applied in chemical synthesis, pharmaceutical research, food processing, mining and agriculture [284-286].

In this chapter, the discussion focuses on synthetic polymer ion-exchangers and its role as a templating matrix for the attachment of silver ions and their subsequent formation into AgNPs. The general principles of ion-exchange matrix synthesis are based on:

1) The nanoreactor effect. The polymer molecules act as a physical confinement for particle nucleation, resulting in a small particle size and narrow particle size distribution.

2) The barrier effect. The polymer molecules isolate the formation of each nanoparticle by preventing contact between individual nanoparticle surfaces and hence prevent aggregation [28].

4.1.1 Ion-Exchange Resins

Ion-exchange resins are porous and insoluble materials, available as a bead or gel. The resin used in this work is the strongly acidic cation-exchange resin beads Dowex™ 50WX8 (hydrogen form), containing sulphonic acid as the active functional group. The beads are specified as 200-400 mesh size in their MSDS, which is between 37-74 µm in diameter.

The ion-exchange mechanism is achieved as a result of the microstructure of the resin. The resin matrix consists of polystyrene main chains and divinylbenzene crosslinks, with negatively charged sulphonate (SO_3^-) groups distributed evenly, acting as fixed ions. To neutralize the charged matrix, a counter-ion of the opposite charge (H^+) is attached to the fixed ion. The immobilization of charged metal ions or complexes on ion-exchange sites occur through non-covalent electrostatic interactions [153]. The H^+ counter-ion is mobile and leaves the resin in the presence of another ion from the solution having a stronger affinity to the SO_3^- group.

The sulphonate groups are capable of attracting cations from solution, depending on the size and the charge of the cation. Generally, the exchange affinity increases with larger ion size and higher valence [153]. The affinity for common cations in dilute solutions is in the order:

$$Hg^{2+} < K^+ \approx NH_4^+ < Cd^{2+} < Cs^+ < Ag^+ < Mn^{2+} < Mg^{2+} < Zn^{2+} < Cu^{2+} < Ni^{2+} <$$
$$Co^{2+} < Ca^{2+} < Sr^{2+} < Pb^{2+} < Al^{3+} < Fe^{3+} \text{ [287]}.$$
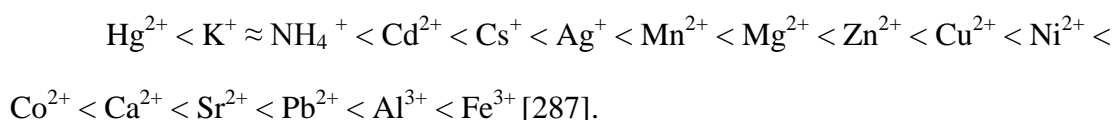
Figure 4.1 schematically shows the microstructure of the cation-exchange bead and its associated fixed sulphonate group (SO_3^-) and the mobile protonated counter-ions (H^+). The porous nature of the polymer matrix increases the availability of active exchange sites [284].

FIXED NEGATIVELY CHARGED EXCHANGE SITE, i.e., SO_3^-

MOBILE, POSITIVELY CHARGED, EXCHANGEABLE CATION, i.e., Na^+

POLYSTYRENE CHAIN

DIVINYLBENZENE CROSS-LINK

WATER OF HYDRATION
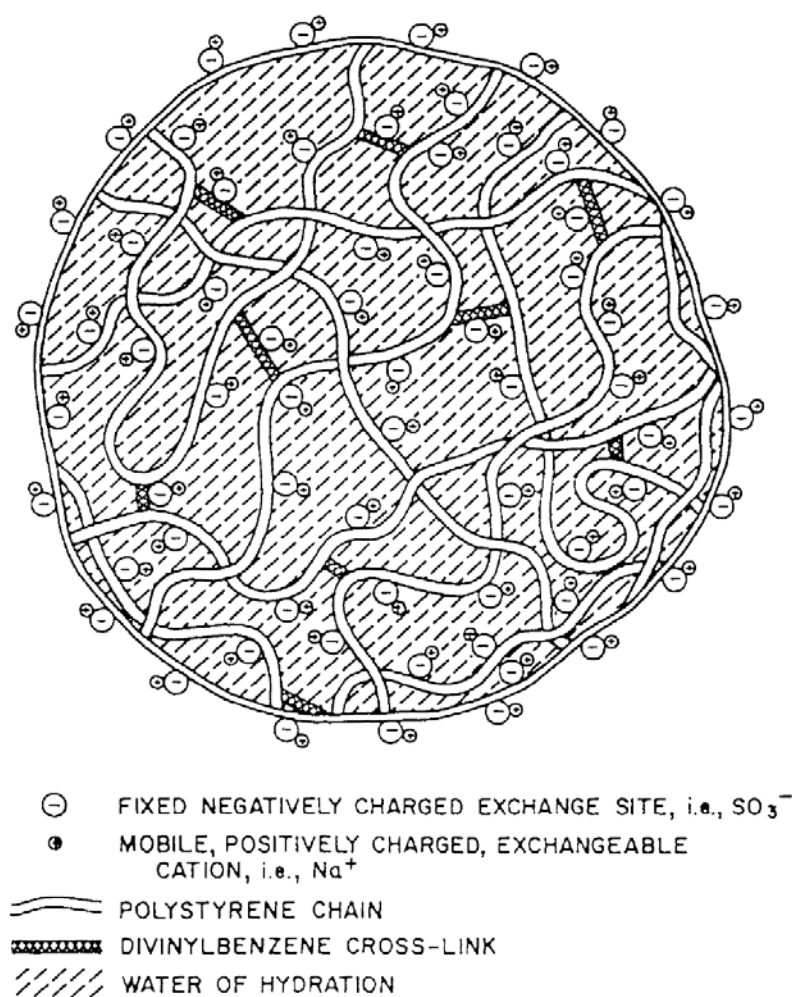
Figure 4.1: Expanded representation of the ion-exchange bead. Figure taken from [287].

4.1.2   Ion-Exchange Resins for *in-situ* Silver Nanoparticle Synthesis

The potency of AgNPs as antimicrobials has been discussed in detail in Chapter 2. However, AgNPs are prone to agglomeration due to their high ratio of surface area-to-volume [288]. Agglomerated AgNPs reduce the availability of active surface areas for bacteria, and hence diminish its antimicrobial efficiency. The presence of polymeric stabilizers is required to prevent agglomeration of nanoparticles through either electrostatic or steric stabilization. Therefore, the development of polymer-stabilized metal nanoparticles is one of the most promising strategies to prepare stable metallic nanoparticles [28].

Several strategies involving polymeric materials have been developed to synthesize and maintain the nanostructure of AgNPs including their immobilization on polymer substrates [33, 52, 63, 139] and dispersion in a colloidal polymeric matrix [59, 289, 290]. In addition, several methods to prepare polymer/silver nanocomposite microspheres were reported previously. These include the suspension polymerization of poly(vinyl acetate) in the presence of AgNPs [152], crosslinkers of AgNPs coated with 4-mercaptomethylstyrene [128] and polystyrene-core/polyacrylic acid brush/Ag [79]. However, the complex polymerization synthetic procedures of these methods, variation in Ag nanoparticle size range, high cost and low yield remain a challenge to their production on the industrial scale.

In this respect, ion-exchange resins emerge as a highly-accessible and facile template for the *in-situ* synthesis of metal and metal oxide nanoparticles [288]. Several synthetic routes of ion-exchange resins were described previously including

reaction of styrene and divinylbenzene monomers via a surfactant reverse micelles swelling method [154] or by conventional radical suspension polymerization method [155]. In the present study, we sought to develop a system to synthesize highly dispersed AgNPs with narrow size distributions on the surface of commercially available Dowex™ ion-exchange resin for anti-microfouling applications.

4.1.3 Rationale of Study

There are 3 important reasons for the use of the Dowex microspheres in the preparation of the Ag-polymer nanocomposite (Ag-PNC) materials:

1) As a template to produce nanostructured Ag particles, and to prevent agglomeration of AgNPs. Nanostructured Ag has been reported to have improved antimicrobial properties compared to bulk Ag [50, 291, 292].

2) As a supporting matrix to immobilize AgNPs on the surface of the nanocomposite in order to provide greater bioavailability for antifouling function.

3) To facilitate a high yield and low cost method of producing the Ag-PNC, appropriate for industrial scale manufacturing and to fulfil the quantitative requirements for antifouling technology applications.

Other advantages of using ion-exchange matrix resins involve their easy recovery by simple filtration or decantation, due to their micron-size and specific

shapes. Their size and shape also ensures ease of handling. Furthermore, the resins have negligible levels of metal leaching and are compatible with water and other reaction solvents [153].

4.1.4   Synthesis Parameters

Solutions of silver nitrate and sodium borohydride in various concentrations were used as varying parameters in the synthesis of Ag-PNCs at room temperature. A fixed amount of ion exchange microbeads was used in each experiment. The use of sodium borohydride as the reducing agent is due to its strong reducing capability especially at low to room temperatures to convert silver ions into metallic Ag. This is especially important in order to achieve rapid synthesis of the Ag-PNC without subjecting it to heat treatment. Further details of the synthesis have been discussed in Section 3.2.1.

4.2   Synthesis of Silver-Polymer Nanocomposite (Ag-PNC)

The synthesis of silver-polymer nanocomposite (Ag-PNC) beads was carried out in two steps as shown in Figure 4.2. In the first step, protonated (H^+) ion exchange copolymer resin beads were stirred with silver nitrate solution to form an intermediate Ag^+-copolymer bead. The ion exchange resin bead is composed of multiple polystyrene chains bound together by divinylbenzene crosslinks. The fixed, negatively-charged SO_3^- exchange sites are distributed across the surface of the beads,

while mobile, positively-charged H^+ are ionically bound to the SO_3^- sites. However, the SO_3^- has a greater affinity for larger cations, such as Ag^+ [293]. The affinity series of sulphonic acid ion exchange resins for cations varies with the ionic size and charge of the cations. For cations with similar charges, the affinity increases with the atomic number of the cation [293]. During the ion exchange process, the reaction proceeds to the right (Equation 4.1), to generate Ag^+-resin, until the exchange capacity of the resin nears exhaustion. In the second step, sodium borohydride was used to chemically reduce the Ag ions *in-situ* to form metallic Ag (Equation 4.2).

$$H^+\text{-resin} + Ag^+ \rightleftarrows Ag^+\text{-resin} + H^+$$

.... Equation 4.1

$$Ag^+\text{-resin} + NaBH_4 \rightarrow Ag\text{-resin} + \tfrac{1}{2}H_2 + \tfrac{1}{2}B_2H_6 + Na^+$$
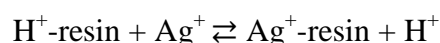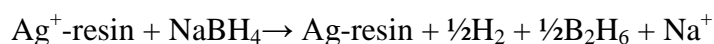
…. Equation 4.2

Alonso et al. [294] have proposed an alternative pathway for the chemical reduction involving the ion-exchanged resin in the formation of AgNPs. The ion exchange resin is regenerated to its original form after the reduction process, whilst the metallic Ag is produced and physisorbed on the surface of the microbeads, according to Equation 4.3 and Equation 4.4.

$$R\text{-}SO_3^-H^+ + AgNO_3 \rightleftarrows R\text{-}SO_3^-Ag^+ + HNO_3$$

…. Equation 4.3

$$R\text{-}SO_3^-Ag^+ + HNO_3 + NaBH_4 + 3H_2O \rightarrow R\text{-}SO_3^-H^+ + 7/2H_2 + B(OH)_3 + NaNO_3 + Ag^0$$
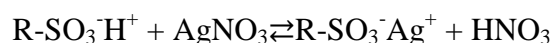
…. Equation 4.4

Equation 4.4 is the sum of the following reactions in Equation 4.5 and Equation 4.6:

$$\text{R-SO}_3^-\text{Ag}^+ + \text{HNO}_3 + \text{Na}^+ \rightarrow \text{R-SO}_3^-\text{H}^+ + \text{NaNO}_3 + \text{Ag}^+$$

…. Equation 4.5

$$\text{Ag}^+ + \text{BH}_4^- + 3\text{H}_2\text{O} \rightarrow 7/2\ \text{H}_2 + \text{B(OH)}_3 + \text{Ag}^0$$
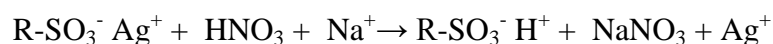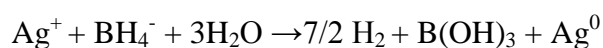
…. Equation 4.6

A deeper look in the second stage reveals that the AgNPs formation (Equation 4.4) is a combination of an ion-exchange reaction and a reduction reaction. The reduction of the Ag^+ ion to zero-valent Ag takes place in the solution boundary, close to the sulphonate exchange site [28].

In the synthesis of AgNPs using cation-exchange resins, it should be noted that the resin matrix and the reducing agent both bear the same charge. Essentially, an electrostatic repulsion exists between the sulphonate groups in the matrix and the reducing species BH_4^-. This prevents the reducing species from penetrating deeper within the polymer matrix. The exclusion of BH_4^- species from penetrating deeply inside the polymer is due to the Donnan-exclusion effect. Consequently, formation of AgNPs is mainly near the surface of the polymer bead.
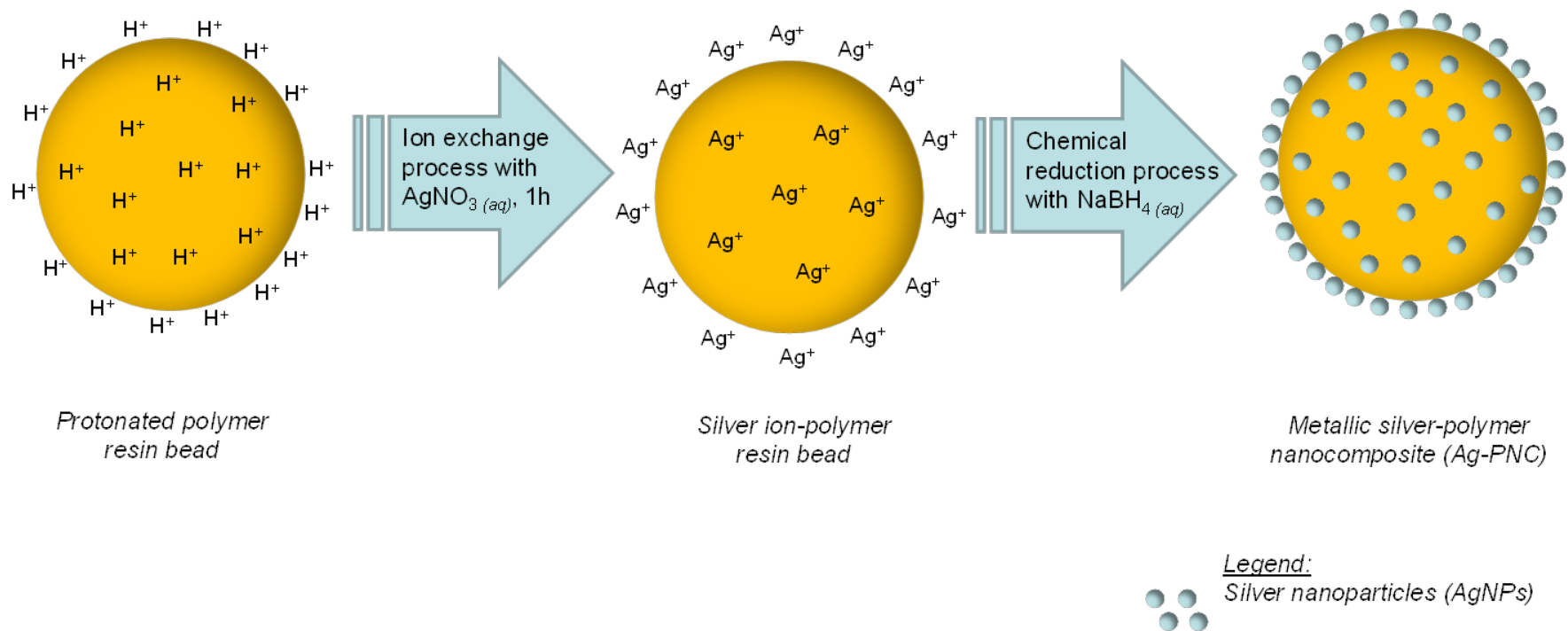
Figure 4.2: Schematic representation of the formation of metallic silver-polymer nanocomposite (Ag-PNC) bead.

4.3   Morphology and Chemical Content of Ag-PNCs

The ion-exchange resin appeared as microspheres with a smooth surface when viewed under scanning electron microscope (SEM) (Figure 4.3). The majority of the beads fall within the 50-89 µm diameter size range, with an average diameter of 69.96 ±12.59 µm. This value falls within the expected upper size limit of the resins of 74 µm according to the material's MSDS.

To quantitate the amount of Ag loaded on the surface of the Ag-PNC materials, the elemental analysis was conducted using the EDX method. As shown in Table 4.1, the Ag content of the nanocomposites increases with increasing concentration of reactants, consistent with Equation 4.2 and Equation 4.4. The maximum loading reached saturation at 66.8 wt% Ag, and further increment in the amounts of Ag precursor did not yield further loading on the resins.
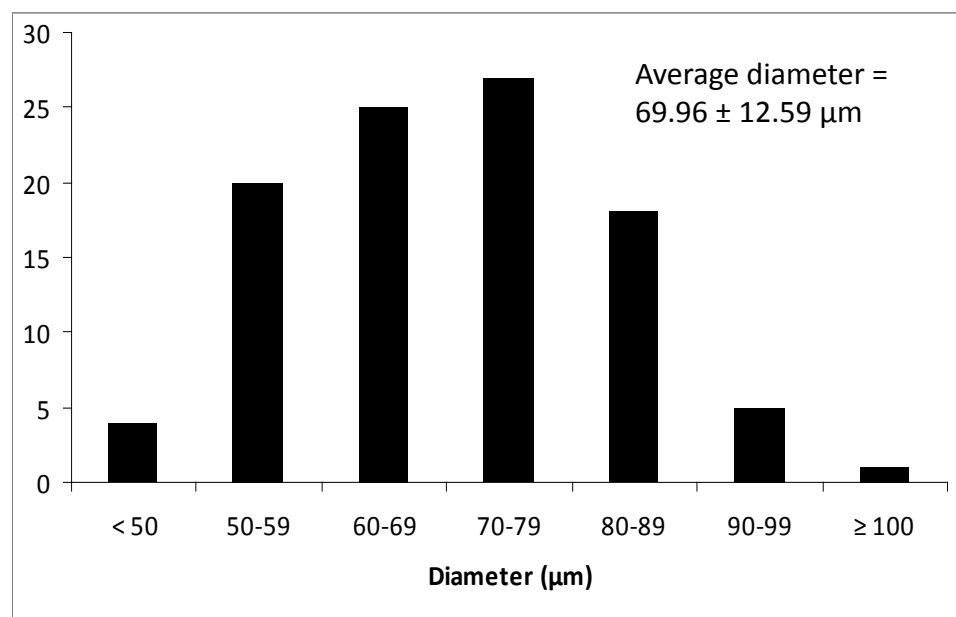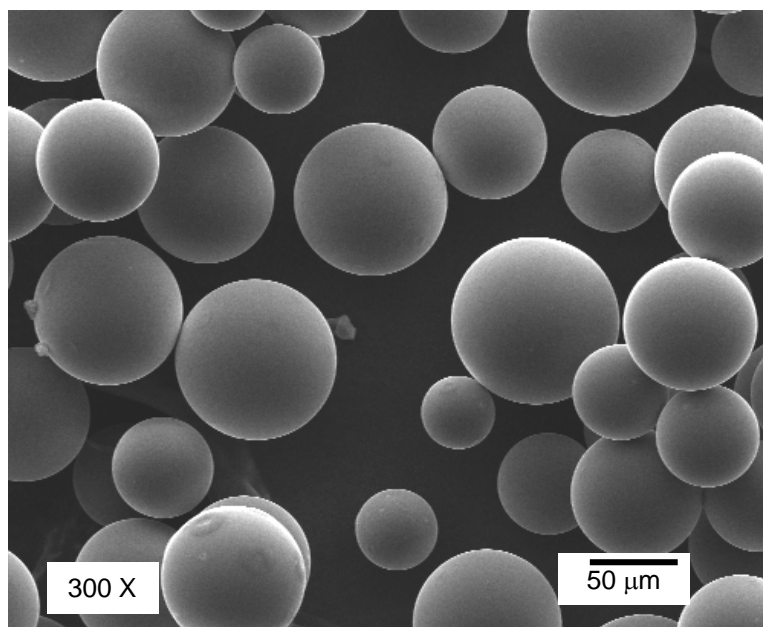
Figure 4.3: SEM micrograph of the ion-exchange copolymer resin prior to ion exchange, and their size distribution. The average diameter of the polymer microspheres was determined by measuring the diameters of 100 individual microspheres under scanning electron microscopy. Data represents mean ± standard deviation.

Table 4.1: Summary of the physical characteristics of Ag-PNC prepared with various concentrations of the silver precursor. The ratio of the $Ag^+:BH_4^-$ is fixed at 1:2 for optimal reduction stoichiometry.

Samples	AgNO₃ concentration (M)	NaBH₄ concentration (M)	Ag content (wt%)	λ_{max}[a] (nm)	AgNPs diameter[b] (nm)
Ag-PNC-1	0.001	0.002	0.19	-	-
Ag-PNC-2	0.01	0.02	1.24	-	20.2 ± 6.5
Ag-PNC-3	0.1	0.2	9.20	406.1	24.5 ± 6.5
Ag-PNC-4	1.0	2.0	66.8	422.0	60.17 ± 41.1

Notes:
[a] λ_{max} is the maximum absorption wavelength when subjected to ultraviolet-visible wavelengths. [b] The size of AgNPs was determined by measuring the diameters of 100 nanoparticles under scanning electron microscopy. Data represents mean $\pm$ standard deviation.

Further analysis using SEM revealed a progressive increase of the Ag loaded on the surface of the resins with concordant increment in the size of the AgNPs being formed (Figure 4.4 and Table 4.1). Importantly, the shape and structure of the polymer resin beads were retained after the ion exchange and chemical reduction processes, suggesting that the copolymer matrix is suitable for use as a stable template for the formation of metallic Ag nanocomposites (Figure 4.4).

In Ag-PNC-1 (Figure 4.4 A), the presence of the AgNPs on the surfaces of the beads was hardly observed, mainly due to the low concentration of Ag precursor. The appearance of uniformly dispersed, discrete, and spherical AgNPs was detected on the surface of Ag-PNC-2 and Ag-PNC-3 (Figure 4.4 B – C). As for Ag-PNC-4, large Ag precipitates were found scattered uniformly, overlapping smaller AgNPs covering the

surface of the polymer bead (Figure 4.4 D). The fixed amount of SO_3^- negatively

charged surface of the ion-exchange resin limits the Ag ions uptake.

In addition, due to the Donnan exclusion principle, the tetrahydroborate ion

(BH_4^-) has a similar negative charge as the sulphonate functional group in the resin,

therefore, preventing its incursion deeper into the polymer bead's centre [28]. Hence,

metallic Ag is formed mostly on the surface of the bead. The excess amount of Ag

precursor used in the preparation of Ag-PNC-4 seemed to inundate the available

surface area on the polymer resin, resulting in the bead surface being covered with a

thick layer of metallic Ag. Furthermore, excess Ag ions in solution were chemically

reduced without an anchoring matrix, resulting in excess free metallic Ag (Figure 4.4

D).
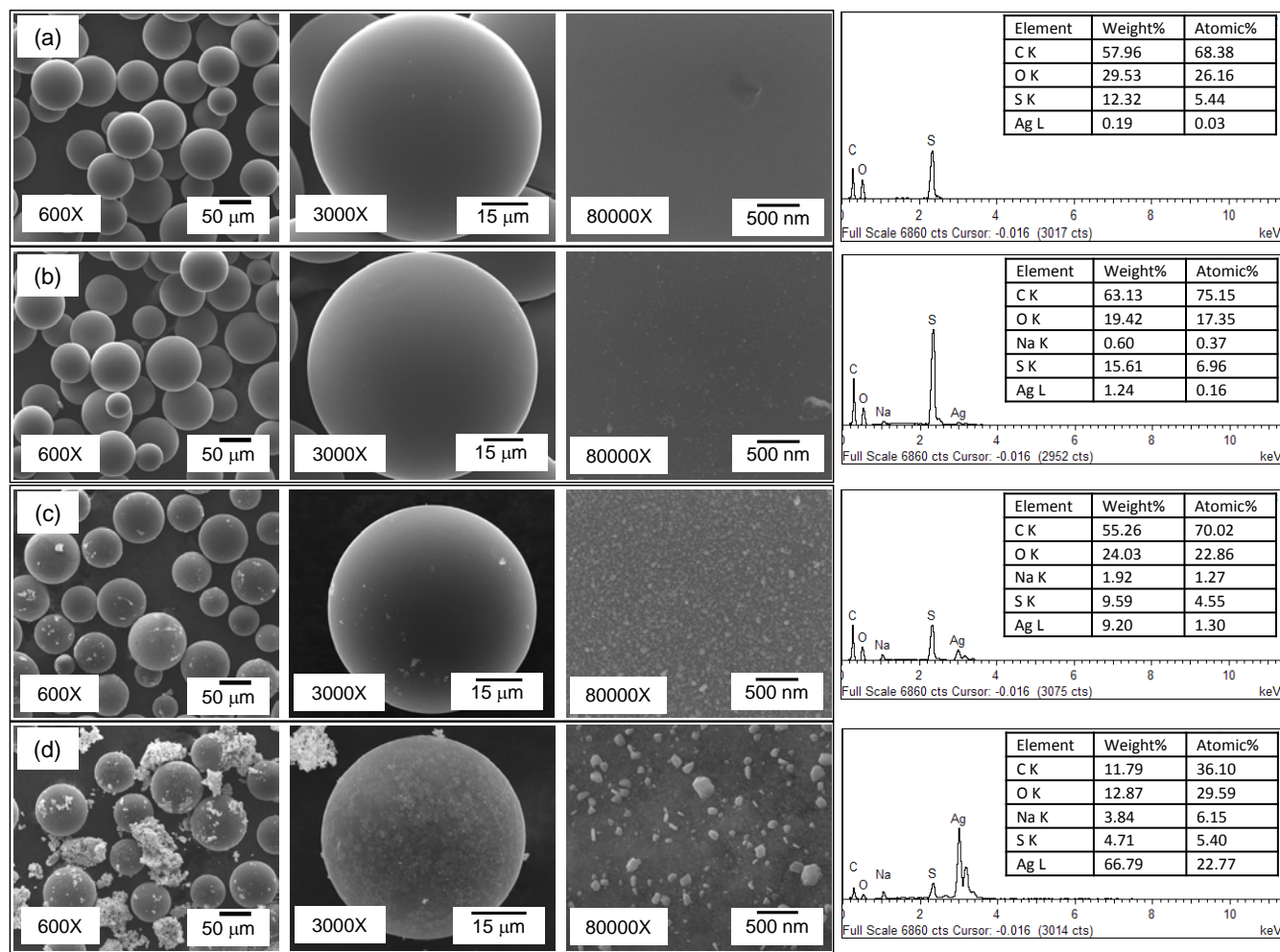
Figure 4.4: SEM micrographs and the corresponding EDX spectra of the Ag-PNC samples prepared with various concentrations of silver precursor solution. (A) Ag-PNC-1 (0.001 M), (B) Ag-PNC-2 (0.01 M), (C) Ag-PNC-3 (0. 1 M), and (D) Ag-PNC-4 (1.0 M).

4.4 Optical Properties of Ag-PNCs

For rapid detection of AgNPs formation, UV-visible spectrophotometry was performed. During the chemical synthesis of colloidal Ag, the coalescence of Ag atoms to form larger particles gives rise to surface plasmon resonance (SPR) of conduction electrons on the surface of AgNPs. For colloidal Ag, a strong absorption peak near 400 nm is observed in the UV-visible spectrum [108], while the full width at half maximum (FWHM) can be used to determine particle size and shape distribution [295].

As shown in Figure 4.5, Ag-PNC-3 displayed the characteristic AgNPs maximum absorption peak at 406.1 nm, confirming the formation of AgNPs, while the narrow absorption peak has an FWHM of approximately 80 nm. A red-shift of the maximum absorption wavelength to 422 nm, accompanied by a broadening of the absorption peak was observed for Ag-PNC-4. Red shifting signifies an increase in the particle size of the AgNPs [295]. The agglomeration of AgNPs in Ag-PNC-4 was clearly seen under scanning electron microscopy, as illustrated in Figure 4.4(d); the interaction between the nanoparticles causes a damping of the surface plasmon absorption [296]. The FWHM for Ag-PNC-4 of approximately 100 nm indicates the production of polydisperse AgNPs [295].

On the other hand, Ag-PNC-1 and Ag-PNC-2 did not exhibit a similar AgNPs absorption peak. As Ag-PNC-1 and Ag-PNC-2 were formed from lower concentrations of silver precursor, the absence of plasmon resonance maximum could be attributed to the small amount of AgNPs formed and thus the absorption was

144

hindered by the polymer bead. This was confirmed by the very low amounts of Ag that were detected by EDX in these two samples, as shown in Table 4.1.
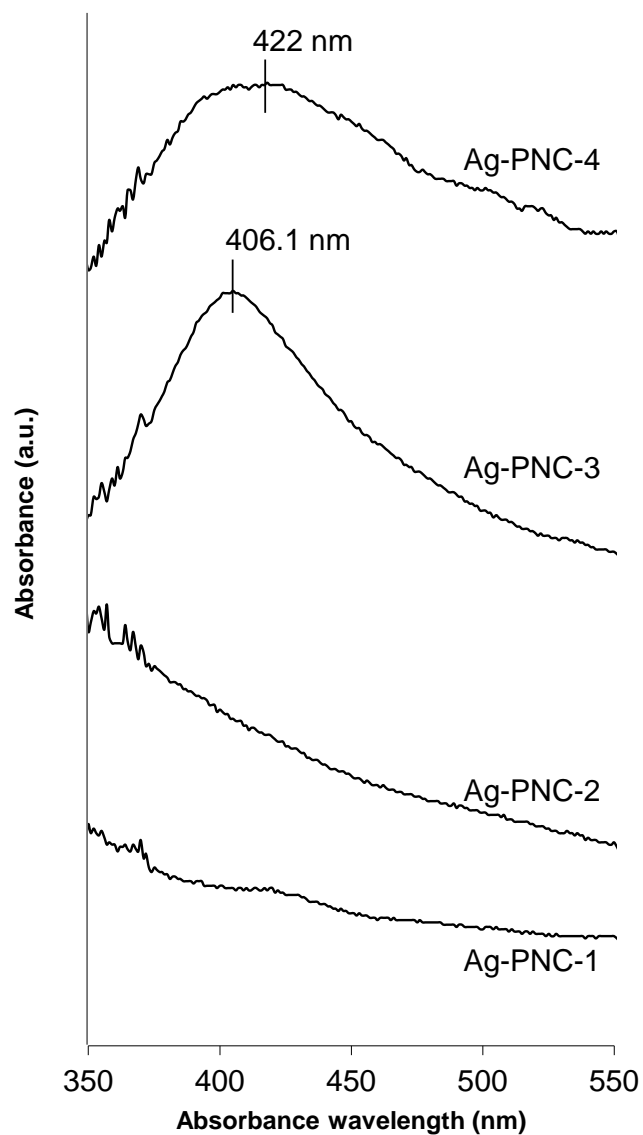
Figure 4.5: UV-visible absorption spectra of Ag-PNC dispersed in water.

4.5 Crystallinity of Ag-PNCs

The crystallinity of the Ag-PNCs was analysed using X-ray diffraction (XRD). The XRD patterns of all Ag-PNCs are shown in Figure 4.6. The Ag-PNC-1 and Ag-PNC-2 with the lowest Ag loading of 0.19 wt% Ag and 1.24 wt% Ag, respectively, does not exhibit any crystalline peaks, due to the high polymeric content of the ion exchange resin.

The broad humps between angle 2θ of $10°$ to $35°$ are attributed to the amorphous structure of the styrene divinylbenzene copolymer [288]. With higher Ag content in Ag-PNC-3 (9.20 wt%), the XRD pattern shows Bragg reflections with maximum at $2\theta = 38.1°$, $44.3°$, $64.4°$ and $77.4°$ amidst an amorphous background. With Ag content increased to 66.8 wt% in the Ag-PNC-4, the intensity of the four diffraction peaks increased, with the first two peaks having particularly large increases.

These four peaks correspond to the (111), (002), (022), and (113) reflections of the face-centred cubic (FCC) structure of metallic silver (ICDD reference pattern: 98-005-0882). In addition, the amorphous spectra of the polymer matrix were not detected in Ag-PNC-4, indicating that the surface of the composite consists entirely of highly crystalline Ag nanomaterial.
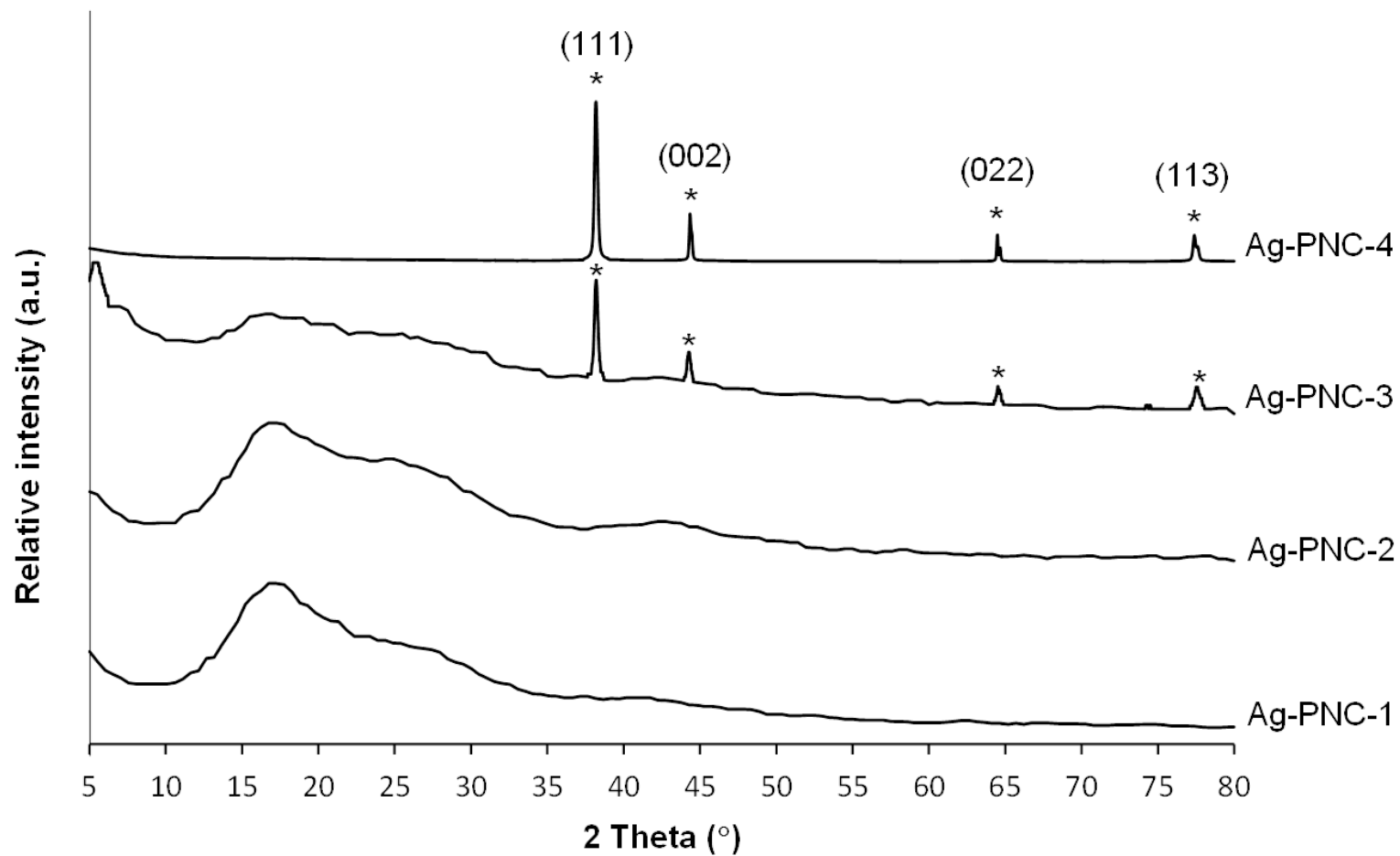
Figure 4.6: XRD spectra of the Ag-PNCs prepared with various concentrations of silver precursor. [*] represents the metallic silver phase (98-005-0882), ICDD reference pattern for Ag.

4.6   Thermal Properties of Ag-PNCs

The thermogravimetric mass losses of the Ag-PNCs are shown in Figure 4.7(a). The full TGA and the corresponding DTG curves of the polymeric ion exchange resin and the Ag-PNCs are provided in the Appendix. From 50°C onwards, the loss of absorbed water molecules (hydration) from the resin is clearly noted up to approximately 170°C. A significant mass loss of approximately 17 – 18% was observed for Ag-PNC-1 and Ag-PNC-2, similar to pure polymer resin. Nevertheless, a smaller weight loss of 12% was observed in Ag-PNC-3, while a mere 5% weight loss was noticed for Ag-PNC-4 in the same temperature range. The major degradation for the resin occurs around 300 °C, and the degradation process results in char formation at around 415 °C with weight loss of approximately 50%. The inclusion of Ag in Ag-PNCs results in a shifting of the degradation temperature up to 350 °C for Ag-PNC-3. Meanwhile, the thermal stability of Ag-PNC-4 sample is improved significantly since only a small fraction of the sample (~ 15%) were degraded up to 460°C before the resin started to decompose.

The copolymer resins were reported to have glass transition temperatures of between 99 – 129°C, depending on the degree of crosslinking of up to 15% with divinylbenzene [155]. Although the glass transition temperature is usually determined at the midpoint of the endothermic displacement between linear baselines [155], the T_g can also be estimated at the minimum point of the first endothermic displacement [128]. Figure 4.7(b) shows the glass transition temperature (T_g) of the pure resin and Ag-PNCs, as measured from differential scanning calorimetry (DSC). The resin had a T_g of 130°C, while a slight increase in glass transition temperature was observed in

Ag-PNC-2 (T_g = 149°C). The T_g of Ag-PNC-4 is further shifted to 323°C, indicating the increasingly crystalline nature of the composite microbeads.

Improved thermal stability is noted for samples with higher Ag content. Metallic Ag has higher thermal stability compared to the polymer matrix. In addition, the increase of T_g is attributed to the presence of AgNPs between the polymeric chains, which act as a barrier to inhibit their thermal rotation and relaxation of the polymer chains during TGA/DSC studies. As a result, more energy is required to cause the thermal relaxation of the polymer chains, and cold crystallization (rearrangement of polymer chains from an amorphous structure to a more crystalline structure), leading to an increase in the glass transition temperature and subsequently to decompose the samples [128, 297].
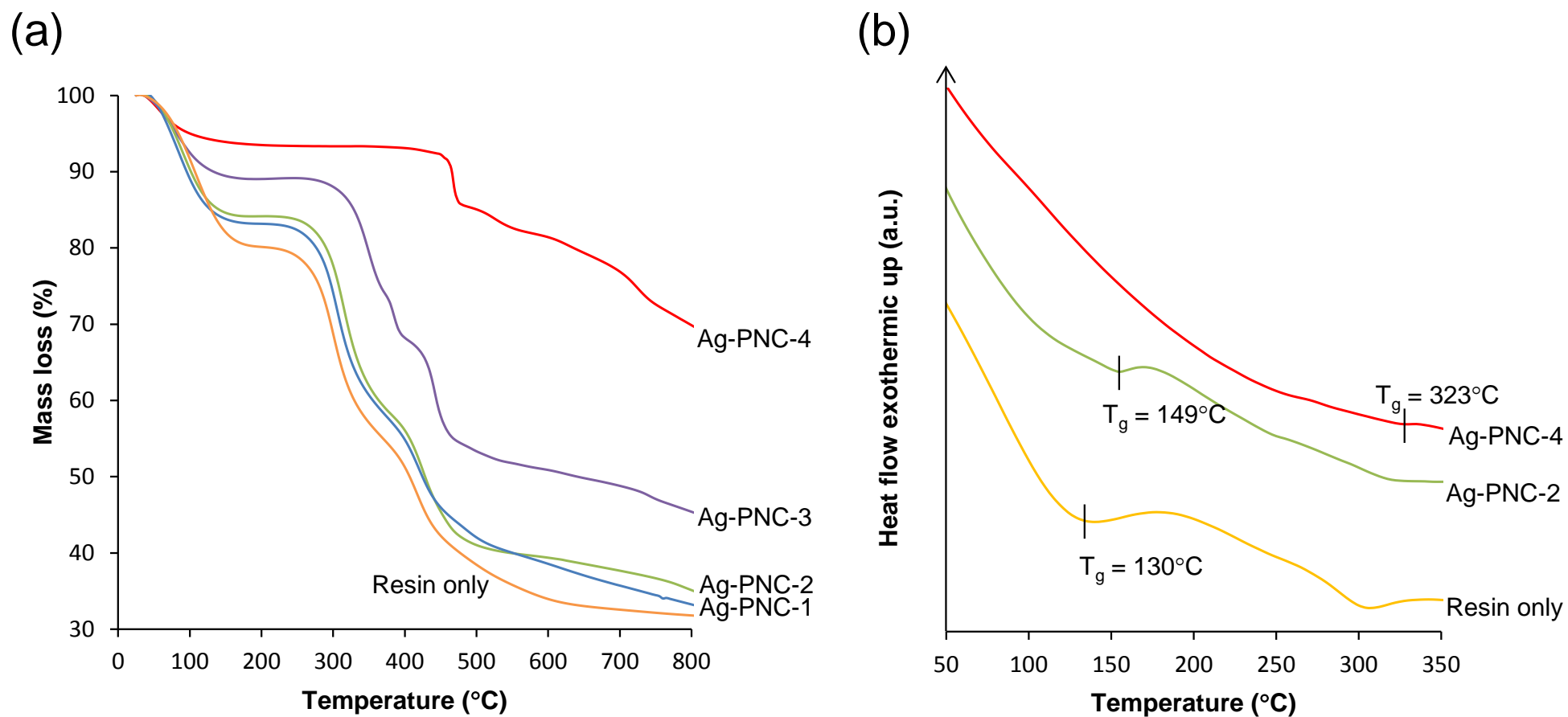
Figure 4.7: Thermal properties of the Ag-PNCs. (a) Thermogravimetric mass loss for styrene divinylbenzene resin and Ag-PNC composite materials, and (b) DSC thermograms of styrene-divinylbenzene copolymer and Ag-PNC microbeads with various Ag content.

4.7   Anti-Microfouling Properties of Ag-PNCs

The formation of a bacterial biofilm is an early stage of a multi-step marine biofouling process, culminating in the attachment and growth of algae and invertebrates on immersed surfaces [231]. It has been shown that invertebrate accumulation will not readily occur if a biofilm does not form on a ship's hull [298].

To test the anti-microfouling effects of Ag-PNCs, a static biofilm assay was carried out using *H. pacifica*. As shown in Figure 4.8, Ag-PNC materials inhibit the attachment of biofilm from *H. pacifica* after an incubation period of 24 hours. In particular, Ag-PNC-3 and Ag-PNC-4 show a potent inhibitory effect on *H. pacifica* biofilm formation, with an average inhibition of $18.59 \pm 2.39\%$ and $76.08 \pm 3.93\%$, respectively ($P < 0.01$, Student's *t*-test).

In contrast, no such effect was observed in bacteria incubated with Dowex resin microbeads alone. Notably, the efficacy of biofilm inhibition correlated directly with the amounts of Ag loading, suggesting that the polymeric Dowex template promote the anti-microfouling properties of the Ag-PNC material by providing a template for nanosized biocidal AgNPs.

Generally, smaller Ag particles are reported to have higher antibacterial properties [299], due to higher active surface area. Nevertheless, in this study, the Ag content appears to be the more important determining factor for antifouling behaviour. As the Ag content within the Ag-PNC is increased, there will be more contact between the Ag nanomaterials with *H. pacifica*, hence leading to more significant

inhibition of biofilm formation. Whether or not the anti-biofilm activity of Ag-PNCs is due to the bactericidal effect of AgNPs on the surface of the Ag-PNCs remains to be investigated further.

Generally, the antibacterial property of nanosilver produces a more adverse effect on Gram-negative bacteria such as *H. pacifica*, by diffusing into the bacterial cell through their thinner peptidoglycan cell walls [300]. It is likely that the AgNPs might become biologically activated in an aqueous medium and interact with structural proteins such as bacteria cell walls to cause lysis [59]. Furthermore, AgNPs penetrate the bacterial cell and preferentially bind with DNA bases to inhibit replication [301]. Hence, the disruption on the biofilm formation will inhibit the subsequent attachment of sessile organisms and distort the progressive fouling process [228, 263].
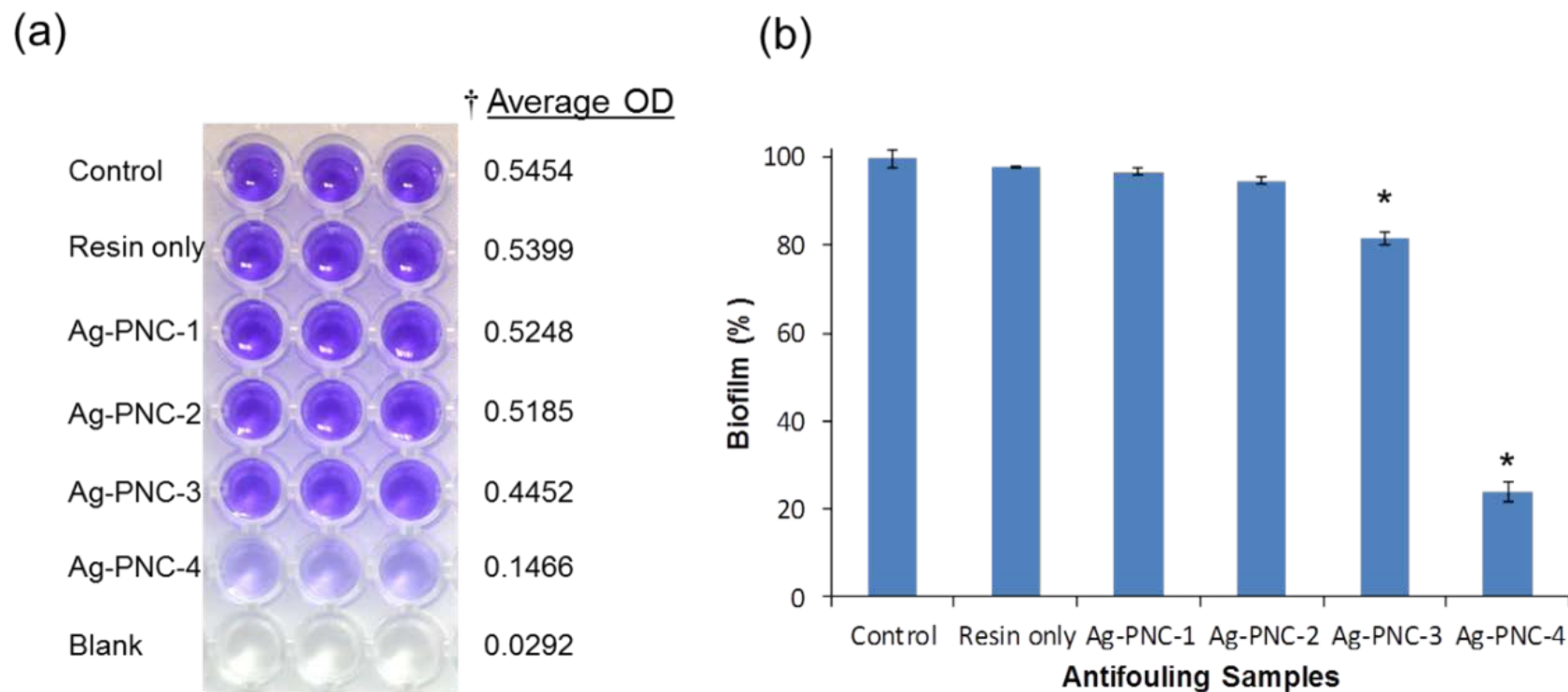
Figure 4.8: Ag-PNC materials inhibit the attachment of biofilm from *H. pacifica.* (a) Anti-biofilm activity of Ag-PNC at 1mg/ml. †indicates the average OD measured at 570 nm, and (b) inhibition of *H. pacifica* bacteria biofilm attachment by Ag-PNCs. The readings were compared with a control (containing bacteria in culture medium, without the presence of nanocomposites) and a blank (containing culture medium only). The blank reading was subtracted from the readings from each well. All data were normalized against the untreated culture. Bars represent mean ± s.d. of 3 independent experiments. * indicates statistical significance compared to control (P < 0.01, Student's *t*-test).

The effect of Ag-PNCs on marine microalgae was also investigated through a growth inhibition assay. As shown in Figure 4.9, 1 mg/ml induced significant growth inhibition in two different species of microalgae, *D. tertiolecta* and *Isochrysis* sp. while no such effect was observed in microalgae treated with the resin alone. Upon observation under light microscopy, no significant morphological changes was observed in *D. tertiolecta* and *Isochrysis* sp. exposed to Ag-PNC-4, suggesting that the biological effects of Ag-PNC-4 is likely to be cytostatic rather than cytotoxic (Figure 4.10).

It is tempting to speculate that contact inhibition might be the predominant mechanism of Ag-PNCs' induced cytostatic effect of the microalgae cells. As such, future efforts to prepare environmentally-friendly surfaces through direct deposition of Ag-PNC coatings that could persist for long-term usage warrant further investigations.
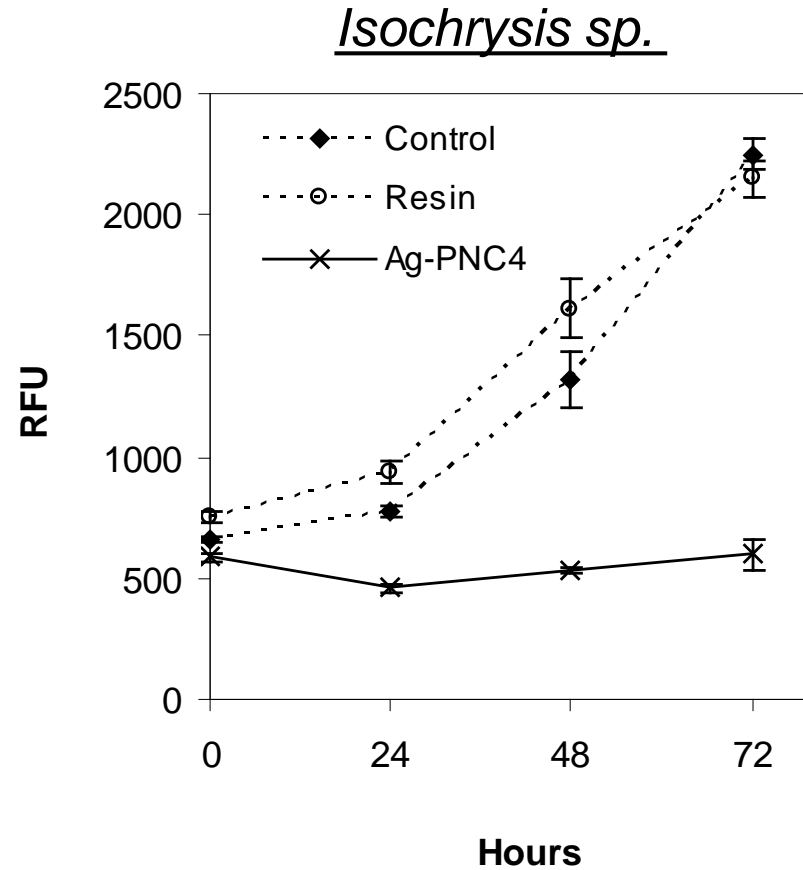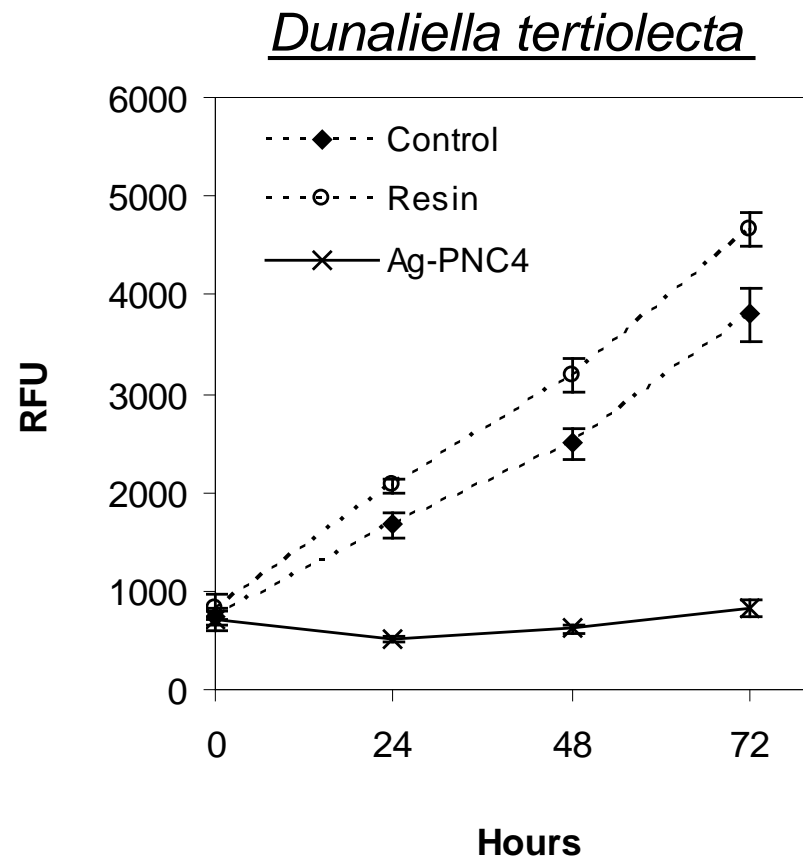
Figure 4.9: Cytostatic effects of Ag-PNC-4 on marine microalgae. Cells were exposed to 1 mg/ml of resin or Ag-PNC-4 for 72 h. Number of cells at 0, 24, 48, and 72 h after treatment were determined using PrestoBlue® staining and fluorescence microscopy (Ex 560 nm/Em 590 nm). Points represent mean ± s.d. of at least three independent experiments.
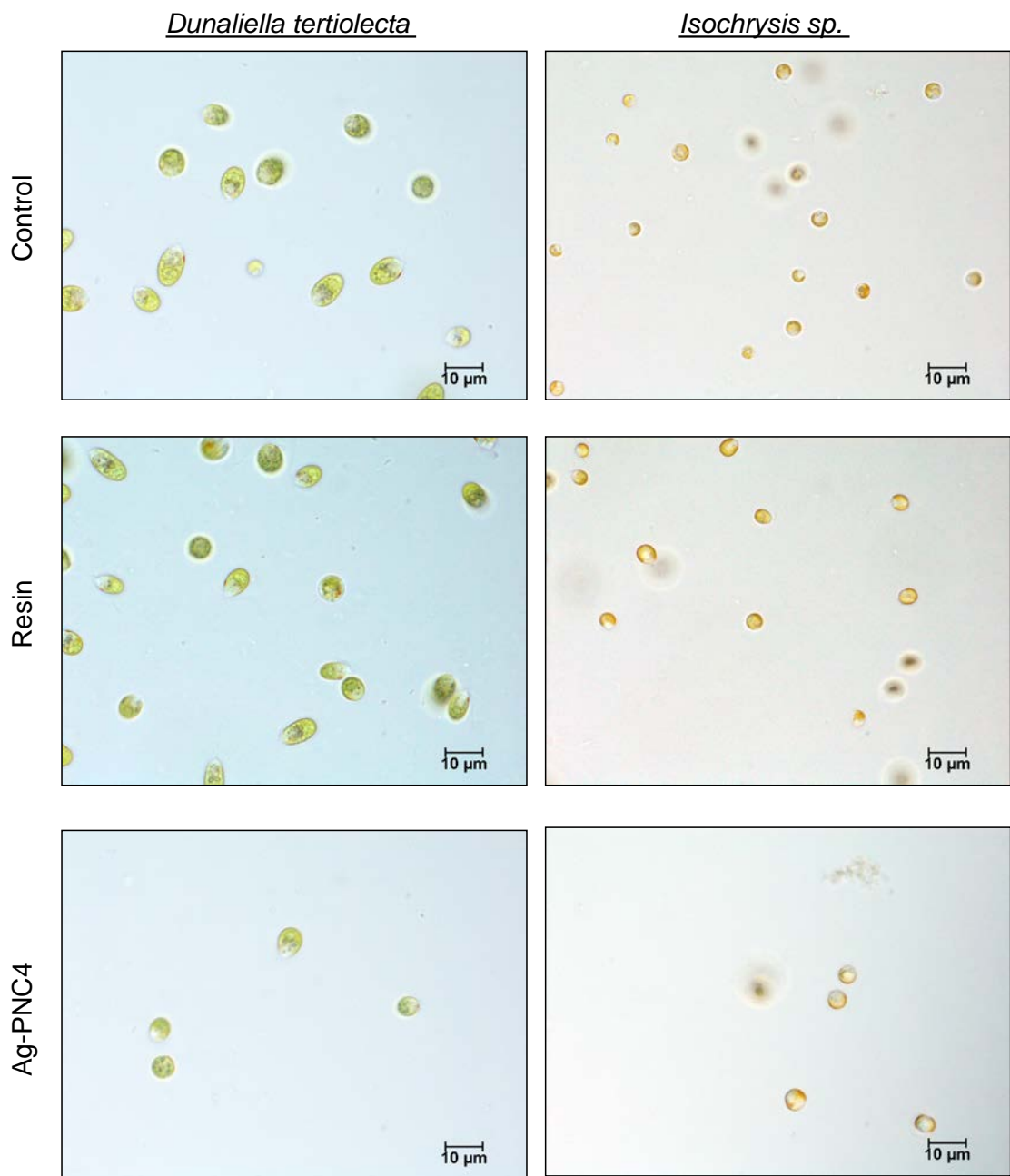
Figure 4.10: Morphology of *D. tertiolecta* and *Isochrysis* sp. following exposure to 1 mg/mL resin or Ag-PNC-4 for 72 hours.

4.8   Summary

Ag-polymer nanocomposite materials were successfully synthesized using an ion-exchange and reduction process occurring *in-situ* on the surface of an ion-exchange polymer bead. The nanocomposite displayed promising anti-microfouling behaviour, as it interferes with the biofilm formation that often precedes macrofouling processes. Previous studies using metallic antifouling agents have focussed on zinc [232] and Cu^{2+} cations [266] as antifouling agents in polymeric matrix. The challenge organisms included hard macrofoulers and microalgae [232], as well as months' long immersion in seawater [266]. This is the first attempt to synthesize Ag containing polymeric materials using a rapid ion exchange process from the microbead resin [302]. This technique is attractive due to its relative simplicity in comparison with other methods of producing polymer-stabilized metal nanoparticles. The polymer ion-exchange microspheres act as a supporting matrix for the immobilization as well as a template for the formation of nanostructured antimicrofouling Ag particles on the polymeric surface.

The amount of metallic Ag loading is relatively high, up to over 60 wt% Ag, using the borohydride reduction method. In addition, physical characterization methods show that nanosized metallic Ag is successfully precipitated on the surface of the polymer microbead, leading to the formation of a stable Ag-polymer nanocomposite. The polymeric microbead serves as a physicochemical anchor for Ag ions to attach to, and subsequently provides a stable matrix for the formation of metallic Ag in nanometre dimensions. This helps to control Ag particle growth and agglomeration.

The processing method and introduction of Ag to the polymer microbead improves the thermal properties of the copolymer by increasing the glass transition temperature and thermal stability of the nanocomposite material. The Ag-PNC material becomes more crystalline with the incorporation of the metallic Ag phase.

The use of cation-exchange polymers coupled with the Donnan effect results in the formation of stabilized AgNPs near the surface of the polymer. The distribution of AgNPs on the polymer surface is favourable for anti-microfouling applications by increasing the effective contact area with the fouling bacteria. The Ag-PNC material is found to be able to effectively inhibit the biofilm formation of *H. pacifica* by up to 76%, as well as cause growth inhibition in marine microalgae *D. tertiolecta* and *Isochrysis sp.*, signifying its anti-microfouling property. These results strongly suggest that Ag-PNCs are promising anti-microfouling agents which warrant further studies in future affordable antifouling technologies.

Chapter 5: Silver-Zeolite Nanocomposite Clusters through A Green and Rapid Solution Growth

5.1 Introduction

Zeolites are a group of mesoporous solids, consisting of hydrated aluminosilicate minerals containing alkali and alkaline-earth metals. Mesoporous materials are classified as having pore diameters between 2-50 nm [303]. Similar to the ion-exchange resins discussed in Chapter 4, zeolites are a class of ion exchangers as well. Specifically, they are used as cation exchangers. This is due to the molecular dimensions of the stable network of hollow channels and pores within the zeolite structure, which are used to selectively sort molecules or cations based on a size exclusion process [157, 304]. Although zeolites occur naturally, artificially synthesized zeolites are preferred for their consistent purity, and are regularly used in industrial applications as catalysts, adsorbents and molecular sieves.

5.1.1 Zeolite ZSM-5

The Zeolite Socony Mobil-5 (ZSM-5) is used in this work. It is a synthetic zeolite belonging to the pentasilicate (pentasil) family, with a chemical formula of $Na_nAl_nSi_{96-n}O_{192} \cdot 16H_2O$ (0<n<27). Patented by the Mobil Oil Company in 1975, it is widely used as a catalyst in the petroleum industry [305]. The pore and channel structures of ZSM-5 are schematically represented in Figure 5.1.

159
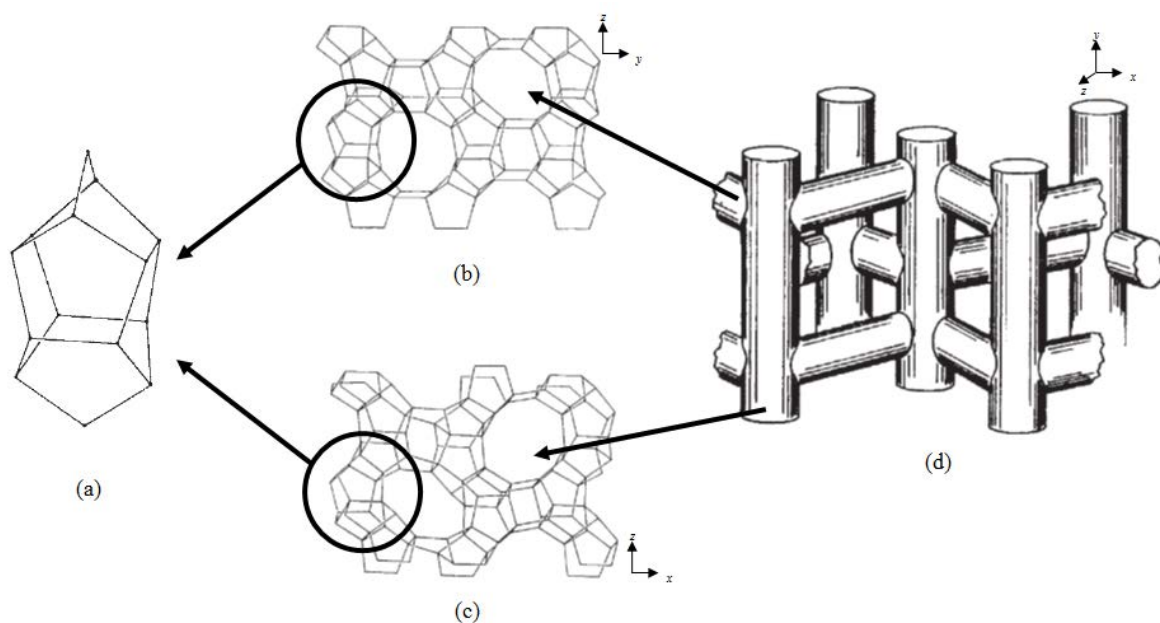
Figure 5.1: Schematic representation of the ZSM-5 zeolite. (a) A pentasilicate structure consisting of a regular arrangement of a three-dimensional pentagonal arrangement of atoms. (b) Skeletal diagram of the (100)-face of the ZSM-5 unit cell. Oxygen atoms are not shown. The nearly circular 10-membered ring apertures shown are the entrances to the sinusoidal channels which run parallel to [100]. (c) Skeletal diagram of the (010)-face of the ZSM-5 unit cell. Oxygen atoms are not shown. The 10-membered ring apertures shown are the entrances to the straight channels which run parallel to [010]. (d) The channel structure in ZSM-5. Images adapted from [305].

5.1.2   Zeolites for *in-situ* Silver Nanoparticle Synthesis

Due to their thermal stability and unique interconnected porous microstructure, natural and synthetic zeolites have been used as templating support materials to host a variety of metallic species including Ag [158], Mg [159], Ni [160], Zn [161], Fe [162], and Ga [163]. These studies have shown that zeolites are efficient reaction templates to produce composite materials for various technological applications. The porous internal network structure of zeolites provides an ideal and stable template for the formation and growth of nanoparticles with nanometre dimensions. Furthermore, nanoparticles are physically prevented from agglomeration

to form micron-sized particles, as they are individually separated within the discrete pores and channels of the zeolite interior. Previous studies on Ag-zeolite nanocomposite materials proposed an ion exchange process followed by high temperature calcination methods [76, 92, 158] to produce metallic Ag-zeolite materials.

Silver-zeolite nanocomposites possess great potential for marine antifouling applications due to the remarkable antimicrobial property of silver against at least 650 unicellular organisms [20]. Furthermore, zeolites have no known environmental hazards and are regularly used for environmental remediation [165], such as the removal of heavy metals from soils [166] and in the treatment of wastewater [167].

However, there have been very limited studies on adopting silver-zeolite nanocomposites for the evaluation of marine antifouling property. Previous related works include that of De Muynck et al. [168], which studied strategies for the prevention of algal fouling of outdoor terrestrial concrete surfaces using a Cu-Ag zeolite and also AgNPs. Krishnani et al. [47] reported on the bactericidal activity of silver ion-exchanged zeolite against shrimp pathogenic bacteria and its efficiency in the removal of ammonia.

This study focuses on a rapid and low-temperature method to synthesize highly dispersed AgNPs with narrow size distribution on the surface and internal structures of commercially available zeolite ZSM-5 for anti-microfouling applications.

5.1.3 Rationale of Study

Zeolite ZSM-5 were used in the synthesis of silver-zeolite nanocomposite materials for the following important reasons:

1) As a support template for the formation of AgNPs. The mesoporous zeolite framework allows the preferential ion exchange of Ag cations with the ammonium cations, whilst maintaining charge neutrality of the zeolite structure. The porous internal structure of zeolites provides an ideal and stable template for the formation and growth of nanoparticles.

2) Prevent agglomeration of AgNPs by physical separation within the pores and channels of the zeolite interior.

3) Zeolites have no known environmental hazards and are regularly used for environmental remediation. Thus, they are safe and suitable for use in a marine environment for anti-fouling applications.

In addition, trisodium citrate, a green reducing agent which does not pose an immediate catastrophic threat to the environment, was used to form Ag-zeolite nanocomposite materials at a low temperature, without the need of high temperature calcination to induce the reduction of silver ions.

5.1.4 Synthesis Parameters

Solutions of silver nitrate and trisodium citrate of various concentrations were used as the varying parameters in the synthesis of AgZ nanocomposites. The amount of zeolite used in each experiment was fixed. Instead of employing high temperature calcination to induce the reduction of silver ions, trisodium citrate was used as a green reducing agent to form Ag-zeolite nanocomposite materials at a low temperature. Further details of the synthesis have been discussed in Section 3.2.2.

5.2   Synthesis of Silver-Zeolite (AgZ) Nanocomposite

The synthesis of silver-zeolite (AgZ) nanocomposite clusters was carried out in two steps as shown in Figure 5.2. In the first step, Ag ions were first introduced into the zeolite ZSM-5 pores through an ion exchange procedure. The ammonium form of zeolite ZSM-5 was stirred with silver nitrate solution to allow the Ag^+ cations to substitute out the NH_4^+ ions and form an intermediate Ag^+/zeolite mixture (Equation 5.1).

$$NH_4^+/zeolite + Ag^+ \rightleftarrows Ag^+/zeolite + NH_4^+$$
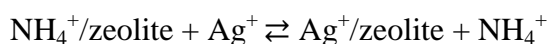
.... Equation 5.1

The reduction of silver ion-doped ZSM-5 zeolite nanocomposites took place via a citrate chemical reduction route according to Equation 5.2:

163

$$4\text{Ag}^+ / \text{Zeolite} + \text{C}_6\text{H}_5\text{O}_7\text{Na}_3 + 2\text{H}_2\text{O} \xrightarrow{\Delta} 4\text{Ag}^0 / \text{Zeolite} + \text{C}_6\text{H}_5\text{O}_7\text{H}_3$$
$$+ 3\text{Na}^+ + \text{H}^+ + \text{O}_2 \uparrow$$
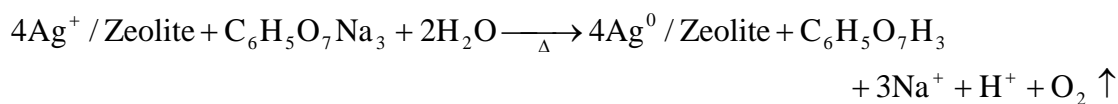
…. Equation 5.2

Prior to the reduction process, the Ag^+/zeolite appeared white, but after the addition of the reducing agent with heating, the colour started to change to brown/grey, indicating the formation of metallic silver in the zeolite sample. The Ag ions were then chemically reduced to metallic Ag by the donation of electrons from the citrate reducing agent. The atomic silver species rapidly nucleates within the zeolite's porous structure and aggregates into AgNPs. However, the formation of large agglomerated particles is physically constrained by the zeolite's nanometre-sized template structure.
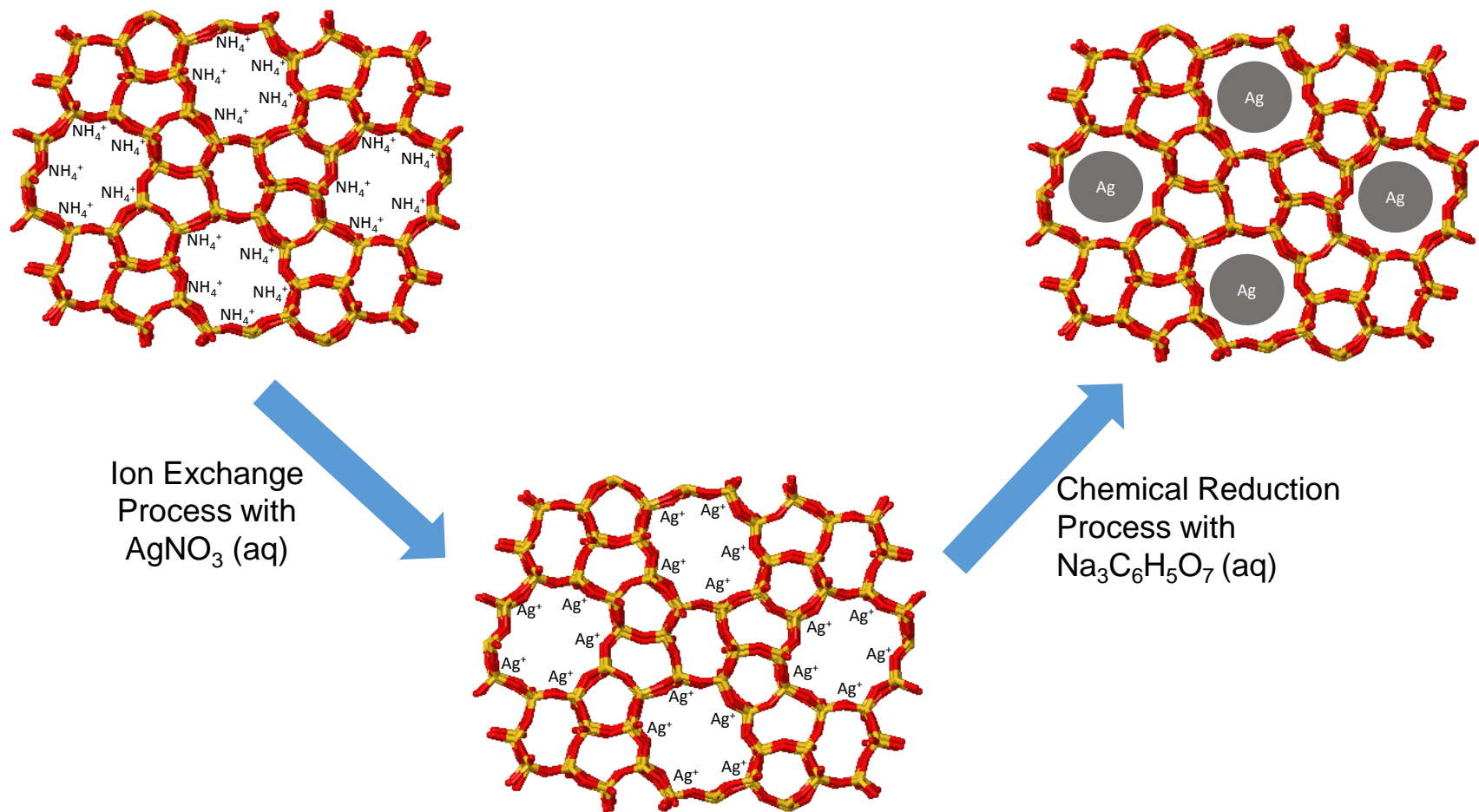
Figure 5.2: The mechanism of Ag NP formation within the internal pores of zeolite ZSM-5.

5.3   Optical Properties of AgZ

The formation of AgNPs is indicated by strong absorption peaks in the UV-visible spectrum, around 400 nm, due to the surface plasmon resonance (SPR) of conduction electrons on the surface of spherical particles [108]. Aggregation and agglomeration of Ag NPs cause the emergence of a secondary absorbance peak or broad shoulder in the UV-visible spectrum up to 500 nm [306].

Figure 5.3 shows the UV-visible spectrum of the AgZ composites. All the AgZ composites except AgZ-1 and AgZ-5 showed a characteristic maximum absorption peak between 408 nm to 449 nm, indicating the formation of Ag NP within the AgZ composite material. The absorption maximum for the AgZ-1 was not obvious, mainly due to the low concentration of Ag NP in the zeolite structure, consistent with the low concentration of Ag precursor used during the synthesis. AgZ-5 displayed a broad absorption spectra with a maximum peak around 500 nm, indicating the presence of aggregated Ag particles [306].

There was a red shift in the maximum absorption peak from 408 nm to 449 nm, attributed to the greater concentration of Ag NP in the sample, leading to multiple particle interactions and causing the red shift of the SPR band [39]. The use of higher concentrations of silver precursor, up to 1.0 M, formed a greater concentration of Ag NPs, causing the formation of larger aggregated Ag particles, hence, contributing to the red shift. These results clearly indicate that, by adopting proper Ag precursor concentration, the zeolite material can serve as a stable and effective template or nanoreactor for the formation of well-dispersed Ag NP.

Sample	λ_{max} (nm)
AgZ-5	500
AgZ-4	449
AgZ-3	443
AgZ-2	408
AgZ-1	-
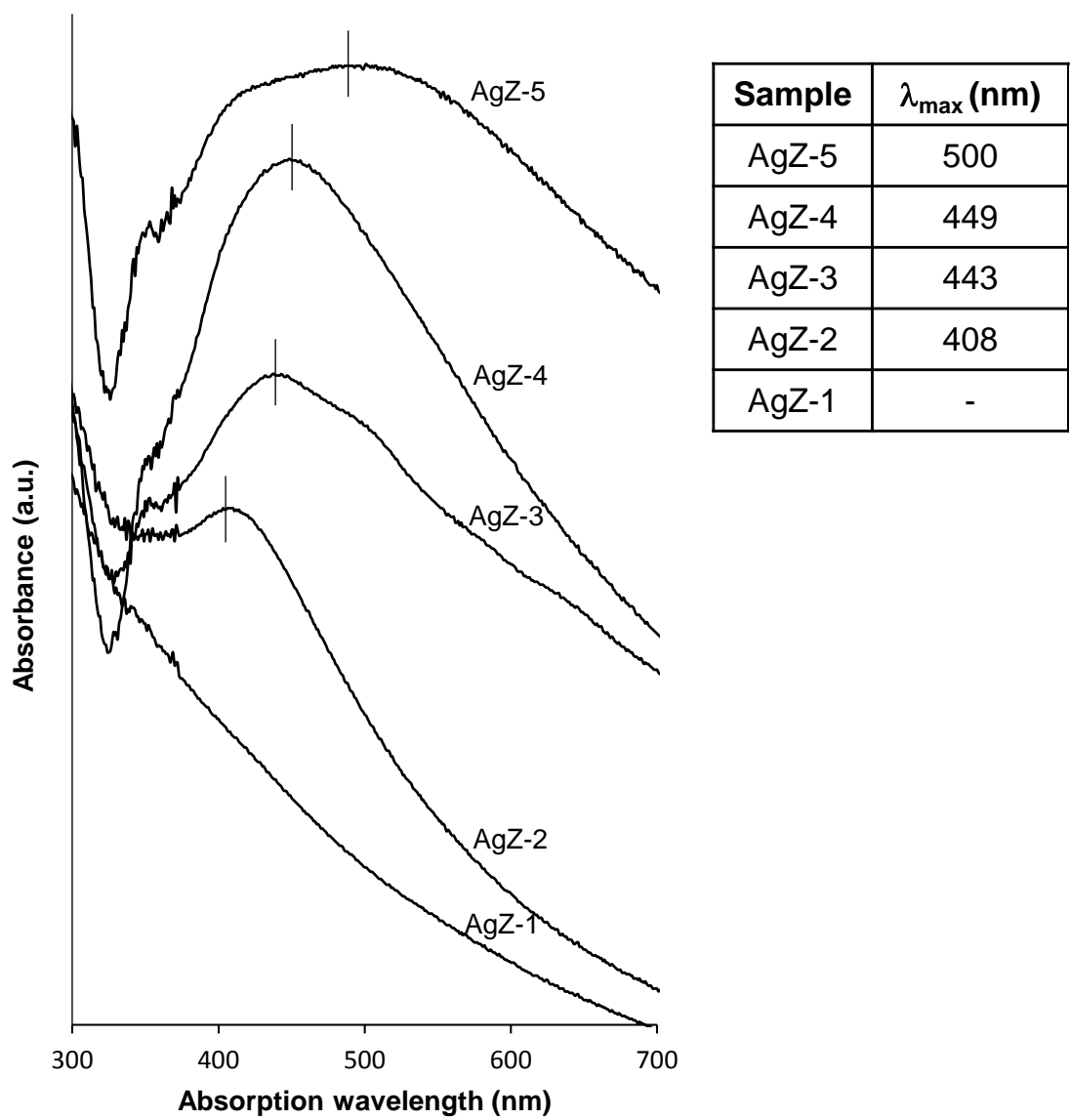
Figure 5.3: UV-visible absorption spectra of AgZ composites dispersed in water.

5.4   Morphology and Chemical Content of AgZ

The silver-zeolite (AgZ) composites appear in an aggregated form consisting of globular clusters of particles. The metallic Ag particles appeared on the surface of the zeolite clusters as shiny spots under backscattered electron imaging, as shown in Figure 5.4. To confirm that the shiny spots were composed mainly of Ag, EDX elemental analysis was conducted on AgZ-5 (magnification 80,000x), which showed 16 wt% Ag in the brighter region (Figure 5.4, Spectrum 1) compared to only 4 wt% Ag in the darker grey region (Figure 5.4, Spectrum 2). Therefore, from the compositional analysis, it was apparent that the AgNPs were characterised by the lighter coloured particle in the SEM micrograph, and were distributed homogeneously on the exterior of the darker zeolite clusters.
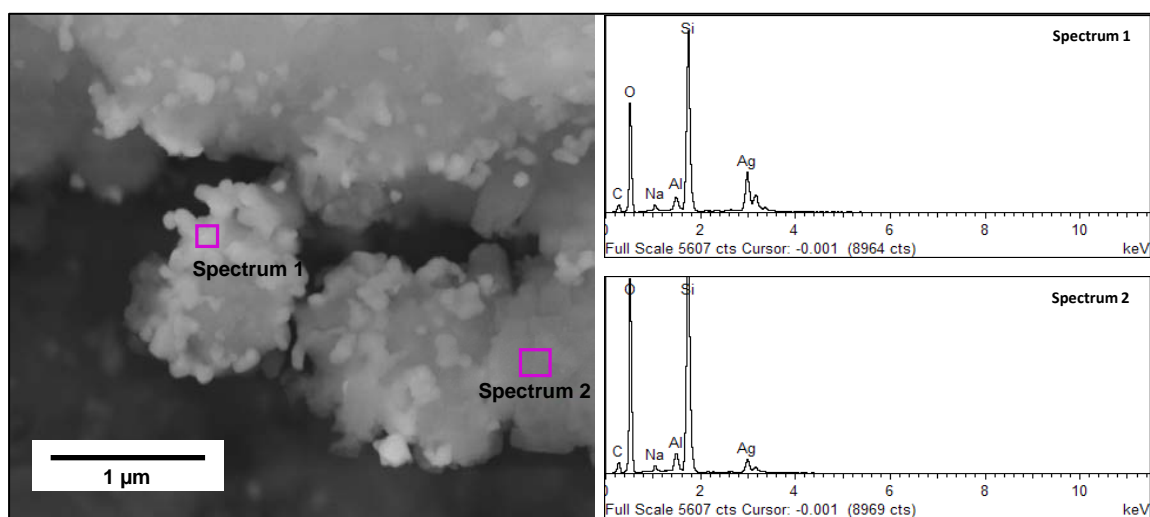
Figure 5.4: EDX analysis of AgZ-5 composite. Bright areas have a higher Ag content (16 wt% Ag) compared to darker regions (4 wt% Ag)

Figure 5.5 shows the general morphology of the AgZ composites prepared with increasing concentrations of silver precursor, with arrows indicating the presence of metallic Ag. The Ag particles appeared with increasing regularity with a higher loading of silver ions, in the order of AgZ-1 < AgZ-2 < AgZ-3 < AgZ-4< AgZ-5. The metallic Ag particles were observed to have a uniform distribution on the surface of the zeolite clusters.

The Ag particles appeared to be slightly larger for AgZ-5 (Figure 5.5F), confirming the occurrence of Ag particle agglomeration, in accordance with the red shift in the SPR band observed in the UV-visible analysis. During the formation of Ag crystallites, through the Ostwald ripening process, smaller crystallites will tend to dissolve back into solution during the citrate reduction process. The redissolved Ag ions will tend to redeposit around larger Ag crystallites. Therefore, on the zeolite surface, the formation of larger Ag particles is promoted at the expense of finer particles [307].

The pure zeolite and AgZ composites appeared as discrete clusters composed of smaller particles. The size analysis of the AgZ clusters was done by measuring 100 clusters from each sample. From these measurements, the cluster size was generally between 1–5 µm in diameter. The use of higher initial concentrations of the silver precursor resulted in an increase in the average cluster diameter, as well as a general increase in the cluster size distribution, in the order of untreated ZSM-5 < AgZ-1 < AgZ-2 < AgZ-3 < AgZ-4< AgZ-5.
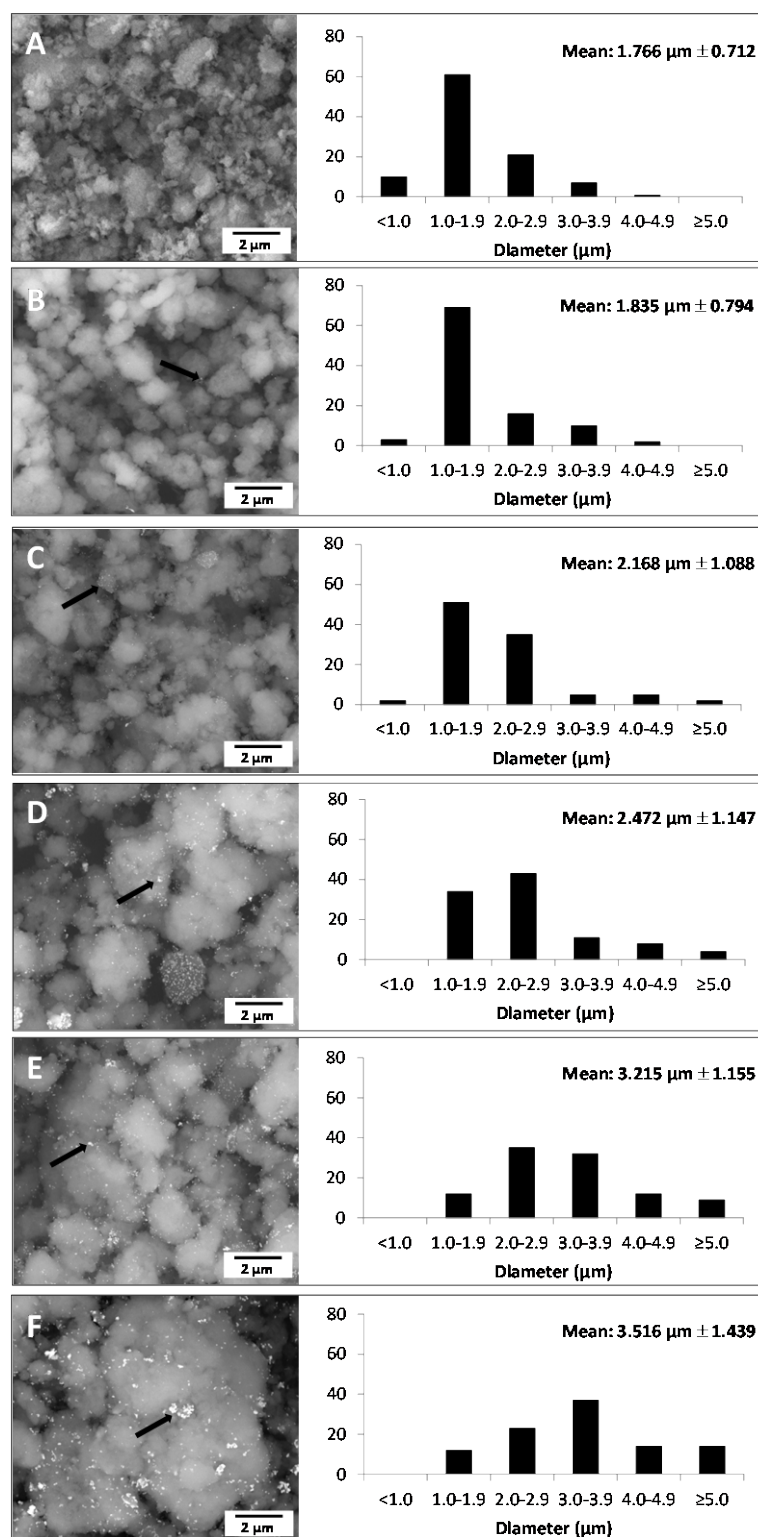
Figure 5.5: Morphology of the Ag-zeolite composites prepared with increasing concentrations of silver precursor. (A) SEM image and cluster size distribution of pure ZSM-5 zeolite. Backscattered electron images of Ag-zeolite (AgZ) composites showed Ag particles appearing as shiny spots on the surface of composites. The corresponding histogram shows the AgZ composite cluster size distributions of (B) AgZ-1, (C) AgZ-2, (D) AgZ-3, (E) AgZ-4, and (F) AgZ-5.

170

The size distribution histograms are also shown in Figure 5.5. The average diameters of the AgZ composite clusters were concordant with the initial concentration of the silver precursor, with AgZ-5 cluster sizes almost double the cluster size of the pure zeolite. The enlargement of the composite cluster size was likely due to the diffusion of Ag ions into the zeolite internal pores, and their subsequent reduction to metallic silver during the chemical reduction process. The nucleation and growth of the metallic Ag within the zeolite internal pores was expected to contribute to an overall increase in the cluster size of the AgZ composites. Furthermore, the cluster size diameter increase was also due to the agglomeration of more silver particles on the surface of the Ag-zeolite composites.

Table 5.1 shows a summary of the physical characteristics of the AgZ composite materials. The EDX results indicate that the use of the silver precursor from 0.1-1.0 M resulted in the incorporation of Ag nanomaterials from 0.8–10.0 wt% Ag within the zeolite framework. This agrees with the increase in Ag ion uptake into the zeolite pores when using higher concentrations of the silver precursor during the ion exchange process [164]. Although a mixing time of 24 h has been regularly reported by other researchers in the preparation of Ag-loaded ZSM-5 [46, 76, 308], the relatively short ion-exchange time of 2 h adopted in the current study is found sufficient to produce optimum Ag ion uptake into the zeolite pores.

In preliminary experiments, there was little difference in Ag ion uptake for ion exchange between 3-96 h when using low concentrations of the silver precursor. In fact, the chemical reduction of Ag ions helped to increase the Ag content in the Ag-zeolite composites, when compared with systems which do not undergo a similar

process. In addition, the Si:Al molar ratio (SAR) for the Ag-zeolite composite varied very slightly (SAR values between 16.3–17.3) in comparison to the pure zeolites (SAR = 17.0), indicating that the zeolite aluminosilicate template structure was not affected by the inclusion of Ag. This indicates that the ZSM-5 zeolite material can be used as an effective templating medium for the fabrication of chemically reduced Ag-zeolite composites.

Table 5.1: The physical properties of the Ag-zeolite nanocomposite prepared with various concentrations of the silver precursor.

Sample	Concentration of silver nitrate (M)	Average cluster size (μm)	Average increase in cluster size compared to pure zeolite	Ag content (wt%)	Si:Al atomic ratio
ZSM-5	-	1.766	-	0	17.0
AgZ-1	0.10	1.835	3.9	0.8	17.3
AgZ-2	0.25	2.168	22.8	1.3	17.2
AgZ-3	0.35	2.472	40.0	2.7	16.8
AgZ-4	0.50	3.215	82.0	6.5	16.7
AgZ-5	1.00	3.516	99.1	10.0	16.3

5.5 Crystallinity of AgZ Nanocomposites

The XRD patterns of all AgZ composite samples are shown in Figure 5.6. For the AgZ-1 and AgZ-2 composites with the lowest loading of 0.8 wt% Ag and 1.3 wt% Ag, respectively, the presence of the crystalline Ag diffraction pattern was hardly detected and thus showed a similar XRD pattern as the pure zeolite, ZSM-5. With 2.7 wt% Ag content, the AgZ-3 composite XRD spectrum was found to exhibit the four main characteristic peaks for metallic silver at $2\theta = 38.1°$, $44.3°$, $64.4°$, and $77.4°$ and these corresponded to the (111), (002), (022), and (113) crystallographic planes of the face-centred cubic (FCC) silver crystals (ICDD pattern, 98-005-0882).

With an increased Ag content of 6.5 wt% Ag and 10 wt% Ag in the composite materials, the intensities of these four diffraction maximums were found to increase gradually as well. This agrees with the observations of Shameli et al. (2011) [164], who also noted increased intensities of the silver crystallographic planes, corresponding to a higher amount of AgNPs detected in the matrix of zeolite-Y. Baek et al. (2004) [309] also observed an increase in peak intensity with higher Ag loading in zeolites between 5.0 and 22.4 wt% Ag.

On the other hand, the five main peaks for ZSM-5 at $2\theta = 7.9°$, $8.8°$, $23.1°$, $23.3°$, and $23.9°$ were still apparent for all the Ag-Z composite samples, and no significant phase shift was observed after the Ag growth process. Nevertheless, there was a reduction in the intensities of these ZSM-5 main peaks, especially for the composite AgZ-5. The reduction of the zeolite main peaks, along with the evolution of higher intensity peaks for metallic Ag, indicate that the incorporation of metallic

173

silver caused a slight reduction in the crystallinity of the zeolite template during the formation of the Ag-Z composites.

Although ZSM-5 was used to host up to 10 wt% metallic silver in AgZ-5, the integrity of the zeolite internal structure remained largely intact. These results are in agreement with Boschetto et al. (2012) [60] who observed similar small decreases in the zeolite-Y peak intensities occurring after the incorporation of Ag^+. This shows that ZSM-5 is a stable inorganic matrix material for the formation of Ag-zeolite composites.
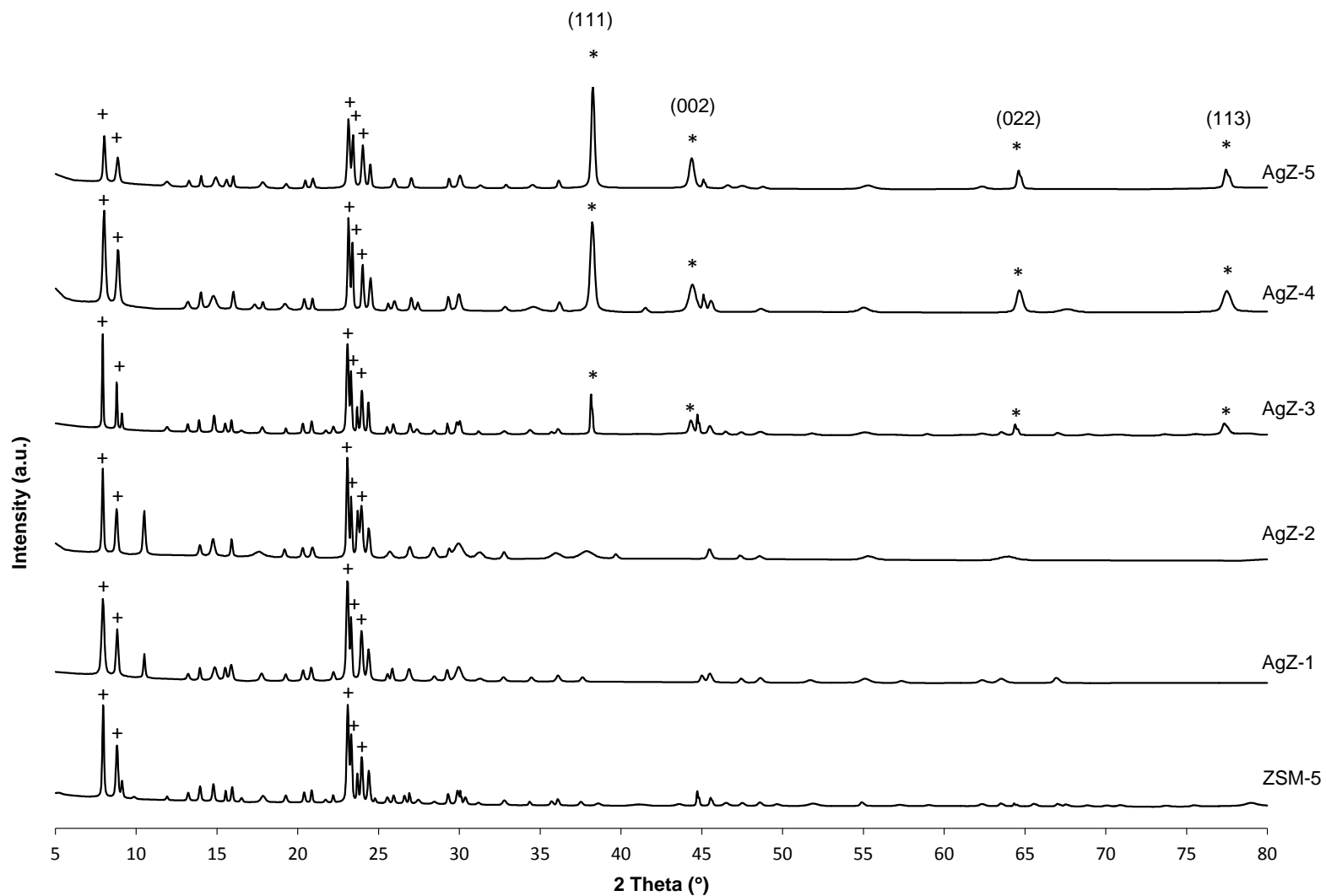
Figure 5.6: XRD spectra of zeolite ZSM-5 and Ag-zeolite composites. * represents the metallic silver phase (98-005-0882), ICDD reference pattern for Ag.[+] represents the five main peaks for ZSM-5 zeolite.

5.6   Surface Area Analysis and Pore Size Distribution of AgZ

As shown in Table 5.2, the specific surface area using the Brunauer-Emmett-Teller technique, S_a, of the AgZ samples decreased with increased doping of metallic Ag. At the same time, a concordant increase in the BJH desorption average pore width was observed. S_a decreased by up to 44% after the introduction of Ag into the zeolite framework. The decrease in the specific surface area of AgZ composites with the higher loading of Ag was attributed to the blockage of the zeolite pores and channels due to the deposition of Ag particles [310], with few significant changes to the zeolite channel structures.

Table 5.2: Specific surface area and BJH average pore width for Ag-zeolite nanocomposites with various Ag loadings.

Ag wt.%	S_a (m^2/g)	BJH desorption average pore width ($\overset{\circ}{A}$)
0	397	60.337
0.8	289	68.087
1.3	285	73.322
6.5	264	88.845
10.0	224	129.339

The BJH desorption pore size analysis also showed that there was a marked increase in the average pore diameter in the AgZ sample, mainly due to the presence of Ag particles in the ZSM-5 framework. The average pore width values using BJH desorption measurements showed a remarkable increase from 60 Å to 129 Å, a rise of more than 115%. The increase in the average pore size of the AgZ materials

compared to the pure zeolite was attributed to the aggregation and growth of AgNPs within the zeolite structure.

The textural study using density functional theory (DFT) showed that the ZSM-5 zeolites were predominantly microporous and mesoporous, with 69% of pores smaller than 50 Å. The inclusion of Ag gradually caused a macroporous structure to emerge, particularly with AgZ-5 (Table 5.3). This is mainly due to the presence of large Ag nanoclusters within the zeolite cages. The development of porosity in the range of 100–500 Å suggests the build-up of porous Ag clusters within the zeolite support channels as suggested by David (2006) [159], who observed similar growth of Mg nanoclusters in zeolite 4A. Similar increases of porosity in the > 500 Å range were observed, which indicates the formation of Ag clusters near the surface of the zeolite template.

Table 5.3: Distribution of pore volume as a function of pore width range for selected Ag-zeolite nanocomposites.

Pore width range	Distribution of volume pores, V_p (cm^3/g)		
	ZSM-5	AgZ-2	AgZ-5
≤25 Å	3.85521	0.09981	-
>25≤50 Å	3.02638	0.01757	-
>50≤100 Å	3.12581	0.01778	0.00516
>100≤500 Å	-	0.03736	0.03580
>500 Å	-	0.04717	0.10921

BJH desorption studies (in Table 5.4) also revealed a similar trend with diminishing micropores and an increasingly larger volume of macropores. There were similar decreases noted in the distribution of mesopores in the AgZ samples compared to the pure zeolite. After the growth of the metallic Ag, it was found that the AgZ samples generally encountered a significant decrease (15-20%) for pores measuring 20-100 Å, whilst a remarkable increase of about 25% for pores > 500 Å was noticeable, if compared to the pure zeolite material. The increase in the macroporous texture was attributed to the formation of Ag within the zeolite framework.

Table 5.4: Distribution of pore volume using BJH desorption studies.

Pore Width Range (Å)	Distribution of volume of pores, V_p (cm^3/g)					
	ZSM-5	AgZ-1	AgZ-2	AgZ-3	AgZ-4	AgZ-5
>15≤25 Å	0.0134	0.0120	0.0130	0.0115	0.0114	0.0087
>25≤50 Å	0.0255	0.0273	0.0250	0.0243	0.0229	0.0214
>50≤100 Å	0.0188	0.0238	0.0230	0.0238	0.0234	0.0207
>100≤500 Å	0.0218	0.0379	0.0340	0.0301	0.0244	0.0269
>500≤1000 Å	0.0213	0.0352	0.0343	0.0584	0.0522	0.0485
>1000 Å	0.0059	0.0411	0.0403	0.0200	0.0183	0.0403
Average radius (Å)	60.337	93.043	91.357	93.613	88.845	109.238

The significant increase in average pore size and volume, however, did not disrupt the crystalline structure of the zeolite material, as evidenced in the XRD patterns (Figure 5.6). Therefore, the ZSM-5 structure is an extremely stable and durable porous template that is suitable for the formation of distinct and homogeneous AgNPs.

5.7   Anti-Microfouling Properties of AgZ

To test the antifouling effects of AgZ composite materials, a static biofilm assay was carried out using *H. pacifica,* a common marine fouling organism. As shown in Figure 5.7, 1mg/mL concentration of AgZ materials inhibit the attachment of biofilm from *H. pacifica* after an incubation period of 24 h. Particularly, AgZ-4 and AgZ-5 had a potent inhibitory effect on *H. pacifica* biofilm formation with an average inhibition of $63.27 \pm 2.64\%$ and $81.29 \pm 1.53\%$, respectively ($P < 0.01$, Student's *t*-test).

In contrast, no such effect was observed in bacteria incubated with the zeolite ZSM-5 alone. Notably, the efficacy of biofilm inhibition correlated directly with the amounts of Ag loading, suggesting that the zeolite ZSM-5 might promote the antifouling properties of the Ag-PNC material by providing a template for nanosized biocidal AgNPs. Silver ions have been shown to disrupt multiple bacterial cellular processes, leading to increased production of reactive oxygen species and increased membrane permeability, eventually causing bacterial cell death [21]. The disruption of biofilm formation will hinder the subsequent attachment of larger fouling organisms and impede the fouling process [228, 263].
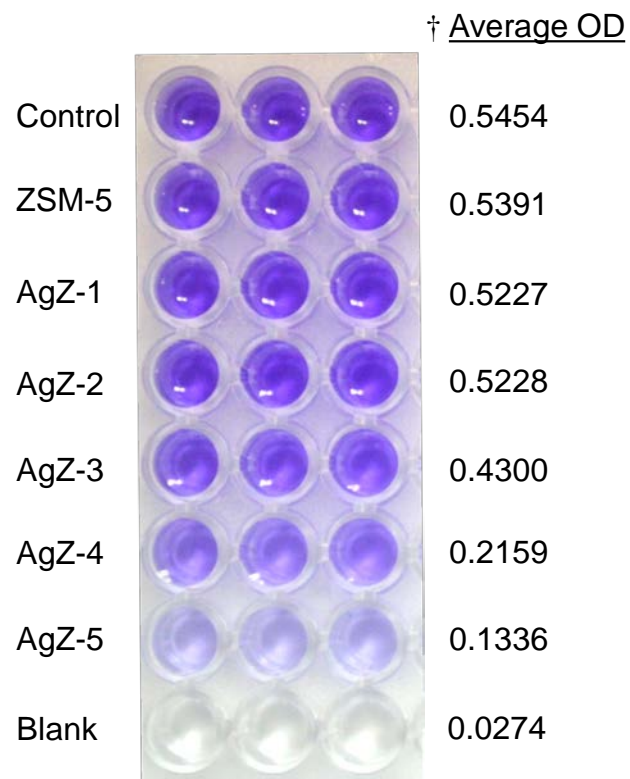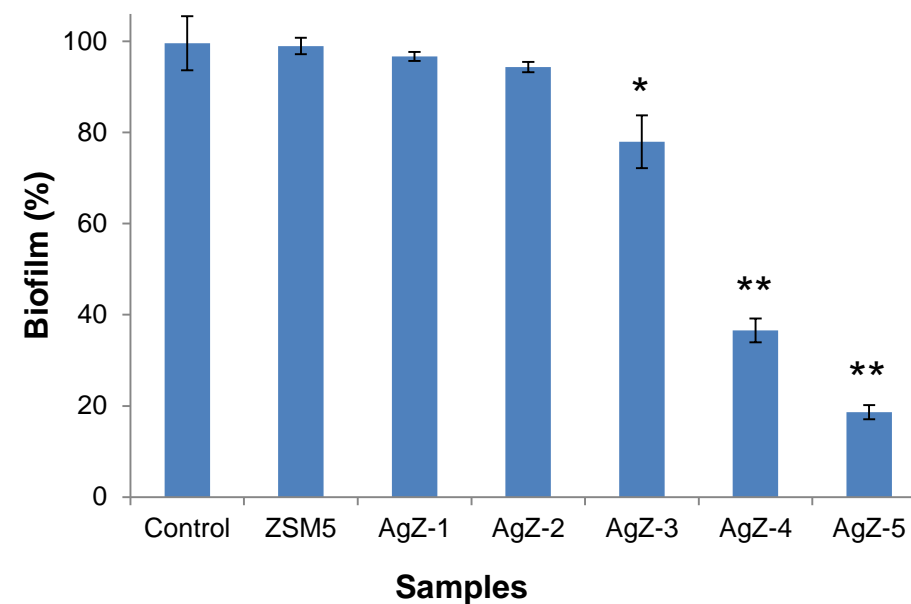
Figure 5.7: AgZ materials inhibit the attachment of biofilm from *H. pacifica*. (a) Anti-biofilm activity of AgZ materials at 1 mg/ml. [†]Average OD measured at 570 nm, and (b) inhibition of *H. pacifica* bacteria biofilm attachment by AgZ materials. Bars represent mean ± s.d. of three independent experiments. * indicates statistical significance compared to control (P < 0.05, Student's *t*-test). ** indicates statistical significance compared to control (P < 0.01, Student's *t*-test).

The biological effects of AgZ-5 were also evaluated on 2 commonly used marine microalgae, *D. tertiolecta* and *Isochrysis* sp. As shown in Figure 5.8 (A), 1mg/mL of AgZ-5 induced significant growth inhibition in both *D. tertiolecta* and *Isochrysis* sp. while no such effect was observed in microalgae treated with the ZSM-5 alone.

Upon observation under light microscopy [Figure 5.8(B)], no significant morphological changes was observed in *D. tertiolecta* suggesting that the biological effects of AgZ-5 is likely to be cytostatic rather than cytotoxic. In contrast, loss of membrane integrity and cytoplasm materials were observed in *Isochrysis* sp., indicating that AgZ-5 is cytotoxic to *Isochrysis* sp.
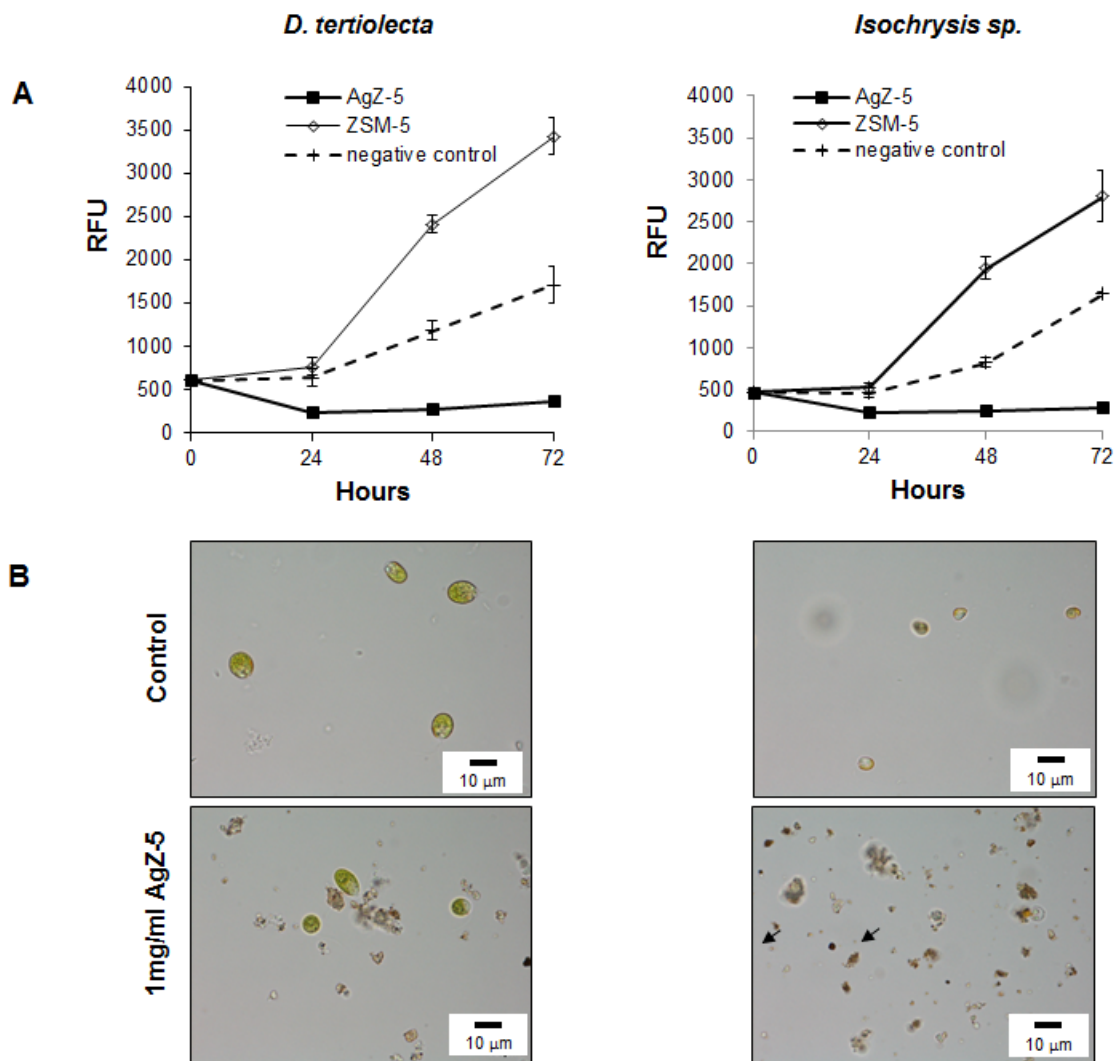
Figure 5.8: Growth inhibition effect of AgZ materials on marine microalgae. (A) *D. tertiolecta* and *Isochrysis* sp. algal cells were exposed to 1mg/mL of AgZ-5 for 72 hours and the number of cells was determined by Presto Blue® stain and spectroscopy. Points represent mean of ± s.d. of at least 3 independent experiments. (B) Morphology of *D. tertiolecta* and *Isochrysis* sp. following exposure to 1 mg/mL of ZSM-5 (control) or AgZ-5 for 72 hours. Arrows indicate empty shell of the algal cell. Magnification at 1000x.

5.8   Summary

Ag-zeolite nanocomposite materials were successfully synthesised using an ion-exchange and low-temperature reduction process. The nanocomposite displayed promising anti-microfouling behaviour as it interferes with the biofilm formation that often precedes macrofouling processes. Although the AgZ nanocomposites were synthesised using a more rapid ion exchange process compared to conventional processing times of 24 h or more, the amount of metallic Ag loading was relatively high, up to 10 wt% Ag, due to the use of an environmentally friendly citrate reduction method.

In addition, physical characterization methods showed that nanosized metallic Ag were successfully precipitated within the confines of the porous structure of the ZSM-5 zeolite, leading to the formation of a stable AgZ nanocomposite. The zeolite template served as a physical nanoreactor and provided a stable matrix for the formation of metallic Ag in nanometre dimensions, which restricted particle agglomeration.

The processing method and introduction of Ag into ZSM-5 changed the porosity characteristics of the zeolite material, with the AgZ composites possessing some degree of macroporous structure in addition to the mesoporous nature of the zeolite. However, it did not cause any destruction of the inorganic zeolite structure, with its crystallinity well-preserved.

Biofilm formation of *H. pacifica* was reduced by up to 82% by the AgZ nanocomposites, demonstrating its anti-microfouling property against a common fouling microorganism. AgZ also displayed cytostatic effect on *D. tertiolecta* and a cytotoxic effect on *Isochrysis* sp., common marine microalgae.

Chapter 6: Enhanced Marine Antifouling Performance of Silver-TiO$_2$ Nanotube Composites via Hydrothermal Processing

6.1   Introduction

The preceding two chapters have dealt with three-dimensional support structures for anchoring and growth of AgNPs to form nanocomposite structures. This chapter shifts focus to discuss about one-dimensional nanoscale support structures.

Ever since the discovery of carbon nanotubes by Iijima in 1991 [169], one-dimensional (1D) nanostructures have sparked intense research interest due to their combination of unique electronic properties and outstanding mechanical strength. In addition, nanotubes are mesoporous in nature, and can be used as adsorbent materials [311]. Bulk titanium dioxide (TiO$_2$), or titania, is a ubiquitous and versatile ceramic compound found in various consumer goods and products. Micron-scale titania is used primarily as a white pigment in paints, dyes, varnishes, plastics, paper and textiles. On the other hand, nanoscale titanium dioxide has photocatalytic properties [173], with applications in photovoltaic, electrochromic, and antifogging devices. Titania has exceptional biocompatibility, making them suitable for biomedical coatings and sensors [312].

6.1.1   TiO$_2$ Nanotubes (TNT)

The hydrothermal synthesis of 1D TiO$_2$ nanostructures was first reported by Kasuga [171, 172]. They are composed of single sheets of TiO$_2$ scrolled into a tubular structure with an exposed edge, as seen in Figure 6.1. The TiO$_2$ nanotubes (TNT) used to produce silver-TiO$_2$ nanotube composites in this work was synthesized by the lab of Dr. S.S. Lim from the University of Nottingham Malaysia Campus.

The Fujishima group discovered the photocatalytic ability of TiO$_2$ nanoparticles under ultraviolet light and the self-cleaning property of TiO$_2$-coated glass when exposed to sunlight [173]. On the other hand, layered titanate materials have ion exchange properties [311]. TNT possess a combination of both conventional TiO$_2$ nanoparticles and layered titanates [311]. TNT has been reported in many diverse applications as a functional component in nanocomposite systems including as a photocatalytic hydrogen generator [174], as an electrode for sodium storage [175], in wastewater treatment [176], as a light-activated anti-bacterial platform [177] and for antifouling property against HeLa cells [178].
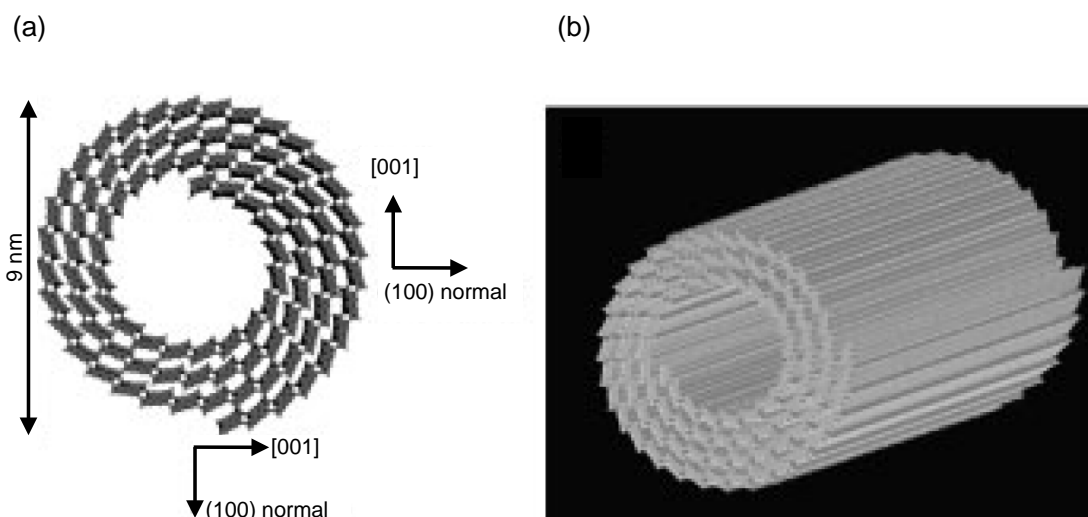
Figure 6.1: The structure of trititanate nanotubes. (a) Schematic drawing of the nanotube structure. (b) Three-dimensional drawing of a nanotube illustrating its scrolled structure. (Image from Chen et al. [170]).

6.1.2 TiO$_2$ Nanotubes for *in-situ* Silver Nanoparticle Synthesis

TiO$_2$ nanotubes are a better support than TiO$_2$ powder for the preparation of TiO$_2$-supported catalysts [313]. This is due to its higher specific surface area on the inner and outer surfaces of the nanotube structure. At the same time, the large specific surface area and strong hydrophilic tendency facilitate the ion-exchange process [314]. Sodium ions introduced during the hydrothermal synthesis of the TiO$_2$ nanotubes have been demonstrated to be replaced by cations of transition metals and proton ions, randomly distributed in the framework of the nanotube structure [314]. Monovalent ions, e.g., Ag$^+$, are less likely to interact with the negatively charged, anionic titanate sheets, in comparison with bivalent cations (Zn^{2+}, Cu^{2+}, Ni^{2+}, Co^{2+}, Cd^{2+}). The higher effective charge density and correspondingly stronger electronic interactions between the nanotube lattice and the bivalent cations prevent them from being reduced into metals [314].

6.1.3 Rationale of Study

The anti-microbial property of both silver and TiO_2 led to the consideration to combine AgNPs and TiO_2 nanotubes as a composite to study its potential as an antifouling agent by inhibiting the biofilm production of marine bacteria.

While the majority of studies have looked at Ag-TiO_2 nanotube composites in the areas of catalysis and energy [82], there have been limited studies on their marine antifouling property. Ruffolo et al. [69] compared the performance of pure TiO_2 nanoparticles and Ag-doped TiO_2 nanoparticles on the marine fouling of marble slabs for protection of underwater archaeological sites. Carl et al. [179] found that the use of TiO_2 as photocatalytic nanofillers in foul-release polydimethylsiloxane (PDMS) coatings improved their antifouling performance against the macrofouling mussel species *Mytilus galloprovincialis*, while TiO_2/fluorinated acrylic nanocomposite was used as a marine antifouling paint [180].

Apart from these scattered antifouling reports, more literature emerged from the field of water treatment depicting TiO_2 as a photocatalytic component of water filtration and microfiltration membrane systems to remove organic fouling matter including humic acid [70]. However, Ag-TiO_2 nanotubular composite materials have not yet been subjected to intensive study in the field of marine antifouling. Therefore, more studies remain to uncover the potential of Ag-TiO_2 nanotubular composites for marine antifouling applications.

Herein, a facile, novel and green method to produce silver-TiO$_2$ nanotubular materials is presented, using a hydrothermal reduction of AgNPs involving the citrate method, on TiO$_2$ nanotubes.

The surface characteristics, structural and antimicrofouling property of silver-TiO$_2$ nanotubular composite materials have been evaluated against a commonly found marine microfouling bacteria, *H. pacifica* as well as the microalgae *D. tertiolecta* and *Isochrysis* sp.

6.1.4 Synthesis Parameters

In order to fabricate composites with high stability and dispersivity, a series of experiments under different weight ratios of AgNO$_3$ / TiO$_2$ nanotubes were conducted. A fixed concentration of sodium citrate was used as a mild reducing agent in the hydrothermal reduction process. Further details of the synthesis have been discussed in Section 3.2.3.

6.2 Synthesis of Silver-TiO$_2$ Nanotube Composites

Figure 6.2 shows a schematic of the Ag/TNT preparation. The alkaline hydrothermal treatment and calcination process to form TiO$_2$ nanotubes (TNT) was performed by Dr. S.S. Lim's group and is briefly discussed here: micron-sized anatase TiO$_2$ particles are transformed into TiO$_2$ nanotubes via an alkaline hydrothermal

process. This is followed by a calcination treatment at 400 °C for 5 hours. The alkaline hydrothermal processing provides a high concentration of sodium cations which catalyses the formation of trititanate nanotubes from TiO_2 [170].

Anatase TiO_2 partially dissolves into single sheets of the trititanate $Ti_3O_7{}^{2-}$, which eventually grows in a two-dimensional plane and simultaneously rolling up into nanotubes [170]. The acid wash on the nanotubes renders the structure as monoclinic titanate $H_2Ti_3O_7$ with a layered morphology [315, 316]. During calcination up to 400°C, the nanostructured $H_2Ti_3O_7$ undergoes a topotactic transformation into the metastable TiO_2 (B) through the intermediate titanate phases $H_2Ti_6O_{13}$ and $H_2T_{12}O_{25}$ whilst retaining the nanotubular morphology [317]. The TiO_2 nanotubes (TNT) appear as a white powder after calcination.

The TNT is subsequently used as a support structure for the growth of AgNPs through a second hydrothermal treatment involving silver nitrate and sodium citrate as a mild reducing agent. After the chemical reduction of silver ions, the resultant Ag/TNT powder is shiny and greyish black in appearance. The reduction of the silver nitrate/TNT mixture took place via the citrate reduction route according to Equation 6.1:

$$4Ag^+/TNT + C_6H_5O_7Na_3 + 2H_2O \xrightarrow{\Delta} 4Ag^0/TNT + C_6H_5O_7H_3 + 3Na^+ + H^+ + O_2 \uparrow$$

…. Equation 6.1
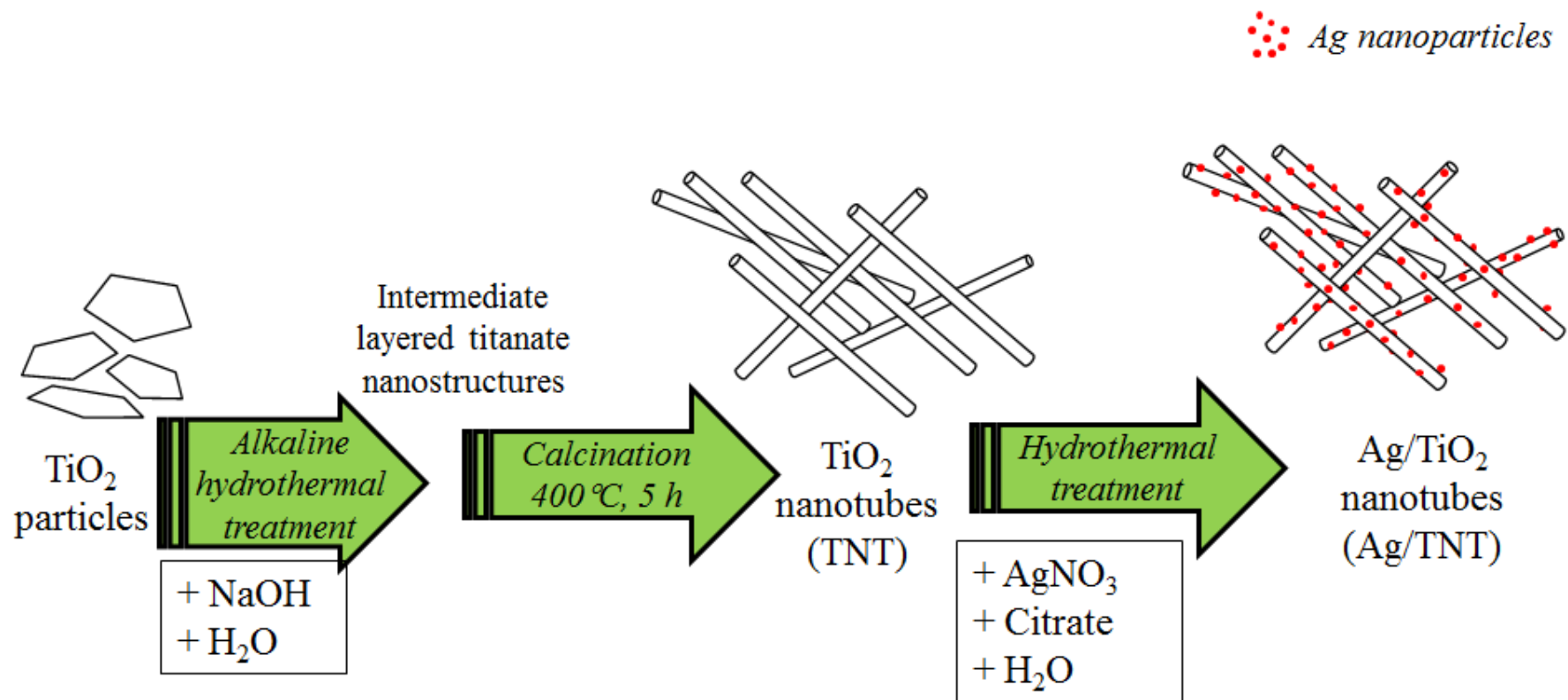
Figure 6.2: A scheme of the multi-step synthesis process for the formation of Ag/TiO₂ nanotubes (Ag/TNT). The alkaline hydrothermal treatment and calcination process to form TiO₂ nanotubes (TNT) was performed by Dr. S.S. Lim's group. The synthesis work discussed in this chapter covers the hydrothermal treatment to form Ag/TNT.

Chemical reduction of Ag ions to metallic Ag is achieved through the donation of electrons from the citrate reducing agent. Citrate is a well-known reducing agent and stabilizer in nanoparticle formation [307], directly influencing the particle size and shape of AgNPs [318] and bimetallic nanoparticles [319] through steric isolation of individual nanoparticles [320]. The TiO_2 nanotubes act as a stable surface to support the deposition of AgNPs.

According to Bavykin et al. (2005) [316], TiO_2 nanotubes formed from alkaline hydrothermal synthesis are negatively charged and interact with cationic species, such as Ag^+. The cation binding sites are ascribed to the presence of sodium ions in the alkaline environment during the initial nanotube formation.

6.3   Morphology and Chemical Content of Ag/TNT Composites

The morphology of the Ag/TNT samples was observed through scanning electron microscopy. Under high magnification (80,000 X), the TiO_2 nanotubes appear as a network of filaments with a length to diameter ratio of approximately 15:1 (Figure 6.3A). For the Ag/TNT samples, equiaxed particles of Ag are observed to be uniformly distributed over the TiO_2 nanotube mesh. The observable Ag particle size increases from 32 nm for Ag/TNT-1 to over 100 nm for Ag/TNT-7 (shown in Table 6.1), while the Ag distribution density also increases directly with the increase of Ag precursor material used in the nanocomposite synthesis (Figures 6.3B – 6.3F).
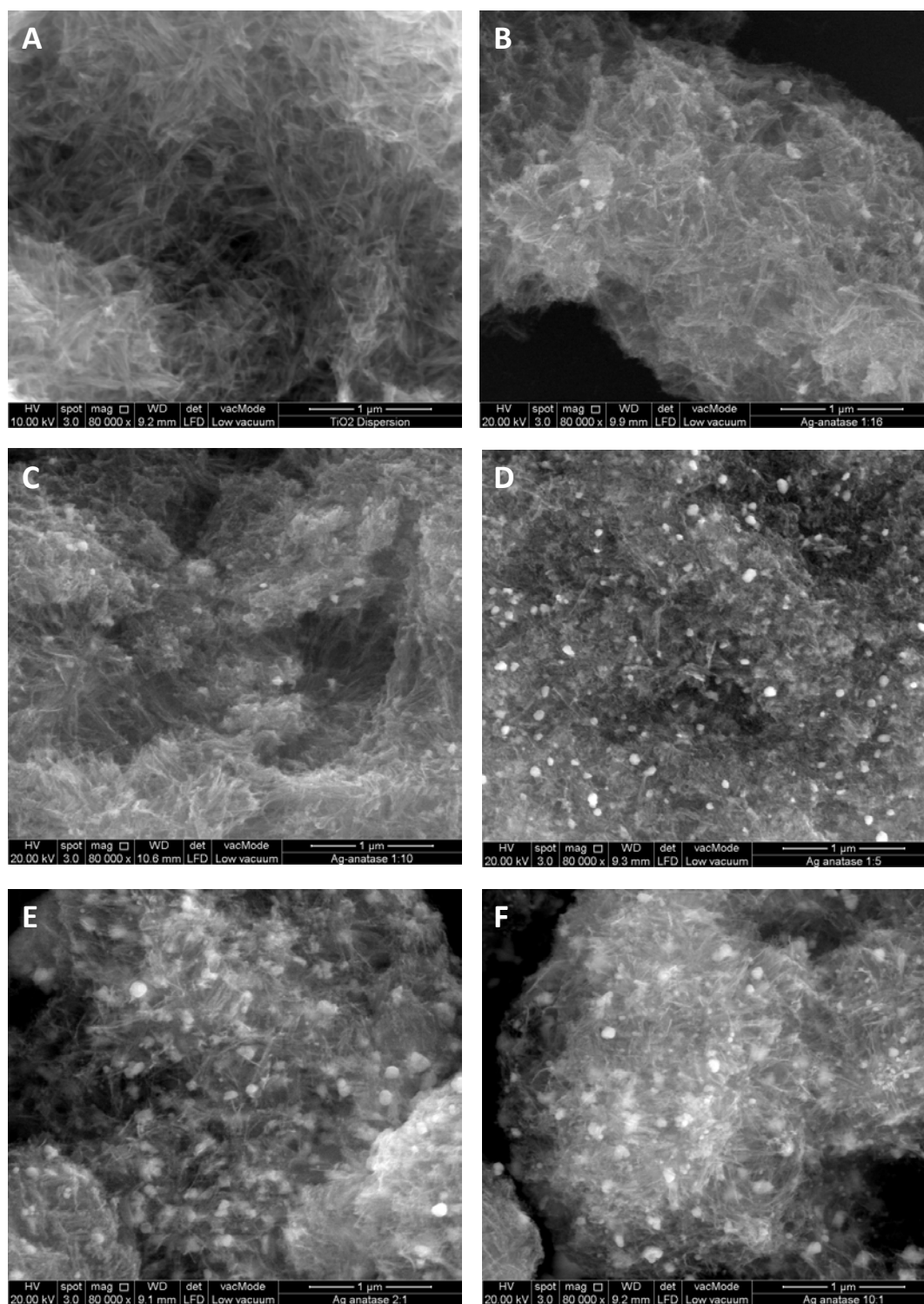
Figure 6.3: High magnification (80,000 X) scanning electron micrographs of Ag/TNT. (A) TiO$_2$ nanotubes (TNT), (B) Ag/TNT-1, (C) Ag/TNT-2, (D) Ag/TNT-3, (E) Ag/TNT-5, and (F) Ag/TNT-7, showing the tangled morphology of the TNT. (B) – (F) shows increased deposition of spheroidal Ag particles with the increase in ratio of Ag precursor to the TNT material.

Table 6.1: Physical characteristics of Ag/TNT nanocomposites.

Sample	Weight ratio of AgNO$_3$ to TiO$_2$ nanotube	Ag/TiO$_2$ nanotube composite		
		[a] Ag content (wt%)	[b] Ag particle size (nm)	[c] Ag crystallite size (Å)
Ag/TNT-1	1:16	0.95	32.39 ± 15.88	2.72
Ag/TNT-2	1:10	1.15	35.98 ± 12.82	3.02
Ag/TNT-3	1:5	4.04	54.50 ± 16.10	4.74
Ag/TNT-4	1:1	9.73	82.23 ± 25.79	11.88
Ag/TNT-5	2:1	16.38	82.11 ± 25.66	10.64
Ag/TNT-6	4:1	13.78	82.55 ± 31.60	13.15
Ag/TNT-7	10:1	15.22	103.55 ± 24.94	12.03

Note:
[a] The Ag wt% was determined from EDX analyses of 3 different spots.
[b] The average size of the Ag nanoparticle supported on TiO$_2$ nanotubes was determined from measurements of at least 30 points.
[c] The crystallite size of the Ag nanoparticle supported on TiO$_2$ nanotubes was calculated from Scherrer's equation after correcting for peak broadening caused by instrumentation factor.

Elemental spot analyses were performed on Ag/TNT-3 to ascertain the location of metallic silver particles on the samples. As shown in Figure 6.4, the spheroidal bright white spots show a high density of elemental Ag (~ 16.5 wt% Ag in Figure 6.4B). Interestingly, the grey area without any discernible bright spots also shows a relatively high amount of Ag (~ 12.4 wt% Ag in Figure 6.4C). This implies that the size of the Ag nanoparticle is too small to be observed with SEM and also, possibly, Ag is precipitated within the internal structure of the TiO$_2$ nanotube.
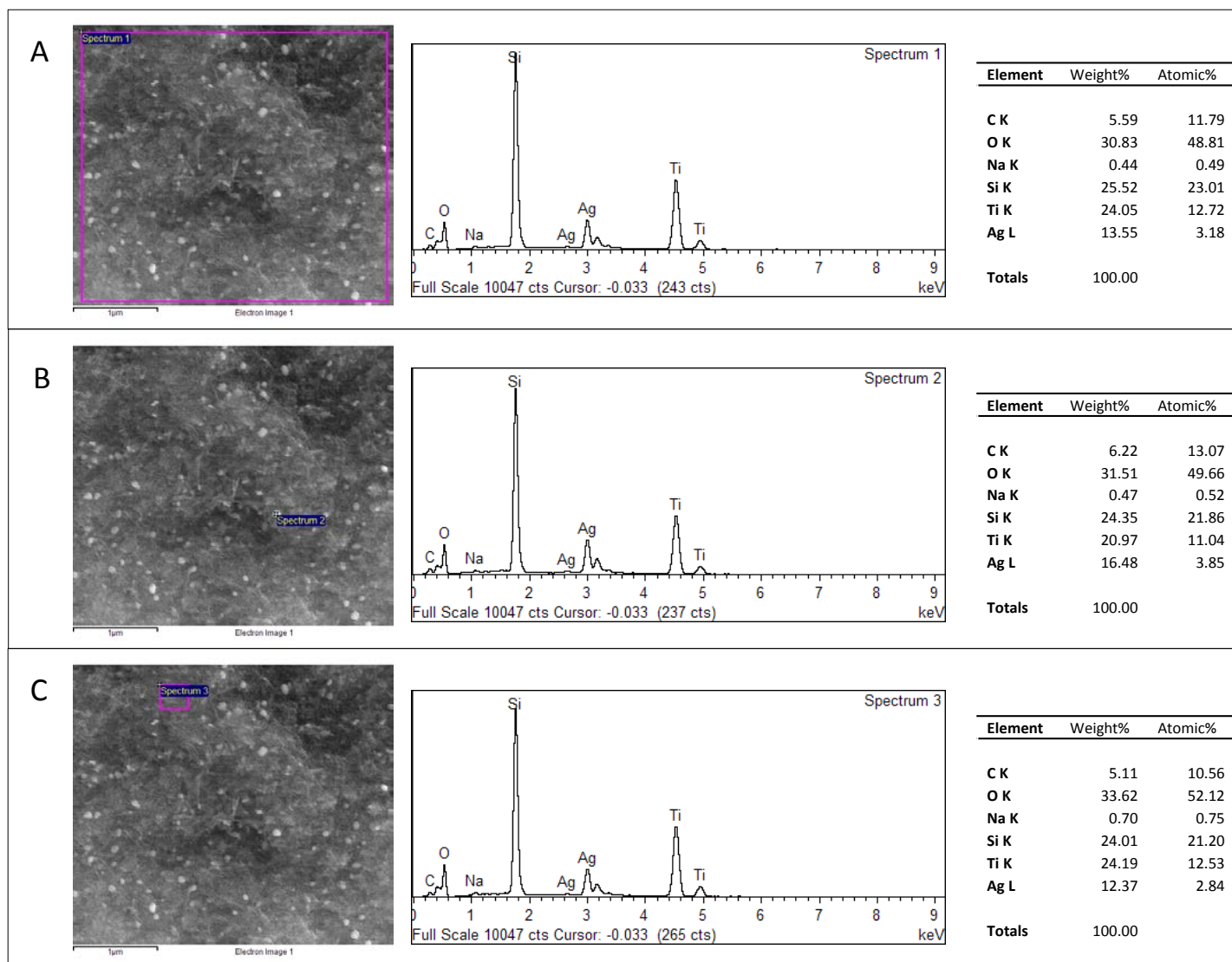
Figure 6.4: SEM imaging and EDX analysis of Ag-TiO$_2$ nanotubes (Ag/TNT). The Ag/TNT suspensions were dropped onto a silicon substrate for the analysis. (A) EDX analysis of Ag/TNT-3. (B) Spot analysis of a silver particle on the composite. (C) Spot analysis of nanocomposite with non-visible Ag section.

A

Element	Weight%	Atomic%
C K	5.59	11.79
O K	30.83	48.81
Na K	0.44	0.49
Si K	25.52	23.01
Ti K	24.05	12.72
Ag L	13.55	3.18
Totals	100.00	

B

Element	Weight%	Atomic%
C K	6.22	13.07
O K	31.51	49.66
Na K	0.47	0.52
Si K	24.35	21.86
Ti K	20.97	11.04
Ag L	16.48	3.85
Totals	100.00	

C

Element	Weight%	Atomic%
C K	5.11	10.56
O K	33.62	52.12
Na K	0.70	0.75
Si K	24.01	21.20
Ti K	24.19	12.53
Ag L	12.37	2.84
Totals	100.00	

The Ag content of all the Ag/TNT samples is also shown in Table 6.1. The amount of Ag in the samples was determined through EDX spot analyses of 3 different spots in each sample. The elemental Ag content ranging from 0.95 wt% in Ag/TNT-1 to 15.22 wt% in Ag/TNT-7, increases concordantly with the higher ratio of Ag precursor to the TiO_2 nanotubes used during the material syntheses. In addition, the low-magnification micrographs in Figure 6.5 show the presence of micron-sized free Ag particles (indicated with red arrows) in the Ag/TNT samples when the ratio of Ag precursor to the TiO_2 nanotubes is ≥ 1.

Low magnification TEM images in Figure 6.6A reveal hollow TiO_2 nanotubes with lengths ranging from ~ 60 nm to ~160 nm, while the high magnification TEM image in Figure 6.6B shows the open-ended nanotube with an inner and outer diameter of 4.9 nm and 14.8 nm respectively. In addition, the nanotube walls contain 4 to 5 layers, with the number of layers on both sides differing by one layer. These structural features and dimensions are comparable with trititanate nanotubes reported by Chen et al. [170].

The nanocomposite with the lowest Ag content, Ag/TNT-1 is shown in Figure 6.6C and Figure 6.6D. Spherical AgNPs with diameter of 2.9 ± 0.5 nm were observed along the outer walls of the TiO_2 nanotubes. The TiO_2 nanotubes are formed into scrolls by rolling up of single sheets of titanium oxide [315]. This phenomenon explains the difference in the number of layers, often by one, observed on both sides of the nanotube walls. The precipitation of metallic AgNPs on the surface of the TiO_2 nanotubes do not appear to distort the nanotube structure, indicating that the

nanotubes are suitable support structures for the formation of Ag-TiO$_2$ nanotube

composites.
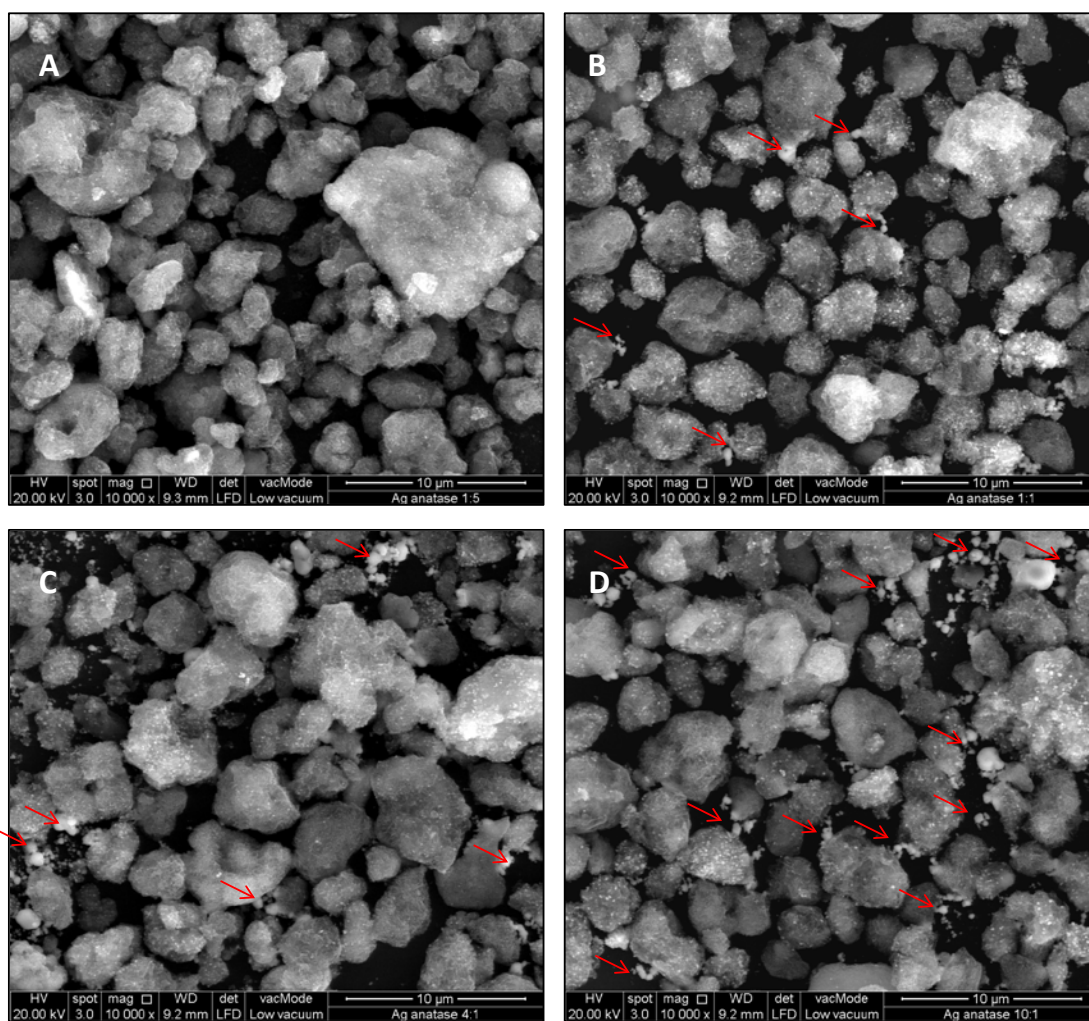
Figure 6.5: Low magnification scanning electron images of Ag/TNT samples. (A) Ag/TNT-3 with silver nitrate:TiO$_2$ nanotubes weight ratio of 1:5, (B) Ag/TNT-4, with equal proportions of silver nitrate and TiO$_2$ nanotubes, (C) Ag/TNT-6 with silver nitrate:TiO$_2$ nanotubes weight ratio of 4:1, and (D) Ag/TNT-7 with silver nitrate:TiO$_2$ nanotubes weight ratio of 10:1. The red arrows indicate the presence of micron-sized, free Ag particles.
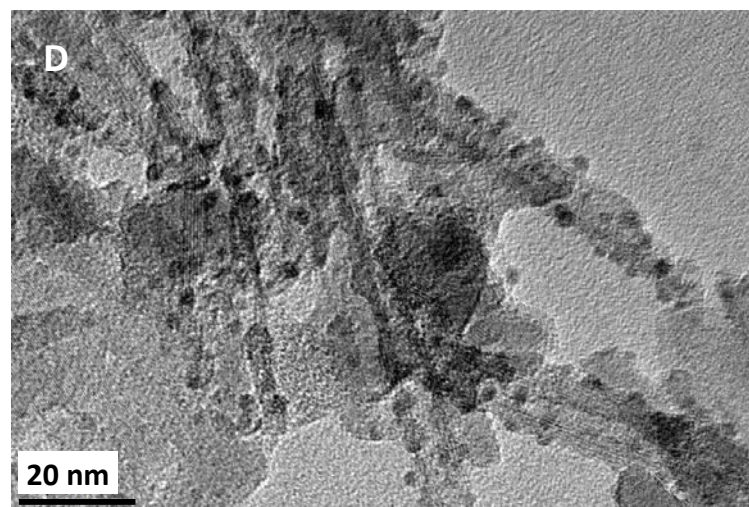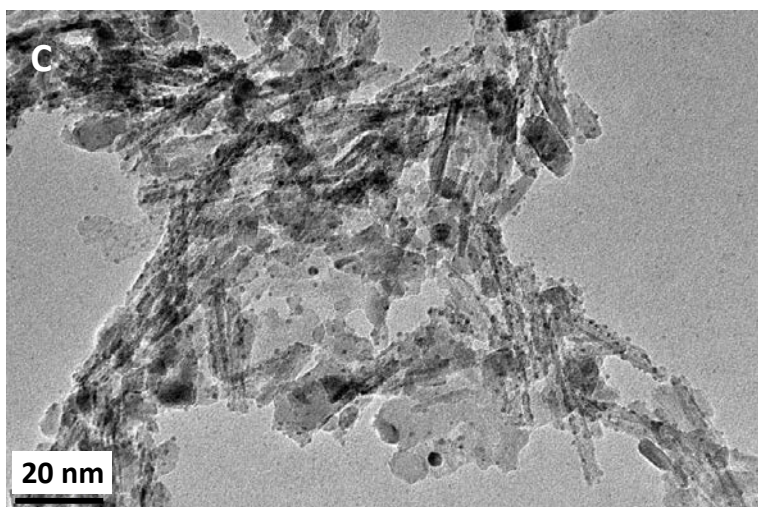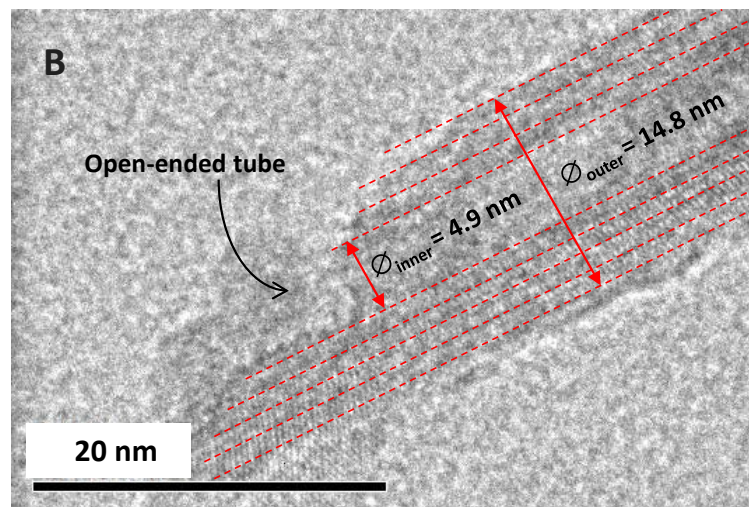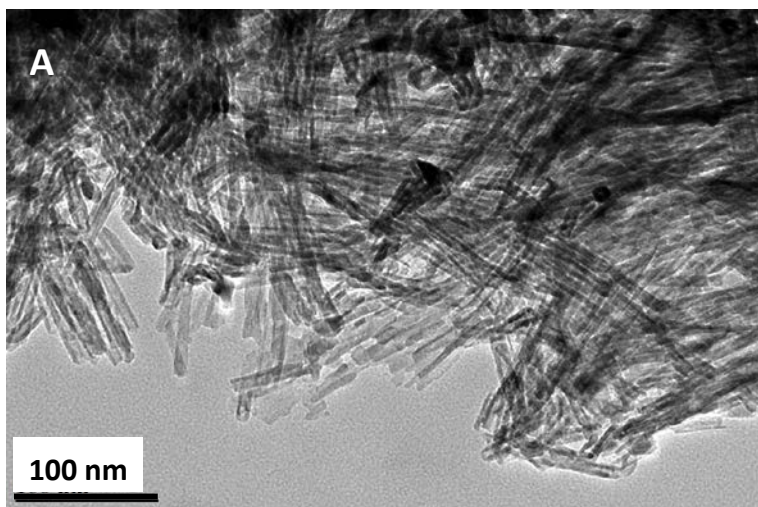
Figure 6.6: Transmission electron micrographs of Ag/TNT. (A) TiO$_2$ nanotubes, (B) high-resolution TEM image of a nanotube, (C) Ag/TNT-1 and (D) high-resolution TEM of Ag/TNT-1 showing spherical AgNPs on TiO$_2$ nanotube surfaces.

6.4   Crystallinity of Ag/TNT Composites

To determine the phase composition of the silver-TiO$_2$ nanotube material, X-ray diffraction was performed. The XRD spectra of the Ag/TNT materials are shown in Figure 6.7. The TiO$_2$ nanotube material exhibited relatively broad peaks at 2θ angles of 25.3°, 37.9°, 48.1°, 54.0°, 55.1°, 62.8°, 68.9°, 70.3° and 75.1°, which corresponded to TiO$_2$ (ICDD PDF 01-086-1157). In addition, broad humps (indicated by * in the spectra of Figure 6.7) are attributed to the phase known as TiO$_2$ (B) at 2θ angles of 13°, 30° and 43.7°. In fact, the first peak around $2\theta \approx 13$° is ascribed to the (0 0 1) plane in a TiO$_2$ (B) structure [317]. According to Morgado et al., heat treatment of trititanate nanotubes causes dehydration and structural changes in the intermediate titanate phases which rearrange into the more condensed TiO$_2$ (B) structure [317].

After the addition of silver nitrate to the TiO$_2$ nanotubes and the subsequent hydrothermal reduction to form Ag/TNT, all the nanocomposite samples, apart from retaining the TiO$_2$ peaks, also exhibited the characteristic peaks for face-centred cubic (FCC) Ag (ICDD PDF 03-065-2871) at angles 2θ of 38.1°, 44.3°, 64.4° and 77.4°. As the ratio of silver nitrate to nanotube material was increased, the peaks assigned to the f.c.c. Ag were also observed to increase accordingly in intensity. In fact, the primary peak of Ag corresponding to the (1 1 1) f.c.c. Ag plane overlaps with the (0 0 4) plane of the TiO$_2$ crystal structure.
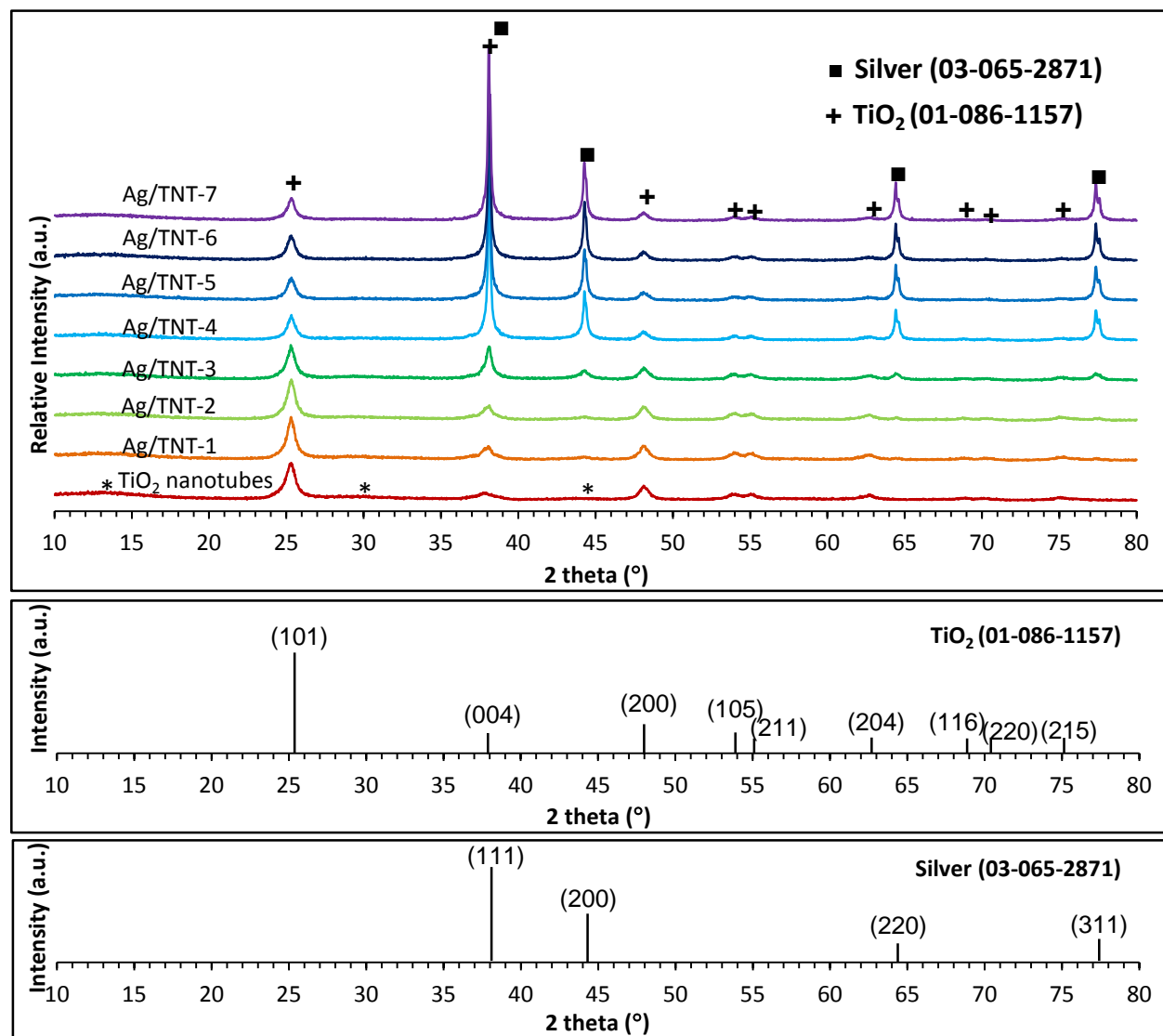
Figure 6.7: XRD spectra of TiO$_2$ nanotubes (TNT) and Ag/TNT composites.

■ represents the metallic Ag phase (ICDD PDF 03-065-2871).

+ represents the peaks for TiO$_2$ (ICDD PDF 01-086-1157).

∗ represents the broad peaks attributed to the metastable TiO$_2$ (B) phase.

The peaks for metallic Ag are enhanced, with greater amounts of Ag precursor, as observed by higher intensities, sharper peaks, and less broadening. These features indicate the formation of larger crystallites and longer range atomic order in the crystalline composite material.

The crystallite size of AgNPs supported on the nanotubes was calculated from Scherrer's equation (Equation 3.5) using the most intense peak for f.c.c Ag at $2\theta =$ 38.1°. As shown in Table 6.2, the Ag crystallite size tripled from 2.7 Å to 13.15 Å as the amount of silver precursor increased more than 60% from Ag/TNT-1 to Ag/TNT-6. In addition, the average crystallite size details calculated with each of the 4 main peaks of f.c.c. Ag are also provided in Table 6.2.

Table 6.2: Scherrer calculation of Ag crystallite size of Ag particles supported on TiO₂ nanotubes.

Sample	Position, x [°]	FWHM (sample)	FWHM (instrument)	Peak width, β	Ag crystallite size, D_{Ag} (Å)	Average crystallite size (Å)
Ag/TNT-1	38.051	0.730	0.054001	0.676	2.720	16.089
	44.202	0.551	0.057354	0.496	4.092	
	64.639	0.411	0.079361	0.332	10.195	
	77.417	0.242	0.101609	0.140	47.349	
Ag/TNT-2	38.068	0.663	0.054009	0.609	3.020	13.339
	44.255	0.700	0.057390	0.643	3.146	
	64.439	0.299	0.079065	0.220	15.261	
	77.590	0.313	0.101955	0.211	31.930	
Ag/TNT-3	38.104	0.442	0.054024	0.388	4.743	8.762
	44.280	0.592	0.057406	0.535	3.784	
	64.458	0.468	0.079093	0.389	8.636	
	77.344	0.471	0.101463	0.370	17.886	
Ag/TNT-4	38.105	0.209	0.054024	0.155	11.875	15.056
	44.302	0.270	0.057421	0.213	9.510	
	64.427	0.310	0.079047	0.233	14.526	
	77.374	0.374	0.101523	0.272	24.315	
Ag/TNT-5	38.116	0.227	0.054029	0.173	10.641	15.825
	44.305	0.278	0.057423	0.221	9.174	
	64.424	0.285	0.079043	0.206	16.287	
	77.369	0.345	0.101513	0.243	27.199	
Ag/TNT-6	38.105	0.194	0.054024	0.140	13.148	19.662
	44.290	0.243	0.057413	0.186	10.901	
	64.421	0.295	0.079038	0.216	15.531	
	77.367	0.271	0.101509	0.170	39.067	
Ag/TNT-7	38.100	0.207	0.054022	0.153	12.030	19.052
	44.282	0.245	0.057408	0.188	10.783	
	64.414	0.296	0.079028	0.217	15.455	
	77.365	0.276	0.101505	0.174	37.941	

6.5 Surface Area Analysis of Ag/TNT Composites

BET analysis was performed on selected Ag/TNT samples. Results shown in Table 6.3 indicate that the specific surface area of TiO_2 nanotubes as 161.9 m^2/g, comparable to values reported by Chen et al. [170], while the Ag/TNT composites have progressively lower specific surface areas, reduced to as low as 83.3 m^2/g for Ag/TNT-7. The reduction of surface area is attributed to the blockage of the nanotube ends by the precipitation and subsequent growth and agglomeration of AgNPs, especially in Ag/TNT-7 which has the highest concentration of Ag precursor.

Table 6.3: Surface area analysis of the TiO_2 nanotubes and the Ag/TNT composites.

Samples	BET Surface Area (m^2/g)
TiO_2 nanotubes	161.9
Ag/TNT-1	155.7
Ag/TNT-3	136.4
Ag/TNT-7	83.3

6.6 Optical Properties of Ag/TNT Composites

UV-visible absorption spectra of the pure TiO_2 nanotube and all the Ag/TNT samples are shown in Figure 6.8. The enhanced absorption of the Ag/TNT composites across the entire visible region is due to the presence of AgNPs. All the samples with equal or greater ratios of silver precursor to the titania nanotubes (Ag/TNT-4 to Ag/TNT-7) showed a maximum absorption peak between 420 nm to 427 nm, due to

the surface plasmon resonance (SPR) of conduction electrons on the surface of the AgNPs.

Furthermore, these samples exhibited a secondary absorbance peak in the absorption spectra at ~500 nm. This is due to the aggregation and agglomeration of AgNPs [306], which is corroborated by SEM images in Figure 6.5. On the other hand, when the silver precursor material ratio was lower than the starting amount of titania nanotubes (Ag/TNT-1 to Ag/TNT-3), there was no discernible absorption peak at the same regions. This is mainly due to the low concentration of AgNPs in the composite. The red shifting of the absorption edges of the Ag/TNT composites also suggest that the energy levels of TiO_2 nanotubes were adjusted [321]. Compared to the pure TiO_2 nanotubes, Ag/TNT composites absorb at longer wavelengths, which suggests that the band gap has been reduced through Ag-doping [69].
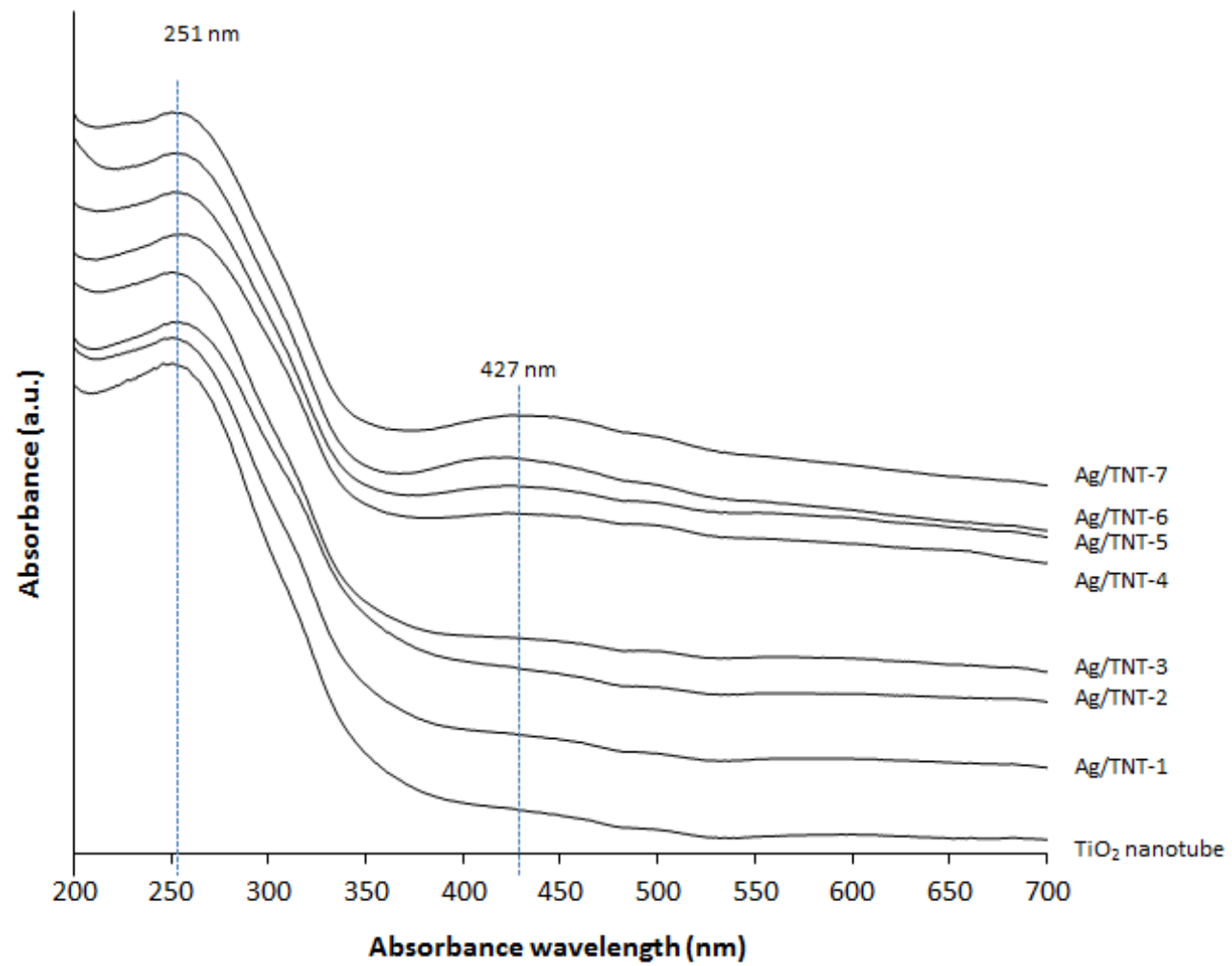
Figure 6.8: UV-visible absorption spectra of TiO₂ nanotubes and Ag/TNT composites.

6.7   Anti-Microfouling Properties of Ag/TNT Composites

To evaluate the antifouling effects of Ag/TNT composites, a static biofilm assay was carried out using *H. pacifica,* a common marine fouling organism. As shown in Figure 6.9, a concentration of at least 0.1 mg/mL of Ag/TNT significantly inhibited the biofilm formation of *H. pacifica* (P < 0.01, Student's *t*-test) while no such effect was observed in bacteria treated with TiO_2 nanotubes or bulk silver alone. The Ag/TNT composites with the lowest ratio of silver precursor to TNT (Ag/TNT-1 and Ag/TNT-2) were particularly potent against *H. pacifica* biofilm formation with an average inhibition of $98.47 \pm 0.11\%$ and $89.39 \pm 0.45\%$, respectively.

It is important to note that, the efficacy of biofilm inhibition was inversely correlated with the amounts of Ag loading, but rather, correlated well with the size of the AgNPs. Ag/TNT materials with smaller Ag nanoparticle sizes were more efficient biofilm inhibitors compared with their counterparts with larger AgNPs. The AgNPs from Ag/TNT-1 and Ag/TNT-2 were estimated from SEM to be ~ 30 nm in size, while TEM observations show that Ag particles as small as 3 nm were present within Ag/TNT-1. These observations support literature relating the size effect of AgNPs enhancing their antimicrobial properties [59, 322]. These results also show that TiO_2 nanotubes and bulk silver do not possess any antifouling quality. However, with a minimal doping of approximately 1 wt% AgNPs on the titania nanotubes, an effective biofilm inhibitor was formed which is able to prevent microfouling. This is believed to be due to the 1-dimensional nanotube structure carrying sub-3 nm AgNPs which are able to penetrate the bacterial cell structure and disrupt cellular activities.
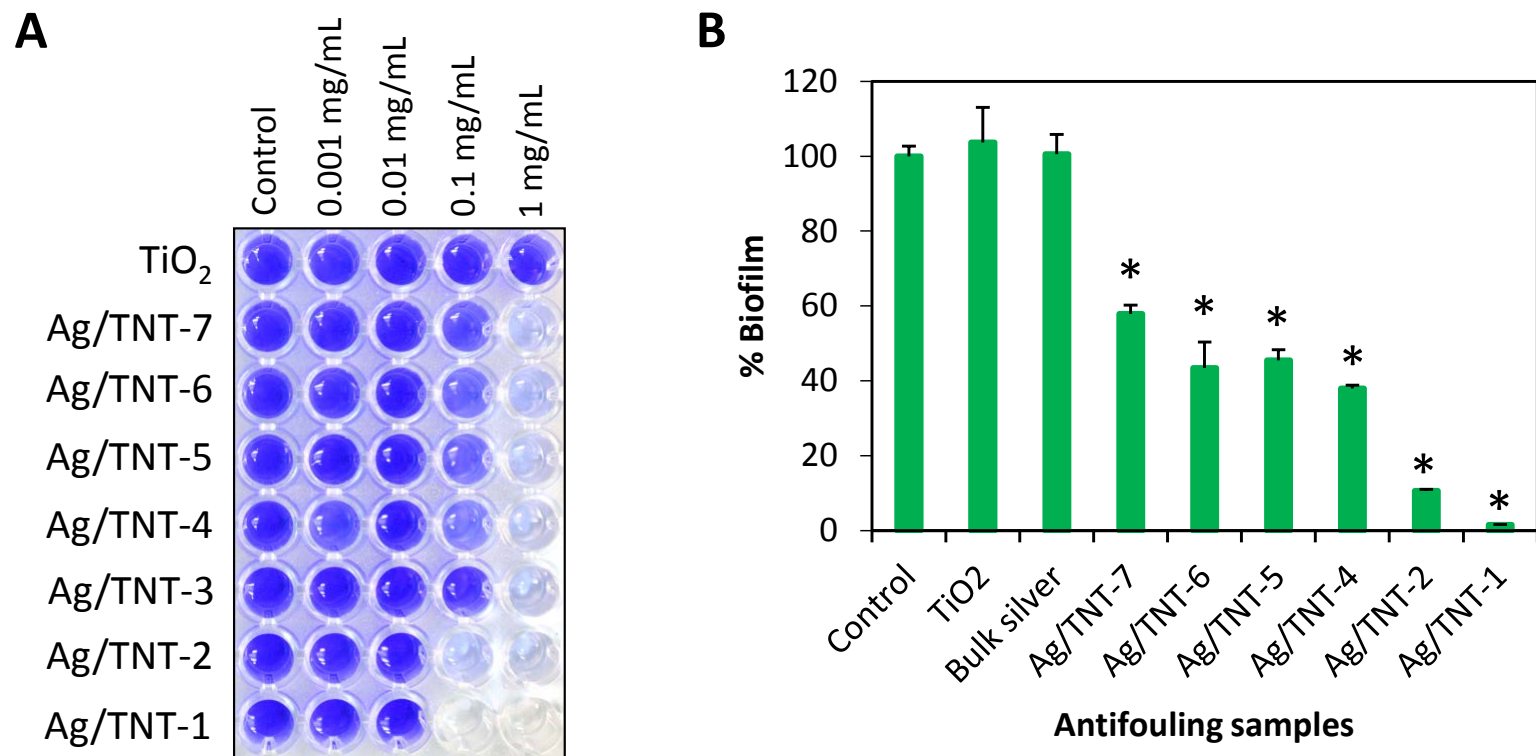
Figure 6.9: Effect of Ag/TNT composites on marine bacteria. (A) Biofilm staining with crystal violet. The picture was taken after dissolution of crystal violet-stained biofilms with 30% acetic acid. Biofilm formation was assessed at 0.001 mg/mL, 0.01 mg/mL, 0.1 mg/mL, and 1 mg/mL Ag/TNT composites. (B) Quantification of biofilm formation following treatment with 0.1 mg/mL of $AgTiO_2$ composites. Bars represent mean ± s.d. of at least three independent experiments. * indicates statistical significance compared to control (P < 0.01, Student's *t*-test).

Finally, the biological effects of Ag/TNT composites on 2 common marine microalgae, *D. tertiolecta* and *Isochrysis sp*. were also evaluated. As shown in Figure 6.10, a concentration of 0.1 mg/mL of Ag/TNT-1 and Ag/TNT-2 induced significant morphological changes and growth inhibition in both *D. tertiolecta* and *Isochrysis sp.* while no such effect was observed in microalgae treated with TiO_2 nanotubes alone. These results suggest that Ag/TNT composites possess antifouling properties on fouling microalgae as well as fouling bacteria.
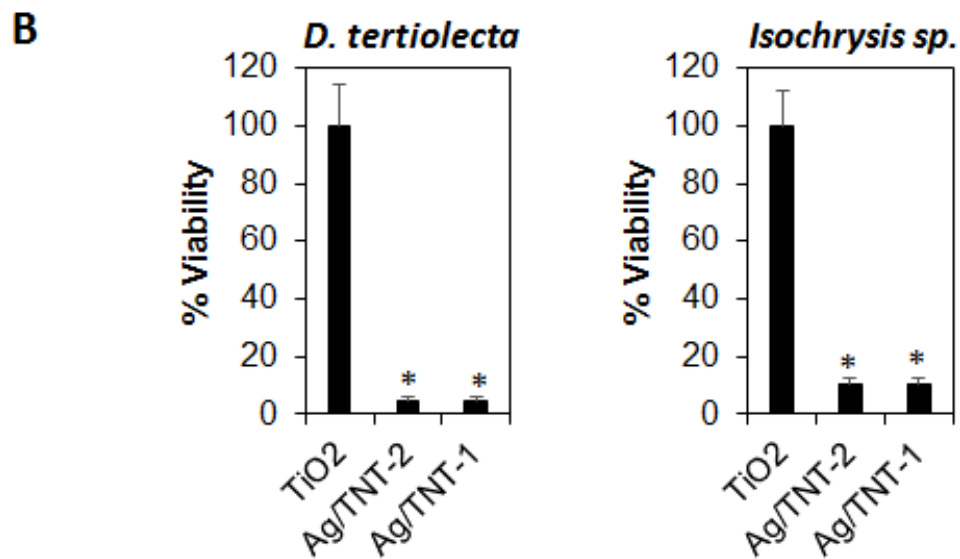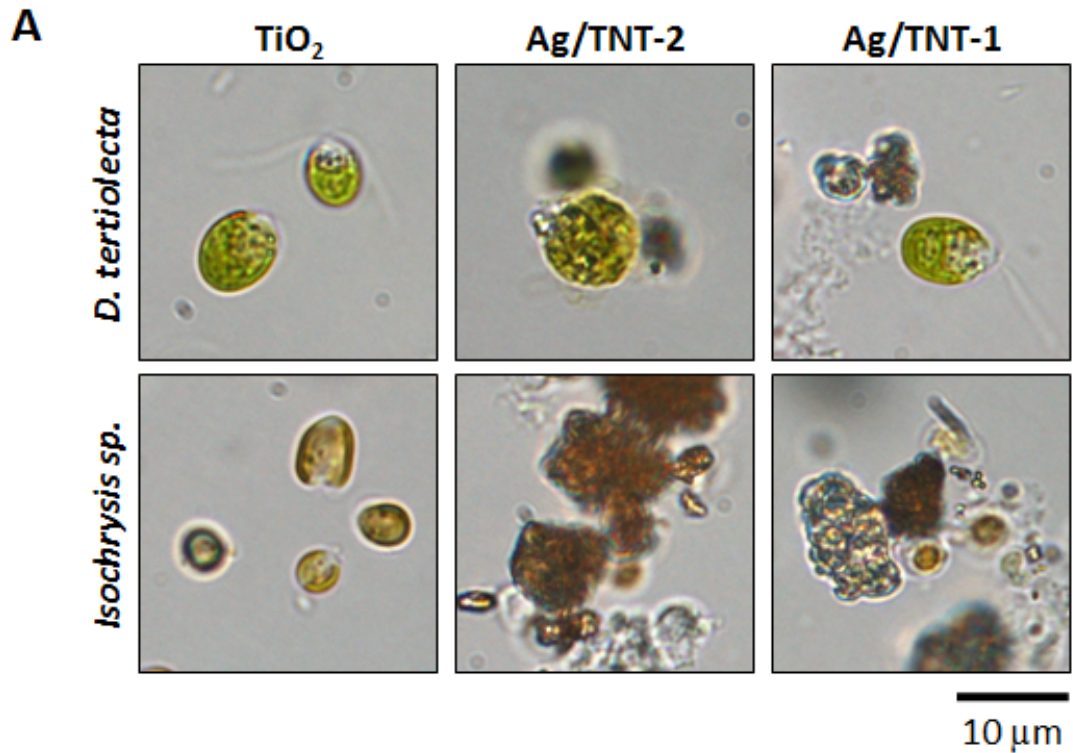
Figure 6.10: Effects of Ag/TNT composites on marine microalgae. Ag/TNT composites induced (A) morphological changes and (B) growth inhibition of *D. tertiolecta* and *Isochrysis sp.* Algal cells were exposed to 0.1 mg/mL of Ag/TNT-1 or Ag/TNT-2 for 72 h and the number of cells was determined by Presto Blue® stain and spectroscopy. Points represent mean of ± s.d. of at least 3 independent experiments.

6.8   Summary

Ag-TiO$_2$ nanotube composite materials were successfully synthesized using a novel 2-step hydrothermal synthetic process. TiO$_2$ nanotubes were directly produced from anatase phase through an alkaline hydrothermal process, before it was used as a support structure for the hydrothermal reduction of AgNPs to form a nanotubular composite for marine antifouling applications.

UV-visible analyses of the composites showed an enhancement of wavelength absorption across the entire visible spectrum due to the addition of Ag to the TiO$_2$ nanotubes, with reduction of the TiO$_2$ band gap. Electron microscopy methods revealed the nanocomposites were composed of nanotubular TiO$_2$ structures with AgNPs uniformly dispersed throughout the material. The AgNPs were estimated to be between 32 – 103 nm in diameter (SEM imaging) whilst TEM images showed AgNPs measuring ~3 nm. Crystallite size of the AgNPs was estimated to be between 2.7 – 12 Angstroms. XRD phase analysis displayed the presence of face-centred cubic Ag and TiO$_2$ only, confirming the purity of the samples.

Compared to pure bulk silver and pure TiO$_2$ nanotubes, the Ag/TNT composite with the lowest concentration of Ag and having the smallest AgNPs, displayed the most promising antimicrofouling behaviour, as it interfered with bacterial biofilm formation. The effectiveness of the biofilm inhibition was directly related to the Ag nanoparticle size. The Ag/TNT composites also showed increased growth inhibitory activity against marine microalgae compared to pure TiO$_2$ nanotubes. This work shows that TiO$_2$ nanotubes are a stable and effective support for

anchoring and growth of the AgNPs. The addition of very low amounts of Ag enhanced the antifouling property of pure TiO_2 to produce an extremely potent antifouling effect on the targeted organisms.

Chapter 7: Green Synthesis of Graphene-Silver Nanocomposite and its Potent Antifouling Effect on Marine Bacteria and Microalgae

7.1   Introduction

After the previous three chapters' discussion on silver nanocomposites grown on three-dimensional and one-dimensional support structures and their potential as marine antifouling agents, this chapter centres on graphene, a 2-dimensional carbon structure, as a layered support for AgNPs. Graphene is the world's first two-dimensional material, first isolated by Novoselov et al. [181] in 2004. In the past decade, it has garnered worldwide attention for its intriguing combination of electrical, mechanical and chemical properties [182]. It has a high inherent strength of 0.142 Nm along the direction of π-carbon bonds, an ultimate tensile strength of 130 GPa, electron mobility up to 2.5 x 10^5 $cm^2V^{-1}s^{-1}$, thermal conductivity greater than 3000 WmK^{-1}, Young's modulus of 1 TPa, and capable of sustaining high current densities [323].

Their potential applications span a far-ranging spectrum, from components of flexible electronics [324], energy storage [325] and conductive inks [326], to biomedicine [327, 328], corrosion prevention [323] and aerospace technologies [329].

7.1.1   Graphene Materials

Graphene is considered as the archetypical nanostructure within the family of carbon nanostructures, among them are the fullerenes, carbon nanotubes as well as graphene quantum dots. The family of graphene materials encompass pristine graphene sheets, few-layer graphene (FLG) flakes, graphene oxide and many other graphene derivatives. In fact, graphene can be classified as single-, double- and few- (3 to 9) layer graphene, based on their distinctive electronic spectra, whilst thicker structures are considered as thin films of graphite [182]. The graphene structure is shown in Figure 7.1.
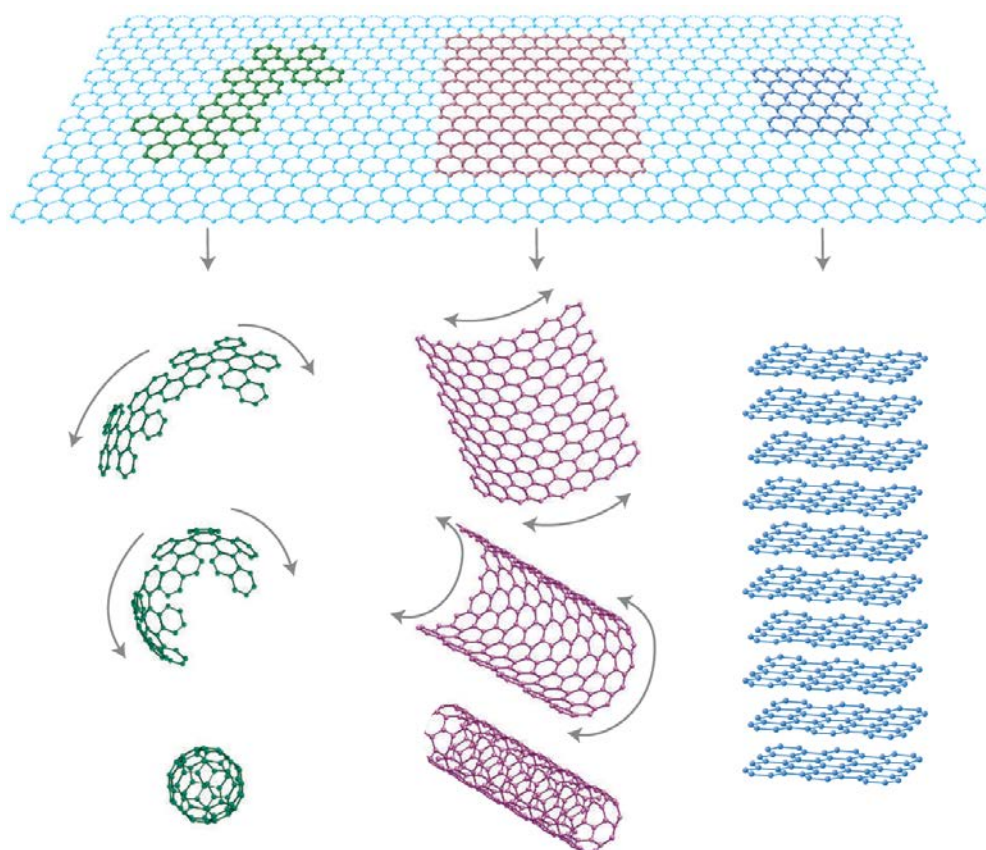
Figure 7.1: Two-dimensional graphene is the basis of all forms of carbon nanostructures. It can form the zero-dimension fullerenes (Buckyballs), rolled into 1-D nanotubes or stacked as 3-D graphite. (Figure taken from Geim & Novoselov [182]).

Such 2-D materials were considered thermodynamically unstable and thus a physical impossibility over 80 years ago, until their experimental discovery. These 2-D crystals become intrinsically stable by gentle warping in the third dimension, leading to a gain of elastic energy but a suppression of thermal vibrations [182].

Graphene was first isolated through mechanical exfoliation using the 'scotch tape method' of highly oriented pyrolytic graphite, which produced relatively large pieces (up to 10 μm) of atomically-thin layers of FLG. This technique is simple and low-cost, which sparked an explosive growth in graphene research. However, the method is not suitable for scale-up applications. Large scale production of graphene and FLG have been obtained through chemical vapour deposition (CVD) on catalytic metal surfaces such as Cu [201]. Due to the minimal solubility of C in Cu, monolayer graphene is grown on the catalytic Cu surface. However, graphene needs to be transferred to an appropriate insulating substrate, a process which negatively impacts the integrity, properties and performance of graphene [330]. Graphene has also been grown on semiconducting SiC wafers, a method which has managed to produce single crystal graphene layers across the wafer, and at the same time, the graphene layer can be used *in situ* without requiring transfer to an insulating substrate [330].

Researchers have also relied on wet chemistry methods, such as that proposed by Hummers & Offeman [331] as a reliable route to produce large quantities of graphite oxide. However, these production methods use harsh acids, involve multiple processing steps and release toxic gases, posing risks to researchers and the environment [332]. In addition, graphene oxide is decorated with various functional groups such as hydroxyls and epoxides, which though removable through reduction

methods, have a tendency to leave a significant number of residual defects [333].

More recently, sonochemistry has been adopted in the preparation of pristine graphene flakes through direct exfoliation of natural graphite in organic solvents including N-methyl-pyrrolidone [333], or a mild mixture of water and ethanol [183].

7.1.2   Graphene for *in-situ* Synthesis of Ag Nanoparticles

The literature on graphene-silver nanocomposite materials is crowded with reports of AgNPs grown on graphene oxide precursors [84, 145, 149-151, 186-188]. The synthesis mostly progressed after a graphene oxide precursor was reduced via chemical methods [84, 149-151, 196, 198, 334-336] or physical methods [186, 187, 337]. Reduced graphene sheets have a strong tendency to agglomerate, due to van der Waals interactions. Introduction of inorganic or metallic species onto the graphene surfaces inhibits their agglomeration [150, 334].

Reduced-graphene oxide decorated with AgNPs have been used for the detection and catalysis of hydrogen peroxide [148, 337], and in food safety for the detection of melamine [84] and prohibited colourants [151]. AgNPs on GO sheets have been reported as promising fuel cell applications [146, 193]. The retention of antimicrobial properties of free AgNPs after their growth on graphene demonstrates their potential as biomaterials [149].

7.1.3   Rationale of Study

In the last decade, there has been explosive growth in graphene-related research, especially in applications that take advantage of its unique electronic properties. However, comprehensive studies on antifouling properties of graphene-silver nanomaterials remain scarce. Although AgNPs have well-documented antimicrobial activity, their effect on biofouling marine bacteria and microalgae, especially when incorporated with a 2-dimensional flexible structure as graphene, has not been fully explored. This report is an investigation into the marine antifouling properties of AgNPs supported on few-layer graphene sheets.

A novel, facile and green method to produce graphene-silver nanomaterials using a hydrothermal reduction of AgNPs on pristine few layer graphene is presented. Graphene is produced through an optimized ethanol-deionized water, mixed-liquid phase exfoliation of graphite [183]. The graphene-silver (GAg) composite synthesis method incorporates a low energy exfoliation method with a low temperature hydrothermal processing approach. This technique completely bypasses the formation of GO. Through a direct exfoliation of graphite, graphene is produced and used as the substrate for the templated growth of metallic nanoparticles. This environment-friendly method is enhanced with the use of sodium citrate as a mild reducing agent for the formation of AgNPs on the graphene surface.

7.1.4 Synthesis Parameters

Various weight ratios of silver nitrate powder to graphene were used as the varying parameter in the synthesis of GAg nanocomposites. A fixed concentration of sodium citrate was used as a mild reducing agent in the hydrothermal reduction process. Further details of the synthesis have been discussed in Section 3.2.4.

7.2　Synthesis of Graphene-Silver Nanocomposites

Figure 7.2 shows a schematic of the two-part procedure to prepare graphene-silver nanocomposites. First, graphene is prepared using a novel sonochemical-assisted liquid exfoliation method in an optimized mixture of 2 parts ethanol and 3 parts deionized water. Exfoliation of bulk graphite into few layer graphene was achieved through lowering of the Hansen Solubility Parameters (HSPs) of graphite in the optimized ethanol-water mixture [183]. Graphene sheets are produced when the magnitude of the shear forces from the 2-hour ultrasonication treatment exceeded the binding energy of the bulk graphite layers.

The graphene flakes were redispersed in the ethanol-water mixture to form a dark grey suspension. After the addition of silver nitrate and trisodium citrate, no physical change was discerned in the suspension. After the completion of the hydrothermal treatment and subsequent cooling, dark grey to black solid precipitates were sedimented in clear liquid.

The reduction of Ag ions-doped graphene nanocomposites took place via a citrate chemical reduction route according to Equation 7.1:

$$4Ag^+/graphene + C_6H_5O_7Na_3 + 2H_2O \xrightarrow{\Delta} 4Ag^0/graphene + C_6H_5O_7H_3$$
$$+ \ 3Na^+ + H^+ + O_2 \uparrow$$
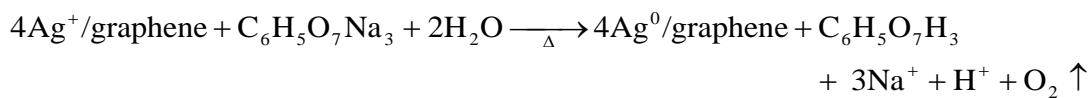
…. Equation 7.1

Chemical reduction of the Ag ions to metallic Ag is achieved through the donation of electrons from the citrate reducing agent. Citrate acts as a capping agent and influences the particle size and shape of AgNPs and nanoalloys [307, 318-320]. The graphene acts as a stable surface to support the deposition of AgNPs and increases the active surface area of the composite. At the same time, the presence of AgNPs prevents the aggregation of graphene.
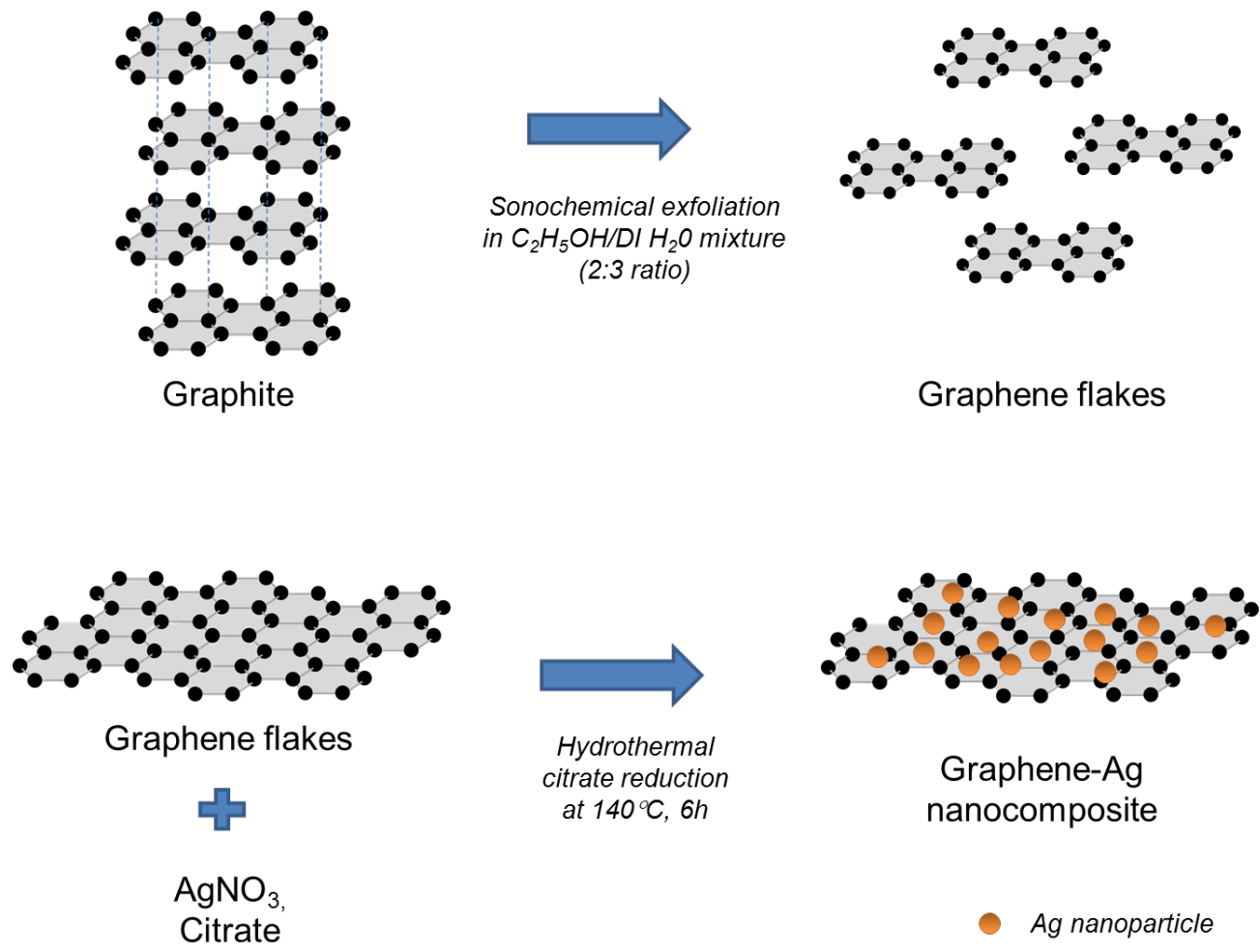
Figure 7.2: A scheme (not to scale) of the synthesis process for few-layer graphene (FLG) flakes and hydrothermal reduction process for the formation of graphene-Ag nanocomposite.

7.3 Morphology and Chemical Content of GAg Composites

The morphology of the graphene and GAg nanocomposite samples was observed under scanning electron microscopy as shown in Figure 7.3. SEM imaging reveals that the graphene sample consisted of few-layer graphene (FLG) flakes with pristine surfaces. This is due to the sonochemical-assisted exfoliation of graphite flakes using the water-ethanol mixture, which gently exfoliates the graphite, resulting in the preservation of large pieces of pristine graphene on the micron scale [183].

After the addition of silver nitrate and undergoing hydrothermal reduction with citrate, the Ag particles are supported on the surface of the micron-sized FLG flakes (Figures 7.3B – 7.3E). The chemical composition of the composites were analysed by EDX. The peaks of C and Ag in the EDX spectrum show only the presence of carbon and silver elements, confirming the purity of the composite (Figure 7.3F). The peak attributed to Si is due to the silicon substrate used to load the graphene-silver nanocomposite material for analysis. The amount of Ag loaded on the surface of the graphene flakes was quantitated through the EDX method as well.
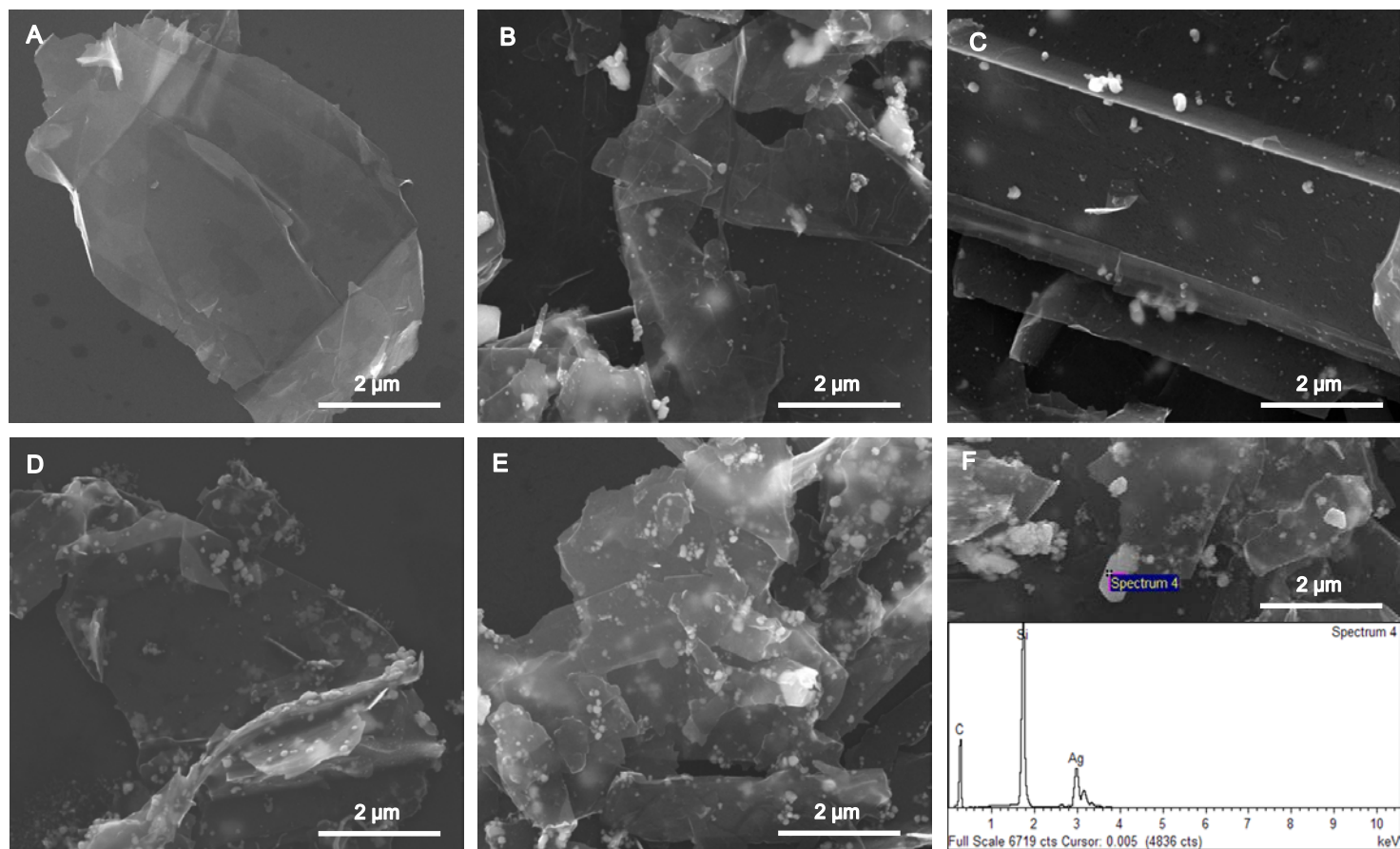
Figure 7.3: Morphology of the graphene and GAg nanocomposite samples observed under scanning electron microscopy. SEM images of (A) graphene and the graphene-silver composites. (B) GAg-1 with graphene:silver nitrate weight ratio of 1:3, (C) GAg-2 with graphene:silver nitrate weight ratio of 1:1, (D) GAg-3 with graphene:silver nitrate weight ratio of 4:1 and (E) GAg-4 with graphene:silver nitrate weight ratio of 10:1. (F) Spot analysis of a silver particle on a graphene flake. Graphene-silver dispersions were dropped onto a silicon substrate for SEM imaging and EDX analysis.

The quantity of the precipitated Ag particles supported on the graphene flakes are concordant with the starting amounts of silver nitrate used, ranging from 1.3 – 4.9 wt.% Ag (Table 7.1), indicating that the yield of Ag nanomaterial is consistent with the stoichiometry as shown in Equation 7.1. Additional analysis from SEM images showed a gradual increase of AgNPs distributed on the surface of the graphene, with the average size of the AgNPs less than 90 nm (Table 7.1). The larger Ag nanoparticle size distribution is due to the use of a low concentration of citrate. Although citrate is an effective stabilizer, obtaining good quality, discrete nanoparticles with a narrow distribution is formed within a small range of citrate concentration of 1 to 5 x 10^{-4} M [318]. Importantly, the integrity and size of the graphene flakes appear to be retained after the hydrothermal processing and the incorporation of AgNPs, suggesting that the graphene material is suitable as a stable substrate for the formation of graphene-Ag nanocomposites.

Table 7.1: Physical characteristics of graphene-Ag (GAg) nanocomposites.

Sample	Weight ratio of graphene:Ag precursor	Graphene-Ag nanocomposite	
		[a]Ag content (wt%)	[b]Average Ag nanoparticle diameter (nm)
GAg-1	3:1	1.3	86.1 ± 20.4
GAg-2	1:1	1.6	72.1 ± 48.0
GAg-3	1:4	2.5	76.0 ± 22.9
GAg-4	1:10	4.9	76.5 ± 24.2

Note:
[a] The Ag wt% was determined from EDX analyses of 3 different spots.
[b] The average size of the Ag nanoparticle supported on graphene nanosheets is determined from measurements of 100 points.

Graphene and GAg-4 nanocomposite samples were observed under transmission electron microscopy to further elucidate their morphology and structure. Figure 7.4A shows the relatively large micron-sized FLG sheets in pristine condition, complementary with the SEM observations. In addition, after hydrothermal processing and doping with Ag, the structure of the graphene sheets appears to be retained, with some slight curling of the graphene edges (Figure 7.4B). The scrolling of graphene nanosheets has been ascribed to a higher thermodynamic stability due to the 2-dimensional structure of graphene [338].

The AgNPs appear to have a random distribution across the graphene surface, with the appearance of several large aggregates. This is most likely due to the highest amount of silver precursor used in conjunction with the high concentration of citrate used as both reducing agent and stabilizer. According to Henglein [318], large lumps of Ag are formed through the coalescence of destabilized smaller Ag particles. However, all Ag particles were observed to be anchored on the graphene substrate, with no free Ag particle being detected. This suggests that graphene is a suitable substrate material for supporting the growth of AgNPs.

The average particle size of AgNPs in GAg-4 is estimated to be 18.1 ± 1.3 nm. At high resolution analysis, the fringe spacing of approximately 0.235 nm corresponding to the (1 1 1) lattice plane for FCC Ag crystal was able to be discerned (Figure 7.4C). The particles also appeared to have lattice arrangements in different orientations, leading to polycrystalline particles. The smaller crystallite size of approximately 1 nm is similar to the value estimated through Scherrer's equation.
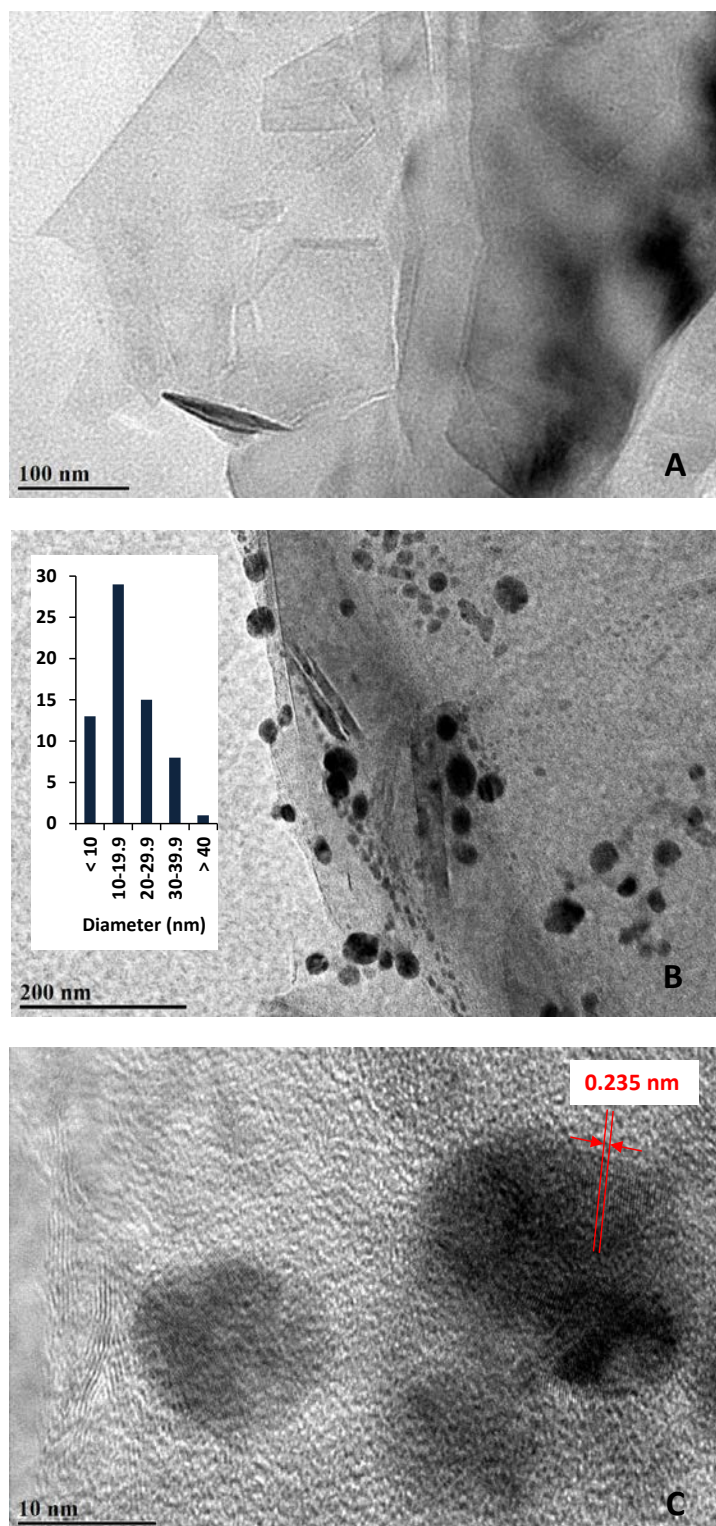
Figure 7.4: Morphology of the graphene and GAg nanocomposite samples observed under transmission electron microscopy. (A) TEM image of graphene shows micron-sized pristine few-layer graphene sheets, (B) TEM image of GAg-4 graphene-silver nanocomposite with AgNPs having an average diameter of 18.1 ± 1.3 nm supported on the graphene surface, and (C) HRTEM image of GAg-4 reveals the lattice spacing corresponding to the (1 1 1) lattice planes of face-centred cubic Ag.

7.4   Crystallinity of GAg Composites

To determine the phase composition of the graphene-Ag nanocomposites, X-ray diffraction analysis was performed. The XRD spectra of the GAg materials are shown in Figure 7.5. The graphene sample exhibited relatively broad diffraction peaks at 2 theta angles of 26.5°, 44.5° and 54.6°, which corresponded to the (0 0 2), (1 0 1) and (0 0 4) family of planes respectively in graphite 2H (ICDD PDF 00-041-1487), as both graphite and graphene possess a similar crystal structure [339].

The GAg samples also exhibited the characteristic peaks for face-centred cubic (FCC) metallic Ag (ICDD PDF 03-065-2871) at angles 2 theta of 38.1°, 44.3°, 64.4° and 77.4°. These peaks corresponded to the (1 1 1), (0 0 2), (0 2 2), and (1 1 3) reflection planes of cubic Ag respectively, indicating that metallic silver was successfully formed without the production of other compounds.

The presence of the graphene diffraction peaks at 26.5° and 54.7° 2 theta angle, corresponding to the (0 0 2) and (0 0 4) family of graphite planes respectively, was clearly observed on the diffraction patterns of the GAg samples as well. In addition, the diffraction peak at 2 theta angle of 44.3°, corresponding to the (1 0 1) family of graphite planes was obscured by the relative prominence of the (0 0 2) planes of cubic Ag. These results clearly show that the crystalline structure of the graphene substrate was retained during the hydrothermal processing.

The crystallite size of Ag nanocrystalline particles was estimated through Scherrer's equation using the diffraction peaks attributed to the Ag planes. The peak

225

width is inversely proportional to the crystallite size of nanocrystalline samples [276]. However, besides crystallite size, peak broadening is also attributed to the instrumental profile and microstrain of the sample [274]. Peak broadening due to the instrumental contribution at position 2 theta of 38.1° was 0.054. Using the corrected peak width and applying Scherrer's equation (Equation 3.5, discussed in Chapter 3) led to estimated crystallite sizes ranging from 1 – 2 nm for the AgNPs.

The estimated crystallite sizes for the GAg samples using a single Ag peak at position 2 theta = 38.1° is presented in Table 7.2, with the crystallite sizes increasing from about 1 nm to 2 nm, concordant with the increasing amounts of silver precursor. The average crystallite size was also estimated using the 4 main peaks of the Ag phase. The Ag crystallites are increasing in size from 1.3 nm for GAg-1 to greater than 4 nm for GAg-3 and up to 4.85 nm for GAg-4 (Table 7.3), with greater crystallite sizes estimated at larger 2 theta angles (Table 7.4) [277].
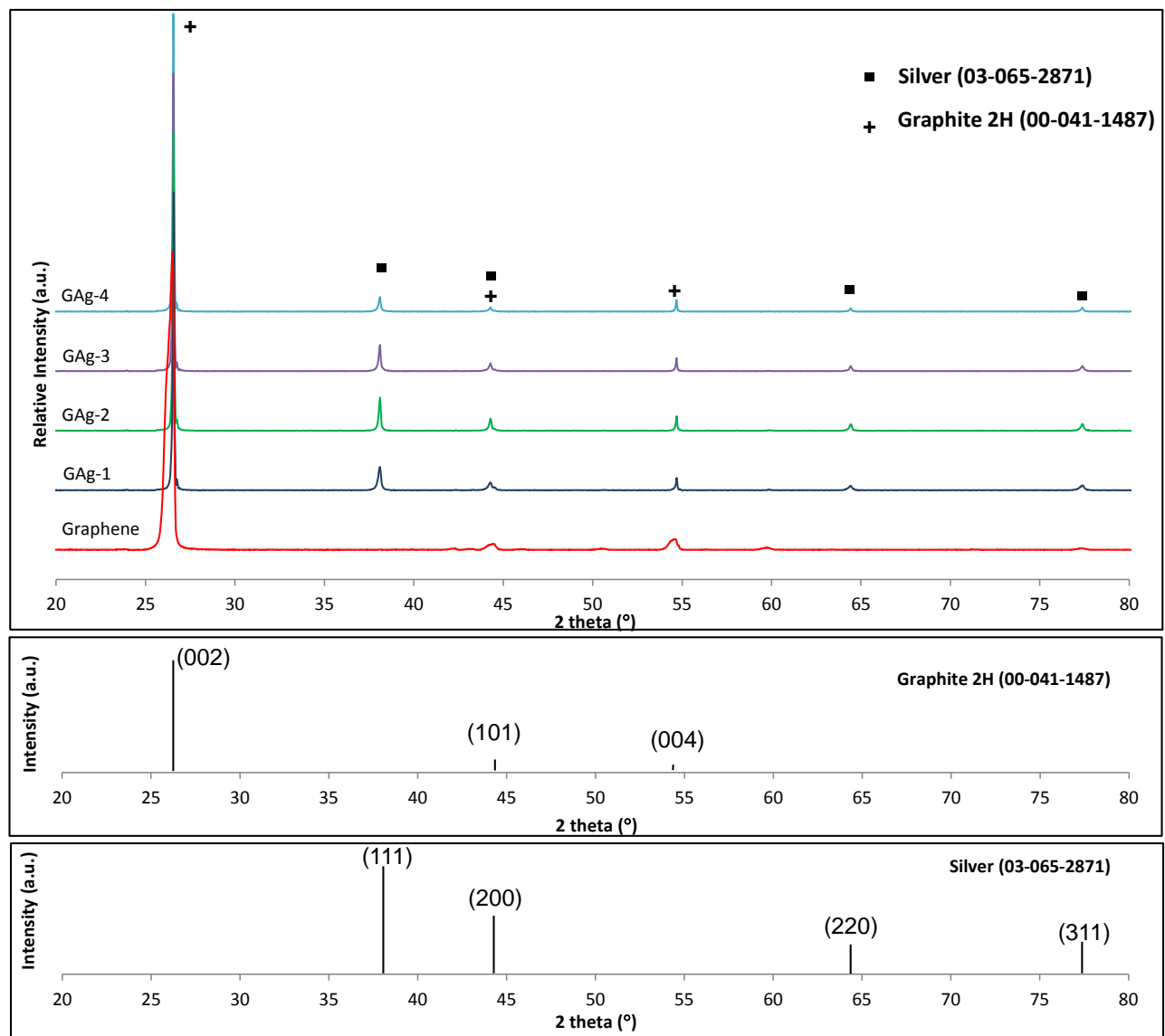
Figure 7.5: XRD spectra of graphene and GAg nanocomposites.
■ represents the metallic silver phase (ICDD PDF 03-065-2871 reference file for Ag).
[+] represents the principal peaks for graphite phase (ICDD PDF 00-041-1487).

Table 7.2: Ag crystallite size calculated from peak broadening of a single peak at $2\theta = 38.1°$.

Sample	Position, x [°]	FWHM (sample)	FWHM (instrument)	Peak width, β	Ag crystallite size, D_{Ag} (nm)
GAg-1	38.1020	0.1968	0.0540	0.1428	1.0274
GAg-2	38.1008	0.1476	0.0540	0.0936	1.5676
GAg-3	38.0947	0.1230	0.0540	0.0690	2.1265
GAg-4	38.0960	0.1230	0.0540	0.0690	2.1266

Table 7.3: Average crystallite size of Ag calculated from peak broadening of 4 peaks.

Sample	Graphene:Ag weight ratio	Ag average crystallite size (nm)
GAg-1	3:1	1.248 ± 0.292
GAg-2	1:1	2.859 ± 1.118
GAg-3	1:4	4.105 ± 2.877
GAg-4	1:10	4.850 ± 3.283

Table 7.4: Estimation of Ag crystallite size for all GAg samples.

Sample	Position, x [°]	FWHM (sample)	FWHM (instrument)	Peak width, β	Ag crystallite size, D_{Ag} (nm)
GAg-1	38.1020	0.1968	0.0540	0.1428	1.03
	44.2858	0.1476	0.0574	0.0902	1.66
	64.4251	0.2100	0.0790	0.1310	1.25
	77.3912	0.2700	0.1016	0.1684	1.05
GAg-2	38.1008	0.1476	0.0540	0.0936	1.57
	44.2821	0.1230	0.0574	0.0656	2.28
	64.4299	0.1230	0.0791	0.0439	3.73
	77.3813	0.1476	0.1015	0.0461	3.86
GAg-3	38.0947	0.1230	0.0540	0.0690	2.13
	44.2786	0.1230	0.0574	0.0656	2.28
	64.4282	0.1230	0.0790	0.0440	3.73
	77.3885	0.1230	0.1016	0.0214	8.28
GAg-4	38.0960	0.1230	0.0540	0.0690	2.13
	44.2806	0.0984	0.0574	0.0410	3.65
	64.4250	0.1200	0.0790	0.0410	4.00
	77.3797	0.1200	0.1015	0.0185	9.62

7.5   Raman Spectroscopy of GAg Nanocomposites

Apart from microscopy techniques which allow surface investigation of the graphene nanocomposite material, Raman spectroscopy is an established tool in the characterization of graphene and graphene-based materials due to their ability to probe the number of layers present in the material [281]. Apart from that, Raman spectroscopy allows the identification of a substance through a characteristic "fingerprint" spectrum, arising from the particular way the molecular vibration in a substance causes a shift in the wavelength of the incident laser light [151].

In the Raman analysis of graphene, three characteristic peaks are prominent: the D peak at wavenumber ~1350 cm^{-1}, the G peak at ~1580 cm^{-1} and the G' peak at ~2720 cm^{-1}, as shown in Figure 7.6. The D peak arises primarily from the existence of defects and disorder, particularly the edge defects in graphene [282]. The G' peak provides information about the number of layers present in the graphene. Specifically, the broadness of the G' peak indicates the presence of few-layer graphene, in contrast to monolayer graphene which has a sharp, single Lorentzian G' peak [281].

The D and G bands of the composite material, with a layer of silver, increased by 68-fold and 8-fold, respectively, compared with the graphene which did not undergo processing. This is likely due to the surface enhanced Raman scattering (SERS) effect of AgNPs on the graphene surface. The SERS effect originates from the interaction of the AgNPs and the specific molecular vibrations of graphene, enhancing the intensity of Raman scattering of the composite material.

Resonant light excitation cause clusters of AgNPs to generate strong localized electric fields at the particle interfaces, an effect of plasmon coupling [340]. Due to the magnitude of the signal enhancement observed, the enhancement effect is likely due to the short-range chemical interactions between AgNPs and graphene. This Raman signal enhancement for GAg nanomaterial is consistent with the SERS effect previously reported in graphene-silver nanocomposites [84].

In addition, several weak bands within the 500 – 1000 cm^{-1} region, which are attributed to AgNPs, can be clearly observed in the spectrum (inset of Fig. 7.6). The main vibrational bands were at 555, 667, 743, 776, 807, 830, 890 and 913 cm^{-1}. The

SERS spectra of bare AgNPs from literature [341] display a group of similar weak bands in this region.

Taken together with the TEM results, the Raman spectroscopy results of graphene indicate the successful exfoliation of graphite yielding large quantities of few-layer graphene. These results also show the interactions of AgNPs with the graphene support.
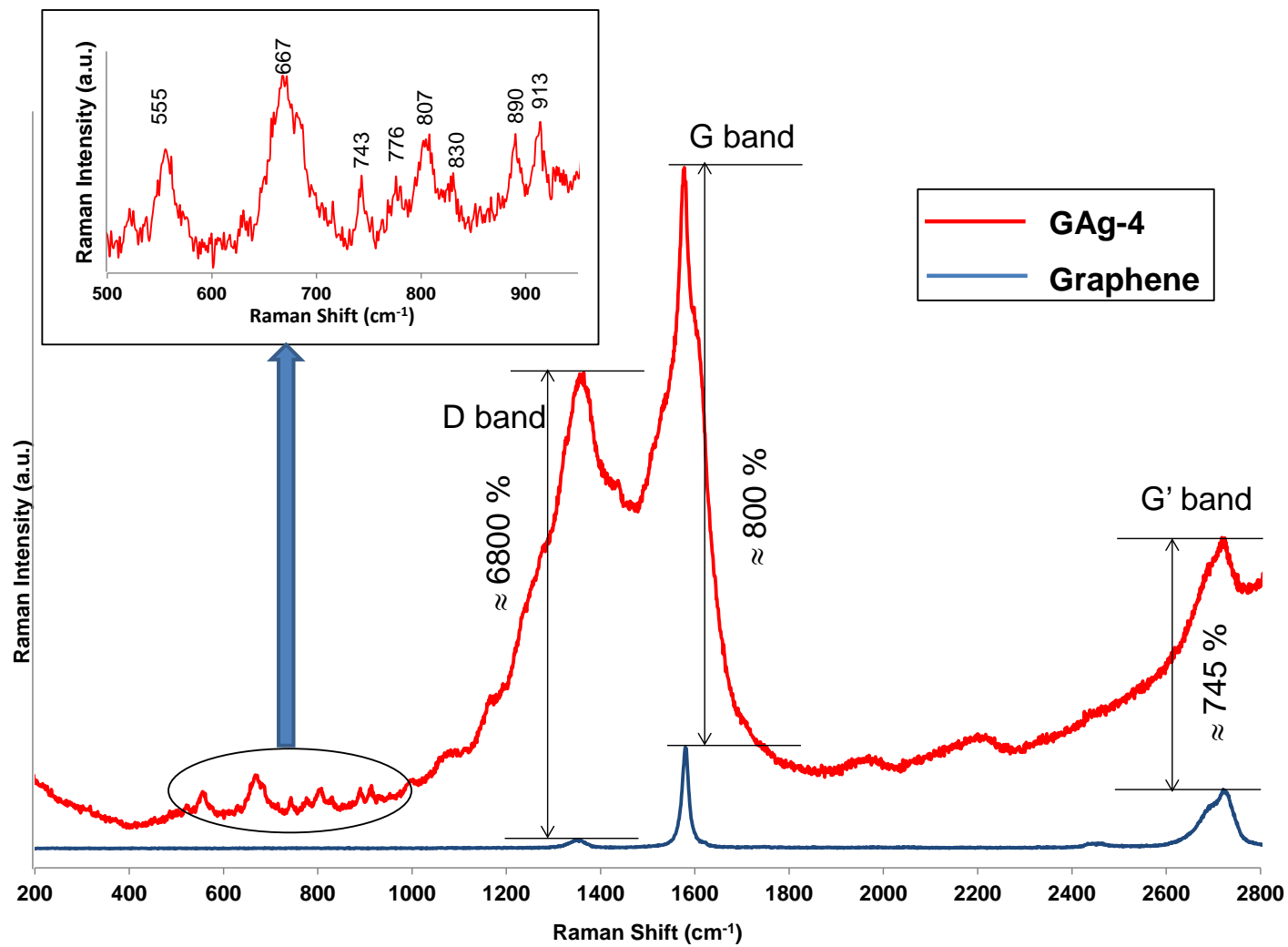
Figure 7.6: Raman spectra of graphene and graphene-silver nanocomposite samples.

7.6   Anti-Microfouling Properties of GAg Nanocomposites

Biofouling in marine environments is a complex process which involves the initial development of a microbial slime (biofilm) on exposed surfaces, eventually culminating in the attachment of algae and invertebrates [231]. The classical model of marine fouling proposed a linear successional progress of fouling species [246], while more dynamic and probabilistic fouling mechanisms have also been described [342]. Whether the progress of maritime fouling follows the 'successional model' or the 'dynamic model', the presence of bacterial biofilms attract the attachment of spores and larvae of macrofouling species [4]. Therefore, the disruption of the microbial biofilm is an important step in the protection of submerged aquatic surfaces.

To evaluate the antifouling effects of graphene-Ag composites, a static biofilm assay was carried out using *H. pacifica,* a common marine fouling bacterium. As shown in Figure 7.7, the GAg materials with a concentration of 0.1 mg/mL inhibit the attachment of biofilm from *H. pacifica* after an incubation period of 24 hours. Figure 7.7(A) shows a decrease in the optical density of crystal violet dye for GAg samples, in contrast to the untreated control and pure graphene sample. The surface-associated crystal violet dye attaches to the biofilm mass. A higher optical density reading is concomitant with a higher quantity of bacterial biofilm matter.

Figure 7.7(B) revealed that all 4 GAg samples exhibited potent inhibitory effect on the production of biofilm by *H. pacifica*, with an average inhibition of 67.4 ±1.8% for GAg-1, 86.9±1.3% for GAg-2, 95.6±0.1% for GAg-3 and 99.6±0.1% for GAg-4 (P < 0.05, Student's *t*-test). On the other hand, the graphene material and

233

graphene-free bulk silver exhibited little to no inhibitory effect on the attachment of biofilm from *H. pacifica*.

These results show that graphene and graphene-free bulk silver alone do not possess any antifouling quality. However, a minimal doping of AgNPs on graphene sheets endowed an effective antifouling effect against bacterial biofilm attachment. Notably, the effectiveness of biofilm inhibition correlated directly with the amounts of Ag loading, suggesting that the graphene nanosheets may promote the antifouling properties of the GAg material by providing a flexible support for nanosized biocidal AgNPs.

The graphene nanosheets are capable of wrapping around the contours of the bacteria cell, maximizing the contact area between the GAg material and the bacteria. In addition, the graphene material and citrate stabilizer promote the formation of AgNPs and minimizes nanosilver agglomeration, enhancing the biocidal activity of metallic silver. Furthermore, the presence of AgNPs inhibits the agglomeration of graphene sheets.
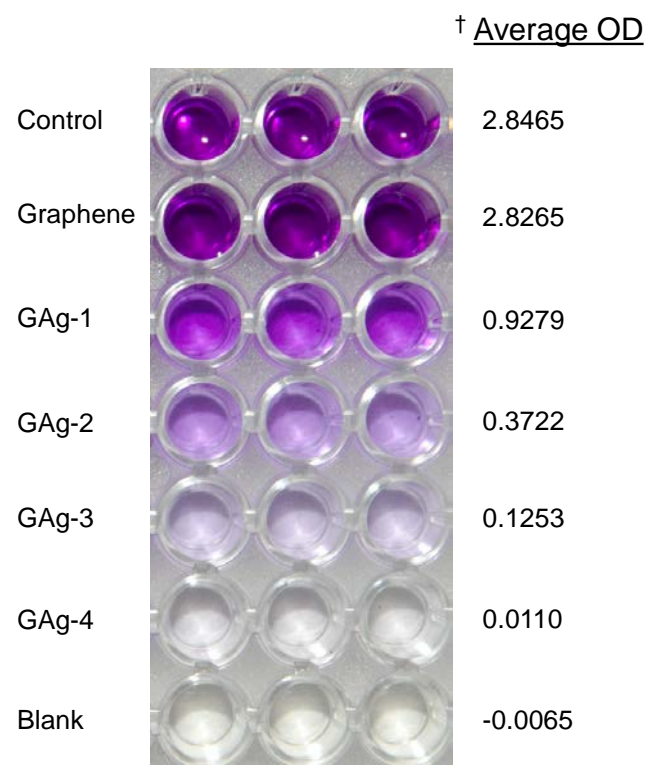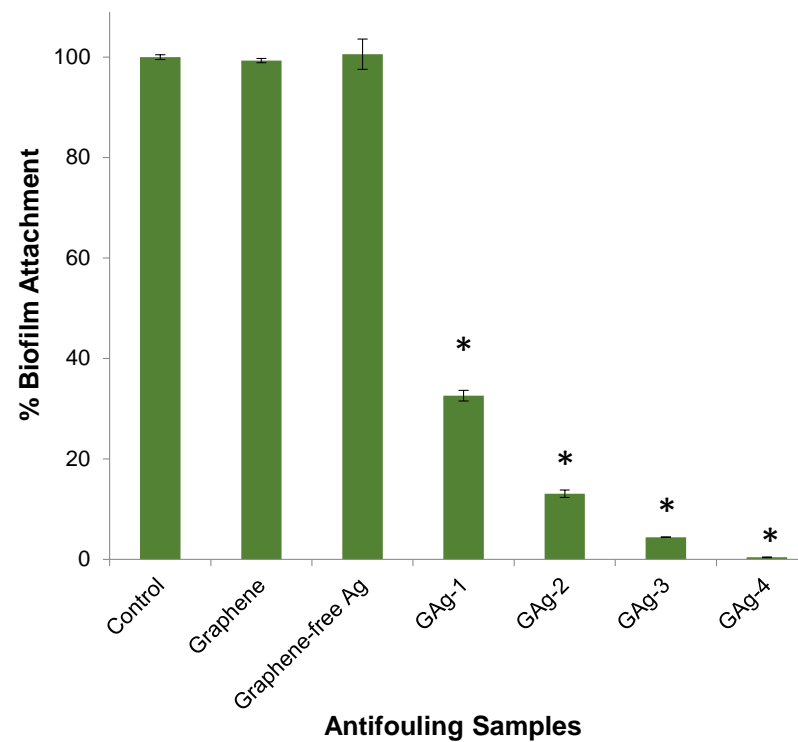
Figure 7.7: GAg materials inhibit the attachment of biofilm from *H. pacifica*. (A) Crystal violet assay results for anti-biofilm activity of GAg materials at 0.1 mg/ml. † indicates the average OD measured at 570 nm, and (B) *H. pacifica* bacteria biofilm attachment by GAg materials at 0.1 mg/ml. Bars represent mean ± s.d. of three independent experiments. * indicates statistical significance compared to control (P < 0.05, Student's *t*-test).

Gram-negative bacteria such as *H. pacifica* have thin peptidoglycan walls, likely making them more susceptible to AgNPs diffusing in to the microbial cells [302]. Another viable explanation is the dissolution of the bacterial outer cell wall by AgNPs, causing leakage of vital cellular constituents, leading to cell death [191]. Similar observations were reported for graphene silver nanocomposites which showed maximum inhibition of *E.coli, S. aureus* and *B.subtilis* compared to graphene oxide which had no activity against the microbe [84, 191]. Graphene oxide-silver nanocomposites were also reported as cytotoxic to eukaryotic cells, compared to pure GO [145].

The effects of graphene and GAg on the marine microalgae *D. tertiolecta* and *Isochrysis* sp. were evaluated using a microalgal growth inhition assay. As shown in Figure 7.8(A) and 7.8(B), 0.1 mg/mL of GAg materials inhibited the growth of both organisms by more than 70% after 96 h of exposure. On the other hand, graphene alone did not show any inhibitory effects on both microalgae. These results are in contrast to a previous report that pristine graphene nanoparticles were found to inhibit the growth of *D. tertiolecta* [343].

Interestingly, light microscopy observation showed significant morphological changes in both *D. tertiolecta* and *Isochrysis* sp. after exposure to the GAg materials. The microalgal cells lost membrane integrity and cytoplasm materials [Fig. 7.8(C) and 7.8(D)], in contrast to the untreated algal cells [Fig. 7.8(E) and 7.8(F)], suggesting that the effect of GAg is likely to be antiproliferative. *D. tertiolecta* has been previously described as a biofouling microalgae, with the induction of oxidative stress in the microalgae through direct contact to AgNPs as a cause of algae toxicity [234].
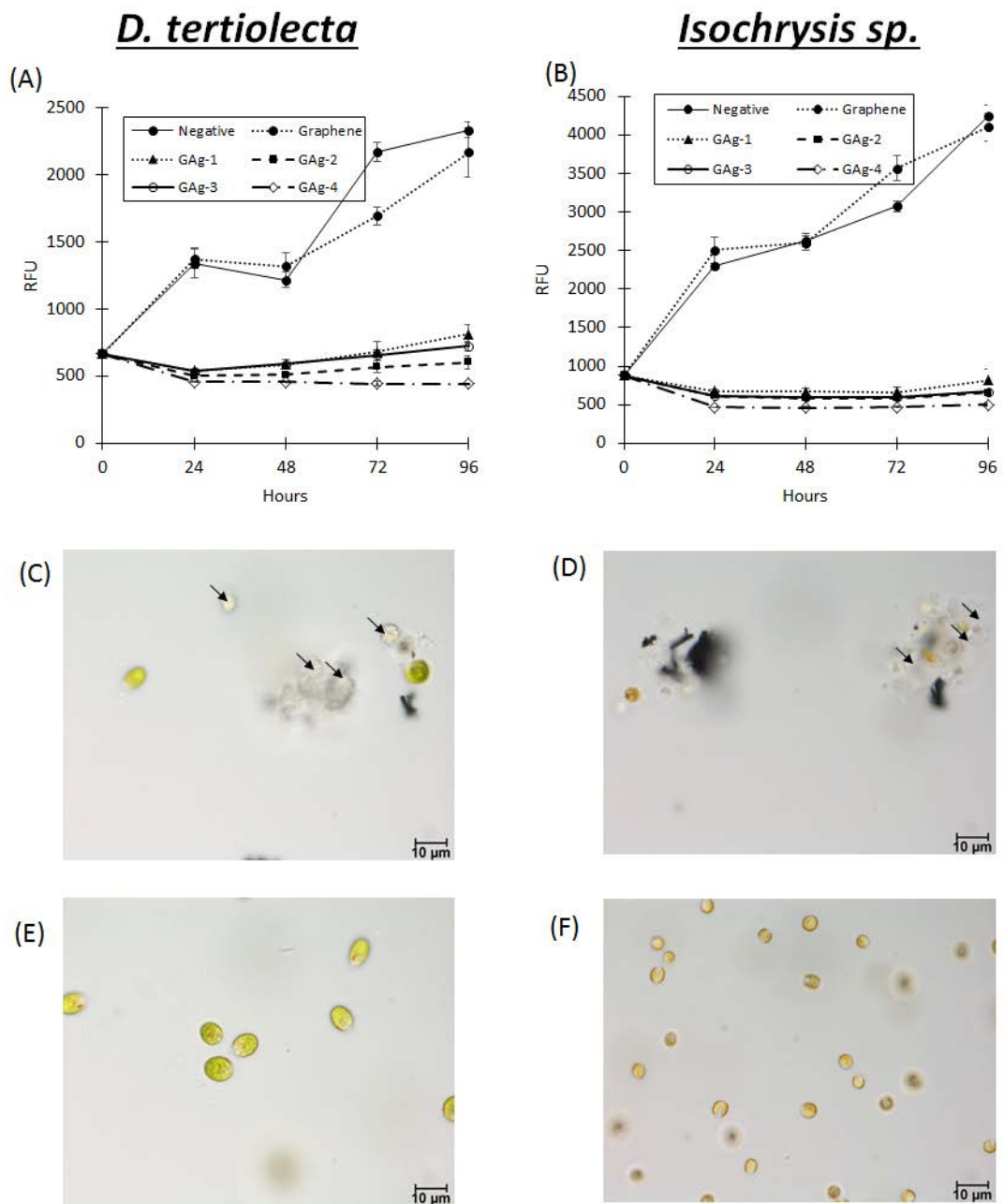
Figure 7.8: Growth inhibition effect of GAg materials on marine microalgae. (A) *D. tertiolecta* and (B) *Isochrysis* sp. algal cells were exposed to 0.1mg/mL of GAg for 96 h and the number of cells was determined by Presto Blue® stain. Points represent mean of ± s.d. of at least 3 independent experiments. (C) – (F) Light micrograph of marine microalgae. (C) *D. tertiolecta* and (D) *Isochrysis* sp. algal cells exposed to 0.1 mg/mL of GAg-3 for 96 h lost its cytoplasmic materials (black arrow pointed) compared to (E) and (F) non-treated algal cells.

7.7   Summary

Graphene-Ag nanocomposite materials were successfully synthesized using a novel 2-step process of sonochemical exfoliation of graphite and a hydrothermal reduction process using citrate as a green reducing agent. Graphene is directly produced from graphite through the facile and low-energy method, without the need of hazardous chemicals or the production of an intermediate graphene oxide. Hence, the pristine nature (lattice) of graphene nanomaterial is preserved effectively.

AgNPs were formed on the graphene flakes through a benign hydrothermal process using trisodium citrate as a green reducing agent. Electron microscopy methods revealed that the nanocomposite was composed of micron-scaled graphene flakes with clusters of AgNPs. In addition, TEM imaging showed that the hydrothermal processing preserved the quality of the few-layer graphene flakes. The AgNPs were estimated to be between 72-86 nm (SEM observations) while estimated average particles size through TEM observation was less than 20 nm. On the other hand, the crystallite size of the AgNPs was estimated to range between 1-5 nm. XRD phase analysis confirms the presence of face-centred cubic Ag and graphene only, while EDX analysis also corroborates the purity of the samples, with the detection of only carbon and silver elements present in the samples. Raman spectroscopy confirmed the interaction of the AgNPs with the graphene substrate with detection of the SERS effect.

The GAg nanocomposite displayed promising anti-microfouling behaviour as it interferes with the biofilm formation of marine bacteria *H. pacifica*. Low amounts

of AgNPs (1.3 wt% Ag) supported on the graphene flakes were able to inhibit the bacteria from forming the fouling biofilms. All the GAg samples displayed statistically significant biofilm inhibition property. The highest wt% of Ag loading was associated with a biofilm inhibition of 99.6%. The GAg materials also showed growth inhibitory activity against marine microalgae *D. tertiolecta* and *Isochrysis* sp., compared to both pure graphene and bulk silver particles, which did not exhibit any significant antifouling properties.

This work shows that the presence of graphene is vital as it provides a stable and effective support for the anchoring and growth of Ag NPs. Trisodium citrate as a green reducing agent is an effective stabilizer for the formation of AgNPs. In addition, the flexible sheets of graphene-Ag nanomaterial are able to improve the contact area with fouling organisms and provide an extremely potent antifouling effect on the bacterial and algal cells.

Chapter 8: Conclusion

8.1   Conclusion

This report has examined the issue of marine fouling and has presented detailed investigations about silver-based nanocomposite materials and their potential as marine antifouling agents.

Chapter 1 has delved into the background of marine fouling and a brief history of engineering solutions to the problem. The rationale of this research work and its research objectives were presented in this chapter. Chapter 2 is an attempt to cover a broad area encompassing silver nanomaterials including their applications and syntheses methods, provide a definition of marine fouling and the organisms which play important roles in the development of the fouling community and discussed various methods of fouling control and prevention. In addition, a survey of methods to evaluate antifouling agents was discussed. After thorough review of the current literature, four classes of novel silver-based nanocomposite materials were selected to be studied as potential antifouling agents. The materials used and the methodology for synthesis of the silver-based nanocomposites were presented in Chapter 3. The physical characterization techniques and the antifouling evaluation methods were also discussed in this chapter.

This was then followed by Chapters 4-7, each focusing on a specific silver-based nanocomposite system, presented with their key characteristics, and evidence of

their antifouling behaviour against targeted marine organisms. Chapter 4 reports on a novel silver nanocomposite material synthesized on a polymeric ion-exchange resin (Ag-PNC), Chapter 5 is an account of a mesoporous silver-ZSM-5 zeolite nanocomposite material (AgZ), Chapter 6 describes a silver-titania nanotubular composite material (Ag/TNT), while Chapter 7 is related to the nanocomposite composed of AgNPs supported on flexible graphene nanosheets, or GAg.

Ag-PNC and AgZ nanomaterials were prepared using rapid, simple and affordable room-temperature or low-temperature chemical processes. Ag/TNT and GAg nanocomposites were prepared from novel and environmentally-friendly hydrothermal processing. All the synthesis methods employed low-energy methods, using easily available materials and achieved high yields with high loading of Ag on the composites, using relatively low amounts of precursor materials.

These various forms of silver-based nanocomposite materials were thoroughly characterized on their morphology, elemental composition, crystallinity, thermal properties, porosity and optical properties where appropriate. Furthermore, these silver nanocomposite materials were evaluated on their antifouling property via biofilm inhibition against a marine bacterium, as well as their biological effects on marine microalgae. Even though all the nanocomposites were prepared using relatively low amounts of silver precursor materials, all of them were highly effective (from more than 70% - 99.6%) in inhibiting biofilm production by *H. pacifica*. The nanocomposites also displayed growth inhibition effects on *D. tertiolecta* and *Isochrysis* sp. These marine microorganisms have previously been identified as macrofoulers in the marine environment.

The results have demonstrated that all four silver-based nanocomposite materials have potent antifouling properties and possess potential as marine antifouling agents. Ag-PNC, AgZ and GAg each displayed different levels of antifouling activity which directly corresponded to the amount of metallic Ag nanomaterial loaded on the support matrix, while Ag/TNT displayed increasingly effective antifouling properties with a decrease in Ag loading. Instead, the antifouling behaviour of Ag/TNT directly correlated with the decreasing size of the AgNPs supported on the nanotube surface. Therefore, Ag/TNT is believed to be the best candidate in terms of antifouling property as a small addition of Ag loading of less than 1 wt% Ag caused almost total inhibition of marine bacteria biofilm formation (98.5%) and disrupted the viability of marine microalgae.

Table 8.1 provides a summary of all the research objectives and the key results of this dissertation, to show that all the objectives have been fulfilled. The summary includes all 4 classes of novel silver nanocomposite materials, their key characteristics and their antifouling activity against the targeted marine microorganisms.

Table 8.1: Summary of research objectives and key results.

Research Objectives	Key Results
1. Synthesize novel silver-polymer nanocomposite (Ag-PNC) materials from low-temperature chemical processing and elucidate the key physical characteristics of the system.	Ag-PNCs were successfully synthesized using a novel, rapid and simple ion-exchange process via a room temperature reduction procedure. Key Characteristics: • Ag-PNCs are polymeric microspheres with surface decorated by AgNP sizes ranging from $20.2 \pm 6.5 - 60.2 \pm 41.1$ nm (SEM observation). • Ag-PNCs possess higher thermal stability and higher glass transition temperatures (T_g ranges from 149 °C – 323 °C) compared to the resin alone (T_g resin = 130 °C). • Ag-PNCs displayed surface plasmon resonance effect, with maximum optical absorption around 406 – 422 nm wavelengths. • The crystallinity of the composites increases with the addition of higher amounts of Ag.
2. Evaluate antifouling property of Ag-PNCs through: (i) biofilm inhibition of marine bacteria (ii) biological effects on marine microalgae	1 mg/mL of Ag-PNC demonstrated antimicrofouling property, correlating with Ag loading. • Ag-PNC-3 and Ag-PNC-4 demonstrated a potent inhibitory effect on *H. pacifica* biofilm formation, with average inhibition of $18.59 \pm 2.39\%$ and $76.08 \pm 3.93\%$, respectively ($P<0.01$, Student's *t*-test). • Ag-PNC-4 caused a cytostatic growth inhibition of *D. tertiolecta* and *Isochrysis* sp., but did not cause any significant morphological changes to the algal cells.

Table 8.1 (continued): Summary of research objectives and key results.

Research Objectives	Key Results
3. Synthesize novel silver-zeolite (AgZ) nanocomposite materials from low-temperature chemical processes, and elucidate the key physical characteristics of the system.	AgZs were successfully synthesized from a rapid ion-exchange and green reduction procedure. Key Characteristics: • Rapid ion exchange, followed by chemical reduction procedure resulted in optimal Ag ion uptake, with up to 10 wt% of Ag loading in zeolite, compared to conventional ion exchange processing times of 24 h or longer. • AgNPs were supported on the surface and within the internal pores of ZSM-5 zeolite • AgZ displayed surface plasmon resonance effect, with maximum optical absorption around 408-449 nm wavelengths. • Crystallinity of zeolite structure was preserved, whilst porosity of structure was altered to include some degree of macroporosity.
4. Evaluate antifouling property of AgZ through: (i) biofilm inhibition of marine bacteria (ii) biological effects on marine microalgae	1 mg/mL of AgZ demonstrated promising antimicrofouling property, correlated well with Ag loading. • AgZ-4 and AgZ-5 had a potent inhibitory effect on *H. pacifica* biofilm formation with average inhibition of $63.27 \pm 2.64\%$ and $81.29 \pm 1.53\%$ respectively ($P<0.01$, Student's *t*-test) • AgZ-5 induced significant growth inhibition and demonstrated a cytostatic effect on *D. tertiolecta*, without significant morphological changes, while a cytotoxic effect was observed on *Isochrysis* sp., with loss of membrane integrity and cytoplasm materials.

Table 8.1 (continued): Summary of research objectives and key results.

Research Objectives	Key Results
5. Synthesize silver-titania nanotubes (Ag/TNT) from novel hydrothermal processing, and elucidate the key physical characteristics of the system.	Silver-titania nanotubular (Ag/TNT) composite materials were synthesized from novel hydrothermal processing using green reducing agent and stabilizer. Key Characteristics: • AgNPs of approximately 3 nm (TEM observation) and 32-103 nm (SEM observation) uniformly dispersed on nanotubular TiO_2 structure. • Samples consist of highly crystalline Ag and TiO_2 phases. • Ag/TNT displayed enhanced optical absorption across entire visible wavelength region and demonstrated surface plasmon resonance effect between 420-427 nm.
6. Evaluate antifouling property of Ag/TNTs through: (i) biofilm inhibition of marine bacteria (ii) biological effects on marine microalgae	0.1 mg/mL of Ag/TNT demonstrated promising antimicrofouling property. Antifouling activity directly related to Ag NP size, smaller-sized AgNPs demonstrated greater antifouling performance. • Minimal doping of Ag (approximately 1 wt%) on TiO_2 nanotubes produced effective antimicrofouling properties compared to no inhibitory effect from bulk silver or TiO_2 nanotubes alone. • 0.1 mg/mL of Ag/TNT-1 and Ag/TNT-2 had a potent inhibitory effect on *H. pacifica* biofilm formation with average inhibition of $98.47 \pm 0.11\%$ and $89.39 \pm 0.45\%$, respectively (P<0.01, Student's *t*-test). • 0.1 mg/mL of Ag/TNT-1 and Ag/TNT-2 induced significant morphological changes and growth inhibition on *D. tertiolecta* and *Isochrysis* sp., compared to pure TiO_2 nanotubes alone.

Table 8.1 (continued): Summary of research objectives and key results.

Research Objectives	Key Results
7. Synthesize novel graphene-silver (GAg) nanocomposite materials from hydrothermal processes, and elucidate the key physical characteristics of the system.	GAg nanocomposites successfully synthesized from a novel 2-step mild hydrothermal processing, completely bypassing the formation of graphene oxide. Key Characteristics: • High purity samples consisting only of micron-scaled few-layer graphene sheets supporting AgNPs average sized between 72-86 nm (SEM observation), while TEM observation of GAg-4 showed AgNPs with average size of 18.1 ± 1.3 nm. • Ag content in composites ranged from 1.3 wt% - 4.9 wt%. • GAg exhibited SERS effect, indicating interaction of Ag NPs and graphene.
8. Evaluate antifouling property of GAg through: (i) biofilm inhibition of marine bacteria (ii) biological effects on marine microalgae	0.1 mg/mL of all GAg samples demonstrated promising antimicrofouling activity, correlated directly with the amount of Ag loading. • Potent inhibitory effect against *H. pacifica* biofilm formation, with average inhibition of $67.4 \pm 1.8\%$ (GAg-1), $86.9 \pm 1.3\%$ (GAg-2), $95.6 \pm 0.1\%$ (GAg-3) and $99.6 \pm 0.1\%$ (GAg-4). Statistically significant ($P<0.05$, Student's *t*-test), compared to no inhibitory effect from pure graphene and bulk silver alone. • 0.1 mg/mL of all GAg inhibited the growth of *D. tertiolecta* and *Isochrysis* sp. by more than 70% after 96 hours of exposure, compared to graphene alone. • Significant morphological changes occurred in both *D. tertiolecta* and *Isochrysis* sp., with loss of membrane integrity and cytoplasm materials, compared to untreated algal cells.

8.2   Contribution of the Thesis

This thesis has resulted in the publication of 4 peer-reviewed journal articles and contributed to the literature in the following aspects:

1) Introduced 4 classes of novel silver-based nanocomposite materials as potent antifouling agents. The nanocomposites were prepared from easily accessible precursor materials, employing environmentally-friendly and low-energy synthesis methods. Whilst comparatively low amounts of Ag precursor were used in their preparation, the resultant Ag nanocomposites are produced with high yield, with relatively high Ag loading.

2) Explored the application of silver nanocomposite materials in the area of marine antifouling technology by demonstrating the highly potent antimicrofouling property of Ag-PNCs, AgZs, Ag/TNTs and GAgs against biofouling marine bacteria and microalgae.

8.3   Future Work

After the success in identifying the 4 classes of silver-based nanocomposite antifouling agents detailed in this report, there are several routes which can be pursued for further studies.

1) Using the silver nanocomposite as marine paint additives. Combining with various paint resins to identify suitable antifouling paint compositions for marine vessels.

2) Evaluating paint characteristics, e.g. solubility parameters, leaching and water absorption of paint, erosion rate of paint, release rate of antifouling agent, water contact angle analysis, etc.

3) Evaluating antifouling paint in static and dynamic conditions in mesocosm challenge tanks and field testing in ocean/river waters.

4) Screening the antifouling agents on macrofouling organisms including barnacles and seaweed.

5) Screening the antifouling agents for ecotoxicological effects.

6) Costing development and industrial synthesis for commercialization.

References

[1] D. M. Yebra, S. Kiil, and K. Dam-Johansen, "Antifouling technology - past, present and future steps towards efficient and environmentally friendly antifouling coatings," *Progress in Organic Coatings,* vol. 50, pp. 75-104, 2004.

[2] WHOI, "The History of the Prevention of Fouling," in *Marine Fouling and Its Prevention*, ed Menasha, Wisconsin, USA: George Banta Publishing Co., 1952, pp. 211-223.

[3] C. F. T. Young, *The fouling and corrosion of iron ships: their causes and means of prevention, with the mode of application to the existing iron-clads*. London: The London Drawing Association, 1867.

[4] J. A. Callow and M. E. Callow, "Trends in the development of environmentally friendly fouling-resistant marine coatings," *Nature Communications,* vol. 2:244, pp. 1-10, 2011.

[5] S. Abarzua and S. Jakubowski, "Biotechnological investigation for the prevention of biofouling. I. Biological and biochemical principles for the prevention of biofouling," *Marine Ecology Progress Series,* vol. 123, pp. 301-312, 1995.

[6] M. E. Callow and J. E. Callow, "Marine biofouling: a sticky problem," *Biologist (London),* vol. 49, pp. 1-5, 2002.

[7] G. S. Caldwell and H. E. Pagett, "Marine glycobiology: current status and future perspectives," *Marine Biotechnology,* vol. 12, pp. 241-52, 2010.

[8] J. C. Lewthwaite, A. F. Molland, and K. W. Thomas, "An investigation into the variation of ship skin frictional resistance with fouling," *Royal Institution of Naval Architects Transactions,* vol. 127, pp. 269-284, 1985.

[9] SWZ. (1999, Developments in TBT-free antifouling technology: Why antifoulings are so important. *Schip en Werf de Zee (October 1999),* 12-16. Available: http://www.swzonline.nl/swz-archief/S&W%20archief/Developments%20in%20TBT-Free%20Antifouling%20Technology.pdf

[10] RTI_International, I. EnSYS_Energy&Systems, and Navigistics_Consulting, "Global Trade and Fuels Assessment - Future Trends and Effects of Requiring Clean Fuels in the Marine Sector," 2008.

[11] IMC, "Coatings Technology: What is Fouling?," ed: International Paint Ltd., 2005.

[12] GISP, "Marine Biofouling: An Assessment of Risks and Management Initiatives," 2008.

[13] E. Almeida, T. C. Diamantino, and O. de Sousa, "Marine paints: The particular case of antifouling paints," *Progress in Organic Coatings,* vol. 59, pp. 2-20, 2007.

[14] A. Milne and G. Hails, "Patent GB 1 457 590," 1974.

[15] G. W. Bryan, P. E. Gibbs, G. R. Burt, and L. G. Hummerstone, "The effects of tributyltin (TBT) accumulation on adult dog-whelks, Nucella lapillus: longterm field and laboratory experiments," *Journal of the Marine Biological Association of the United Kingdom,* vol. 67, pp. 525-544, 1987.

[16] D. Santillo, P. Johnston, and W. J. Langston, "Tributyltin (TBT) antifoulants: a tale of ships, snails and imposex," in *Late lessons from early warnings: the*

precautionary principle 1896–2000, D. Gee, P. Harremoes, J. Keys, M. MacGarvin, A. Stirling, S. Vaz, and B. Wynne, Eds., ed Copenhagen: European Environment Agency, 2001, pp. 135-148.

[17] International_Maritime_Organization. (2016, 19th April 2016). *International Convention on the Control of Harmful Anti-fouling Systems on Ships*. Available: http://www.imo.org/en/About/Conventions/ListOfConventions/Pages/International-Convention-on-the-Control-of-Harmful-Anti-fouling-Systems-on-Ships-(AFS).aspx

[18] F. Cassé and G. W. Swain, "The development of microfouling on four commercial antifouling coatings under static and dynamic immersion," *International Biodeterioration and Biodegradation,* vol. 57, pp. 179-185, 2006.

[19] F. C. Campbell, "Introduction to Composite Materials," in *Structural Composite Materials*, ed: ASM International, 2010, pp. 1-30.

[20] J. W. Alexander, "History of the medical use of silver," *Surgical Infections,* vol. 10, pp. 289-292, 2009.

[21] J. R. Morones-Ramirez, J. A. Winkler, C. S. Spina, and J. J. Collins, "Silver enhances antibiotic activity against gram-negative bacteria," *Science Translational Medicine,* vol. 5, p. 190ra81, 2013.

[22] C. N. Lok, C. M. Ho, R. Chen, Q. Y. He, W. Y. Yu, H. Sun, P. K. Tam, J. F. Chiu, and C. M. Che, "Silver nanoparticles: partial oxidation and antibacterial activities," *Journal of Biological Inorganic Chemistry,* vol. 12, pp. 527-34, 2007.

[23] M. Sathishkumar, K. Sneha, S. W. Won, C. W. Cho, S. Kim, and Y. S. Yun, "Cinnamon zeylanicum bark extract and powder mediated green synthesis of nano-crystalline silver particles and its bactericidal activity," *Colloids and Surfaces B: Biointerfaces,* vol. 73, pp. 332-8, 2009.

[24] N. M. Huang, S. Radiman, H. N. Lim, P. S. Khiew, W. S. Chiu, K. H. Lee, A. Syahida, R. Hashim, and C. H. Chia, "γ-Ray assisted synthesis of silver nanoparticles in chitosan solution and the antibacterial properties," *Chemical Engineering Journal,* vol. 155, pp. 499-507, 2009.

[25] H. V. Tran, L. D. Tran, C. T. Ba, H. D. Vu, T. N. Nguyen, D. G. Pham, and P. X. Nguyen, "Synthesis, characterization, antibacterial and antiproliferative activities of monodisperse chitosan- based silver nanoparticles," *Colloids and Surfaces A: Physicochemical and Engineering Aspects,* vol. 360, pp. 32-40, 2010.

[26] A. Travan, E. Marsich, I. Donati, and S. Paoletti, "Silver nanocomposites and their biomedical applications," in *Nanomaterials for the Life Sciences*. vol. 8: Nanocomposites, C. S. S. R. Kumar, Ed., ed Weinheim: Wiley-VCH Verlag GmbH & Co. KGaA, 2010, pp. 81-137.

[27] nanoComposix. (2012, 29 November 2012). *General: Plasmonics*. Available: http://nanocomposix.com/kb/general/plasmonics

[28] B. Domènech, J. Bastos-Arrieta, A. Alonso, J. Macanás, M. Muñoz, and D. N. Muraviev. (2012). *Bifunctional Polymer-Metal Nanocomposite Ion Exchange Materials*. Available: https://www.intechopen.com/books/ion-exchange-technologies/bifunctional-polymer-metal-nanocomposite-ion-exchange-materials

[29] Agaunews.com. (2016, 20 April 2016). *The Royal Mint debuts its annual silver lunar privy Britannia bullion coin*. Available: http://agaunews.com/the-royal-mint-debuts-its-annual-silver-lunar-privy-britannia-bullion-coin/

[30] M. S. L. Yee, "Photograph of silver nanoparticles," Unpublished_photograph, Ed., ed, 2012.

[31] M. Auffan, J. Rose, J.-Y. Bottero, G. V. Lowry, J.-P. Jolivet, and M. R. Wiesner, "Towards a definition of inorganic nanoparticles from an environmental, health and safety perspective," *Nature Nanotechnology,* vol. 4, pp. 634-641, 2009.

[32] D. Rana, Y. Kim, T. Matsuura, and H. A. Arafat, "Development of antifouling thin-film-composite membranes for seawater desalination," *Journal of Membrane Science,* vol. 367, pp. 110-118, 2011.

[33] I. Sawada, R. Fachrul, T. Ito, Y. Ohmukai, T. Maruyama, and H. Matsuyama, "Development of a hydrophilic polymer membrane containing silver nanoparticles with both organic antifouling and antibacterial properties," *Journal of Membrane Science,* vol. 387-388, pp. 1-6, 2012.

[34] A. Kumar, P. K. Vemula, P. M. Ajayan, and G. John, "Silver-nanoparticle-embedded antimicrobial paints based on vegetable oil," *Nature Materials,* vol. 7, pp. 236-241, 2008.

[35] R. D. Holtz, B. A. Lima, A. G. Souza Filho, M. Brocchi, and O. L. Alves, "Nanostructured silver vanadate as a promising antibacterial additive to water-based paints," *Nanomedicine: Nanotechnology, Biology and Medicine,* vol. 8, pp. 935-940, 2012.

[36] R. W. Cahn, *The Coming of Materials Science*. Oxford, UK: Elsevier Science Ltd., 2001.

[37] G. Zhu and D. Chen, "Solvothermal fabrication of uniform silver nanowires," *Journal of Materials Science: Materials in Electronics,* pp. 1-7, 2012.

[38] nanoComposix. (2012, 15 January 2013). *The Effect of Aggregation on Optical Properties*. Available: http://nanocomposix.com/kb/silver/optical-properties#aggregation

[39] S. Park, P. S. K. Murthy, S. Park, Y. M. Mohan, and W.-G. Koh, "Preparation of silver nanoparticle-containing semi-interpenetrating network hydrogels composed of pluronic and poly(acrylamide) with antibacterial property," *Journal of Industrial and Engineering Chemistry,* vol. 17, pp. 293-297, 2011.

[40] R. Srivastava, D. K. Tiwari, and P. K. Dutta, "4-(Ethoxycarbonyl) phenyl-1-amino-oxobutanoic acid–chitosan complex as a new matrix for silver nanocomposite film: Preparation, characterization and antibacterial activity," *International Journal of Biological Macromolecules,* vol. 49, pp. 863-870, 2011.

[41] H. Jia, W. Hou, L. Wei, B. Xu, and X. Liu, "The structures and antibacterial properties of nano-SiO2 supported silver/zinc-silver materials," *Dental Materials,* vol. 24, pp. 244-9, 2008.

[42] M. J. Sánchez, P. Gamero, and D. Cortés, "Bioactivity assessment of ZSM-5 type zeolite functionalized with silver or zinc," *Materials Letters,* vol. 74, pp. 250-253, 2012.

[43] V. V. Kravets, K. Culhane, I. M. Dmitruk, and A. O. Pinchuk, "Glycine-coated photoluminescent silver nanoclusters," in *SPIE Colloidal Nanocrystals for Biomedical Applications*, San Francisco, California, 2012.

[44] K. D. Bhatte, K. M. Deshmukh, Y. P. Patil, D. N. Sawant, S.-I. Fujita, M. Arai, and B. M. Bhanage, "Synthesis of powdered silver nanoparticles using hydrogen in aqueous medium," *Particuology,* vol. 10, pp. 140-143, 2012.

[45] K. Vora, S. Kang, S. Shukla, and E. Mazur, "Fabrication of disconnected three-dimensional silver nanostructures in a polymer matrix," *Applied Physics Letters,* vol. 100, pp. 063120-3, 2012.

[46] S. Bhatia, A. Z. Abdullah, and C. T. Wong, "Adsorption of butyl acetate in air over silver-loaded Y and ZSM-5 zeolites: Experimental and modelling studies," *Journal of Hazardous Materials,* vol. 163, pp. 73-81, 2009.

[47] K. K. Krishnani, Y. Zhang, L. Xiong, Y. Yan, R. Boopathy, and A. Mulchandani, "Bactericidal and ammonia removal activity of silver ion-exchanged zeolite," *Bioresource Technology,* vol. 117, pp. 86-91, 2012.

[48] L. Piao, K. H. Lee, B. K. Min, W. Kim, Y. R. Do, and S. Yoon, "A facile synthetic method of silver nanoparticles with a continuous size range from sub-10 nm to 40 nm," *Bulletin of the Korean Chemical Society,* vol. 32, pp. 117-121, 2011.

[49] T. K. Malongo, S. Patris, P. Macours, F. Cotton, J. Nsangu, and J. M. Kauffmann, "Highly sensitive determination of iodide by ion chromatography with amperometric detection at a silver-based carbon paste electrode," *Talanta,* vol. 76, pp. 540-7, 2008.

[50] K. P. Bankura, D. Maity, M. M. R. Mollick, D. Mondal, B. Bhowmick, M. K. Bain, A. Chakraborty, J. Sarkar, K. Acharya, and D. Chattopadhyay, "Synthesis, characterization and antimicrobial activity of dextran stabilized silver nanoparticles in aqueous medium," *Carbohydrate Polymers,* vol. 89, pp. 1159-1165, 2012.

[51] S. N. Barnaby, S. M. Yu, K. R. Fath, A. Tsiola, O. Khalpari, and I. A. Banerjee, "Ellagic acid promoted biomimetic synthesis of shape-controlled silver nanochains," *Nanotechnology,* vol. 22, p. 225605, 2011.

[52] T. He and V. Chan, "Covalent layer-by-layer assembly of polyethyleneimine multilayer for antibacterial applications," *Journal of Biomedical Materials Research. Part A,* vol. 95, pp. 454-464, 2010.

[53] V. Melinte, T. Buruiana, I. D. Moraru, and E. C. Buruiana, "Silver-polymer composite materials with antibacterial properties," *Digest Journal of Nanomaterials and Biostructures,* vol. 6, pp. 213-223, 2011.

[54] D. Gu, X. Chang, X. Zhai, S. Sun, Z. Li, T. Liu, L. Dong, and Y. Yin, "Efficient synthesis of silver-reduced graphene oxide composites with prolonged antibacterial effects," *Ceramics International,* vol. 42, pp. 9769-9778, 2016.

[55] N. S. Flores-López, J. Castro-Rosas, R. Ramírez-Bon, A. Mendoza-Córdova, E. Larios-Rodríguez, and M. Flores-Acosta, "Synthesis and properties of crystalline silver nanoparticles supported in natural zeolite chabazite," *Journal of Molecular Structure,* vol. 1028, pp. 110-115, 2012.

[56] M. A. Carvalho, R. E. F. de Paiva, F. R. G. Bergamini, A. F. Gomes, F. C. Gozzo, W. R. Lustri, A. L. B. Formiga, S. M. Shishido, C. V. Ferreira, and P. P. Corbi, "A silver complex with tryptophan: Synthesis, structural characterization, DFT studies and antibacterial and antitumor assays in vitro," *Journal of Molecular Structure,* vol. 1031, pp. 125-131, 2013.

[57] A. Travan, C. Pelillo, I. Donati, E. Marsich, M. Benincasa, T. Scarpa, S. Semeraro, G. Turco, R. Gennaro, and S. Paoletti, "Non-cytotoxic Silver

Nanoparticle-Polysaccharide Nanocomposites with Antimicrobial Activity," *Biomacromolecules,* vol. 10, pp. 1429-1435, 2009.

[58] M. G. Guzman, J. Dille, and S. Godet, "Synthesis of silver nanoparticles by chemical reduction method and their antibacterial activity," *International Journal of Chemical and Biological Engineering,* vol. 2, pp. 104-111, 2009.

[59] H. J. Lee, S. G. Lee, E. J. Oh, H. Y. Chung, S. I. Han, E. J. Kim, S. Y. Seo, H. D. Ghim, J. H. Yeum, and J. H. Choi, "Antimicrobial polyethyleneimine-silver nanoparticles in a stable colloidal dispersion," *Colloids and Surfaces B: Biointerfaces,* vol. 88, pp. 505-511, 2011.

[60] D. L. Boschetto, L. Lerin, R. Cansian, S. B. C. Pergher, and M. Di Luccio, "Preparation and antimicrobial activity of polyethylene composite films with silver exchanged zeolite-Y," *Chemical Engineering Journal,* vol. 204–206, pp. 210-216, 2012.

[61] R. Tankhiwale and S. K. Bajpai, "Graft copolymerization onto cellulose-based filter paper and its further development as silver nanoparticles loaded antibacterial food-packaging material," *Colloids and Surfaces B: Biointerfaces,* vol. 69, pp. 164-168, 2009.

[62] H. Barani, M. Montazer, N. Samadi, and T. Toliyat, "Nano silver entrapped in phospholipids membrane: synthesis, characteristics and antibacterial kinetics," *Molecular Membrane Biology,* vol. 28, pp. 206-215, 2011.

[63] K. Zodrow, L. Brunet, S. Mahendra, D. Li, A. Zhang, Q. Li, and P. J. J. Alvarez, "Polysulfone ultrafiltration membranes impregnated with silver nanoparticles show improved biofouling resistance and virus removal," *Water Research,* vol. 43, pp. 715-723, 2009.

[64] T. Haile, G. Nakhla, and E. Allouche, "Evaluation of the resistance of mortars coated with silver bearing zeolite to bacterial-induced corrosion," *Corrosion Science,* vol. 50, pp. 713-720, 2008.

[65] C. Aymonier, U. Schlotterbeck, L. Antonietti, P. Zacharias, R. Thomann, J. C. Tiller, and S. Mecking, "Hybrids of silver nanoparticles with amphiphilic hyperbranched macromolecules exhibiting antimicrobial properties," *Chemical Communications,* vol. 0, pp. 3018-3019, 2002.

[66] Q. Shi, N. Vitchuli, J. Nowak, J. Noar, J. M. Caldwell, F. Breidt, M. Bourham, M. McCord, and X. Zhang, "One-step synthesis of silver nanoparticle-filled nylon 6 nanofibers and their antibacterial properties," *Journal of Materials Chemistry,* vol. 21, pp. 10330-10335, 2011.

[67] Y. Zhang, H. Peng, W. Huang, Y. Zhou, and D. Yan, "Facile preparation and characterization of highly antimicrobial colloid Ag or Au nanoparticles," *Journal of Colloid and Interface Science,* vol. 325, pp. 371-376, 2008.

[68] R. Konwarh, B. Gogoi, R. Philip, M. A. Laskar, and N. Karak, "Biomimetic preparation of polymer-supported free radical scavenging, cytocompatible and antimicrobial "green" silver nanoparticles using aqueous extract of Citrus sinensis peel," *Colloids and Surfaces B: Biointerfaces,* vol. 84, pp. 338-345, 2011.

[69] S. A. Ruffolo, A. Macchia, M. F. La Russa, L. Mazza, C. Urzi, F. De Leo, M. Barberio, and G. M. Crisci, "Marine Antifouling for Underwater Archaeological Sites: TiO2 and Ag-Doped TiO2," *International Journal of Photoenergy,* vol. 2013, p. 6, 2013.

[70] N. Ma, Y. Zhang, X. Quan, X. Fan, and H. Zhao, "Performing a microfiltration integrated with photocatalysis using an Ag-TiO2/HAP/Al2O3 composite membrane for water treatment: Evaluating effectiveness for humic

acid removal and anti-fouling properties," *Water Research,* vol. 44, pp. 6104-6114, 2010.

[71]   K. J. Kim, W. S. Sung, S. K. Moon, J. S. Choi, J. G. Kim, and D. G. Lee, "Antifungal effect of silver nanoparticles on dermatophytes," *Journal of Microbiology and Biotechnology,* vol. 18, pp. 1482-1484, 2008.

[72]   G. Von White, P. Kerscher, R. M. Brown, J. D. Morella, W. McAllister, D. Dean, and C. L. Kitchens, "Green Synthesis of Robust, Biocompatible Silver Nanoparticles Using Garlic Extract," *Journal of Nanomaterials,* vol. 2012, p. 12, 2012.

[73]   A. V. Singh, R. Patil, M. B. Kasture, W. N. Gade, and B. L. Prasad, "Synthesis of Ag-Pt alloy nanoparticles in aqueous bovine serum albumin foam and their cytocompatibility against human gingival fibroblasts," *Colloids and Surfaces B: Biointerfaces,* vol. 69, pp. 239-245, 2009.

[74]   R. Porter, A. Kabil, C. Forstern, C. Slevin, K. Kouwenberg, M. Szymanski, and B. Birch, "A novel, generic, electroanalytical immunoassay format utilising silver nano-particles as a bio-label," *Journal of Immunoassay and Immunochemistry,* vol. 30, pp. 428-440, 2009.

[75]   A. M. Abdel-Mohsen, R. Hrdina, L. Burgert, G. Krylová, R. M. Abdel-Rahman, A. Krejčová, M. Steinhart, and L. Beneš, "Green synthesis of hyaluronan fibers with silver nanoparticles," *Carbohydrate Polymers,* vol. 89, pp. 411-422, 2012.

[76]   C. T. Wong, A. Z. Abdullah, and S. Bhatia, "Catalytic oxidation of butyl acetate over silver-loaded zeolites," *Journal of Hazardous Materials,* vol. 157, pp. 480-489, 2008.

[77]   A. Jodaei, D. Salari, A. Niaei, M. Khatamian, and N. Caylak, "Preparation of Ag-M (M: Fe, Co and Mn)-ZSM-5 bimetal catalysts with high performance for catalytic oxidation of ethyl acetate," *Environmental Technology,* vol. 32, pp. 395-406, 2011.

[78]   Y. Chi, L. Zhao, Q. Yuan, X. Yan, Y. Li, N. Li, and X. Li, "In situ auto-reduction of silver nanoparticles in mesoporous carbon with multifunctionalized surfaces," *Journal of Materials Chemistry,* vol. 22, pp. 13571-13577, 2012.

[79]   Y. Lu, Y. Mei, M. Schrinner, M. Ballauff, M. W. Möller, and J. Breu, "In Situ Formation of Ag Nanoparticles in Spherical Polyacrylic Acid Brushes by UV Irradiation," *The Journal of Physical Chemistry C,* vol. 111, pp. 7676-7681, 2007.

[80]   X. Cai, K. C. Anyaogu, and D. C. Neckers, "Photopolymerization of conductive polymeric metal nanoparticles," *Photochemical and Photobiological Sciences,* vol. 8, pp. 1568-1573, 2009.

[81]   R. Yang, C. Yang, X. Cui, and Z. Zhang, "Silver dendrite-based nanocomposites for current cutting-off fuse," in *2015 16th International Conference on Electronic Packaging Technology (ICEPT)*, 2015, pp. 462-466.

[82]   Y. Q. Liang, Z. D. Cui, S. L. Zhu, Y. Liu, and X. J. Yang, "Silver nanoparticles supported on TiO2 nanotubes as active catalysts for ethanol oxidation," *Journal of Catalysis,* vol. 278, pp. 276-287, 2011.

[83]   R. Das, S. S. Nath, D. Chakdar, G. Gope, and R. Bhattacharjee. (2009, 31/12/2012). *Preparation of silver nanoparticles and their characterization.* Available: http://www.azonano.com/article.aspx?ArticleID=2318

[84]   S. V. Kumar, N. M. Huang, H. N. Lim, M. Zainy, I. Harrison, and C. H. Chia, "Preparation of highly water dispersible functional graphene/silver

nanocomposite for the detection of melamine," *Sensors and Actuators B: Chemical,* vol. 181, pp. 885-893, 2013.

[85] P. Barone, F. Stranges, M. Barberio, D. Renzelli, A. Bonanno, and F. Xu, "Study of Band Gap of Silver Nanoparticles - Titanium Dioxide Nanocomposites," *Journal of Chemistry,* vol. 2014, p. 6, 2014.

[86] R. S. Bedi, R. Cai, C. O'Neill, D. E. Beving, S. Foster, S. Guthrie, W. Chen, and Y. Yan, "Hydrophilic and antimicrobial Ag-exchanged zeolite a coatings: A year-long durability study and preliminary evidence for their general microbiocidal efficacy to bacteria, fungus and yeast," *Microporous and Mesoporous Materials,* vol. 151, pp. 352-357, 2012.

[87] S. K. Yip, C. L. Chan, W. H. Lam, K. K. Cheung, and V. W. Yam, "Synthesis, structure and luminescence studies of heterometallic gold(I)-copper(I) and -silver(I) alkynyl clusters/aggregates," *Photochemical and Photobiological Sciences* vol. 6, pp. 365-71, 2007.

[88] J. Zheng, Y. Ding, B. Tian, Z. L. Wang, and X. Zhuang, "Luminescent and Raman Active Silver Nanoparticles with Polycrystalline Structure," *Journal of the American Chemical Society,* vol. 130, pp. 10472-10473, 2008.

[89] P. S. Sathish Kumar, A. Manivel, and S. Anandan, "Synthesis of Ag-ZnO nanoparticles for enhanced photocatalytic degradation of acid red 88 in aqueous environment," *Water Science and Technology,* vol. 59, pp. 1423-1430, 2009.

[90] F. F. Bamoharram, M. M. Heravi, M. M. Heravi, and M. Meraji, "Synthesis of Silver Nanoparticles in the Presence of A Green Heteropolyacid, H14[NaP5W30O110], and Their Catalytic Activity for Photodegradation of Methylene Blue and Methyl Orange," *International Journal of Green Nanotechnology: Physics and Chemistry,* vol. 1, pp. 26-31, 2009.

[91] R. Maiti, T. K. Sinha, S. Mukherjee, B. Adhikari, and S. K. Ray, "Enhanced and Selective Photodetection Using Graphene-Stabilized Hybrid Plasmonic Silver Nanoparticles," *Plasmonics,* pp. 1-8, 2016.

[92] H. H. Patterson, R. S. Gomez, H. Lu, and R. L. Yson, "Nanoclusters of silver doped in zeolites as photocatalysts," *Catalysis Today,* vol. 120, pp. 168-173, 2007.

[93] Y. F. Huang, K. Sefah, S. Bamrungsap, H. T. Chang, and W. Tan, "Selective photothermal therapy for mixed cancer cells using aptamer-conjugated nanorods," *Langmuir,* vol. 24, pp. 11860-5, 2008.

[94] D. K. Božanić, L. V. Trandafilović, A. S. Luyt, and V. Djoković, "'Green' synthesis and optical properties of silver–chitosan complexes and nanocomposites," *Reactive and Functional Polymers,* vol. 70, pp. 869-873, 2010.

[95] E. Filippo, A. Serra, A. Buccolieri, and D. Manno, "Controlled synthesis and chain-like self-assembly of silver nanoparticles through tertiary amine," *Colloids and Surfaces A: Physicochemical and Engineering Aspects,* vol. 417, pp. 10-17, 2013.

[96] M. Berchel, T. L. Gall, C. Denis, S. L. Hir, F. Quentel, C. Elleouet, T. Montier, J.-M. Rueff, J.-Y. Salaun, J.-P. Haelters, G. B. Hix, P. Lehn, and P.-A. Jaffres, "A silver-based metal-organic framework material as a 'reservoir' of bactericidal metal ions," *New Journal of Chemistry,* vol. 35, pp. 1000-1003, 2011.

[97] K. Dağcı and M. Alanyalıoğlu, "Preparation of Free-Standing and Flexible Graphene/Ag Nanoparticles/Poly(pyronin Y) Hybrid Paper Electrode for

Amperometric Determination of Nitrite," *ACS Applied Materials & Interfaces,* vol. 8, pp. 2713-2722, 2016.

[98]   J.-S. Chung, B. G. Kim, S. Shim, S.-E. Kim, E.-H. Sohn, J. Yoon, and J.-C. Lee, "Silver-perfluorodecanethiolate complexes having superhydrophobic, antifouling, antibacterial properties," *Journal of Colloid and Interface Science,* vol. 366, pp. 64-69, 2012.

[99]   X. Hou and Y. Fang, "Surface-enhanced Raman scattering of single-walled carbon nanotubes on modified silver electrode," *Spectrochimica acta. Part A, Molecular and biomolecular spectroscopy,* vol. 69, pp. 1140-5, 2008.

[100]   D. Wei, W. Qian, D. Wu, Y. Xia, and X. Liu, "Synthesis, properties, and surface enhanced Raman scattering of gold and silver nanoparticles in chitosan matrix," *Journal of Nanoscience and Nanotechnology,* vol. 9, pp. 2566-73, 2009.

[101]   P. Yu, J. Huang, and J. Tang, "Observation of coalescence process of silver nanospheres during shape transformation to nanoprisms," *Nanoscale Research Letters,* vol. 6, 2011.

[102]   Y. Jiang, D. Liu, M. Cho, S. S. Lee, F. Zhang, P. Biswas, and J. D. Fortner, "In Situ Photocatalytic Synthesis of Ag Nanoparticles (nAg) by Crumpled Graphene Oxide Composite Membranes for Filtration and Disinfection Applications," *Environmental Science & Technology,* vol. 50, pp. 2514-2521, 2016.

[103]   IUPAC. (1997). *Compendium of Chemical Terminology (Second Edition ed.).* Available: http://goldbook.iupac.org

[104]   Z. Modrzejewska, R. Zarzycki, and J. Sielski, "Synthesis of silver nanoparticles in a chitosan solution," *Progress on Chemistry and Application of Chitin and its Derivatives,* vol. XV, pp. 63-72, 2010.

[105]   K. M. M. Abou El-Nour, A. a. Eftaiha, A. Al-Warthan, and R. A. A. Ammar, "Synthesis and applications of silver nanoparticles," *Arabian Journal of Chemistry,* vol. 3, pp. 135-140, 2010.

[106]   L. F. Hohnstedt, B. O. Miniatas, and S. M. C. Waller, "Aqueous Sodium Borohydride Chemistry. The Colnage Metals, Copper, Silver, and Gold," *Analytical Chemistry,* vol. 37, pp. 1163-1164, 1965.

[107]   R. F. Aroca, R. A. Alvarez-Puebla, N. Pieczonka, S. Sanchez-Cortez, and J. V. Garcia-Ramos, "Surface-enhanced Raman scattering on colloidal nanostructures," *Advances in Colloid and Interface Science,* vol. 116, pp. 45-61, 2005.

[108]   L. Mulfinger, S. D. Solomon, M. Bahadory, A. V. Jeyarajasingam, S. A. Rutkowsky, and C. Boritz, "Synthesis and study of silver nanoparticles," *Journal of Chemical Education,* vol. 84, p. 322, 2007.

[109]   A. Sileikaite, I. Prosycevas, J. Puiso, A. Juraitis, and A. Guobiene, "Analysis of Silver Nanoparticles Produced by Chemical Reduction of Silver Salt Solution," *Materials Science (Medziagotyra),* vol. 12, pp. 287-291, 2006.

[110]   A. K. Jha, K. Prasad, and A. R. Kulkarni, "Plant system: nature's nanofactory," *Colloids and Surfaces B: Biointerfaces,* vol. 73, pp. 219-223, 2009.

[111]   C. H. Ramamurthy, M. Padma, I. D. mariya samadanam, R. Mareeswaran, A. Suyavaran, M. S. Kumar, K. Premkumar, and C. Thirunavukkarasu, "The extra cellular synthesis of gold and silver nanoparticles and their free radical scavenging and antibacterial properties," *Colloids and Surfaces B: Biointerfaces,* vol. 102, pp. 808-815, 2013.

[112] M. M. R. Mollick, D. Rana, S. K. Dash, S. Chattopadhyay, B. Bhowmick, D. Maity, D. Mondal, S. Pattanayak, S. Roy, M. Chakraborty, and D. Chattopadhyay, "Studies on green synthesized silver nanoparticles using Abelmoschus esculentus (L.) pulp extract having anticancer (in vitro) and antimicrobial applications," *Arabian Journal of Chemistry,* vol. Article in press, corrected proof http://dx.doi.org/10.1016/j.arabjc.2015.04.033, 2015.

[113] H. Bar, D. K. Bhui, G. P. Sahoo, P. Sarkar, S. Pyne, and A. Misra, "Green synthesis of silver nanoparticles using seed extract of Jatropha curcas," *Colloids and Surfaces A: Physicochemical and Engineering Aspects,* vol. 348, pp. 212-216, 2009.

[114] T. Klaus, R. Joerger, E. Olsson, and C.-G. r. Granqvist, "Silver-based crystalline nanoparticles, microbially fabricated," *Proceedings of the National Academy of Sciences,* vol. 96, pp. 13611-13614, 1999.

[115] P. Sivalingam, J. J. Antony, D. Siva, S. Achiraman, and K. Anbarasu, "Mangrove Streptomyces sp. BDUKAS10 as nanofactory for fabrication of bactericidal silver nanoparticles," *Colloids and Surfaces B: Biointerfaces,* vol. 98, pp. 12-17, 2012.

[116] S. Sadhasivam, P. Shanmugam, and K. Yun, "Biosynthesis of silver nanoparticles by Streptomyces hygroscopicus and antimicrobial activity against medically important pathogenic microorganisms," *Colloids and Surfaces B: Biointerfaces,* vol. 81, pp. 358-362, 2010.

[117] L. R. Jaidev and G. Narasimha, "Fungal mediated biosynthesis of silver nanoparticles, characterization and antimicrobial activity," *Colloids and Surfaces B: Biointerfaces,* vol. 81, pp. 430-433, 2010.

[118] K. C. Bhainsa and S. F. D'Souza, "Extracellular biosynthesis of silver nanoparticles using the fungus Aspergillus fumigatus," *Colloids and Surfaces B: Biointerfaces,* vol. 47, pp. 160-164, 2006.

[119] D. S. Balaji, S. Basavaraja, R. Deshpande, D. B. Mahesh, B. K. Prabhakar, and A. Venkataraman, "Extracellular biosynthesis of functionalized silver nanoparticles by strains of Cladosporium cladosporioides fungus," *Colloids and Surfaces B: Biointerfaces,* vol. 68, pp. 88-92, 2009.

[120] A. Ahmad, P. Mukherjee, S. Senapati, D. Mandal, M. I. Khan, R. Kumar, and M. Sastry, "Extracellular biosynthesis of silver nanoparticles using the fungus Fusarium oxysporum," *Colloids and Surfaces B: Biointerfaces,* vol. 28, pp. 313-318, 2003.

[121] E. Castro-Longoria, A. R. Vilchis-Nestor, and M. Avalos-Borja, "Biosynthesis of silver, gold and bimetallic nanoparticles using the filamentous fungus Neurospora crassa," *Colloids and Surfaces B: Biointerfaces,* vol. 83, pp. 42-48, 2011.

[122] K. Kathiresan, S. Manivannan, M. A. Nabeel, and B. Dhivya, "Studies on silver nanoparticles synthesized by a marine fungus, Penicillium fellutanum isolated from coastal mangrove sediment," *Colloids and Surfaces B: Biointerfaces,* vol. 71, pp. 133-137, 2009.

[123] E. S. Abdel-Halim and S. S. Al-Deyab, "Utilization of hydroxypropyl cellulose for green and efficient synthesis of silver nanoparticles," *Carbohydrate Polymers,* vol. 86, pp. 1615-1622, 2011.

[124] M. A. Hettiarachchi and P. A. S. R. Wickramarachchi, "Synthesis of chitosan stabilized silver nanoparticles using gamma ray irradiation and characterization," *Journal of Science of the University of Kelaniya Sri Lanka,* vol. 6, pp. 65-75, 2011.

[125] C. M. Ng, P. C. Chen, and S. Manickam, "Green High-Gravitational Synthesis of Silver Nanoparticles Using a Rotating Packed Bed Reactor (RPBR)," *Industrial & Engineering Chemistry Research,* vol. 51, pp. 5375-5381, 2012.

[126] Y. Zhang, H. Peng, W. Huang, Y. Zhou, X. Zhang, and D. Yan, "Hyperbranched Poly(amidoamine) as the Stabilizer and Reductant To Prepare Colloid Silver Nanoparticles in Situ and Their Antibacterial Activity," *The Journal of Physical Chemistry C,* vol. 112, pp. 2330-2336, 2008.

[127] S. Y. Ai, J. G. Gao, L. S. Zhu, Z. J. Ma, and X. C. Li, "Preparation and spectroscopic studies of nanosilver/silk-fibroin composite," *Guang Pu Xue Yu Guang Pu Fen Xi,* vol. 28, pp. 2126-2129, 2008.

[128] A. A. Farah, R. A. Alvarez-Puebla, and H. Fenniri, "Chemically stable silver nanoparticle-crosslinked polymer microspheres," *Journal of Colloid and Interface Science,* vol. 319, pp. 572-576, 2008.

[129] M. Jiang, C. M. Cobley, B. Lim, and Y. Xia, "Noble-metal nanostructures with controlled morphologies," *Material Matters,* vol. 4, pp. 8-10, 2009.

[130] X. K. Meng, S. C. Tang, and S. Vongehr, "A Review on Diverse Silver Nanostructures," *Journal of Materials Science & Technology,* vol. 26, pp. 487-522, 2010.

[131] H. H. Huang, X. P. Ni, G. L. Loy, C. H. Chew, K. L. Tan, F. C. Loh, J. F. Deng, and G. Q. Xu, "Photochemical Formation of Silver Nanoparticles in Poly(N-vinylpyrrolidone)," *Langmuir,* vol. 12, pp. 909-912, 1996.

[132] A. Henglein, "Colloidal Silver Nanoparticles: Photochemical Preparation and Interaction with O2, CCl4, and Some Metal Ions," *Chemistry of Materials,* pp. 444-450, 1998.

[133] S. E. Skrabalak and Y. Xia, "Pushing nanocrystal synthesis toward nanomanufacturing," *ACS Nano,* vol. 3, pp. 10-15, 2009.

[134] S. Mann, "Molecular tectonics in biomineralization and biomimetic materials chemistry," *Nature,* vol. 365, pp. 499-505, 1993.

[135] V. Deepak, K. Kalishwaralal, S. R. K. Pandian, and S. Gurunathan, "An Insight into the Bacterial Biogenesis of Silver Nanoparticles, Industrial Production and Scale-up," in *Metal Nanoparticles in Microbiology*, M. Rai and N. Duran, Eds., ed. Berlin Heidelberg: Springer-Verlag, 2011, pp. 17-35.

[136] K. B. Narayanan and N. Sakthivel, "Green synthesis of biogenic metal nanoparticles by terrestrial and aquatic phototrophic and heterotrophic eukaryotes and biocompatible agents," vol. 169, pp. 59-79, 2011.

[137] H. R. Pant, D. R. Pandeya, K. T. Nam, W.-i. Baek, S. T. Hong, and H. Y. Kim, "Photocatalytic and antibacterial properties of a TiO2/nylon-6 electrospun nanocomposite mat containing silver nanoparticles," *Journal of Hazardous Materials,* vol. 189, pp. 465-471, 2011.

[138] H. Ke, M. u. H. Ghulam, Y. Li, J. Wang, B. Peng, Y. Cai, and Q. Wei, "Ag-coated polyurethane fibers membranes absorbed with quinary fatty acid eutectics solid-liquid phase change materials for storage and retrieval of thermal energy," *Renewable Energy,* vol. 99, pp. 1-9, 2016/12/01/ 2016.

[139] E. Marsich, A. Travan, I. Donati, G. Turco, J. Kulkova, N. Moritz, H. T. Aro, M. Crosera, and S. Paoletti, "Biological responses of silver-coated thermosets: An in vitro and in vivo study," *Acta Biomaterialia,* vol. 9, pp. 5088-5099, 2013.

[140] Y. Park, Y. N. Hong, A. Weyers, Y. S. Kim, and R. J. Linhardt, "Polysaccharides and phytochemicals: a natural reservoir for the green

synthesis of gold and silver nanoparticles," *IET Nanobiotechnol,* vol. 5, pp. 69-78, 2011.

[141] G.-J. Sui, Q.-L. Sun, D. Wu, W.-J. Meng, H. Wang, and J.-X. Lu, "Electrocatalytic reduction of PhCH2Cl on Ag-ZSM-5 zeolite modified electrode," *RSC Advances,* vol. 6, pp. 63493-63496, 2016.

[142] A. Griffith, S. Neethirajan, and K. Warriner, "Development and Evaluation of Silver Zeolite Antifouling Coatings on Stainless Steel for Food Contact Surfaces," *Journal of Food Safety,* vol. 35, pp. 345-354, 2015.

[143] B. Dong, S. Belkhair, M. Zaarour, L. Fisher, J. Verran, L. Tosheva, R. Retoux, J. P. Gilson, and S. Mintova, "Silver confined within zeolite EMT nanoparticles: preparation and antibacterial properties," *Nanoscale,* vol. 6, pp. 10859-10864, 2014.

[144] L.-j. Huang, Y.-x. Wang, J.-g. Tang, Y. Wang, J.-x. Liu, J.-q. Jiao, and W. Wang, "Preparation of Graphene/Silver Nanohybrid Composite with Good Surface-Enhanced Raman Scattering Characteristics," *Int J Electrochem Sci,* vol. 11, pp. 398-405, 2016.

[145] C. Li, X. Wang, F. Chen, C. Zhang, X. Zhi, K. Wang, and D. Cui, "The antifungal activity of graphene oxide–silver nanocomposites," *Biomaterials,* vol. 34, pp. 3882-3890, 2013.

[146] N. Atar, T. Eren, B. Demirdögen, M. L. Yola, and M. O. Çağlayan, "Silver, gold, and silver@gold nanoparticle-anchored l-cysteine-functionalized reduced graphene oxide as electrocatalyst for methanol oxidation," *Ionics,* vol. 21, pp. 2285-2293, 2015.

[147] N. Atar, T. Eren, M. L. Yola, H. Gerengi, and S. Wang, "Fe@Ag nanoparticles decorated reduced graphene oxide as ultrahigh capacity anode material for lithium-ion battery," *Ionics,* vol. 21, pp. 3185-3192, 2015.

[148] F. Lorestani, Z. Shahnavaz, P. Mn, Y. Alias, and N. S. A. Manan, "One-step hydrothermal green synthesis of silver nanoparticle-carbon nanotube reduced-graphene oxide composite and its application as hydrogen peroxide sensor," *Sensors and Actuators B: Chemical,* vol. 208, pp. 389-398, 2015.

[149] J. Shen, M. Shi, N. Li, B. Yan, H. Ma, Y. Hu, and M. Ye, "Facile synthesis and application of Ag-chemically converted graphene nanocomposite," *Nano Research,* vol. 3, pp. 339-349, 2010.

[150] R. Pasricha, S. Gupta, and A. K. Srivastava, "A Facile and Novel Synthesis of Ag–Graphene-Based Nanocomposites," *Small,* vol. 5, pp. 2253-2259, 2009.

[151] Y. Xie, Y. Li, L. Niu, H. Wang, H. Qian, and W. Yao, "A novel surface-enhanced Raman scattering sensor to detect prohibited colorants in food by graphene/silver nanocomposite," *Talanta,* vol. 100, pp. 32-37, 2012.

[152] J. H. Yeum, Q. Sun, and Y. Deng, "Poly(vinyl acetate)/Silver Nanocomposite Microspheres Prepared by Suspension Polymerization at Low Temperature," *Macromolecular Materials and Engineering,* vol. 290, pp. 78-84, 2005.

[153] P. Barbaro and F. Liguori, "Ion exchange resins: catalyst recovery and recycle," *Chemical Reviews,* vol. 109, pp. 515-529, 2009.

[154] W.-Q. Zhou, T.-Y. Gu, Z.-G. Su, and G.-H. Ma, "Synthesis of macroporous poly(styrene-divinyl benzene) microspheres by surfactant reverse micelles swelling method," *Polymer,* vol. 48, pp. 1981-1988, 2007.

[155] W. Kangwansupamonkon, S. Damronglerd, and S. Kiatkamjornwong, "Effects of the crosslinking agent and diluents on bead properties of styrene–divinylbenzene copolymers," *Journal of Applied Polymer Science,* vol. 85, pp. 654-669, 2002.

[156] Dow_Water_Solutions, "DOWEX(TM) Fine Mesh Spherical Ion Exchange Resins," The_Dow_Chemical_Company, Ed., ed, p. 9.

[157] H. S. Sherry, "The ion-exchange properties of zeolites. I. Univalent ion exchange in synthetic faujasite," *The Journal of Physical Chemistry,* vol. 70, pp. 1158-1168, 1966.

[158] R. Bartolomeu, R. Bértolo, S. Casale, A. Fernandes, C. Henriques, P. da Costa, and F. Ribeiro, "Particular characteristics of silver species on Ag-exchanged LTL zeolite in K and H form," *Microporous and Mesoporous Materials,* vol. 169, pp. 137-147, 2013.

[159] E. David, "Metal clusters in zeolite 4A obtained by synthesis process," *Journal of Achievements in Materials and Manufacturing Engineering,* vol. 19, pp. 26-31, 2006.

[160] M. Zahmakıran, T. Ayvalı, S. Akbayrak, S. Çalışkan, D. Çelik, and S. Özkar, "Zeolite framework stabilized nickel(0) nanoparticles: Active and long-lived catalyst for hydrogen generation from the hydrolysis of ammonia-borane and sodium borohydride," *Catalysis Today,* vol. 170, pp. 76-84, 2011.

[161] J.-F. Wang, K.-X. Wang, J.-Q. Wang, L. Li, Y.-M. Jiang, X.-X. Guo, and J.-S. Chen, "Elucidation of the chemical environment for zinc species in an electron-rich zinc-incorporated zeolite," *Journal of Solid State Chemistry,* vol. 202, pp. 111-115, 2013.

[162] P. Boroń, L. Chmielarz, J. Gurgul, K. Łątka, T. Shishido, J.-M. Krafft, and S. Dzwigaj, "BEA zeolite modified with iron as effective catalyst for N2O decomposition and selective reduction of NO with ammonia," *Applied Catalysis B: Environmental,* vol. 138–139, pp. 434-445, 2013.

[163] C.-Y. Sung, S. Al Hashimi, A. McCormick, M. Cococcioni, and M. Tsapatsis, "A DFT study on multivalent cation-exchanged Y zeolites as potential selective adsorbent for H2S," *Microporous and Mesoporous Materials,* vol. 172, pp. 7-12, 2013.

[164] K. Shameli, M. bin Ahmad, M. Zargar, W. M. Z. Wan Yunus, and N. A. Ibrahim, "Fabrication of silver nanoparticles doped in the zeolite framework and antibacterial activity," *International Journal of Nanomedicine,* vol. 6, pp. 331-341, 2011.

[165] S. S. Rayalu, A. K. Bansiwal, S. U. Meshram, N. Labhsetwar, and S. Devotta, "Fly ash based zeolite analogues: versatile materials for energy and environment conservation," *Catalysis Surveys from Asia,* vol. 10, pp. 74-88, 2006.

[166] M. K. Doula, K. Elaiopoulos, V. A. Kavvadias, and V. Mavraganis, "Use of clinoptilolite to improve and protect soil quality from the disposal of olive oil mills wastes," *Journal of Hazardous Materials,* vol. 207–208, pp. 103-110, 2012.

[167] R. Vignola, R. Bagatin, A. De Folly D'Auris, C. Flego, M. Nalli, D. Ghisletti, R. Millini, and R. Sisto, "Zeolites in a permeable reactive barrier (PRB): One year of field experience in a refinery groundwater—Part 1: The performances," *Chemical Engineering Journal,* vol. 178, pp. 204-209, 2011.

[168] W. De Muynck, A. M. Ramirez, N. De Belie, and W. Verstraete, "Evaluation of strategies to prevent algal fouling on white architectural and cellular concrete," *International Biodeterioration and Biodegradation,* vol. 63, pp. 679-689, 2009.

[169] S. Iijima, "Helical microtubules of graphitic carbon," *Nature,* vol. 354, pp. 56-58, 1991.

[170] Q. Chen, W. Zhou, G. H. Du, and L. M. Peng, "Trititanate Nanotubes Made via a Single Alkali Treatment," *Advanced Materials,* vol. 14, pp. 1208-1211, 2002.

[171] T. Kasuga, M. Hiramatsu, A. Hoson, T. Sekino, and K. Niihara, "Formation of Titanium Oxide Nanotube," *Langmuir,* vol. 14, pp. 3160-3163, 1998.

[172] T. Kasuga, M. Hiramatsu, A. Hoson, T. Sekino, and K. Niihara, "Titania Nanotubes Prepared by Chemical Processing," *Advanced Materials,* vol. 11, pp. 1307-1311, 1999.

[173] A. Fujishima, T. N. Rao, and D. A. Tryk, "Titanium dioxide photocatalysis," *Journal of Photochemistry and Photobiology C: Photochemistry Reviews,* vol. 1, pp. 1-21, 2000.

[174] X. Zhou, V. Häublein, N. Liu, N. T. Nguyen, E. M. Zolnhofer, H. Tsuchiya, M. S. Killian, K. Meyer, L. Frey, and P. Schmuki, "TiO2 Nanotubes: Nitrogen-Ion Implantation at Low Dose Provides Noble-Metal-Free Photocatalytic H2-Evolution Activity," *Angewandte Chemie International Edition,* vol. 55, pp. 3763-3767, 2016.

[175] J. Ni, S. Fu, C. Wu, J. Maier, Y. Yu, and L. Li, "Self-Supported Nanotube Arrays of Sulfur-Doped TiO2 Enabling Ultrastable and Robust Sodium Storage," *Advanced Materials,* vol. 28, pp. 2259-2265, 2016.

[176] Y. Yang and M. R. Hoffmann, "Synthesis and Stabilization of Blue-Black TiO2 Nanotube Arrays for Electrochemical Oxidant Generation and Wastewater Treatment," *Environmental Science and Technology,* vol. 50, pp. 11888-11894, 2016.

[177] J. Xu, Y. Li, X. Zhou, Y. Li, Z.-D. Gao, Y.-Y. Song, and P. Schmuki, "Graphitic C3N4-Sensitized TiO2 Nanotube Layers: A Visible-Light Activated Efficient Metal-Free Antimicrobial Platform," *Chemistry – A European Journal,* vol. 22, pp. 3947-3951, 2016.

[178] Y. K. Kim, S. M. Sharker, I. In, and S. Y. Park, "Surface coated fluorescent carbon nanoparticles/TiO2 as visible-light sensitive photocatalytic complexes for antifouling activity," *Carbon,* vol. 103, pp. 412-420, 2016.

[179] C. Carl, A. J. Poole, M. J. Vucko, M. R. Williams, S. Whalan, and R. de Nys, "Enhancing the efficacy of fouling-release coatings against fouling by Mytilus galloprovincialis using nanofillers," *Biofouling,* vol. 28, pp. 1077-1091, 2012.

[180] J. Zhang, M. Pan, C. Luo, X. Chen, J. Kong, and T. Zhou, "A novel composite paint (TiO2/fluorinated acrylic nanocomposite) for antifouling application in marine environments," *Journal of Environmental Chemical Engineering,* vol. 4, pp. 2545-2555, 2016.

[181] K. S. Novoselov, A. K. Geim, S. V. Morozov, D. Jiang, Y. Zhang, S. V. Dubonos, I. V. Grigorieva, and A. A. Firsov, "Electric Field Effect in Atomically Thin Carbon Films," *Science,* vol. 306, pp. 666-669, 2004.

[182] A. K. Geim and K. S. Novoselov, "The rise of graphene," *Nature Materials,* vol. 6, pp. 183-191, 2007.

[183] J. S. Y. Chia, M. T. T. Tan, P. S. Khiew, J. K. Chin, H. Lee, D. C. S. Bien, and C. W. Siong, "A novel one step synthesis of graphene via sonochemical-assisted solvent exfoliation approach for electrochemical sensing application," *Chemical Engineering Journal,* vol. 249, pp. 270-278, 2014.

[184] J. S. Y. Chia, M. T. T. Tan, P. S. Khiew, J. K. Chin, and C. W. Siong, "A bio-electrochemical sensing platform for glucose based on irreversible, non-covalent pi–pi functionalization of graphene produced via a novel, green

synthesis method," *Sensors and Actuators B: Chemical,* vol. 210, pp. 558-565, 2015.

[185] V. K. Gupta, N. Atar, M. L. Yola, M. Eryılmaz, H. Torul, U. Tamer, İ. H. Boyacı, and Z. Üstündağ, "A novel glucose biosensor platform based on Ag@AuNPs modified graphene oxide nanocomposite and SERS application," *Journal of Colloid and Interface Science,* vol. 406, pp. 231-237, 2013.

[186] X.-Z. Tang, Z. Cao, H.-B. Zhang, J. Liu, and Z.-Z. Yu, "Growth of silver nanocrystals on graphene by simultaneous reduction of graphene oxide and silver ions with a rapid and efficient one-step approach," *Chemical Communications,* vol. 47, pp. 3084-3086, 2011.

[187] M. Zainy, N. M. Huang, S. Vijay Kumar, H. N. Lim, C. H. Chia, and I. Harrison, "Simple and scalable preparation of reduced graphene oxide–silver nanocomposites via rapid thermal treatment," *Materials Letters,* vol. 89, pp. 180-183, 2012.

[188] W.-P. Xu, L.-C. Zhang, J.-P. Li, Y. Lu, H.-H. Li, Y.-N. Ma, W.-D. Wang, and S.-H. Yu, "Facile synthesis of silver@graphene oxide nanocomposites and their enhanced antibacterial properties," *Journal of Materials Chemistry,* vol. 21, pp. 4593-4597, 2011.

[189] A. Reina, X. Jia, J. Ho, D. Nezich, H. Son, V. Bulovic, M. S. Dresselhaus, and J. Kong, "Large Area, Few-Layer Graphene Films on Arbitrary Substrates by Chemical Vapor Deposition," *Nano Letters,* vol. 9, pp. 30-35, 2008.

[190] M. Ishigami, J. H. Chen, W. G. Cullen, M. S. Fuhrer, and E. D. Williams, "Atomic Structure of Graphene on SiO2," *Nano Letters,* vol. 7, pp. 1643-1648, 2007.

[191] M. R. Das, R. K. Sarma, S. C. Borah, R. Kumari, R. Saikia, A. B. Deshmukh, M. V. Shelke, P. Sengupta, S. Szunerits, and R. Boukherroub, "The synthesis of citrate-modified silver nanoparticles in an aqueous suspension of graphene oxide nanosheets and their antibacterial activity," *Colloids and Surfaces B: Biointerfaces,* vol. 105, pp. 128-136, 2013.

[192] M. L. Yola, V. K. Gupta, and N. Atar, "New molecular imprinted voltammetric sensor for determination of ochratoxin A," *Materials Science and Engineering: C,* vol. 61, pp. 368-375, 2016.

[193] V. K. Gupta, M. L. Yola, N. Atar, Z. Üstündağ, and A. O. Solak, "Electrochemical studies on graphene oxide-supported metallic and bimetallic nanoparticles for fuel cell applications," *Journal of Molecular Liquids,* vol. 191, pp. 172-176, 2014.

[194] N. Atar, M. L. Yola, and T. Eren, "Sensitive determination of citrinin based on molecular imprinted electrochemical sensor," *Applied Surface Science,* vol. 362, pp. 315-322, 2016.

[195] M. L. Yola, T. Eren, and N. Atar, "A sensitive molecular imprinted electrochemical sensor based on gold nanoparticles decorated graphene oxide: Application to selective determination of tyrosine in milk," *Sensors and Actuators B: Chemical,* vol. 210, pp. 149-157, 2015.

[196] Y. Zhou, J. Yang, T. He, H. Shi, X. Cheng, and Y. Lu, "Highly Stable and Dispersive Silver Nanoparticle–Graphene Composites by a Simple and Low-Energy-Consuming Approach and Their Antimicrobial Activity," *Small,* vol. 9, pp. 3445-3454, 2013.

[197] Q. Zhuo, Y. Ma, J. Gao, P. Zhang, Y. Xia, Y. Tian, X. Sun, J. Zhong, and X. Sun, "Facile Synthesis of Graphene/Metal Nanoparticle Composites via Self-

Catalysis Reduction at Room Temperature," *Inorganic Chemistry,* vol. 52, pp. 3141-3147, 2013.

[198] K. S. Subrahmanyam, A. K. Manna, S. K. Pati, and C. N. R. Rao, "A study of graphene decorated with metal nanoparticles," *Chemical Physics Letters,* vol. 497, pp. 70-75, 2010.

[199] S. Park and R. S. Ruoff, "Chemical methods for the production of graphenes," *Nature Nanotechnology,* vol. 4, pp. 217-224, 2009.

[200] J. Chen, B. Yao, C. Li, and G. Shi, "An improved Hummers method for eco-friendly synthesis of graphene oxide," *Carbon,* vol. 64, pp. 225-229, 2013.

[201] K. C. Kwon, J. Ham, S. Kim, J.-L. Lee, and S. Y. Kim, "Eco-friendly graphene synthesis on Cu foil electroplated by reusing Cu etchants," *Scientific Reports,* vol. 4:4830, 2014.

[202] D. A. Boyd, W. H. Lin, C. C. Hsu, M. L. Teague, C. C. Chen, Y. Y. Lo, W. Y. Chan, W. B. Su, T. C. Cheng, C. S. Chang, C. I. Wu, and N. C. Yeh, "Single-step deposition of high-mobility graphene at reduced temperatures," *Nature Communications,* vol. 6:6620, 2015.

[203] G. Park, L. Bartolome, K. G. Lee, S. J. Lee, D. H. Kim, and T. J. Park, "One-step sonochemical synthesis of a graphene oxide-manganese oxide nanocomposite for catalytic glycolysis of poly(ethylene terephthalate)," *Nanoscale,* vol. 4, pp. 3879-3885, 2012.

[204] A. B. Searle, *The Use of Colloids in Health and Disease*. London: Constable & Company Ltd, 1920.

[205] M. Rai, A. Yadav, and A. Gade, "Silver nanoparticles as a new generation of antimicrobials," *Biotechnology Advances,* vol. 27, pp. 76-83, 2009.

[206] S. S. Khan, A. Mukherjee, and N. Chandrasekaran, "Studies on interaction of colloidal silver nanoparticles (SNPs) with five different bacterial species," *Colloids and Surfaces B: Biointerfaces,* vol. 87, pp. 129-38, 2011.

[207] D. Inbakandan, C. Kumar, L. S. Abraham, R. Kirubagaran, R. Venkatesan, and S. A. Khan, "Silver nanoparticles with anti microfouling effect: a study against marine biofilm forming bacteria," *Colloids and Surfaces B: Biointerfaces,* vol. 111, pp. 636-643, 2013.

[208] B. Yu, K. M. Leung, Q. Guo, W. M. Lau, and J. Yang, "Synthesis of Ag-TiO2 composite nano thin film for antimicrobial application," *Nanotechnology,* vol. 22, p. 115603, Mar 18 2011.

[209] International_Maritime_Organization. (2002, Anti-fouling systems. *Focus on IMO (15/1/2014),* 1-31. Available: http://www.imo.org/OurWork/Environment/Anti-foulingSystems/Documents/FOULING2003.pdf

[210] I. Banerjee, R. C. Pangule, and R. S. Kane, "Antifouling coatings: recent developments in the design of surfaces that prevent fouling by proteins, bacteria, and marine organisms," *Advanced Materials,* vol. 23, pp. 690-718, 2011.

[211] A. Matin, Z. Khan, S. M. J. Zaidi, and M. C. Boyce, "Biofouling in reverse osmosis membranes for seawater desalination: Phenomena and prevention," *Desalination,* vol. 281, pp. 1-16, 2011.

[212] H. C. Flemming, "Biofouling in water systems--cases, causes and countermeasures," *Applied Microbiology and Biotechnology,* vol. 59, pp. 629-640, 2002.

[213] N. Muthukumar, A. Rajasekar, S. Ponmariappan, S. Mohanan, S. Maruthamuthu, S. Muralidharan, P. Subramanian, N. Palaniswamy, and M.

Raghavan, "Microbiologically influenced corrosion in petroleum product pipelines--a review," *Indian Journal of Experimental Biology,* vol. 41, pp. 1012-1022, 2003.

[214] W. Sand and T. Gehrke, "Extracellular polymeric substances mediate bioleaching/biocorrosion via interfacial processes involving iron(III) ions and acidophilic bacteria," *Research in Microbiology,* vol. 157, pp. 49-56, 2006.

[215] P. J. Krug, "Defense of Benthic Invertebrates Against Surface Colonization by Larvae: A Chemical Arms Race," in *Antifouling Compounds.* vol. 42, N. Fusetani and A. Clare, Eds., ed: Springer Berlin Heidelberg, 2006, pp. 1-53.

[216] R. A. Braithwaite and L. A. McEvoy, "Marine biofouling on fish farms and its remediation," *Advances in Marine Biology,* vol. 47, pp. 215-52, 2005.

[217] B. Q. Liao, D. M. Bagley, H. E. Kraemer, G. G. Leppard, and S. N. Liss, "A review of biofouling and its control in membrane separation bioreactors," *Water Environ Research,* vol. 76, pp. 425-436, 2004.

[218] H. C. Flemming, "Role and levels of real-time monitoring for successful anti-fouling strategies--an overview," *Water Science and Technology,* vol. 47, pp. 1-8, 2003.

[219] P. J. Molino and R. Wetherbee, "The biology of biofouling diatoms and their role in the development of microbial slimes," *Biofouling,* vol. 24, pp. 365-379, 2008.

[220] M. Fletcher, "Attachment of Pseudomonas fluorescens to glass and influence of electrolytes on bacterium-substratum separation distance," *Journal of Bacteriology,* vol. 170, pp. 2027-2030, 1988.

[221] M. G. Hadfield, "Biofilms and marine invertebrate larvae: what bacteria produce that larvae use to choose settlement sites," *Annual Review of Marine Science,* vol. 3, pp. 453-470, 2011.

[222] J. A. Callow and M. E. Callow, "Biofilms," *Progress in Molecular and Subcellular Biology,* vol. 42, pp. 141-169, 2006.

[223] A. I. Railkin, *Marine Biofouling: Colonization Processes and Defenses*. Boca Raton, Florida, USA: CRC Press, 2004.

[224] E. Subramanyam, S. Mohandoss, and H.-W. Shin, "Synthesis, characterization, and evaluation of antifouling polymers of 4-acryloyloxybenzaldehyde with methyl methacrylate," *Journal of Applied Polymer Science,* vol. 112, pp. 2741-2749, 2009.

[225] L. K. Ista, M. E. Callow, J. A. Finlay, S. E. Coleman, A. C. Nolasco, R. H. Simons, J. A. Callow, and G. P. Lopez, "Effect of Substratum Surface Chemistry and Surface Energy on Attachment of Marine Bacteria and Algal Spores," *Applied and Environmental Microbiology,* vol. 70, pp. 4151-4157, 2004.

[226] N. Ismail, F. Nadzari, A. G. Izzatul Huda, A. R. Nazeerah, M. Taib, A. Chatterji, and A. Shamsuddin, "Potential of antibacterial and antifouling from horseshoe crabs, Tachypleus gigas and Carcinoscorpius rotundicauda against gram-positive and negative bacteria," in *Universiti Malaysia Terengganu 10th International Annual Symposium (UMTAS 2011)*, Universiti Malaysia Terengganu, 2011, pp. 717-720.

[227] B. Ortega-Morales, M. Chan-Bacab, E. Miranda-Tello, M.-L. Fardeau, J. Carrero, and T. Stein, "Antifouling activity of sessile bacilli derived from marine surfaces," *Journal of Industrial Microbiology & Biotechnology,* vol. 35, pp. 9-15, 2008.

[228] C. Melander, P. D. R. Moeller, T. E. Ballard, J. J. Richards, R. W. Huigens, and J. Cavanagh, "Evaluation of dihydrooroidin as an antifouling additive in marine paint," *International Biodeterioration and Biodegradation,* vol. 63, pp. 529-532, 2009.

[229] D. P. Bakker, J. W. Klijnstra, H. J. Busscher, and H. C. van der Mei, "The effect of dissolved organic carbon on bacterial adhesion to conditioning films adsorbed on glass from natural seawater collected during different seasons," *Biofouling,* vol. 19, pp. 391-397, 2003.

[230] S.-H. Qi, Y. Xu, H.-R. Xiong, P.-Y. Qian, and S. Zhang, "Antifouling and antibacterial compounds from a marine fungus <i>Cladosporium sp. F14," *World Journal of Microbiology and Biotechnology,* vol. 25, pp. 399-406, 2009.

[231] G. Zanaroli, A. Negroni, C. Calisti, M. Ruzzi, and F. Fava, "Selection of commercial hydrolytic enzymes with potential antifouling activity in marine environments," *Enzyme and Microbial Technology,* vol. 49, pp. 574-579, 2011.

[232] M. Löschau and R. Krätke, "Efficacy and toxicity of self-polishing biocide-free antifouling paints," *Environmental Pollution,* vol. 138, pp. 260-267, 2005.

[233] C. Grandison, A. Scardino, and S. Ovenden, "An Investigation of the Antifouling Potential of Extracts of the Periostracum of Mytilus sp.," DSTO Defence Sciece and Technology Organisation, Australia2011.

[234] J. Ren, P. Han, H. Wei, and L. Jia, "Fouling-Resistant Behavior of Silver Nanoparticle-Modified Surfaces against the Bioadhesion of Microalgae," *ACS Applied Materials & Interfaces,* vol. 6, pp. 3829-3838, 2014.

[235] J. W. Bartels, P. M. Imbesi, J. A. Finlay, C. Fidge, J. Ma, J. E. Seppala, A. M. Nystrom, M. E. Mackay, J. A. Callow, M. E. Callow, and K. L. Wooley, "Antibiofouling Hybrid Dendritic Boltorn/Star PEG Thiol-ene Cross-Linked Networks," *ACS Applied Materials & Interfaces,* vol. 3, pp. 2118-2129, 2011.

[236] M. Heydt, A. Rosenhahn, M. Grunze, M. Pettitt, M. E. Callow, and J. A. Callow, "Digital In-Line Holography as a Three-Dimensional Tool to Study Motile Marine Organisms During Their Exploration of Surfaces," *The Journal of Adhesion,* vol. 83, pp. 417-430, 2007.

[237] A. I. Railkin, "Behavioral and physiological responses of hydroid polyps and bivalves to some antifouling compounds," *Hydrobiological Journal,* vol. 31, p. 66, 1995.

[238] M. Zapata, F. Silva, Y. Luza, M. Wilkens, and C. Riquelme, "The inhibitory effect of biofilms produced by wild bacterial isolates to the larval settlement of the fouling ascidia Ciona intestinalis and Pyura praeputialis," *Electronic Journal of Biotechnology,* vol. 10, pp. 117-126, 2007.

[239] M. Tasso, S. L. Conlan, A. S. Clare, and C. Werner, "Active Enzyme Nanocoatings Affect Settlement of Balanus amphitrite Barnacle Cyprids," *Advanced Functional Materials,* vol. 22, pp. 39-47, 2012.

[240] F. Garaventa, C. Corra, V. Piazza, E. Giacco, G. Greco, L. Pane, and M. Faimali, "Settlement of the alien mollusc Brachidontes pharaonis in a Mediterranean industrial plant: Bioassays for antifouling treatment optimization and management," *Marine Environmental Research,* vol. 76, pp. 1-7, 2012.

[241] G. Blustein, M. Pérez, M. García, M. Stupak, and C. Cerruti, "Reversible effect of potassium sorbate on Balanus amphitrite larvae. Potential use as antifoulant," *Biofouling,* vol. 25, pp. 573-580, 2009.

[242] N. Aldred, I. Y. Phang, S. L. Conlan, A. S. Clare, and G. J. Vancso, "The effects of a serine protease, Alcalase®, on the adhesives of barnacle cyprids (Balanus amphitrite)," *Biofouling,* vol. 24, pp. 97-107, 2008.

[243] B. del Amo, G. Blustein, M. Pérez, M. García, M. Deyá, M. Stupak, and R. Romagnoli, "A multipurpose compound for protective coatings," *Colloids and Surfaces A: Physicochemical and Engineering Aspects,* vol. 324, pp. 58-64, 2008.

[244] S. Ortlepp, M. Sjögren, M. Dahlström, H. Weber, R. Ebel, R. Edrada, C. Thoms, P. Schupp, L. Bohlin, and P. Proksch, "Antifouling Activity of Bromotyrosine-Derived Sponge Metabolites and Synthetic Analogues," *Marine Biotechnology,* vol. 9, pp. 776-785, 2007.

[245] S. Ananda Kumar and A. Sasikumar, "Studies on novel silicone/phosphorus/sulphur containing nano-hybrid epoxy anticorrosive and antifouling coatings," *Progress in Organic Coatings,* pp. 189-200, 2010.

[246] L. D. Chambers, K. R. Stokes, F. C. Walsh, and R. J. K. Wood, "Modern approaches to marine antifouling coatings," *Surface & Coatings Technology,* pp. 3642-3652, 2006.

[247] G. S. Bohlander, "Biofilm effects on drag: measurements on ships," *The Institute of Marine Engineers Third International Conference Polymers in a Marine Environment,* vol. 103, pp. 135-138, 1991.

[248] WHOI, "The Effects of Fouling," in *Marine Fouling and Its Prevention*, ed Menasha, Wisconsin, USA: George Banta Publishing Co., 1952, pp. 3-19.

[249] R. F. Piola, K. A. Dafforn, and E. L. Johnston, "The influence of antifouling practices on marine invasions," *Biofouling,* vol. 25, pp. 633-644, 2009.

[250] L. S. Godwin, "Hull fouling of maritime vessels as a pathway for marine species invasions to the Hawaiian Islands," *Biofouling,* vol. 19 Suppl, pp. 123-131, 2003.

[251] S. Gollasch, "Assessment of the introduction potential of aquatic alien species in new environments," in *Assessment and Control of Biological Invasion Risks*, F. Koike, M. N. Clout, M. Kawamichi, M. De Poorter, and K. Iwatsuki, Eds., ed. Gland, Switzerland: World Conservation Union (IUCN), 2006, pp. 88-91.

[252] A. Turner, "Marine pollution from antifouling paint particles," *Marine Pollution Bulletin,* vol. 60, pp. 159-171, 2010.

[253] P. Y. Qian, S. Lau, H. U. Dahms, S. Dobretsov, and T. Harder, "Marine Biofilms as Mediators of Colonization by Marine Macroorganisms: Implications for Antifouling and Aquaculture," *Marine Biotechnology,* vol. 9, pp. 399-410, 2007.

[254] W. Cai, J. Wu, C. Xi, and M. E. Meyerhoff, "Diazeniumdiolate-doped poly(lactic-co-glycolic acid)-based nitric oxide releasing films as antibiofilm coatings," *Biomaterials,* vol. 33, pp. 7933-7944, 2012.

[255] ORTEP_Association. (2012, 1 August 2012). *Types of Tributyltin Paints*. Available: http://www.ortepa.org/pages/b1pt5.htm

[256] L. Martensson. (2005, 18 December 2012). *Marine biofouling - a sticky problem or Gluing in seawater*. Available: http://www.bioscience-explained.org/ENvol2_2/pdf/barnaceng.pdf

[257] A. Rosenhahn, T. Ederth, and M. E. Pettitt, "Advanced nanostructures for the control of biofouling: The FP6 EU Integrated Project AMBIO," *Biointerphases,* vol. 3, pp. IR1-5, 2008.

[258] N. Voulvoulis, M. D. Scrimshaw, and J. N. Lester, "Comparative environmental assessment of biocides used in antifouling paints," *Chemosphere,* vol. 47, pp. 789-795, 2002.

[259] I. K. Konstantinou and T. A. Albanis, "Worldwide occurrence and effects of antifouling paint booster biocides in the aquatic environment: a review," *Environment International,* vol. 30, pp. 235-248, 2004.

[260] V. W. W. Bao, K. M. Y. Leung, J. W. Qiu, and M. H. W. Lam, "Acute toxicities of five commonly used antifouling booster biocides to selected subtropical and cosmopolitan marine species," *Marine Pollution Bulletin,* vol. 62, pp. 1147-1151, 2011.

[261] J. Genzer and K. Efimenko, "Recent developments in superhydrophobic surfaces and their relevance to marine fouling: a review," *Biofouling,* vol. 22, pp. 339-60, 2006.

[262] C. M. Magin, S. P. Cooper, and A. B. Brennan, "Non-toxic antifouling strategies," *Materials Today,* vol. 13, pp. 36-44, 2010.

[263] J. B. Kristensen, R. L. Meyer, B. S. Laursen, S. Shipovskov, F. Besenbacher, and C. H. Poulsen, "Antifouling enzymes and the biochemistry of marine settlement," *Biotechnology Advances,* vol. 26, pp. 471-81, 2008.

[264] P.-Y. Qian, Y. Xu, and N. Fusetani, "Natural products as antifouling compounds: recent progress and future perspectives," *Biofouling,* vol. 26, pp. 223-234, 2009.

[265] K. Sepcic and T. Turk, "3-Alkylpyridinium compounds as potential non-toxic antifouling agents," *Progress in Molecular and Subcellular Biology,* vol. 42, pp. 105-124, 2006.

[266] E. K. Oikonomou, Z. Iatridi, M. Moschakou, P. Damigos, G. Bokias, and J. K. Kallitsis, "Development of Cu^{2+}- and/or phosphonium-based polymeric biocidal materials and their potential application in antifouling paints," *Progress in Organic Coatings,* vol. 75, pp. 190-199, 2012.

[267] C. Ma, H. Yang, X. Zhou, B. Wu, and G. Zhang, "Polymeric material for anti-biofouling," *Colloids and Surfaces B: Biointerfaces,* vol. 100, pp. 31-35, 2012.

[268] J. H. Merritt, D. E. Kadouri, and G. A. O'Toole, "Growing and Analyzing Static Biofilms," in *Current Protocols in Microbiology*, ed: John Wiley & Sons, Inc., 2005.

[269] E. Armstrong, K. G. Boyd, and J. G. Burgess, "Prevention of marine biofouling using natural compounds from marine organisms," *Biotechnology Annual Review,* vol. 6, pp. 221-41, 2000.

[270] D. Rittschof, A. S. Clare, D. J. Gerhart, S. A. Mary, and J. Bonaventura, "Barnacle in vitro assays for biologically active substances: Toxicity and Settlement inhibition assays using mass cultured Balanus amphitrite amphitrite darwin," *Biofouling,* vol. 6, pp. 115-122, 1992.

[271] J. R. Lauth, D. S. Cherry, A. L. Buikema, and G. I. Scott, "A modular estuarine mesocosm," *Environmental Toxicology and Chemistry,* vol. 15, pp. 630-637, 1996.

[272] CMRF. (2016, 11/4/2016). *Transmission Electron Microscopy*. Available: http://cmrf.research.uiowa.edu/transmission-electron-microscopy

[273] B. D. Cullity, *Elements of X-ray Diffraction*. Massachusetts, USA: Addison-Wesley Publishing Co., 1956.

[274] E. J. Mittemeijer and U. Welzel, "The "state of the art" of the diffraction analysis of crystallite size and lattice strain," *Zeitschrift Fur Kristallographie,* vol. 223, pp. 552-560, 2008.

[275] U. Holzwarth and N. Gibson, "The Scherrer equation versus the 'Debye-Scherrer equation'," *Nature Nanotechnology,* vol. 6, pp. 534-534, 2011.

[276] J. I. Langford and A. J. C. Wilson, "Scherrer after sixty years: A survey and some new results in the determination of crystallite size," *Journal of Applied Crystallography,* vol. 11, pp. 102-113, 1978.

[277] S. A. Speakman. (2013). *Estimating Crystallite Size Using XRD*. Available: www.ncl.ac.uk/acma/resources/documents/MIT_CrystalSizeAnalysis_SpeakmanS.pptx

[278] S. Lowell, *Introduction to Powder Surface Area*. New York: John Wiley & Sons, 1979.

[279] Micromeritics. (2017). *Surface Area Webinar 2017*. Available: https://www.youtube.com/watch?v=rlF2ortLqJ8&feature=youtu.be

[280] Mettler-Toledo. (2013). *Thermal Analysis of Polymers Selected Applications*. Available: http://us.mt.com/dam/non-indexed/po/ana/thermal-analysis/TA_Polymers_EN.pdf

[281] L. M. Malard, M. A. Pimenta, G. Dresselhaus, and M. S. Dresselhaus, "Raman spectroscopy in graphene," *Physics Reports,* vol. 473, pp. 51-87, 2009.

[282] Z. Xu and G. Hu, "Simple and green synthesis of monodisperse silver nanoparticles and surface-enhanced Raman scattering activity," *RSC Advances,* vol. 2, pp. 11404-11409, 2012.

[283] Invitrogen. (2010). *PrestoBlue (TM) Cell Viability Reagent Protocol Product Information Sheet*. Available: https://tools.thermofisher.com/content/sfs/manuals/PrestoBlue_Reagent_PIS_15Oct10.pdf

[284] I. M. Abrams and J. R. Millar, "A history of the origin and development of macroporous ion-exchange resins," *Reactive and Functional Polymers,* vol. 35, pp. 7-22, 1997.

[285] S. D. Alexandratos, "Ion-exchange resins: a retrospective from industrial and engineering chemistry research," *Industrial & Engineering Chemistry Research,* vol. 48, pp. 388-398, 2009.

[286] X. Guo, R.-K. Chang, and M. A. Hussain, "Ion-exchange resins as drug delivery carriers," *Journal of Pharmaceutical Sciences,* vol. 98, pp. 3886-3902, 2009.

[287] D. Alchin and H. Wansborough. (2002, 21/4/2016). Ion Exchange Resins. Available: http://nzic.org.nz/ChemProcesses/water/13D.pdf

[288] J. C. Hoh and I. I. Yaacob, "Polymer matrix templated synthesis: Cobalt ferrite nanoparticles preparation," *Journal of Materials Research,* vol. 17, pp. 3105-3109, 2002.

[289] J. Ellison, G. Wykoff, A. Paul, R. Mohseni, and A. Vasiliev, "Efficient dispersion of coated silver nanoparticles in the polymer matrix," *Colloids and Surfaces A: Physicochemical and Engineering Aspects,* vol. 447, pp. 67-70, 2014.

[290] P.-L. Kuo and W.-F. Chen, "Formation of Silver Nanoparticles under Structured Amino Groups in Pseudo-dendritic Poly(allylamine) Derivatives," *The Journal of Physical Chemistry B,* vol. 107, pp. 11267-11272, 2003.

[291] Q. Li, S. Mahendra, D. Y. Lyon, L. Brunet, M. V. Liga, D. Li, and P. J. Alvarez, "Antimicrobial nanomaterials for water disinfection and microbial control: potential applications and implications," *Water Research,* vol. 42, pp. 4591-602, 2008.

[292] K.-H. Cho, J.-E. Park, T. Osaka, and S.-G. Park, "The study of antimicrobial activity and preservative effects of nanosilver ingredient," *Electrochimica Acta,* vol. 51, pp. 956-960, 2005.

[293] Z. Hubicki and D. Kołodyńska, "Selective Removal of Heavy Metal Ions from Waters and Waste Waters Using Ion Exchange Methods," in *Ion Exchange Technologies*, A. Kilislioğlu, Ed., ed: InTech, 2012, pp. 193-240.

[294] A. Alonso, J. Macanas, A. Shafir, M. Munoz, A. Vallribera, D. Prodius, S. Melnic, C. Turta, and D. N. Muraviev, "Donnan-exclusion-driven distribution of catalytic ferromagnetic nanoparticles synthesized in polymeric fibers," *Dalton Transactions,* vol. 39, pp. 2579-2586, 2010.

[295] R. Stiufiuc, C. Iacovita, C. Lucaciu, G. Stiufiuc, A. Dutu, C. Braescu, and N. Leopold, "SERS-active silver colloids prepared by reduction of silver nitrate with short-chain polyethylene glycol," *Nanoscale Research Letters,* vol. 8, p. 47, 2013.

[296] T. Senoy, K. N. Saritha, E. M. A. Jamal, S. H. Al-Harthi, V. Manoj Raama, and M. R. Anantharaman, "Size-dependent surface plasmon resonance in silver silica nanocomposites," *Nanotechnology,* vol. 19, p. 075710, 2008.

[297] K. A. Juby, C. Dwivedi, M. Kumar, S. Kota, H. S. Misra, and P. N. Bajaj, "Silver nanoparticle-loaded PVA/gum acacia hydrogel: Synthesis, characterization and antibacterial study," *Carbohydrate Polymers,* vol. 89, pp. 906-913, 2012.

[298] I. B. Beech, J. A. Sunner, and K. Hiraoka, "Microbe-surface interactions in biofouling and biocorrosion processes," *International Microbiology,* vol. 8, pp. 157-68, 2005.

[299] Q. Sun, X. Cai, J. Li, M. Zheng, Z. Chen, and C.-P. Yu, "Green synthesis of silver nanoparticles using tea leaf extract and evaluation of their stability and antibacterial activity," *Colloids and Surfaces A: Physicochemical and Engineering Aspects,* vol. 444, pp. 226-231, 2014.

[300] L. Guo, W. Yuan, Z. Lu, and C. M. Li, "Polymer/nanosilver composite coatings for antibacterial applications," *Colloids and Surfaces A: Physicochemical and Engineering Aspects,* vol. 439, pp. 69-83, 2013.

[301] R. Bhattacharya and P. Mukherjee, "Biological properties of "naked" metal nanoparticles," *Advanced Drug Delivery Reviews,* vol. 60, pp. 1289-1306, 2008.

[302] M. S.-L. Yee, P. S. Khiew, Y. F. Tan, Y.-Y. Kok, K. W. Cheong, W. S. Chiu, and C.-O. Leong, "Potent antifouling silver-polymer nanocomposite microspheres using ion-exchange resin as templating matrix," *Colloids and Surfaces A: Physicochemical and Engineering Aspects,* vol. 457, pp. 382-391, 2014.

[303] IUPAC, "Recommendations for the characterization of porous solids," *Pure & Appl. Chem.,* vol. 66, pp. 1739-1758, 1994.

[304] D. W. Breck, *Zeolite Molecular Sieves: Structure, Chemistry, and Use*. New York: John Wiley & Sons, Inc., 1974.

[305] G. T. Kokotailo, S. L. Lawton, D. H. Olson, and W. M. Meier, "Structure of synthetic zeolite ZSM-5," *Nature,* vol. 272, pp. 437-438, 1978.

[306] S. J. Oldenburg. (2012, 28 November 2012). *Silver nanoparticles: properties and applications*. Available: http://www.sigmaaldrich.com/materials-science/nanomaterials/silver-nanoparticles.html

[307] Z. S. Pillai and P. V. Kamat, "What factors control the size and shape of silver nanoparticles in the citrate ion reduction method?," *The Journal of Physical Chemistry B,* vol. 108, pp. 945-951, 2004.

[308] P. Lalueza, M. Monzon, M. Arruebo, and J. Santamaria, "Antibacterial action of Ag-containing MFI zeolite at low Ag loadings," *Chemical Communications,* vol. 47, pp. 680-682, 2011.

[309] S.-W. Baek, J.-R. Kim, and S.-K. Ihm, "Design of dual functional adsorbent/catalyst system for the control of VOC's by using metal-loaded hydrophobic Y-zeolites," *Catalysis Today,* vol. 93–95, pp. 575-581, 2004.

[310] H.-H. Cheng, C.-C. Hsieh, and C.-H. Tsai, "Antibacterial and regenerated characteristics of Ag-zeolite for removing bioaerosols in indoor environment," *Aerosol and Air Quality Research,* vol. 12, pp. 409-419, 2012.

[311] D. V. Bavykin, J. M. Friedrich, and F. C. Walsh, "Protonated Titanates and TiO2 Nanostructured Materials: Synthesis, Properties, and Applications," *Advanced Materials,* vol. 18, pp. 2807-2824, 2006.

[312] P. Roy, S. Berger, and P. Schmuki, "TiO2 nanotubes: synthesis and applications," *Angewandte Chemie International Edition,* vol. 50, pp. 2904-2939, 2011.

[313] B. Zhu, X. Zhang, S. Wang, S. Zhang, S. Wu, and W. Huang, "Synthesis and catalytic performance of TiO2 nanotubes-supported copper oxide for low-temperature CO oxidation," *Microporous and Mesoporous Materials,* vol. 102, pp. 333-336, 2007.

[314] X. Sun and Y. Li, "Synthesis and characterization of ion-exchangeable titanate nanotubes," *Chemistry,* vol. 9, pp. 2229-2238, 2003.

[315] Q. Chen, G. H. Du, S. Zhang, and L. Peng, "The structure of trititanate nanotubes," *Acta Crystallogr B,* vol. 58, pp. 587-593, 2002.

[316] D. V. Bavykin, E. V. Milsom, F. Marken, D. H. Kim, D. H. Marsh, D. J. Riley, F. C. Walsh, K. H. El-Abiary, and A. A. Lapkin, "A novel cation-binding TiO2 nanotube substrate for electro- and bioelectro-catalysis," *Electrochemistry Communications,* vol. 7, pp. 1050-1058, 2005.

[317] E. Morgado, Jr., P. M. Jardim, A. M. Bojan, C. R. Fernando, A. S. d. A. Marco, L. Z. José, and S. A. Antonio, "Multistep structural transition of hydrogen trititanate nanotubes into TiO 2 - B nanotubes: a comparison study between nanostructured and bulk materials," *Nanotechnology,* vol. 18, p. 495710, 2007.

[318] A. Henglein and M. Giersig, "Formation of Colloidal Silver Nanoparticles: Capping Action of Citrate," *The Journal of Physical Chemistry B,* vol. 103, pp. 9533-9539, 1999.

[319] Z. Zhang, T. M. Nenoff, J. Y. Huang, D. T. Berry, and P. P. Provencio, "Room Temperature Synthesis of Thermally Immiscible Ag−Ni Nanoalloys," *The Journal of Physical Chemistry C,* vol. 113, pp. 1155-1159, 2009.

[320] Z. Zhang, T. M. Nenoff, K. Leung, S. R. Ferreira, J. Y. Huang, D. T. Berry, P. P. Provencio, and R. Stumpf, "Room-Temperature Synthesis of Ag−Ni and Pd−Ni Alloy Nanoparticles," *The Journal of Physical Chemistry C,* vol. 114, pp. 14309-14318, 2010.

[321] K. Zhou, Y. Zhu, X. Yang, X. Jiang, and C. Li, "Preparation of graphene-TiO2 composites with enhanced photocatalytic activity," *New Journal of Chemistry,* vol. 35, pp. 353-359, 2011.

[322] A. Panáček, L. Kvítek, R. Prucek, M. Kolář, R. Večeřová, N. Pizúrová, V. K. Sharma, T. Nevěčná, and R. Zbořil, "Silver Colloid Nanoparticles: Synthesis,

Characterization, and Their Antibacterial Activity," *The Journal of Physical Chemistry B,* vol. 110, pp. 16248-16253, 2006.

[323]   S. Bohm, "Graphene against corrosion," *Nature Nanotechnology,* vol. 9, pp. 741-742, 2014.

[324]   J.-H. Ahn and B. H. Hong, "Graphene for displays that bend," *Nature Nanotechnology,* vol. 9, pp. 737-738, 2014.

[325]   J. Liu, "Charging graphene for energy," *Nature Nanotechnology,* vol. 9, pp. 739-741, 2014.

[326]   F. Torrisi and J. N. Coleman, "Electrifying inks with 2D materials," *Nature Nanotechnology,* vol. 9, pp. 738-739, 2014.

[327]   K. Kostarelos and K. S. Novoselov, "Graphene devices for life," *Nature Nanotechnology,* vol. 9, pp. 744-745, 2014.

[328]   M. Drndic, "Sequencing with graphene pores," *Nature Nanotechnology,* vol. 9, pp. 743-743, 2014.

[329]   E. J. Siochi, "Graphene in the sky and beyond," *Nature Nanotechnology,* vol. 9, pp. 745-747, 2014.

[330]   P. Avouris and C. Dimitrakopoulos, "Graphene: synthesis and applications," *Materials Today,* vol. 15, pp. 86-97, 2012.

[331]   W. S. Hummers and R. E. Offeman, "Preparation of Graphitic Oxide," *Journal of the American Chemical Society,* vol. 80, pp. 1339-1339, 1958.

[332]   W. Gao, "Chapter 15: Graphite Oxide," in *Springer Handbook of Nanomaterials*, R. E. Vajtai, Ed., ed Berlin Heidelberg: Springer-Verlag, 2013, pp. 571-604.

[333]   Y. Hernandez, V. Nicolosi, M. Lotya, F. M. Blighe, Z. Sun, S. De, I. T. McGovern, B. Holland, M. Byrne, Y. K. Gun'Ko, J. J. Boland, P. Niraj, G. Duesberg, S. Krishnamurthy, R. Goodhue, J. Hutchison, V. Scardaci, A. C. Ferrari, and J. N. Coleman, "High-yield production of graphene by liquid-phase exfoliation of graphite," *Nature Nanotechnology,* vol. 3, pp. 563-568, 2008.

[334]   C. Xu, X. Wang, and J. Zhu, "Graphene−Metal Particle Nanocomposites," *The Journal of Physical Chemistry C,* vol. 112, pp. 19841-19845, 2008.

[335]   H.-W. Tien, Y.-L. Huang, S.-Y. Yang, J.-Y. Wang, and C.-C. M. Ma, "The production of graphene nanosheets decorated with silver nanoparticles for use in transparent, conductive films," *Carbon,* vol. 49, pp. 1550-1560, 2011.

[336]   H.-W. Tien, S.-T. Hsiao, W.-H. Liao, Y.-H. Yu, F.-C. Lin, Y.-S. Wang, S.-M. Li, and C.-C. M. Ma, "Using self-assembly to prepare a graphene-silver nanowire hybrid film that is transparent and electrically conductive," *Carbon,* vol. 58, pp. 198-207, 2013.

[337]   S. Liu, J. Tian, L. Wang, and X. Sun, "Microwave-assisted rapid synthesis of Ag nanoparticles/graphene nanosheet composites and their application for hydrogen peroxide detection," *Journal of Nanoparticle Research,* vol. 13, pp. 4539-4548, 2011.

[338]   W. Xialie, W. Xiaohong, L. Zhanpeng, T. Yi, Y. Ye, and Z. Ping, "Rapid and efficient synthesis of soluble graphene nanosheets using N -methyl- p -aminophenol sulfate as a reducing agent," *Nanotechnology,* vol. 23, p. 485604, 2012.

[339]   J. Guo, T. Zhang, C. Hu, and L. Fu, "A three-dimensional nitrogen-doped graphene structure: a highly efficient carrier of enzymes for biosensors," *Nanoscale,* vol. 7, pp. 1290-1295, 2015.

[340] Y. Zhang, B. Walkenfort, J. H. Yoon, S. Schlucker, and W. Xie, "Gold and silver nanoparticle monomers are non-SERS-active: a negative experimental study with silica-encapsulated Raman-reporter-coated metal colloids," *Physical Chemistry Chemical Physics,* vol. 17, pp. 21120-21126, 2015.

[341] G. Naja, P. Bouvrette, S. Hrapovic, and J. H. T. Luong, "Raman-based detection of bacteria using silver nanoparticles conjugated with antibodies," *Analyst,* vol. 132, pp. 679-686, 2007.

[342] D. Rittschof, "Research on Practical Environmentally Benign Antifouling Coatings," in *Biofouling*, S. Dürr and J. C. Thomason, Eds., ed: Wiley-Blackwell, 2010, pp. 396 - 409.

[343] C. Pretti, M. Oliva, R. D. Pietro, G. Monni, G. Cevasco, F. Chiellini, C. Pomelli, and C. Chiappe, "Ecotoxicity of pristine graphene to marine organisms," *Ecotoxicology and Environmental Safety,* vol. 101, pp. 138-145, 2014.

TGA and DTG curves for Ag-PNC samples

Figure A1: TGA and DTG curves for the Dowex polymeric ion exchange resin.
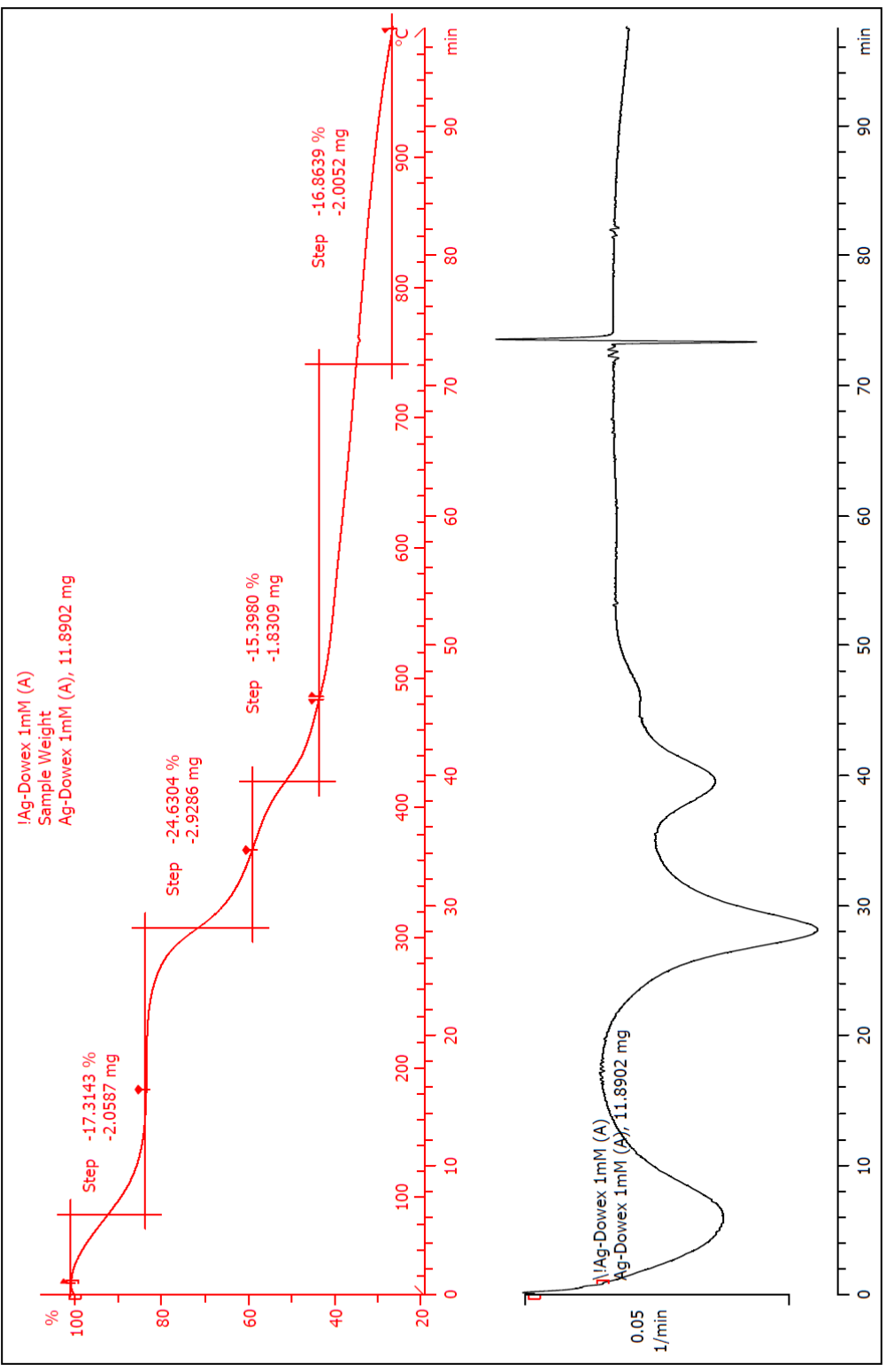
Figure A2: TGA and DTG curves for Ag-PNC-1.
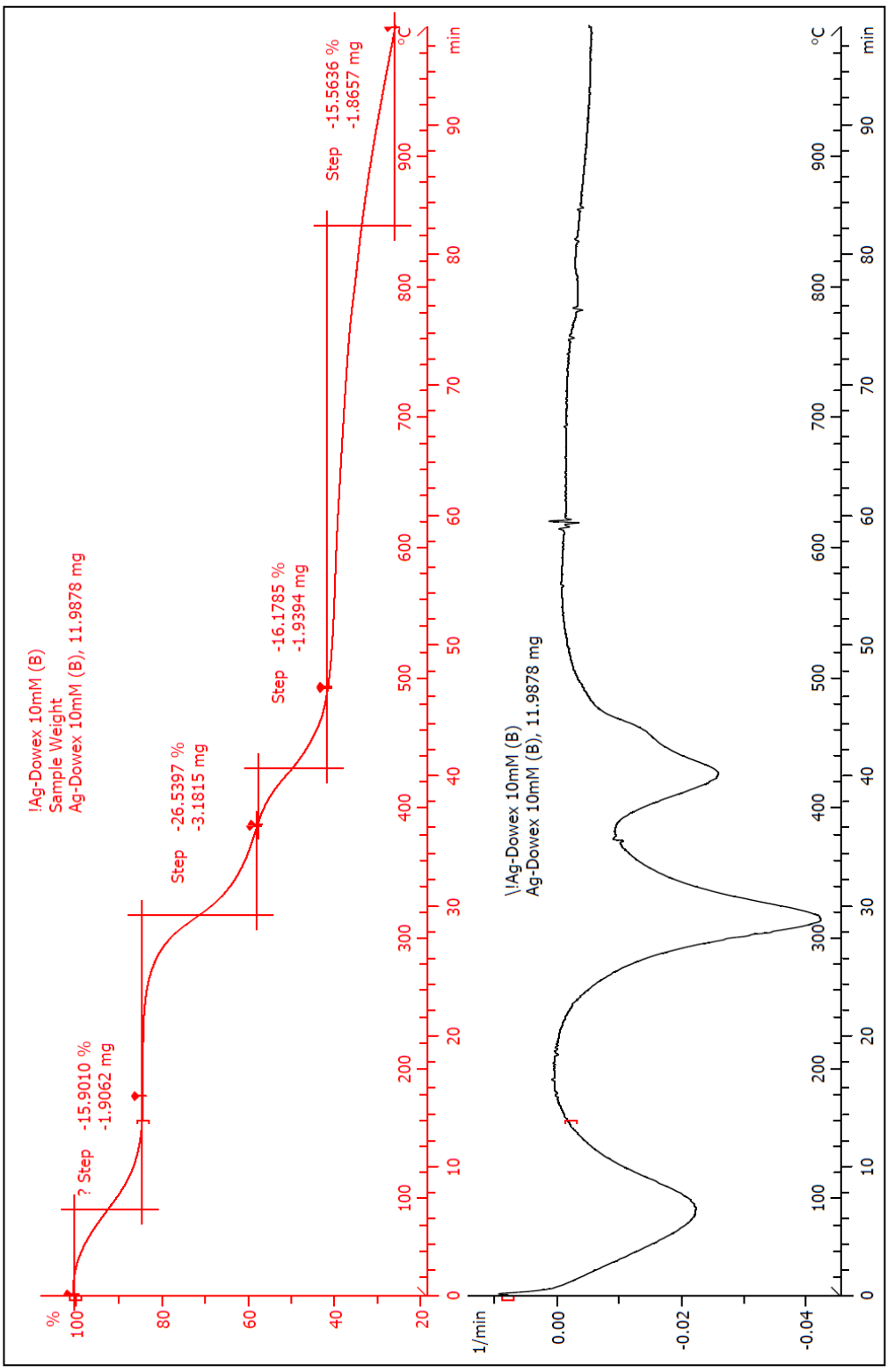
Figure A3: TGA and DTG curves for Ag-PNC-2.
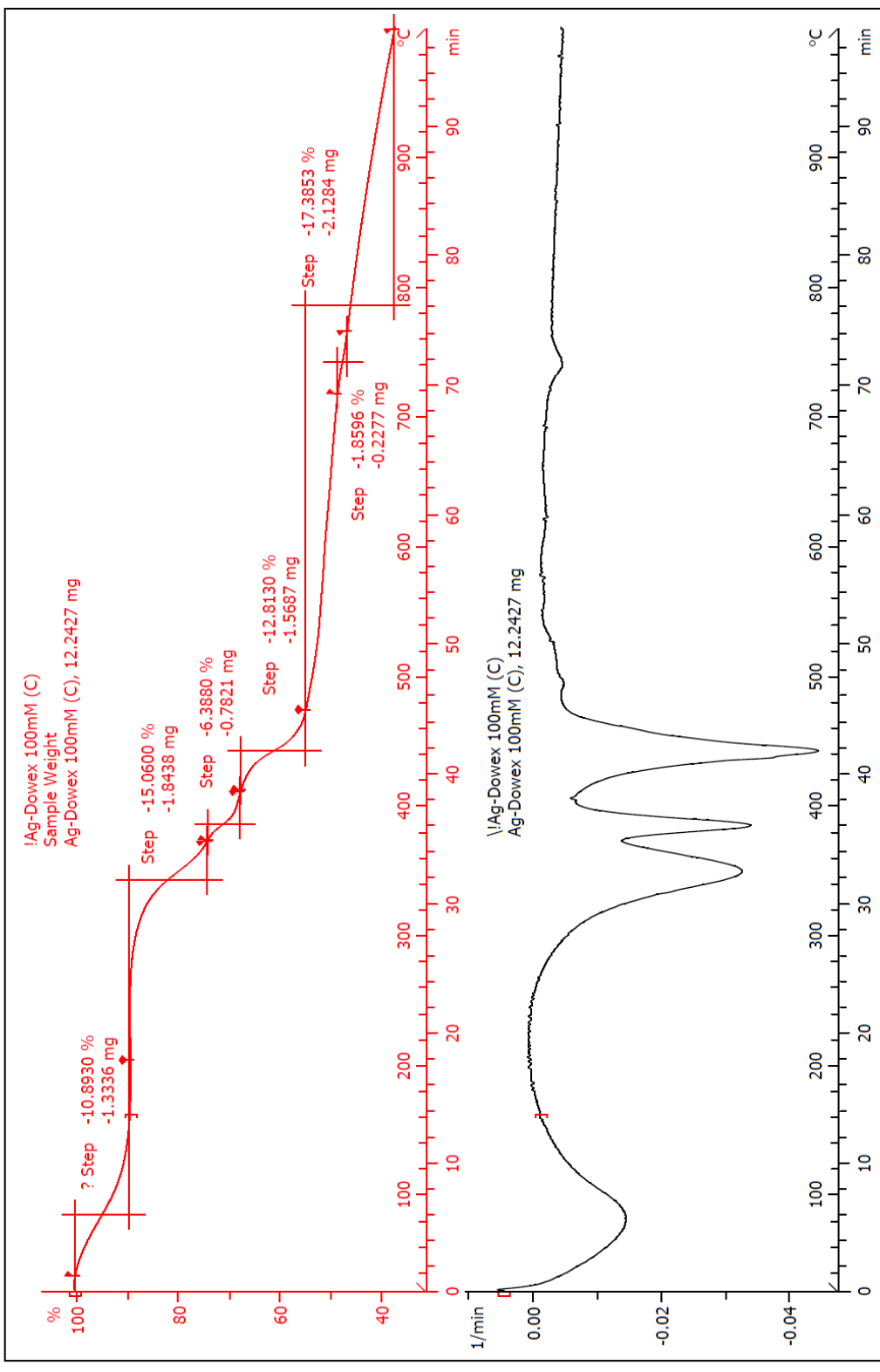
Figure A4: TGA and DTG curves for Ag-PNC-3.
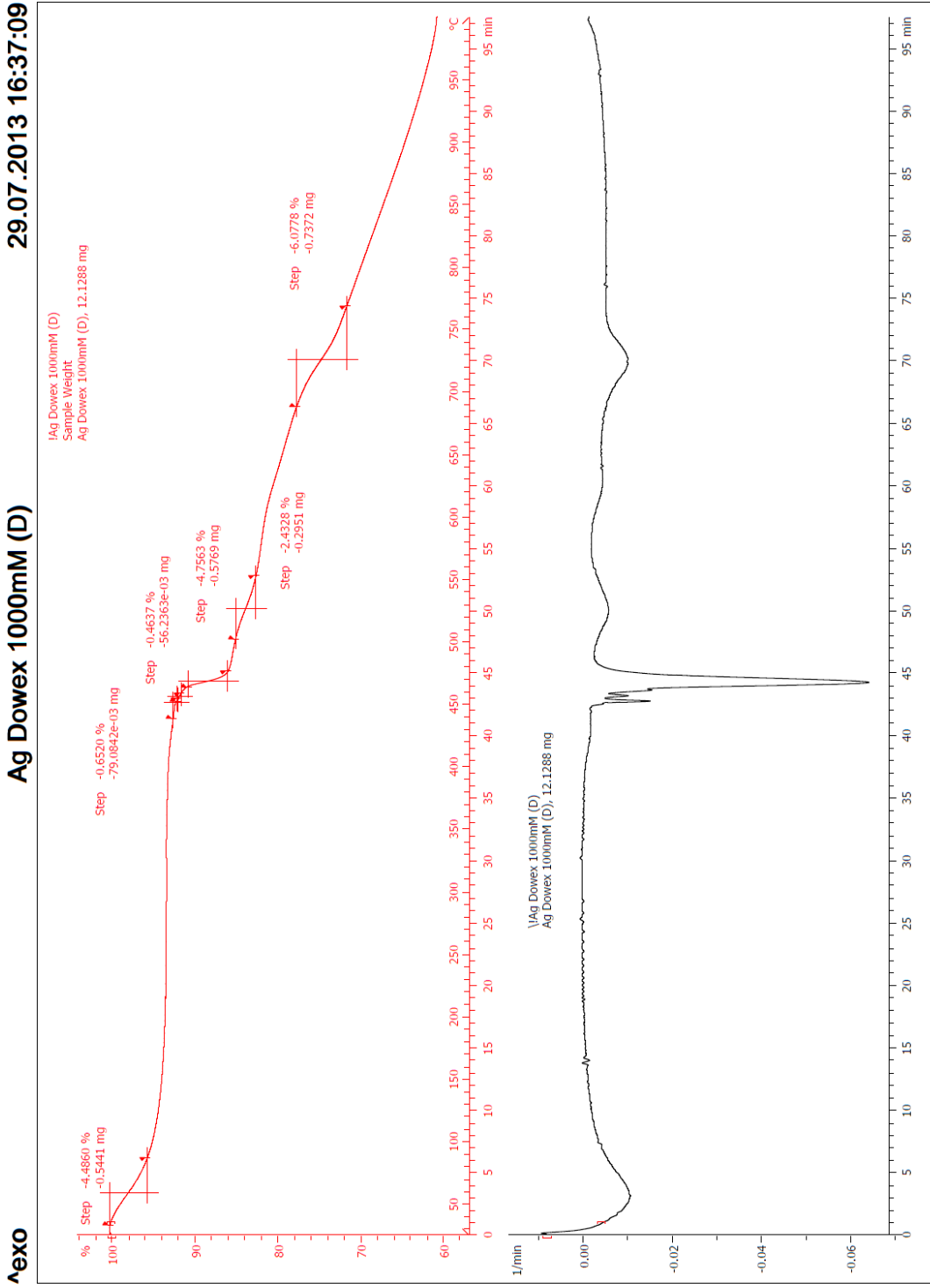
Figure A5: TGA and DTG curves for Ag-PNC-4.